Experimental And Theoretical Studies On The Nucleation, Growth and Habit Modification of Some Inorganic Carbonates, Phosphates and Sulphates

Paul Meenan

Department of Pure and Applied Chemistry,
University of Strathclyde.

Degree of Doctor of Philosophy
1992

To my parents, family and friends

Acknowledgements

I would like to thank my supervisors Dr. K.J. Roberts (University of Strathclyde), Dr. P.C. Knight and Dr. K.R. Yuregir (Unilever Research) for their support during this project. I am deeply indebted to Dr. R. Docherty (ICI Colours and Fine Chemicals), Dr. A.R. Gerson (Exxon Chemicals), Dr. R.A. Jackson (University of Keele) and Dr. G. Clydesdale (University of Strathclyde) for their useful advice and encouragement throughout this project. I would also like to thank Louise Albiston, Neil Clegg, Jane Drage, Diane Savage, Ian Tucker (Unilever Research), Lesley MacAlman and Audrey Taggart (University of Strathclyde) for their unselfish assistance in obtaining the Scanning Electron Micrographs and X-ray powder diffraction patterns required during this project, and to Stephen Craig (University of Strathclyde), for his invaluable assistance in proof reading this thesis. I gratefully acknowledge the Department of Pure and Applied Chemistry of the University of Strathclyde, SERC Daresbury Laboratory and Unilever Research Port Sunlight Laboratory for the use of their research facilities. Finally I would like to express my deepest gratitude to my parents for their constant support during this study.

Abstract

A detailed study has been conducted on the crystallisation kinetics and growth of some inorganic sulphates and carbonates, in view of their growing importance as enviromentally friendly high surface area powders in detergent applications. Predictions of the crystal morphology based on lattice geometry laws have been obtained and compared to the growth morphology. A mechanism for habit modification has been postulated and compared to experimental studies of the effects of impurities on the crystallisation of sodium carbonate monohydrate and sodium carbonate decahydrate.

Intermolecular force potentials have been empirically derived for β potassium sulphate which accurately predict its solid state properties. The intermolecular force potentials are successfully transferred and applied to a simulation of the low temperature phase of sodium sulphate.

The phase diagram of the Na_2CO_3-Na_2SO_4-H_2O system has been redetermined using powder diffraction, chemical analysis and Scanning Electron Microscopy as analysis tools. Evidence for burkeite supercell formation has been noted at a variety of solution compositions and crystallisation temperatures. The degree of agglomeration present in the system has been determined to be a function of the carbonate content of the crystallising solution. Burkeite is noted to act as an agglomeration nucleator, extensively binding to the other phases present. A reduction in precipitation temperature leads to a corresponding increase in the particle size distribution.

The application of nucleation theory to inorganic systems is examined through the use of an automated crystallisation cell employing solution turbidometry, conductivity and temperature, to probe nuclei formation in the cases of potash alum ($AlK(SO_4)_2.12H_2O$), ammonium dihydrogen orthophosphate ($NH_4H_2PO_4$), sodium carbonate decahydrate ($Na_2CO_3.10H_2O$) and sodium sulphate decahydrate ($Na_2SO_4.10H_2O$). Turbidometry is determined to be the most reliable means of detecting the onset of nucleation. Reasonable correlation is noted for the systems studied, between measured saturation curves as determined by this instrument and previous observations. Interfacial energies based on induction time measurements are determined to be significantly smaller than those determined in previous kinetic and dissolution enthalpy studies.

The preparation of highly porous, high surface area powders for carrying liquids in detergent powders has been examined. It was determined that a significant proportion of the desirable powder porosity for a burkeite powder occurred during the initial batch crystallisation stage. No evidence for a burkeite powder to tend towards a monosize particle distribution was noted. Milling and spray drying of slurry lead to a significant increase in powder porosity. Increasing the drying time during spray drying led to a corresponding increase in the powder porosity. It was observed that further studies of the spray drying conditions employed for burkeite production are required, for optimisation of the liquid uptake of the resultant powder.

Contents

Chapter 1

Introduction

During the last thirty years the vast increase in importance of industrial crystallisation has coincided with a greater fundamental understanding of the processes occuring at the molecular level; and has now become the predominantly preferred technique in the preparation of many diverse materials ranging from high value added products, to products encountered in everyday life. Examples range from superconductors, pharmaceutics, dyes and speciality chemicals to sugar, salt, detergent powders etc.

Each stage in the crystallisation process must be carefully considered and understood in order to obtain the desired effects. A certain level of supersaturation may be required in order to obtain a product of a particular habit, however the level of supersaturation generated must not be too large, leading to massive nucleation upon agitation. There may exist the possibility of polymorphs, or different hydrated products at different crystallising temperatures, thus knowledge of the phase diagram of a system is necessary. The crystal morphology has to be considered in relation to the processing conditions and the consumer needs, e.g. higher surface area materials can be achieved if a system is crystallised in a dendritic form, but if the crystals are fragile or brittle, then excessive disintegration leading to dust problems during subsequent processing may be encountered. Thus modification of the crystal morphology may be required for optimum processing. In order to achieve this, an understanding of the crystal structure and crystal chemistry of the particular material is necessary. Knowledge of the crystal structure may also allow prediction of the equilibrium crystal morphology and crystal chemistry and allow postulation of possible habit modification

mechanisms.

It is against this industrial perspective that the research described in this thesis came about. Its purposes were to examine various aspects of each of the processes in crystallisation that have been detailed. More specifically, studies have been carried out on the nucleation, crystal growth and habit modification of various inorganic salts with comparison of the observed growth morphologies to predicted morphologies. A possible habit modification mechanism is compared and contrasted to observed findings.

The materials examined in the course of this study were taken from inorganic carbonates, sulphates and phosphates. These material groups are applied in many diverse areas, ranging from the glass industry [1], the pulp industry [2] and specifically the detergent industry [3-5], to use as bath salts [6].

When prepared as high surface area, highly porous powders, phosphates, carbonates and sulphates play a major role in the detergent industry and can have many functions: they may act as carrier materials for the incorporation of various components necessary for detergent operation and in the case of carbonate based materials, may have the secondary function of acting as water softeners. In previous years phosphates have been the preferred carrier in the detergent industry, due to morphological and solubility considerations however enviromental implications have lead to carbonate and sulphate based materials to be employed as alternatives to phosphates as detergent carriers. A particular carrier material, the double salt burkeite $Na_2CO_3(Na_2SO_4)_2$, and its role as a detergent carrier is studied.

The body of this thesis comprises eight chapters. Chapter two presents an overview of crystallography and the various aspects of crystallisation; the relationship between structure and morphology is reviewed and the current theories describing crystal growth are briefly summarised. Chapter three deals with the prediction of crystal morphology based on the geometric laws of Donnay-Harker-Bravais-Friedel [7,8]. The systems studied are sodium tripolyphosphate hexahydrate ($Na_5P_3O_{10}6.H_2O$), and the components of the Na_2CO_3-Na_2SO_4-H_2O. The resultant predicted morphologies are compared and contrasted to observed growth morphologies. Using a combination of crystal structure and crystal habit, the crystal chemical factors important

in habit modification are presented and discussed in terms of a possible mechanism for habit modifying polyacrylates on sodium carbonate monohydrate ($Na_2CO_3.H_2O$). This model is compared and contrasted to experimental studies of the influences of various additives on its growth morphology.

In order to satisfactorily predict morphologies based on lattice energy and intermolecular force calculations for inorganic materials, intermolecular force potentials have to be derived that model all interatomic interactions accurately. Chapter four deals with the empirical derivation of intermolecular force potentials and prediction of solid state properties for beta potassium sulphate (β K_2SO_4). Attempts to obtain attachment energies for morphological prediction from lattice energy calculations are outlined. The determined potential paramaters describing the sulphate grouping are transferred to a simulation of sodium sulphate and the resultant structure and solid state properties predicted.

The redetermination of the phase diagram of the Na_2CO_3-Na_2SO_4-H_2O system is examined in chapter five. Powder diffraction, chemical analysis, Scanning Electron Microscopy and Energy Dispersive X-Ray microanalysis are employed as analysis tools. The influences of solution composition and precipitation temperature on the agglomeration and particle size of the crystallising phases are examined in detail.

Chapter six describes the application of an automated crystallisation rig to inorganic salts and its application to determine various crystallisation kinetic parameters employing conductivity, turbidometry and temperature as methods of detecting crystallisation. The chapter concludes with a discussion of the crystallisation parameters of potash alum ($AlK(SO_4)_2.12H_2O$), *ammonium dihydrogen orthophosphate* ($NH_4H_2PO_4$), sodium carbonate decahydrate ($Na_2CO_3.10H_2O$) and sodium sulphate decahydrate ($Na_2SO_4.10H_2O$), as determined by this instrument.

A particular industrial aspect of carbonates and sulphates, i.e. the preparation of high surface area, highly porous powders for carrying liquids in detergent powders is examined in chapter seven. The production of such a powder by spray drying is discussed, using burkeite ($Na_2CO_3(Na_2SO_4)_2$), as an example. Agglomeration and porosity are of critical importance in the production of a powder of desired characteristics and the effects of variations in the mixing/crystallisation and the spray drying

conditions on particle properties are examined, using Scanning Electron Microscopy and mercury intrusion porosimetry.

The conclusions drawn from the preceding chapters are summarised in chapter eight, together with suggestions for further work.

References

1. G.T. Austin; "Shreves Chemical Process Industries", McGraw-Hill, New York, London (1984) 193-213

2. F.C. Klaessig and D.F. Jacques; U.S. Pat. US4263092, (1981), 5pp.

3. J.R. Van Wazer; "Phosphorus and its compounds" Vol. 1, Interscience Publications, New York & London, Chapter 27, 1732-1771

4. C. Atkinson & T. Taylor; Unilever Research Port Sunlight Laboratory Progress Report LPRPS851255

5. C. Atkinson, M.J.H. Heybourne, W.J. Iley, P.C. Knight, P.J. Russell, T. Taylor, D.P. Jones; Eur. Pat. EP221776A (1987) 37pp

6. C.T. Simpson-Ludick; Pat. ZA7303350-A, (1974) 15pp

7. A. Bravais; Etudes Crystallographiques Paris (1913)

8. J.D.H. Donnay & D. Harker; Amer. Miner. **22** (1937) 463-485

Chapter 2

Crystals, Crystallography And Crystallisation.

Contents

2.1 Introduction

This chapter presents a summary of the theories describing the nature of the crystallisation process. The relationship between crystal structure and morphology is highlighted and the available theories describing the processes that occur during crystallisation, crystal growth and habit modification are reviewed. An overview is presented of how the relationship between crystal structure and morphology may be employed for predictions of crystal morphology. Some techniques employed for the growth of crystals at laboratory and industrial scales are highlighted and a crystallisation rig designed for solution crystal growth used in this study is detailed.

2.2 Crystals And Crystallography

2.2.1 The Seven Crystal Systems

A crystal may be defined as a regular periodic array (lattice) of points with each point having the same local environment by definition. At each of these lattice points is situated a chemical entity, the entity dependent on the material in question. Depending on the material a crystal may be defined as being ionic (e.g. NaCl), metallic (e.g. silicon) or covalent (e.g. anthracene).

The crystal lattice may be regarded as being infinite in extent, with three dimensional order. A single crystal may be defined as a crystalline solid where the 3-D order extends from microscopic (e.g. a structure comprising of a few unit cells) through to macroscopic proportions (ie cm^3). The primary unit of any crystal lattice is known as the unit cell and this primary cell in conjunction with translation operations in three dimensions defines the crystal structure. The crystal lattice can be represented by three principle lattice vectors "a", "b" and "c" and three angles "α", "β" and "γ" (figure 2.1), where "α" is the angle between "b" and "c", "β" is the angle between "a"and "c" and "γ" is the angle between "a" and "b".

Variations in the relationships between these six lattice parameters gives rise to the seven basic crystal systems (table 2.1). The hexagonal system is slightly different, with the inclusion of an extra axis "a_3" perpendicular to "c", forming 60^0 angles with

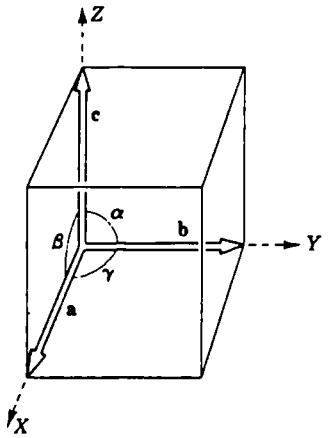

Figure 2.1: Representation of axial system employed in crystal lattices

the a_1 and a_2 axis.

System	Unit cell dimensions
triclinic	$a \neq b \neq c$ $\alpha \neq \beta \neq \gamma \neq 90^0$
monoclinic	$a \neq b \neq c$ $\alpha = \gamma = 90^0, \beta \neq 90^0$
orthorhombic	$a \neq b \neq c$ $\alpha = \beta = \gamma = 90^0$
tetragonal	$a = b \neq c$ $\alpha = \beta = \gamma = 90^0$
trigonal	$a = b = c$ $\alpha = \beta \neq \gamma = 90^0$
hexagonal	$a_1 = a_2 = a_3 \neq c$ $\alpha = \beta = 90^0, \gamma = 120^0$
cubic	$a = b = c$ $\alpha = \beta = \gamma = 90^0$

Table 2.1: The seven crystal systems.

2.2.2 Crystal Chemistry

The crystal structure of a material and the crystal system it will belong to depend on various factors, namely the size and shape of the entity and the nature of the bonding between the entities. In the case of molecular crystals, the bonding between the crystallising entities are relatively weak, isotropic (Van der Waals) interactions, leading to soft, low melting point materials and the (normally) nonspherical crystallising entities decrease the resultant symmetry of the close packed crystal structure (figure 2.2). Approximately 90% of organic materials crystallise in monoclinic, orthorhombic and triclinic structures.

This may be contrasted to ionic crystals, where the strong bonding leads to hard, high melting point crystals. The normally spherical entities lead to a high degree of symmetry in the crystal structure (usually cubic or tetragonal), although the ionic radii

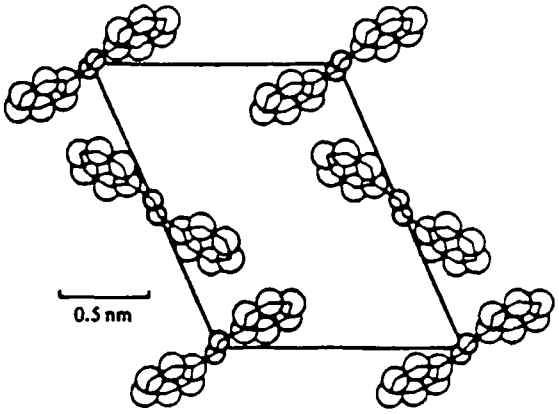

Figure 2.2: Typical low symmetry crystal structure (monoclinic) of a molecular crystal.

of the entities involved determine the crystal packing. The group one chlorides NaCl and CsCl highlight the differences in packing due to ionic radii (figure 2.3 (a&b)).

2.2.3 Crystal Morphology

The overall description of the shape of a crystal is its habit or morphology. There are some simple descriptions of habit that may be employed, e.g. cube, needle, plate, octahedrea etc (figure 2.4). The form of a crystal defines what crystallographic faces are present, e.g. {111}, {001} etc. A crystal may have the same habit, but different forms present(figure 2.15 (a)), or the same forms present but a different habit (figure 2.15 (b)). However it is obvious that this method of describing the crystal morphology is clearly limited in its use. For a more detailed description of crystal morphologies/crystal chemistries, then a systematic description of the crystallographic forms in a system are required. The nomenclature (hkl) devised by Miller is used as the standard identifying tool for crystallographic forms. Consider the axial system a,b,c as shown in figure 2.6. The repeat dimension along each axis is a,b,c respectively. The intercepts of the plane ABC are OA, OB and OC respectively, which is equivalent

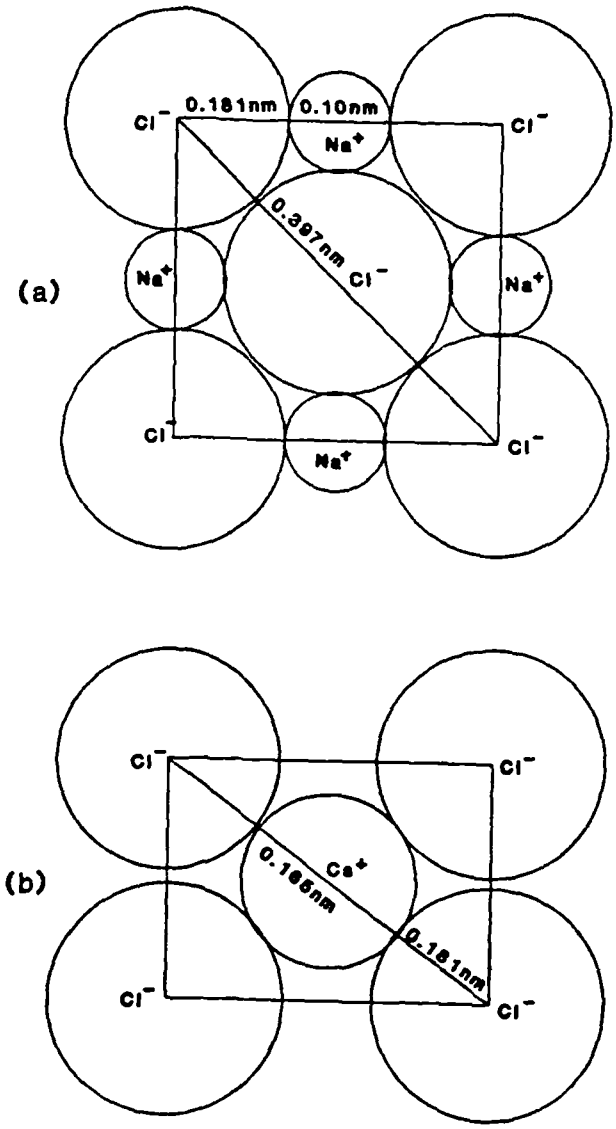

(a) Plane cut through a NaCl crystal structure (b) Plane cut through a CsCl crystal structure

Figure 2.3: Schematic of the crystal structures of NaCl and CsCl, illustrating the influence of ionic radii on crystal packing.

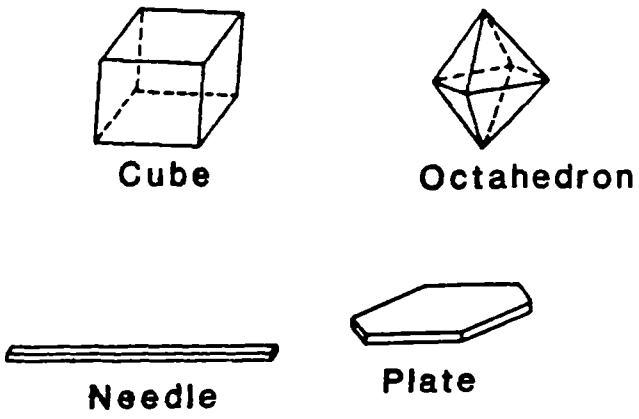

Figure 2.4: Some simple habits of crystals.

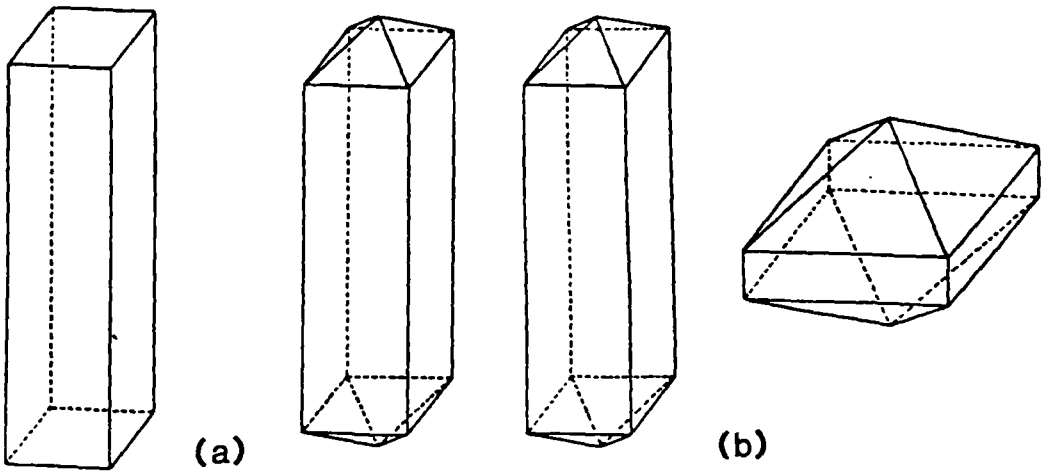

Figure 2.5: Crystal habit/form relationship [1].

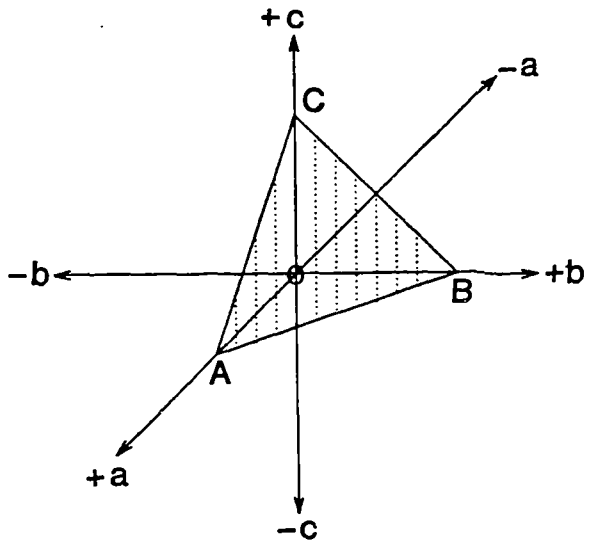

Figure 2.6: Representation of a (111) crystallographic form.

to a,b and c. Thus h,k and l may be defined as:

$$h = a/OA,\ k = b/OB,\ l = c/OC \tag{2.1}$$

Thus for the above case

$$h = a/a,\ k = b/b,\ l = c/c \tag{2.2}$$

which is equivalent to a (111) crystallographic form. A specific notation also governs whether (111) or {111} is employed. In general (111) refers to a specific crystallographic form whereas {111} refers to all possible (hkl) combinations that can be derived from symmetry operations related to the crystal system in question, e.g. $(1\bar{1}1)$ is a member of the {111} group.

2.2.4 Defects In Crystals

Crystals are rarely completely free of defects. There are a variety of defects that can exist in crystals, which can be classified by the dimensional extent of propagation into the lattice structure. These range from zero dimensional atomic defects to

three dimensional gross defects. A zero dimensional defect is termed a point defect and can consist of missing crystallising entities (vacancy), entities occupying sites not normally occupied in the lattice (interstitial) and foreign atoms occupying lattice sites (impurities). Essentially this defect exists on the atomic scale. A one dimensional defect is known as a line defect or dislocation. Two basic types exist known as the edge and screw dislocation which can be characterised depending on the relationship between the strain direction "$\underline{b}$", known as the Burger's vector and the line direction "$\underline{l}$". The edge dislocation comprises an extra half plane of atoms that have been inserted into the crystal (figure 2.7), the Burger's vector "$\underline{b}$" being perpendicular to the line of disturbance "$\underline{l}$". This results in strain and energetic factors being introduced into the system, due to compressed interatomic distances. The screw dislocation is a crystal distortion noted in the form of a "step" on the crystal surface, formed by the Burgers Vector "$\underline{b}$", being parallel to "$\underline{l}$" (figure 2.8). This step forms ideal conditions for crystallising entities to be incorporated into the crystal, leading to the formation of a distinctive spiral on the crystal surface. Screw dislocations play an important role in crystal growth mechanisms, and will be discussed further in section 2.3.3. Two dimensional defects (known as planar defects) propagate much further

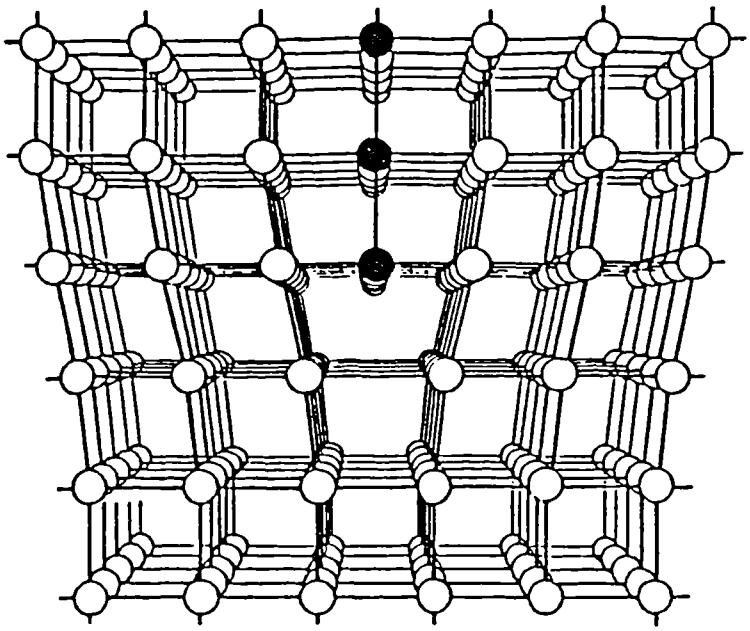

Figure 2.7: Representation of an edge dislocation.

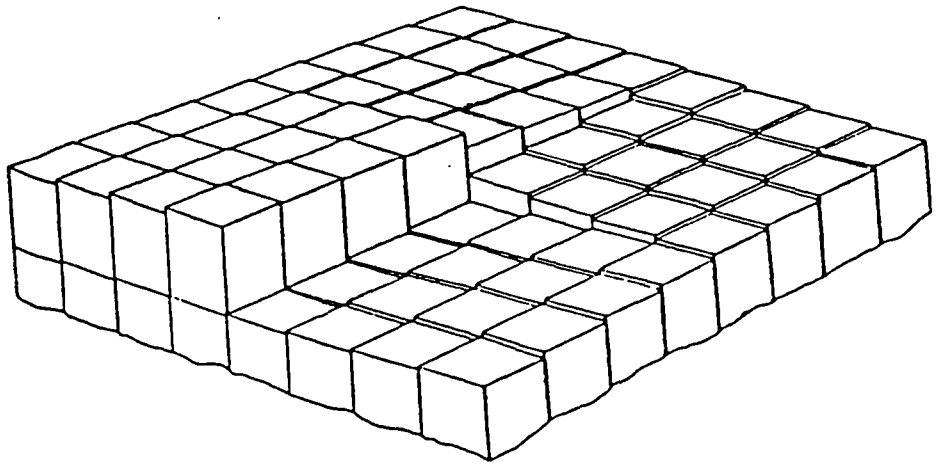

Figure 2.8: Representation of a screw dislocation.

into the lattice than point defects (normally a few microns) and can be formed from growth sector boundaries, twinning and stacking faults. Three dimensional defects or volume defects are gross distortions to the lattice and can result from the inclusion of a material of a different composition or crystal structure into the main lattice, e.g. a solvent inclusion.

2.3 Crystallisation And Growth Kinetics

Crystallisation essentially may be defined as the formation of a crystal from a parent phase e.g. solution etc, where the diordered entities in solution are transformed to highly ordered species within a crystalline structure. There are a several important aspects to be considered in crystallisation.

a) supersaturation,

b) nucleation,

c) crystal growth,

d) morphology,

d) growth techniques.

2.3.1 Supersaturation

If a solid phase is in equilibrium with a solution, then the solution may be said to be saturated with respect to the solid. However, when a solution contains more than the equilibrium concentration of dissolved solid, then the solution is said to be supersaturated with respect to the solid. Supersaturation is often known as the basic "driving force" in crystallisation and may be defined in different ways, e.g. as the concentration driving force "Δc", the relative supersaturation "σ", and the supersaturation ratio "S", where:

$$\Delta c = c - c^* \tag{2.3}$$

$$\sigma = \Delta c / c^* \tag{2.4}$$

$$S = c / c^* \tag{2.5}$$

where "c*" is the saturation solution concentration at a given temperature and "c" is the actual solution concentration.

Supersaturation may be induced in a system in a variety of different ways. Figure 2.9 illustrates a typical solubility curve as a function of temperature. The upper dotted line refers to the temperatures and concentrations where spontaneous crystallisation will occur and is known as the supersolubility curve. Three different regions may be defined in this plot, the stable, metastable and labile regions, the latter two terms being coined by Miers [2]. The stable region is where the solution is undersaturated with respect to the dissolved solid phase, the labile and metastable regions refer to regions where supersaturation is present which spontaneous deposition (nucleation) of the solid phase is likely and not likely to occur, respectively. The width of the metastable region is not absolute for any system and can be varied by, e.g. the degree of agitation present. Supersaturation may be induced in a variety of ways. Referring to figure 2.9, an undersaturated solution (A) may be cooled until supersaturation is achieved (region BC) until spontaneous nucleation is likely to occur (C), although further cooling may be necessary for this to occur. Another method would be solvent

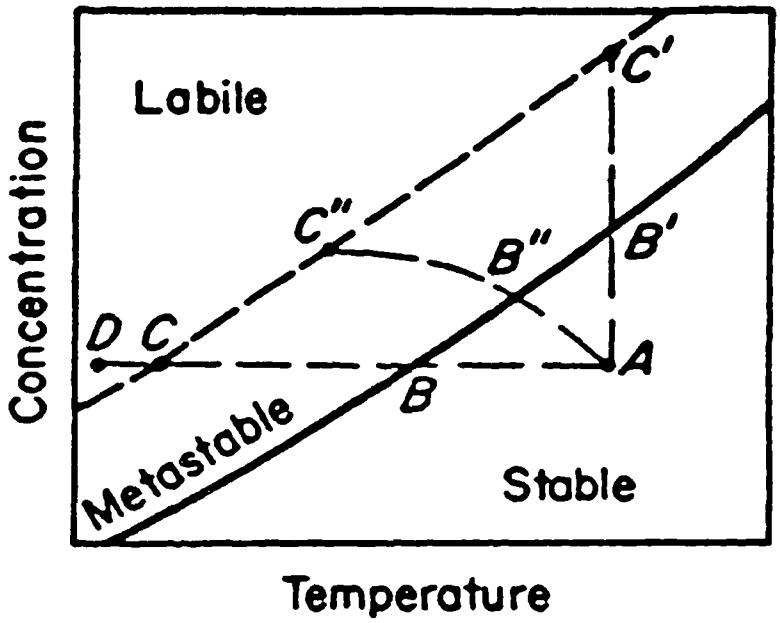

Figure 2.9: Representation of typical solubility/supersolubility curves as a function of time [3].

evaporation at constant temperature (AB'C') until supersaturation and spontaneous nucleation occurs. A combination of these methods (AB"C") may also be employed.

2.3.2 Nucleation

Once a degree of supersaturation has been achieved in a system, then nucleation may occur. There are two possible mechanisms for nucleation, one a progressive build-up of a number of particles forming a nucleus or less likely, the simultaneous collision of a number of particles to form a nucleus. Nucleation can be divided in two separate categories; primary and secondary nucleation, with primary nucleation further subdivided into primary homogeneous and heterogeneous nucleation (figure 2.10). The basic principals of classic nucleation theory have been derived from the nucleation of water droplets from vapour [4,5] and there are now available many comprehensive reviews on nucleation [6,7]. In order for the classic theories of nucleation to apply to solution systems, liquids are considered to be examples of very compressed vapours. As this study was concerned with primary nucleation, this aspect will now be examined in further detail.

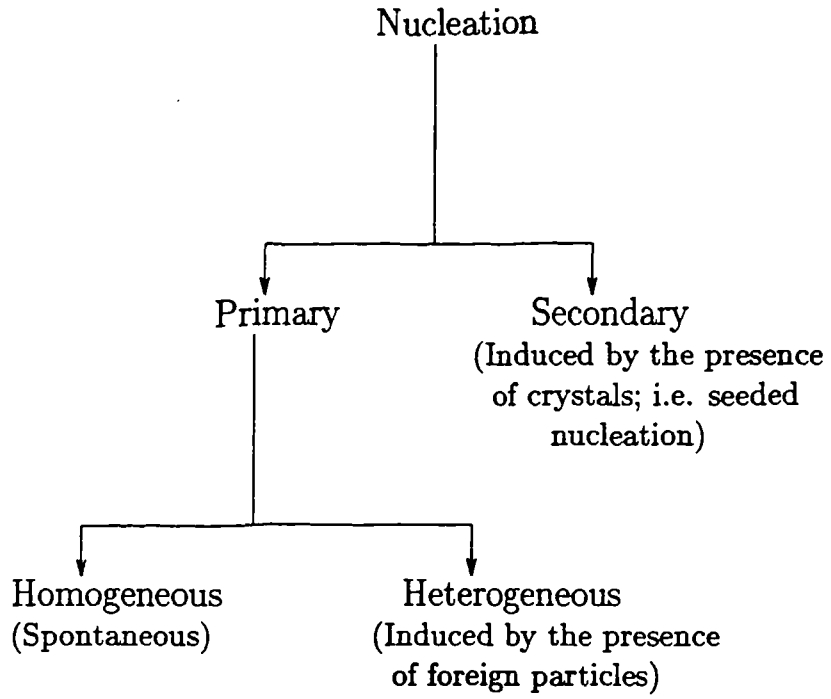

Figure 2.10: Primary and secondary nucleation [3].

2.3.2.1 Homogeneous Nucleation

The theories of Gibbs [8], Volmer and Weber [9], Becker and Doring [10] consider the growth of clusters initiated by saturation fluctuations within the system. The resultant free energy of these nuclei clusters is a combination of the bulk volume "ΔG_v" and surface free energies "ΔG_s" respectively:

$$\Delta G = \Delta G_v + \Delta G_s \tag{2.6}$$

and may be described in more detail by:

$$\Delta G = -4/3r^3 \Delta G_v + 4\pi r^2 \gamma \tag{2.7}$$

where "γ" is the interfacial surface free energy between the nucleus and the solution (also known as the surface tension), "r" is the radius of the nucleus and "ΔG_v" is the bulk free energy difference per unit volume between the solid and liquid phases. The surface free energy term is positive and the bulk free energy term is negative. The combination of these energy factors is shown in figure 2.11. It can be seen that there is a stationary point where the Gibbs free energy reaches a maximum; at this

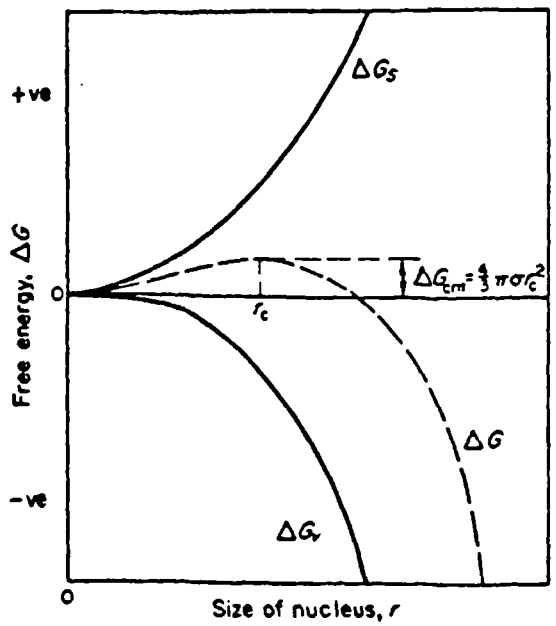

Figure 2.11: Interaction of surface free energy and bulk volume energy terms within nucleation [3].

point the cluster forms a "critical nucleus"; i.e. a point where the nucleus has an equal chance of disintegration or continued growth. The maximum value of "ΔG", i.e. "ΔG_{crit}" occurs at this point and can be obtained by differentiation of the free energy with respect to "r", the nucleus radius. Differentiation of equation 2.7 leads to:

$$dG/dr = -4\pi r_c^2 \Delta G_v + 8\pi r_c \gamma = 0 \tag{2.8}$$

Thus:

$$4\pi r_c^2 \Delta G_v = 8\pi r_c \gamma \tag{2.9}$$

and hence "r_c", the critical radius may be expressed as:

$$r_c = 2\gamma/\Delta G_v \tag{2.10}$$

Further substitution into equation 2.7 leads to:

$$\Delta G = 4\pi r_c^2 \gamma/3 \tag{2.11}$$

The Gibbs-Thomson equation [8] may be used as an expression for supersaturation:

$$ln(S) = 2\gamma v/kTr \tag{2.12}$$

where "v" is the molecular volume and "k" is Boltzmans constant (1.38 x 10^{-23} JK^{-1}). Thus equation 2.10 may be reexpressed as:

$$\Delta G_v = kTln(S)/v \tag{2.13}$$

and equation 2.11 can be written as:

$$\Delta G_{crit} = 16\pi\gamma^3 v^2/3(kTln(S))^2 \tag{2.14}$$

In classic terms, the nucleation rate may be expressed as follows:

$$J = A^* w^* n_i^* \tag{2.15}$$

where "J" is the nucleation rate, "A^*" is the critical nucleus surface area, "w^*" is the molecular attachment rate and "n_i^*" the concentration of critical nuclei. The concentration of critical nuclei may also be expressed as:

$$n_i^* = n_1 e^{-\Delta G^*/kT} \tag{2.16}$$

Thus:

$$J = A^* w^* n_1 e^{-\Delta G^*/kT} \tag{2.17}$$

which is equivalent to an Arrhenius type rate equation:

$$J = Ce^{-\Delta G^*/kT} \tag{2.18}$$

and further substitution into equation 2.17 leads to:

$$J = A^* w^* n_1 e^{(-16\pi\gamma^3 v^2/3k^3T^3ln(S)^2)} \tag{2.19}$$

which may be simplified to:

$$J = Ce^{(-16\pi\gamma^3 v^2/3k^3T^3ln(S)^2)} \tag{2.20}$$

where "C" is a constant. Various assumptions have been made in the derivation of this equation. The most important are

- that the nuclei are spherical and the interfacial energy is isotropic,

- that bulk properties of the solution can be extrapolated to predict occurrences on the molecular scale

It can be seen that the nucleation rate is critically dependent on the interfacial energy "γ", the temperature "T" and especially the supersaturation "S". The huge variation of nucleation rate that can be achieved by supersaturation can be illustrated by the example of potassium sulphate K_2SO_4 [1] (figure 2.12). These huge variations have prompted the term "critical supersaturation", i.e. the supersaturation at which the nucleation rate becomes appreciable.

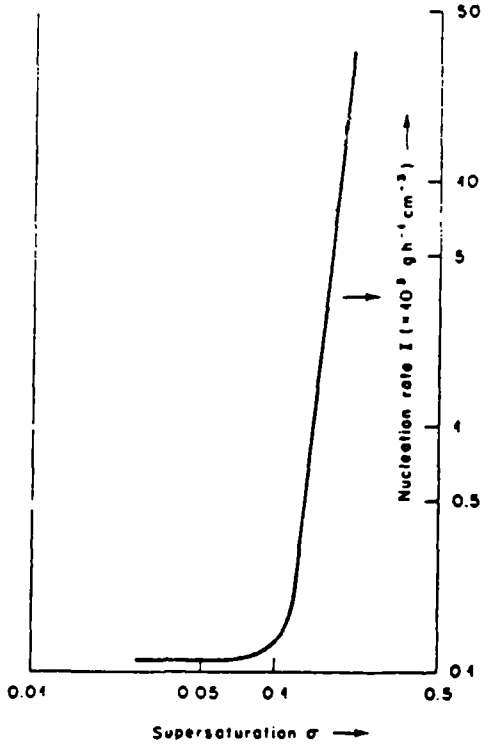

Figure 2.12: Variation of nucleation rate with supersaturation for K_2SO_4 [1].

Although classic theory predicts an exponential curve for the nucleation rate/supersaturation relationship, deviations have been noted from this curve. Tammann [11] highlighted (figure 2.13) the variations in nucleation rate with supersaturation, showing a maximum in nucleation rate, the rate decreasing rapidly after this maximum. An increase in viscosity, inhibiting the formation of ordered crystal structures was suggested as a reason for this deviation, which prompted Turnbull and Fisher [12] to suggest that the inclusion of a further term ($\Delta G'/kT$), was

necessary to account for viscosity effects, i.e.

$$J = A^* w^* n_1 e^{(\Delta G^* + \Delta G')/kT} \tag{2.21}$$

where "$\Delta G'$" is the activation energy for molecular motion across the nuclei-matrix interface. This deviation from classic theory has been predominantly noted in studies of nucleation from melts.

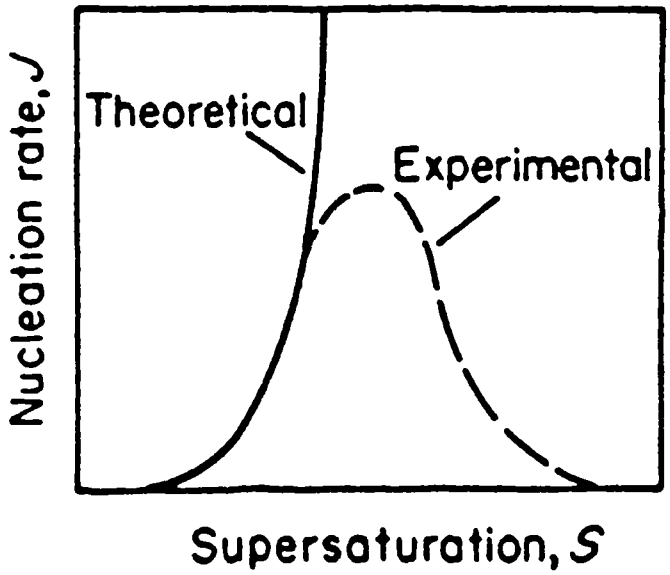

Figure 2.13: Variation of nucleation rate with supersaturation noted by Tammnan [11].

An appreciable time may elapse between the achievement of supersaturation and the onset of nucleation. This time period is known as the "induction time", "τ". If the assumption is made that the induction time is primarily due to the formation of the nucleus, then this period of time is considered (although dimensionally incorrect) inversely proportional to the nucleation rate "J" [13], i.e.

$$\tau \, \alpha \, (1/J) \, \alpha \, \gamma^3 / T^3 ln(S)^2 \tag{2.22}$$

Reservations have been expressed over certain aspects of the derivation of the classic theories for nucleation. It has been felt by certain authors [14,15] that various correction terms should be included in equation 2.18. Lothe and Pound [15] considered that the greatest alteration to nucleation theory should be the inclusion

of factors accounting for the rotational and translational degrees of freedom of the molecular clusters. However it has been shown in many experiments of nucleation from the vapour that predicted critical supersaturations and nucleation rates based upon the inclusion of these correction terms differs significantly from data obtained by cloud chamber experiments, e.g., deviations of up to 10^{17} between prediction and experiment for nucleation rates have been observed. Clearly, equation 2.20 can only be used to obtain semi-quantitative data and not absolute values for e.g. nucleation rates, induction times etc.

The theory of homogeneous nucleation is based on the assumption that the surface tension "γ" is not dependent on nucleus size. However it has been shown [16] that the surface tension is a function of the curvature of a surface. If this is taken into account in classic homogeneous nucleation theory, then it can be shown that under certain conditions, the spontaneous formation of clusters can lead to a decrease in the free energy "ΔG" (figure 2.14).

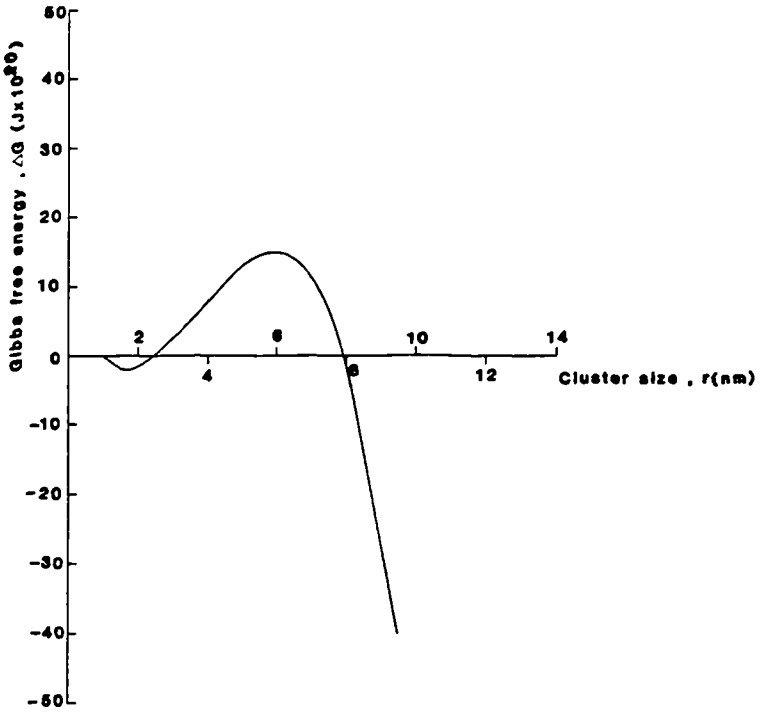

Figure 2.14: Free energy change for nucleation, incorporating a size dependent surface tension [16].

The existence of these clusters may account for certain nucleation phenomena, e.g. the occurrence of massive nucleation with the onset of agitation and these clusters

may possibly play a significant role in crystal growth, possibly acting as crystallising entities that are adsorbed onto kink sites on a crystal surface.

2.3.2.2 Heterogeneous Nucleation

Homogeneous nucleation is assumed to occur in a solution that is completely free of impurities. In practice this is literally impossible to achieve and almost certainly impurities will be present in solution, usually in the form of dust particles. These particles already provide nuclei in the solution, hence nucleation of the solution will occur on these centres. Thus, heterogeneous nucleation occurs and the free energy of the system will be modified correspondingly, to account for the presence of the impurities, e.g.

$$\Delta G = 4\pi r_p^2(\gamma_{ps} - \gamma_{pl}) - 4/3r_p^3\Delta G_v \tag{2.23}$$

where "γ_{ps}" is the surface free energy of the particle/solid interface, "γ_{pl}" is the surface free energy of the particle/liquid interface and "r_p" is the radius of the foreign particle. The presence of the impurities tends to reduce the width of the metastable zone compared to that of a pure solution, i.e. the crystallising temperature increases and the supersaturation decreases, implying that "γ_{ps}" < "γ_{pl}". In this case "ΔG" is negative at all times; thus these particles act as spontaneous nucleation centres for the solution. There can be other sites within a system for heterogeneous nucleation, e.g. on a microscopic level, cracks on the surface of the vessel wall may provide centres of nucleation for a system.

The presence of heteronuclei in a system influence the free energy "ΔG" (equation 2.18), and thus an expression for heterogeneous nucleation rate [6] can be derived from that based on homogeneous nucleation:

$$J = Ce^{(-16\pi\gamma^3 v^2 f(\varphi)/3k^3T^3 ln(S)^2)} \tag{2.24}$$

where "J", "γ", "v", "k" and "S" are as defined for equation 2.20 and "f(φ)" is a correction factor for the influence of heteronuclei on "γ" the interfacial tension and lies in the range $0 \leq f(\varphi) \leq 1$.

In practice heterogeneous nucleation is the predominant mode of nucleation obtained, extreme difficulties being encountered in the preparation of a solution sample

completely free of foreign bodies. It has been estimated that a carefully filtered solution will still contain up to 10^3 particles per cm^3 of solution [3].

2.3.2.3 Empirical Relationships for Nucleation

Various empirical relationships have been devised to simulate nucleation, and are especially applicable in larger scale crystallisation systems. Various relationships have been proposed for the relationship between supersaturation and induction time or nucleation rate. An example of such a relationship is that derived by Christiansen and Nielsen [17]

$$\tau = kc^{1-p} \tag{2.25}$$

where "k" is a constant, "c" the concentration of the supersaturated solution and "p" the number of molecules in the critical nucleus. Another model has been forwarded by Nyvlt [18]

$$J = k_n \Delta S_{max}^m \tag{2.26}$$

where "J" is the nucleation rate, "k_n" is a rate constant "ΔS_{max}^m" is the maximum supersaturation in the system and "m" the order of reaction. This equation may be further expanded so that an expression for the dependence of the maximum undercooling "ΔT" may be obtained with respect to a cooling rate "b":

$$logb = (m-1)logdc/dt - log\epsilon + logk_n + mlog\Delta T_{max} \tag{2.27}$$

where "b" is the solution cooling rate, "dc/dt" the rate of equilibrium concentration change with respect to temperature, "ϵ" the ratio of hydrated salt to anhydrous salt and "k_n" the rate constant. It should be noted that "m" the order of reaction has no fundamental significance and cannot imply any information as to the number of reacting species, unlike classic rate equations. A plot of log (ΔT_{max}) versus log(b) should yield a straight line of slope "m". A drawback has been noted from such an assessment [19] in that the undercooling and growth rate of the resultant crystals are dependent on the cooling rate. Thus the slope of the plot should always be steeper than that expected for nucleation alone, by a factor dependent on the sensitivity of the detection method used to detect the onset of nucleation.

2.3.3 Crystal Growth

As soon as nucleation has occured, then crystal growth will be initiated. The following steps are generally thought to summarise the events occuring during crystal growth (shown schematically in figure 2.15) :

i) Bulk transport of crystallising entities to the edge of the boundary layer.

ii) Diffusion though the boundary layer to the surface of the growing crystal.

iii) Adsorption onto the crystal surface.

iv) Diffusion along the crystal surface and

v) Attachment to the surface step.

vi) Diffusion along step and

vii) Integration into crystal at a kink.

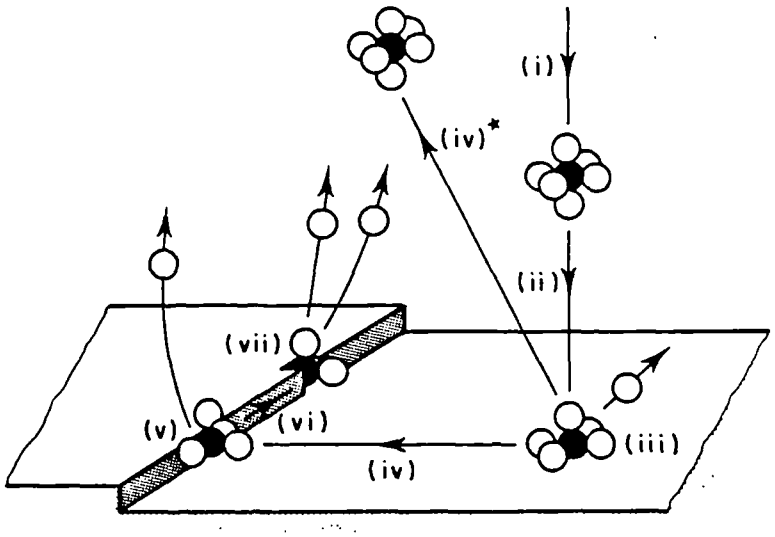

Figure 2.15: Representation of crystal growth events.

If the crystallising entities are solvated, then during the above processes solvent molecules will be removed from the crystallising entities, e.g. a cation species M^{x+} in aqueous solution will exist in the form $M(H_2O)_6^{x+}$ and these solvent molecules have to be removed before final integration into the crystal structure can occur.

Diffusion of the crystallising entities through the boundary layer will follows Ficks

laws of diffusion, e.g.

$$F = D_v(dn/dz) \tag{2.28}$$

Where "F" is the rate of supply of solute by diffusion, "D_v" is the solute volume diffusion coefficient and "dn/dz" is the concentration gradient perpendicular to the crystal surface. The thickness of the boundary layer "δ", may be defined as

$$\delta = D_v(n_b - n_i)/F \tag{2.29}$$

where "n_b" and "n_i" are the bulk and interface concentrations respectively.

The adsorption of the crystallising entities onto the crystal surface will occur at the energetically most favourable sites, which have been determined as being kink sites [20]. This will continue until the layer is complete. New sites for growth must then be created, and this occurs by two dimensional growth as illustrated in figure 2.16.

This nucleus will form and then spread out, known as two dimensional nucleation or the "birth and spread" model [21], with resultant growth normal to the crystal face. The rate determining step in this model is the formation of the two dimensional nucleus. The Kossel variation in this model [20] is somewhat more complex, showing incomplete steps, kinks and vacancies, all of which provide sites for incorporation for the crystallising entities. There is a possibility of growth occuring at all these sites simultaneously. Since nucleation rate (hence growth rate) is dependent on supersaturation, at low supersaturations the predicted growth rates from theory are very low. However, major discrepancies are noted in many cases between predicted and observed growth rates at low supersaturations. These discrepancies lead Burton, Cabrerra and Frank to develop a theory [22] based on a continuous source of steps being available for the incorporation of crystallising entities onto a crystal surface, to account for the much higher growth rates observed at low supersaturations than those predicted, based on the "birth and spread model". This theory postulated that the presence of a screw dislocation on a crystal surface would remove the necessity of two dimensional surface nucleation and would provide a continuous source of steps for crystallisation, leading to the formation of the classic screw dislocation growth spiral figure 2.17, which has been observed in the growth of many systems. The Burton,

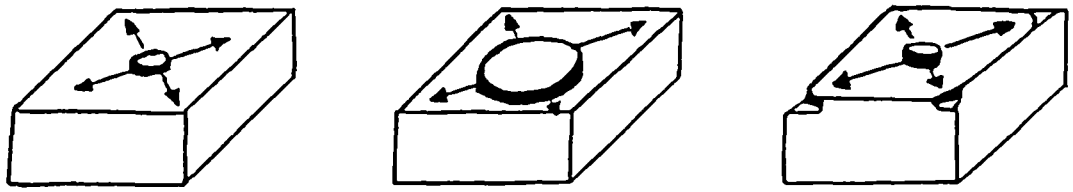

Figure 2.16: Representation of two dimensional nucleation and growth.

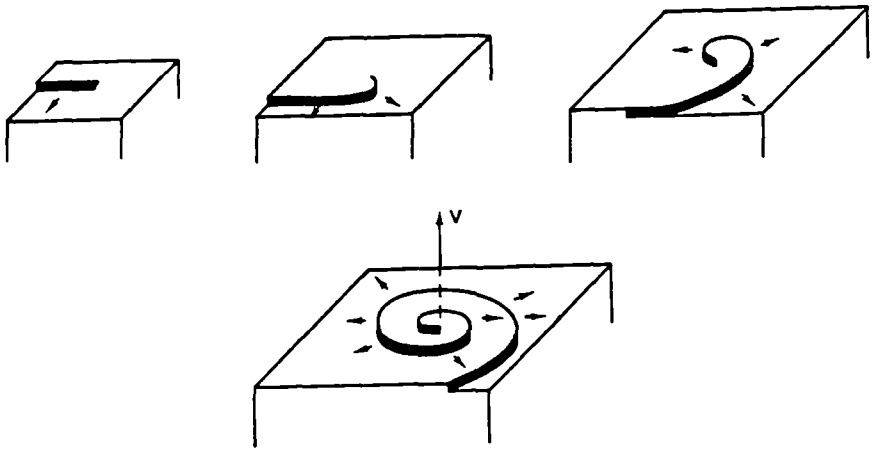

Figure 2.17: Representation of spiral growth as initiated by a screw dislocation [1].

Cabrerra and Frank theory, or BCF theory has assumed great importance in crystal growth, as the predicted growth rates at low supersaturations from this theory do show good correlation to observed growth rates, which the predicted growth rates based on the two dimensional "birth and spread" model could not reproduce. The general BCF relationship may be written as

$$R = A\sigma^2 tanh(B/\sigma) \tag{2.30}$$

where "R" is the crystal growth rate, "A" and "B" are complex temperature dependent constants and "σ" the relative supersaturation. Depending on the degree of supersaturation, different relationships between growth rate and supersaturation can be noted (figure 2.18). At low supersaturations, the relationship may be approximated by

$$R \alpha \sigma^2 \tag{2.31}$$

crystal growth being dominated by the screw dislocation mechanism. At higher

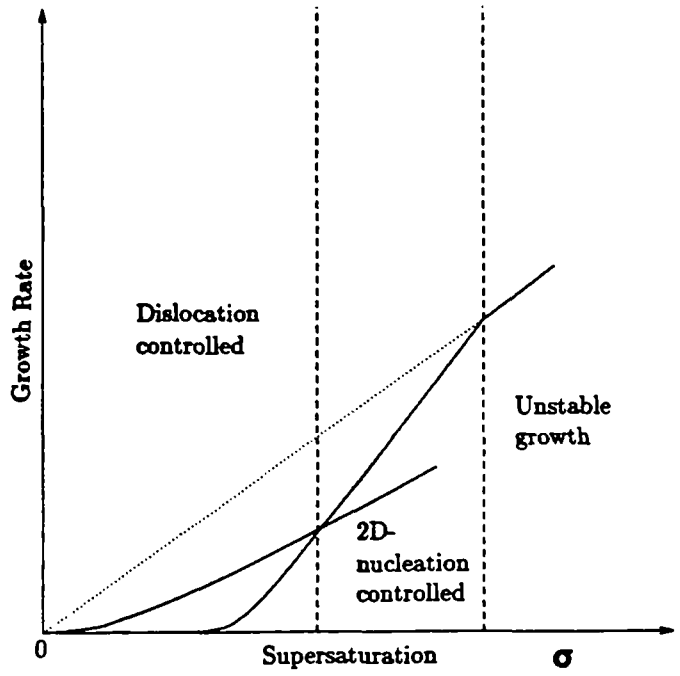

Figure 2.18: Relationship between growth rate and supersaturation in the BCF theory.

supersaturations, the growth rate approximates to an exponential relationship with the supersaturation:

$$R \alpha \sigma^{5/6} exp(\sigma) \tag{2.32}$$

in this region two dimensional nucleation predominate. At high supersaturations the relationship becomes linear, e.g.

$$R \alpha \sigma \tag{2.33}$$

this region signifying the predominance of rough growth.

2.3.4 Habit Modification

Habit modification for a system is obtained when some factor is introduced to the system that alters the crystal growth rates and hence morphology. There are many variables that may be altered within a crystallising system that may effect the resultant habit, e.g. choice of solvent, levels of supersaturation and the presence of impurities. The use of impurities to alter crystal habit is a major field both in laboratory and industrial crystallisation. Many theories have abounded over the years as to the possible mechanisms explaining the effects that impurities have on crystallisation. Early theories includes that of Bunn [23], who studied the adsorption/inclusion of impurities in various systems, concluding that the only difference between crystals containing adsorbed impurity and mixed crystals is the amount of impurity present. Crystals containing adsorbed impurity could be regarded as unstable mixed crystals. The faces containing the impurity are composed of this unstable mixed crystal, hence will redissolve with a corresponding reduction in the growth rate. The factor that determined what faces were the habit modifying faces was the degree of lattice matching between the impurity/modifer and the host crystal for the particular faces. Theories based on impurity adsorption altering crystal surface kinetics (especially since the advent of the BCF theory) and impurities altering the degree of solvation of crystal surfaces have since surfaced on a number of occasions. It is now generally accepted that impurities present in a crystallising system are adsorbed onto the crystal surface, altering growth rates. The modifier may physically hinder incoming crystallising entities by blocking adsorption sites (figure 2.19) or adsorption onto the surface alters the energy characteristics of the surface, thus altering growth rates. Factors such as the size and mobility of the impurity may determine what mode of habit modification occurs [24]. Models have been put forward on the modification of surface energy

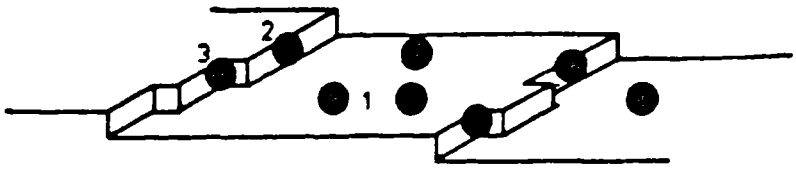

Positions 1,2 and 3 refer to ledge, step and kink sites respectively.

Figure 2.19: Representation of possible site blockage by impurities [26].

charcteristics based on a Kossel crystal model [25] or adsorption mechanisms onto ledge, step and edge sites based on the BCF theory [26]. The latter review highlighted predictions of step velocities and thus growth rates and correlated these with experimental observations of various systems. A modification of Bliznakov's equation [27] may be used to relate the degree of coverage of an impurity on a surface to step velocity and leads to:

$$(V_0 - V_\infty)/(V_0 - V) = 1 + 1/KX \tag{2.34}$$

where, $K = e^{-\Delta G/RT}$, "ΔG" the free energy of adsorption of the impurity, "V_0", "V" and "V_∞", the step velocities and "X" the mole fraction.

In contrast to absorption of cations onto steps, Mullin [28] postulated that for the case of Cr^{3+}, Fe^{3+} and Al^{3+} impurites in the presence of ammonium dihydrogen orthophosphate (ADP) and Potassium dihydrogen orthophosphate (KDP) that the hydrated cations, e.g. $M(H_2O)_6^{X+}$ impose steric and dissolution effects near the crystal surface and thus alter growth rates. If the cation is adsorbed into the crystal structure, the resultant counter flow of water away from the crystal surface imposes a further dissolution effect, thus reducing the growth rate further. An advantage of this theory is that it could explain why variation of pH (which has the same effects

as $M(H_2O)_6^{x+}$) has a modifying effect on the habit of both ADP and KDP.

Thus observations of the effects of impurities on crystal growth and habit have given rise to a number of theories to account for these effects. The possibility does exist however, that the actual crystal growth processes and their interaction with impurities is a combination of all the theoretical mechanisms mentioned. Obviously such complex interactions necessitate the need for more experiments to probe the crystal-solution interface.

2.4 Crystallography and Crystal Morphology

2.4.1 Equilibrium Morphology Simulation Using Lattice Geometry Models

Hauy's classic illustration [29] showed that by stacking/ordering cubes, various basic crystal morphologies could be obtained. The advent of X-ray crystallography allowed the internal structure of a crystal to be probed and determined these basic building blocks to be the unit cells of a crystal. Gibbs [30] related the crystal morphology to energetic considerations stating that the equilibrium crystal morphology was one in which the total free energy was minimised. Wulff [31] defined the relationship between surface energy and equilibrium morphology. A Wulff plot is a 3-D polar representation of the surface energy, which reveals (see figure 2.20) several well-defined minima which correspond to the expected low surface energy directions for crystal growth. Constructing planes tangent to the cusp minimum for each growth vector, a regular polyhedron typical for a freely grown crystal, results. Such plots can be prepared using the gnomonic projection [32] and several computer programs [eg 33] are now available to draw these automatically.

The Bravais/Friedel/Donnay/Harker (BFDH) rules [34,35] enable a measure of the relative growth along a specific crystal plane (hkl) to be related to the internal structure of a crystal using lattice geometry considerations. The BFDH laws may be summarised as :

The greater the interplanar spacing d_{hkl}, the greater the importance of the corre-

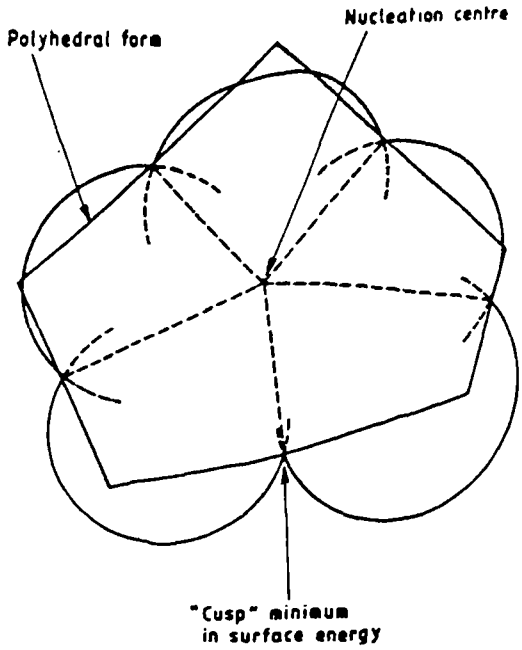

Figure 2.20: Representation of the classical wulff plot for the derivation of equilibrium form [31].

sponding crystal form (hkl), after allowance has been made for translational crystal symmetry elements such as Bravais lattice centring, glide planes and screw axes.
i.e. $d1_{hkl} > d2_{hkl} \Longrightarrow M.I.1_{hkl} > M.I.2_{hkl}$ (M.I. = morphological importance). This model is outlined in more detail in a recent review [36] and calculations using it can be made using the computer program MORANG [37]. Using the BFDH law a morphological index can be defined as the reciprocal of the interplanar spacing ($1/d_{hkl}$) and employed as an alternative to surface energy in the Wulff plot. Predicted morphologies obtained using this model have been derived for a variety of materials and show good correlation to the observed morphologies [36,38,39]. However, this method is purely geometric in nature and makes no considerations of atom charge and type, which have consequences on crystal growth. If structural factors are taken into account, e.g. crystal structure, inter- and intramolecular interactions then a morphological prediction more analogous to the actual "as-grown" morphology may be obtained.

2.5 Crystal Growth Techniques

There are a variety of techniques that may be used to grow crystals, depending on the physical properties of the material in question. Techniques such as growth from the vapour phase have the advantage of removing any possibility of habit change due to solvent interaction with the crystal however certain problems may arise, such as the possibility of sample decomposition and the introduction of strain or defects into the crystal during cooling of the samples to room temperature. These same problems may be also be encountered with crystal growth from the melt. Crystal growth from solution is an alternative that normally takes place close to equilibrium and thus can be used to obtain strain free crystals of high quality. However a negative factor is the possibility of solvent-crystal interactions, leading to modification of habit.

2.5.1 Laboratory Scale Crystallisation

Crystal growth from solution has been the sole technique for growth of all systems during this study. Normal growth from solution occurs at low supersaturations, hence this technique is ideal for crystal growth close to equilibrium conditions and thus unstrained crystals of high quality may be prepared. However certain factors must be taken into account. The solvent employed (in this case water) may exert habit modifying properties on the material to be grown, as may impurities in the system. If there is dust contamination of the system, massive nucleation may occur upon the production of a supersaturation, rendering controlled crystal growth useless. Thus the material to be grown should be recrystallised at least once to remove all impurities and the resultant solution filtered to remove dust particles in the system. Supersaturation may be obtained by controlled solvent evaporation or temperature lowering. A typical crystal growth rig for solution crystal growth is shown in figure 2.21. Essentially the material to be grown is present as a saturated solution within the growth flask. This growth flask is surrounded by a large stirred water bath for controlled temperature conditions. A seed crystal of the material in question is introduced to the saturated solution, being suspended via a nylon thread on a stirrer. A small hole may be drilled in the seed using a solvent drill, in order that the seed may be suspended. The

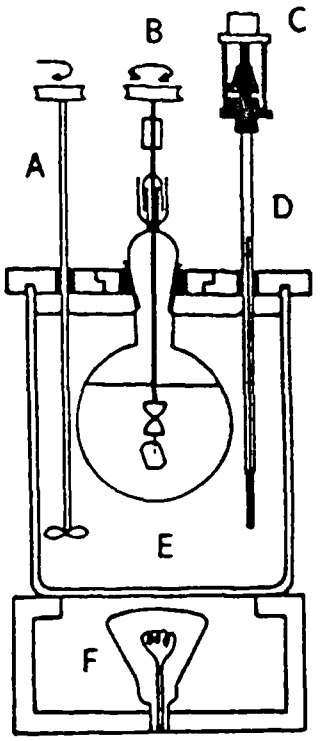

A - Water Stirrer
B - Solution Stirrer
C - Temperature Lowering
D - Contact Thermometer
E - Water Bath
F - Infra-red Heater

Figure 2.21: Typical rig employed in solution crystal growth.

objective is to obtain supersaturation and focus the resultant nucleation on the seed. Supersaturation may be obtained by controlled solvent evaporation or temperature lowering. The objective is to maintain supersaturation within the metastable zone region. If too great a supersaturation is obtained, e.g. entering the labile zone in figure 2.9, then uncontrolled spontaneous nucleation will occur. This will lead to nucleation and competing crystal growth in the solution surrounding the crystal. Agitation levels must also be controlled. If the level of agitation is too high then the metastable zone will be reduced, thus increasing the probability of uncontrolled spontaneous nucleation. Either of these factors may lead to the growth of low quality crystals with solvent inclusions etc. If the rate of agitation is too low, then a concentration gradient will occur, which may lead to crystal growth in another area of the growth flask, rather than on the seed.

2.5.2 Industrial Crystallisation

Crystallisation is a major industrial process in the production of pure materials, frequently proving to be the most cost effective method of producing high purity mate-

rials of an attractive appearance. There are many crystallisation techniques available; however all have in common the aim to produce a desired controllable supersaturation. The most common industrial crystallisation techniques are temperature lowering and solvent evaporation; some other crystallisation techniques are spray crystallisation, "salting out" in a second solvent and reaction precipitation. The choice of crystallisation technique is primarily dependent on the characteristics of a material, e.g. the solution solubility of a material can play an important role in determining what technique is employed. Slow cooling may be employed to achieve a desired controlled supersaturation for a material with a reasonable positive solubility curve, e.g. sodium sulphate decahyhdrate $Na_2SO_4.10H_2O$. If a material has a very high positive solubility, e.g. potash alum $AlK(SO_4)_2.12H_2O$, then employing slow cooling may not be sufficent to reduce the solubility of the solute in the solvent, hence a second component may be added to reduce the solute solubility. This technique is known as "salting out" and a particular example of salting out of $AlK(SO_4)_2.12H_2O$ from aqueous solution by acetone is highlighted. If a material has a negative solubility, e.g. Na_2SO_4 or $Na_2CO_3.H_2O$ (see chapter 6), then slow heating has to be employed to achieve supersaturation. However, if the solubility curve is only slightly negative, then the levels of supersaturation obtained may not be sufficient for efficient crystallisation. Hence solvent evaporation again must also be employed to obtain much higher levels of supersaturation.

Chemical reaction as a crystallisation process is employed in many industries and can be especially useful in the recycling of valuable waste materials such as powder fines and exhaust gases. High supersaturation levels can be obtained, thus production of fine particles is possible.

Particles of different size distribution may be produced by spray crystallisation. This technique is similar to spray drying; solid deposited from solution by the rapid evaporation of solvent. Particle size is determined by the droplet size, which is in turn controlled by the atomisation of the solution into droplets. This technique is particularly favoured when a materials crystallisation characteristics or the final product form desired imply that conventional crystallisation techniques may not be suitable, e.g., the crystallisation of heat sensitive materials, or where particle size is

of fundamental consideration. Spray drying as a technique for producing burkeite ($Na_2CO_3(Na_2SO_4)_2$) crystals of a particular size distribution is discussed in chapter seven.

The presence of heteronuclei is literally unavoidable in crystallisation systems. These reduce the width of the metastable zone shown in figure 2.6 by reduction of the free energy of the system (section 2.3.2). Hence problems may be encountered by the presence of these nuclei causing the solution to enter the labile region in figure 2.6, therefore crash nucleation occurs. The presence of these nuclei must be taken into account in any industrial crystallisation system. However, nuclei may be introduced into systems (known as "controlled seeding") of large metastable zonewidths in order to induce crystallisation. The nuclei may or may not be the same material as the desired crystallising material, depending on the purity levels required. This technique has been employed in the crystallisation of sodium sulphate decahydrate, which has a very large metastable zonewidth (see chapter six), hence problems may be encountered during crystallisation due to the large undercoolings required. However, the introduction of small amounts of sodium tetraborate decahydrate reduces the width of the metastable zone sufficiently to induce crystallisation at much smaller undercoolings.

2.6 Conclusions

This chapter has briefly reviewed the theories underlying all the factors that must be taken into account during crystallisation; namely supersaturation, nucleation, resultant crystal growth and habit modification.

The relationship between structure and morphology has been emphasised and the model forwarded by Bravias-Friedel-Donnay-Harker to correlate lattice geometry and crystal morphology explained. This model forms the basis of the morphological predictions obtained during this study.

Some of the various crystallisation techniques available at laboratory and industrial levels and the conditions that determine what is the preferable crystallisation technique for a system have been outlined.

2.7 References

1. D. Elwell & H. Scheel; "Crystal Growth From High Temperature Solutions", Academic Press, New York, (1975)
2. H.A. Miers; J. Inst. Metals, **37** (1927) 331
3. J.W. Mullin; "Crystallisation", Second Edition, Butterworths, London (1972)
4. D. Turnbull; "Solid State Physics", New York Academic Press, **3** (1956) p225-306
5. G.M. Pound; Ing. Eng. Chem.; **44** (1952) 1278-1283
6. A.C. Zettlomoyer; "Nucleation", Dekker, New York (1963)
7. J.P Hirth & G.M. Pound; "Condensation and Evaporation, Nucleation and Growth Kinetics", Pergamon, Oxford, (1963)
8. J.W. Gibbs, "Collected Works" Longmans Green, New York, (1928)
9. M. Volmer & W. Weber; Z. Physik. Chem., **119** (1926) 277-301
10. R. Becker & W. Döring; Ann. Physik., no.5, **24** (1935) 719
11. G. Tammann; "States of Aggregation", Van Nostrand Press, New York, (1975)
12. D. Turnbull & J.D. Fisher; J. Chem. Phys. **17** (1949) 71-73
13. G. Nancollas & N. Purdie; Q. Rev. Chem. Soc. **18** (1964) 1-15
14. R.A. Oriani & B.E. Sundquist; J. Chem. Phys. **38** no.9 (1963) 2082-2089
15. J. Lothe & G.M. Pound; J. Chem. Phys. **36** (1962) 2080-2094
16. M.A. Larson & J. Garside; J. Cryst. Growth **76** (1986) 88-91
17. J.A.C. Christiansen & A.E. Nielsen; Acta. Chem. Scand. **5** (1951) 673
18. J. Nývlt; J. Cryst. Growth, **3,4** (1968) 377-383
19. J.W. Mullin & J.J. Jancic; Trans. I. ChemE, **57** (1979) 188-193
20. W. Kossel; Annln. Phys., **21** (1934) 457
21. M. Volmer; "Kinetik der Phasenbildung" Steinkopff, Dresden and Leipzig (1939)
22. W.K. Burton, N. Cabrera & F.C. Frank; Phil. Trans. **A243** (1951) 299-358
23. C.W. Bunn; Proc. Royal Soc. **141** (1933) 567-593
24. A.A. Chernov; Growth of Crystals, **3** (1962) 31
25. I.N. Stranski; Bull. Soc. Franc. Mineral. Crist., **79** (1956) 359-376
26. R.J. Davey; J. Cryst. Growth, **34** (1976) 109-119
27. G. Blitznakov; "Adsorption et Croissance Cristalline", Paris, C.N.R.S., Colloq.

no 152, (1965)

28. J.W. Mullin, A. Amatavivadhana & M. Chakraborty; J. Appl. Chem., 20 (1970) 153-158

29. R.J. Hauy; J. Phys. 19 (1792) 366

30. J.W. Gibbs; Trans. Acad. Connecticut Acad., Vol. 3 (1875)

31. G. Wulff; Z. Krist. 34 (1901) 499

32. F.C. Phillips; "An Introduction to Crystallography", 3rd ed.(Longmans Green, London, 1963)

33. E. Dowty; Amer. Miner. 65 (1980) 465-471

34. A. Bravais; Etudes Crystallographiques Paris (1913)

35. J.D.H. Donnay & D. Harker; Amer. Miner. 22 (1937) 463

36. R. Docherty & K.J. Roberts; J. Crystal Growth, 88 (1988) 159

37. R. Docherty, K.J. Roberts & E. Dowty; Computer Physics Communications 51 (1988) 423

38. R. Docherty; PhD Thesis, University of Strathclyde (1989)

39. G. Clydesdale; PhD Thesis, University of Strathclyde (1991)

Chapter 3

Structure, Morphology And Habit Modification Of Some Carbonates, Sulphates And Phosphates.

Contents

3.1 Introduction

Crystallisation and crystal morphology play a significant role in many industrial separation systems. Poorly defined crystal morphology can have serious detrimental effects on an industrial process:

- crystal morphology can reduce the efficiency of the separation of solid from mother liquor or washing processes, e.g. "platelike crystals" can block filtration processes.
- whenever a product is part of a formulation the morphology is often crucial in altering the rheology of the formulation.

In the case of post-production, the potential end-user of a product may experience problems associated with crystal morphology:

- large crystals may adhere (caking) together, thus creating packing/storage problems,
- small crystals may disintegrate easily into dust particles which may present a toxicity hazard.

This chapter will highlight some models used in the prediction of equilibrium morphology and for assessing likely habit modification effects. Predicted morphologies based on lattice geometrical models are presented. These models will be applied to various inorganic salts, in particular to some inorganic salts which are employed as carrier powders in detergents. These high surface area materials boost detergency by being able to hold the surfactants within a porous matrix structure. The salts investigated are sodium tripolyphosphate hexahydrate and various compounds from the sodium carbonate/sulphate phase system. These predicted morphologies are compared and contrasted to previous morphology observations and to growth morphologies obtained during this study. The surface chemistry of sodium tripolyphosphate hexahydrate is examined, with a view to morphological modification. A theoretical mechanism for habit modification on a general ionic crystal is presented, and applied to sodium carbonate monohydrate. This mechanism is extended to sodium carbonate decahydrate and verified by experimental observations on the effects of various

additives on the crystal morphology of sodium carbonate monohydrate and sodium carbonate decahydrate.

3.2 Modelling of Crystal Morphology of Some Sodium Based Salts

3.2.1 Methodology

As explained in chapter 2, the laws of Bravais, Friedel, Donnay and Harker [1,2] may be used to predict the crystal forms likely to predominate in a morphology of a system. This model forms the basis of the computer program MORANG [3], which may be used to calculate an index of morphologically important forms, based on the reciprocal of the interplanar spacing d_{hkl}. Crystal properties such as interfacial angles, may also be predicted using MORANG. The subsequent morphological index may be graphically displayed using the crystal drawing program SHAPE [4]. For the ionic salts examined during this study, MORANG was employed to predict the morphologically important forms/interfacial angles and SHAPE employed to obtain the predicted crystal morphology. The ionic salts studied are $Na_5P_3O_{10}.6H_2O$ and various salts present in the Na_2CO_3-Na_2SO_4-H_2O system.

All the crystals obtained during this study have been grown from the solution phase. In all cases, the crystals have been grown in a growth flask as shown in figure 2.21 (see chapter 2). Crystals of $Na_2SO_4.10H_2O$ were grown by the slow cooling (0.1^0C/day) a solution containing Na_2SO_4 from 30^0C. Crystals of the other phases studied were grown by the controlled solvent evaporation of solutions at constant temperature. These are now detailed, with the respective growth temperature: $Na_2CO_3.H_2O$ - 45^0C, $Na_2CO_3.7H_2O$ - 33^0C, $Na_2CO_3.10H_2O$ - 30^0C, $Na_2CO_3(Na_2SO_4)_2$ - 80^0C, $Na_2SO_4)_2$ - 45^0C.

In each case, the resultant crystals were washed in n-hexane and stored in paraffin oil for isolation from atmospeheric conditions to prevent possible sample degradation.

3.2.2 Sodium Tripolyphosphate Hexahydrate

Sodium Tripolyphosphate Hexahydrate ($Na_5P_3O_{10}6.H_2O$, hereinafter referred as STP) crystallises in a triclinic crystal structure (spacegroup $P\bar{1}$) with unit cell parameters: a=10.37$\mathring{A}$ b=9.224$\mathring{A}$ c=9.455$\mathring{A}$, $\alpha = 92.24°\beta = 94.55°\gamma = 90.87°$, Z=2 [5] . The morphological importance based on the BFDH laws is summarised in table 3.1 and resultant morphology simulated in figure 3.1.

Form	$1/d_{hkl}$
H K L	(Angstroms)
1 0 0	0.09675
0 1 0	0.10164
0 0 1	0.13180
1 $\bar{1}$ 0	0.13903
1 1 0	0.14161
1 0 $\bar{1}$	0.15717
0 1 $\bar{1}$	0.16319
1 0 1	0.16966
0 1 1	0.16969
1 1 $\bar{1}$	0.18523

Table 3.1: BFDH analysis of sodium tripolyphosphate hexahydrate.

It can be seen that the main face is {100} type, which is of slightly more importance than the {010} forms. The effect of these forms predominating in the morphology causes the overall morphology to resemble a thick faceted plate, almost "blocklike" in nature. The $\{10\bar{1}\}$, $\{1\bar{1}0\}$ and $\{01\bar{1}\}$ forms are of less importance in the morphology, forming "edge" facets on the morphology. This is in reasonable agreement with the observed morphology reported by Troost [6] (figure 3.2), although the predicted $\{01\bar{1}\}$ and $\{10\bar{1}\}$ forms are not observed on the growth morphology.

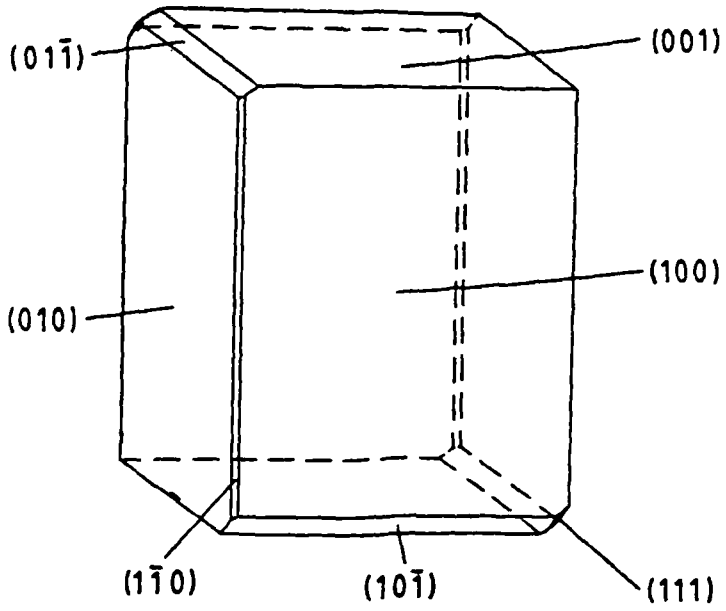

Figure 3.1: Predicted morphology of $Na_5P_3O_{10}(H_2O)_6$ based on the BFDH laws.

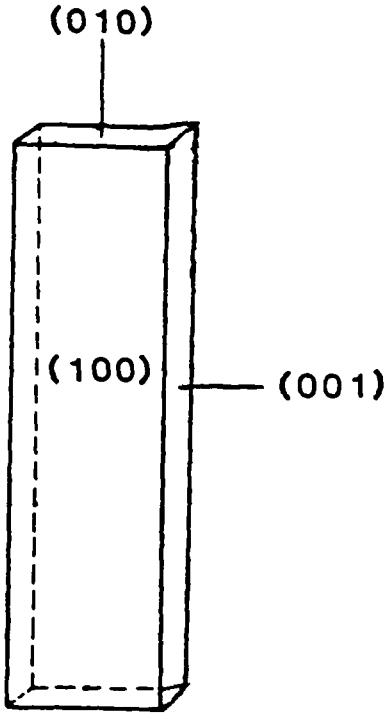

Figure 3.2: Observed growth morphology of $Na_5P_3O_{10}.6H_2O$ [6]

3.2.3 Carbonate/Sulphate Systems

Alternatives to sodium tripolyphosphate hexahydrate as a detergent carrier have been extensively researched. It has been found that various carbonate/sulphate salts have exhibited comparable performances as carriers for detergent applications. The phase diagram [7] for the Na_2CO_3-Na_2SO_4-H_2O system is shown in figure 3.3 and reveals the following phases:

- sodium carbonate monohydrate, $Na_2CO_3.H_2O$ [8]
- sodium carbonate heptahydrate, $Na_2CO_3.7H_2O$ [9]
- sodium carbonate decahydrate, $Na_2CO_3.10H_2O$ [10]
- sodium sulphate Na_2SO_4 [11]
- sodium sulphate decahydrate $Na_2SO_4.10H_2O$ [12]
- Burkeite $Na_2CO_3(Na_2SO_4)_2$ [13]

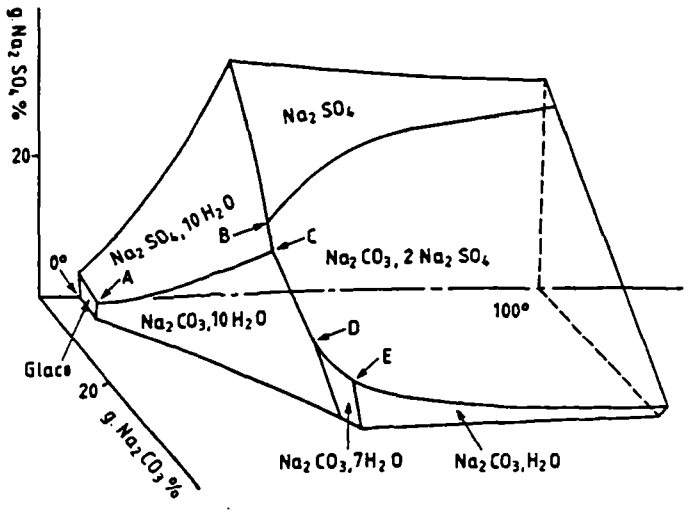

Figure 3.3: Phase diagram of the Na_2CO_3-Na_2SO_4-H_2O system [7].

Crystallographic data for each of the phases is summarised in Table 3.2. Sections 3.2.3, 3.2.4 and 3.2.5 highlight the comparison between predicted and observed

growth morphologies for the sodium carbonate based salts, sodium sulphate based salts and burkeite respectively.

3.2.4 Sodium Carbonate And Related Hydrates

The predicted morphologies for $Na_2CO_3.H_2O$, $Na_2CO_3.7H_2O$ and $Na_2CO_3.10H_2O$ are shown in figures 3.4-3.6 respectively. The main face for the orthorhombic carbonates $Na_2CO_3.H_2O$ and $Na_2CO_3.7H_2O$ is {020}, with both crystals possessing a prismatic habit. The only difference noted between these predicted morphologies is the additional presence of {001} forms in $Na_2CO_3.H_2O$. Whilst the morphology of the monoclinic $Na_2CO_3.10H_2O$ is also prismatic, the distribution of forms is distinctly different with $\{11\bar{1}\}$ forms predominating over $\{1\bar{1}0\}$ forms.

A comparison may be made of these predicted morphologies to observed morphological information [14] (figures 3.7-3.9) and to growth morphologies obtained during this study. Typical crystals of $Na_2CO_3.H_2O$, $Na_2CO_3.7H_2O$ and $Na_2CO_3.10H_2O$ grown during this study are shown in figures 3.10-3.12. In each case the crystals were removed from solution, washed with an inert solvent (e.g. n-hexane) and stored under paraffin oil to prevent the possibility of sample degradation due to hydration from atmospheric conditions. The resultant crystals were transparent. When washed of mother liquor using n-hexane and left exposed to the atmosphere, the crystals rapidly degraded, forming a white deposit on the surface. For treatment and resultant storage of $Na_2CO_3.H_2O$, Rolfe [14] has suggested that the crystals be washed of mother liquor in the following sequence: 80% ethanol/water mixture, followed by 100% ethanol and 100% acetone. Crystals of $Na_2CO_3.H_2O$ treated in this fashion have been left exposed to atmospheric conditions without any degradation. Treatment of $Na_2CO_3.H_2O$ crystals by this method has proved successful, raising the point that washing crystals of $Na_2CO_3.H_2O$ of mother liquor by n-hexane may precipitate surface damage leading to further degradation of the crystals.

The hydration content of crystals of these materials led to efflorescence in the vacuum conditions required for Scanning Electron Microscopy (SEM). The re-

sultant sample degradation creates difficulties in comparison of predicted to observed morphologies. Observed morphologies of $Na_2CO_3.H_2O$, $Na_2CO_3.7H_2O$ and $Na_2CO_3.10H_2O$ obtained from Rolfe [14] (figures 3.7-3.9) allow a better comparison between predicted and observed growth morphologies.

Phase	Space Group	unit cell dimensions
$Na_2CO_3.H_2O$	P21ab	a= 6.472Å, b= 10.724Å, c= 5.259Å $\alpha = \beta = \gamma = 90^0$
$Na_2CO_3.7H_2O$	Pbca	a= 14.492Å, b= 19.490Å, c= 7.017Å $\alpha = \beta = \gamma = 90^0$
$Na_2CO_3.10H_2O$	Cc	a=12.83Å, b= 9.026Å, c= 13.44Å $\alpha = 90^0 \beta = 123.0^0 \gamma = 90^0$
Na_2SO_4	Fddd	a= 5.8596Å, b= 12.3044Å, c= 9.817Å $\alpha = 90^0 \beta = \gamma = 90^0$
$Na_2SO_4.10H_2O$	P21/c	a= 11.512Å, b= 10.370Å, c= 12.847Å $\alpha = 90^0 \beta = 107.8^0 \gamma = 90^0$

Table 3.2: Crystallographic Data for Phases Present in the Na_2CO_3-Na_2SO_4-H_2O System.

A vast amount of morphological information obtained for a range of materials by a variety of authors has been summarised by Groth [15]. This information may be used in conjunction with crystals of the various phases grown during this study to ascertain the validity of the morphological predictions.

Previous studies [15] on the growth of $Na_2CO_3.H_2O$ indicate that the {100} forms predominate, with {010},{001},{110},{101} and {201} forms present to a lesser extent; the predicted order of morphological importance indicates the presence of these forms, but with the {020} forms predominating over the {001} forms. The small observed {201} and {041} growth forms are not predicted by the BFDH model.

The growth morphology of $Na_2CO_3.H_2O$ obtained in a more recent study [14] is shown in figure 3.7. The {001} forms predominate over {100} forms, with {101}, {201}, {110}, {121} and {010} forms also present. A typical growth morphology obtained during the present study is shown in figure 3.10. The {001} forms

can be identified, as can the {101}, {010} {121}, {041} and {010} forms. These morphologies are in reasonable agreement; however the {100} and {201} forms are not observed in the current study. When these growth morphologies are compared to the predicted morphology good agreement is noted, moreso between the growth morphology observed by Rolfe [14] and the predicted morphology. The majority of the observed forms are predicted, with the exception of the small {201} and {041} forms. Hence the BFDH model may be employed to simulate crystal morphology accurately, possible differences between predicted and observed orders of morphological importance may mean that certain observed growth forms, e.g. the {201} forms are underestimated in morphological importance and are consequently not observed on the predicted morphology.

The same trends are noted for $Na_2CO_3.7H_2O$. In general good agreement is noted between predicted and observed morphologies; the majority of the observed forms are predicted correctly, however certain observed growth forms of lesser morphological importance are not predicted. Previous studies [15] on the morphology of $Na_2CO_3.7H_2O$ have revealed that the {010} forms predominate, with {021}, {100}, {111}, {210}, {230} and {121} present to a lesser extent. Observations of the morphology by Rolfe [14] (figure 3.8) show good agreement to these studies with the morphology prismatic in nature. Typical crystals of $Na_2CO_3.7H_2O$ obtained during the redetermination of the Na_2CO_3-Na_2SO_4-H_2O phase system (chapter 5) are shown in figure 3.11. Sample degradation has made it impossible to identify all forms present explicitly, although the {020}, {021} and {111} forms can be identified. These observed morphologies show reasonable correlation to the predicted morphology (figure 3.5), although the observed small {121} and {230} forms are not predicted. Differences may also be observed in the morphological order of importance of certain forms, e.g. the observed {021} forms have much more morphological significance than the predicted {021} forms.

Reported observed growth forms for $Na_2CO_3.10H_2O$ are a combination of $\{11\bar{1}\}$ and {010} forms predominating, with {100} and $\{10\bar{1}\}$ forms also present [15]. This contrasts to a more recent study [10] (figure 3.9), where the {100} forms predominate, with {111}, {110} and {001} forms present to a lesser extent. A typical growth

morphology of $Na_2CO_3.10H_2O$ obtained during this study is highlighted in figure 3.12. Sample degradation due to effloroescence is clearly observed, however the {100}, {001} and {111} faces can be identified. The previously reported small {110} faces cannot be distinguished. The predicted morphology of $Na_2CO_3.10H_2O$ (figure 3.6) shows the {111} forms slightly predominating over {110} forms, with {112} and {200} also present to a lesser extent. Thus, the predicted order of morphological importance is in good agreement with previous studies [14,15], although in more recent studies and in the present study, the {100} forms predominate rather than the {111} or {110} forms as predicted and previously observed [15].

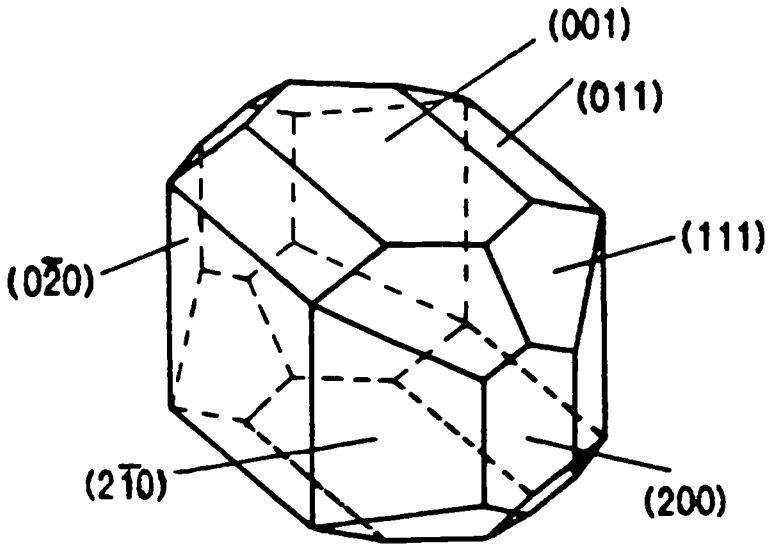

Figure 3.4: Predicted morphology of $Na_2CO_3.H_2O$ based on the BFDH laws.

It may be summarised for the sodium carbonate system that the predicted morphologies in general show good agreement to observed morphologies, although differences are noted between the predicted and observed order of morphological importance and certain observed growth faces of lesser importance are not predicted by the BFDH model. However for any material, large variations in morphology may occur according to growth conditions, but the interfacial angles between forms will remain invariant [16]. Hence a more accurate estimation of the correlation between predicted and observed morphologies may be obtained by comparison between pre-

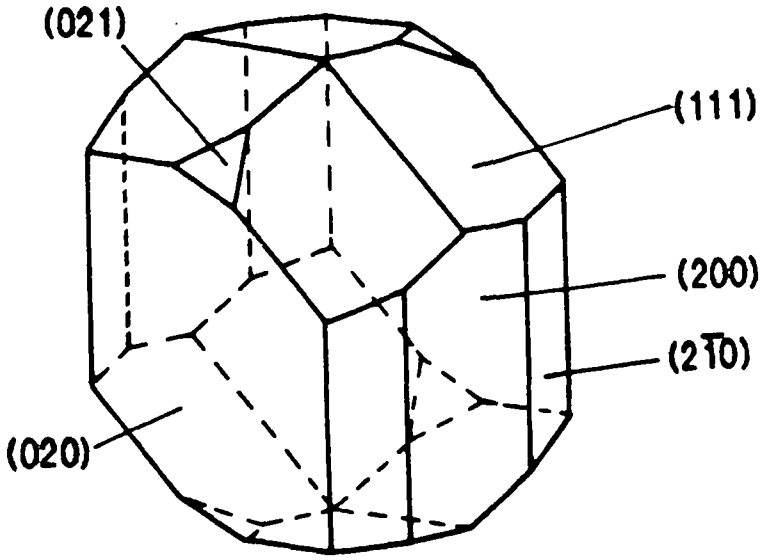

Figure 3.5: Predicted morphology of $Na_2CO_3.7H_2O$ based on the BFDH laws.

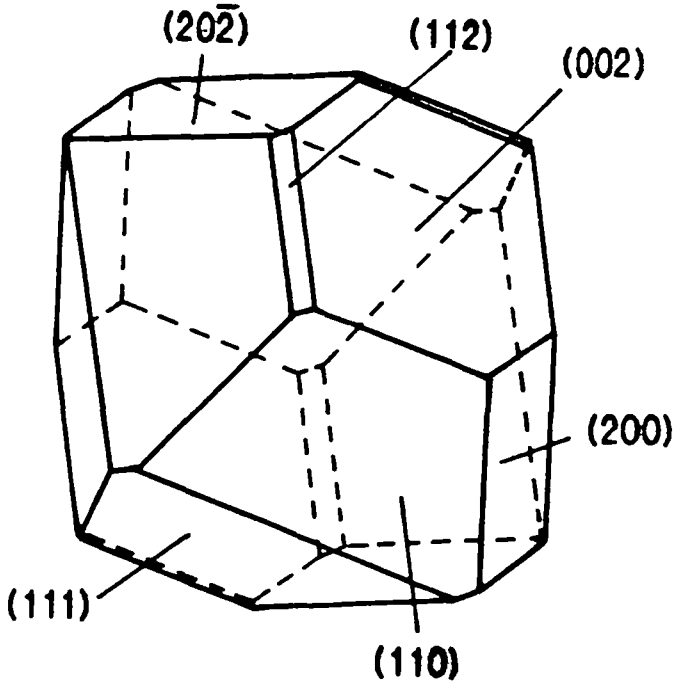

Figure 3.6: Predicted morphology of $Na_2CO_3.10H_2O$ based on the BFDH laws.

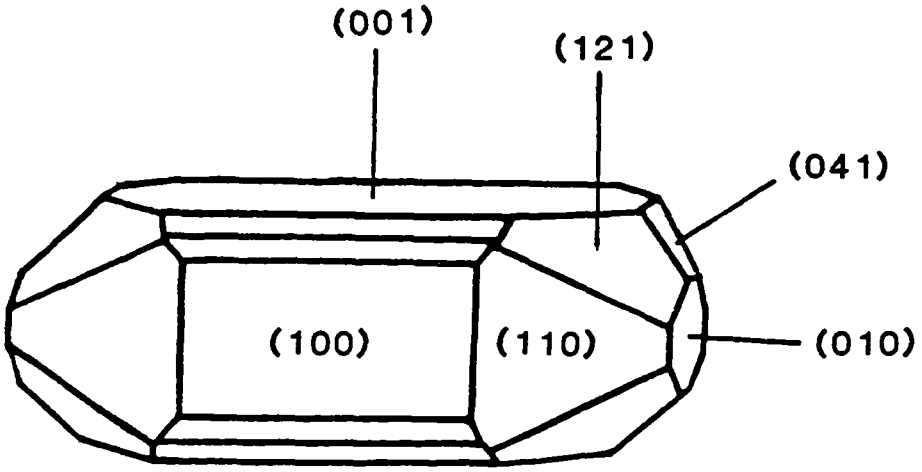

Figure 3.7: Previously reported morphology of $Na_2CO_3.H_2O$ [14].

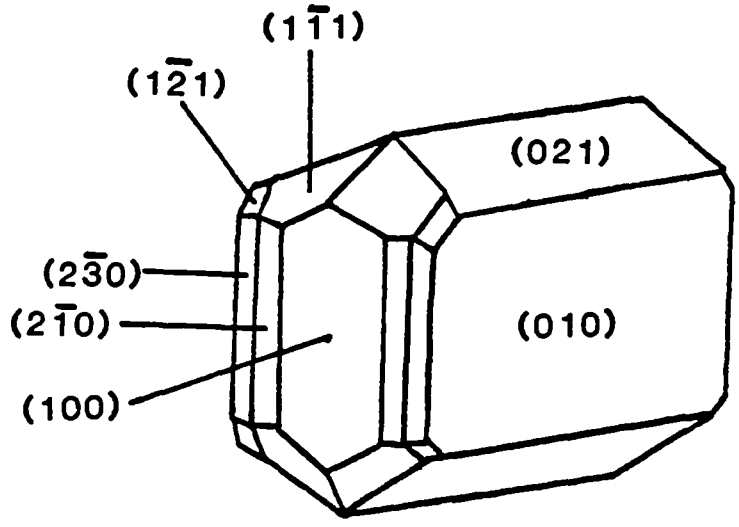

Figure 3.8: Previously reported morphology of $Na_2CO_3.7H_2O$ [14].

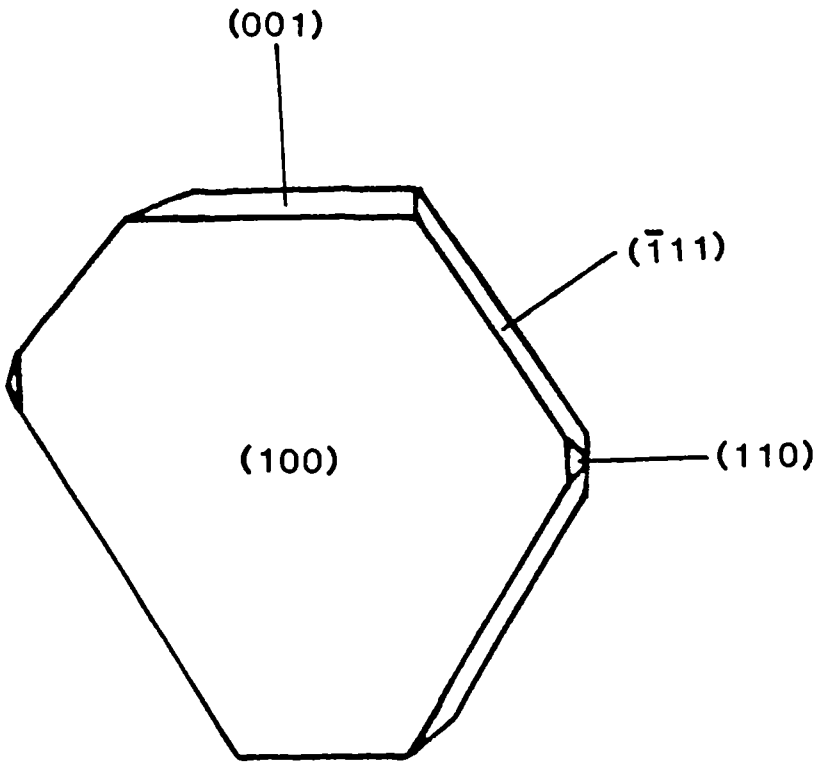

Figure 3.9: Previously reported morphology of $Na_2CO_3.10H_2O$ [14].

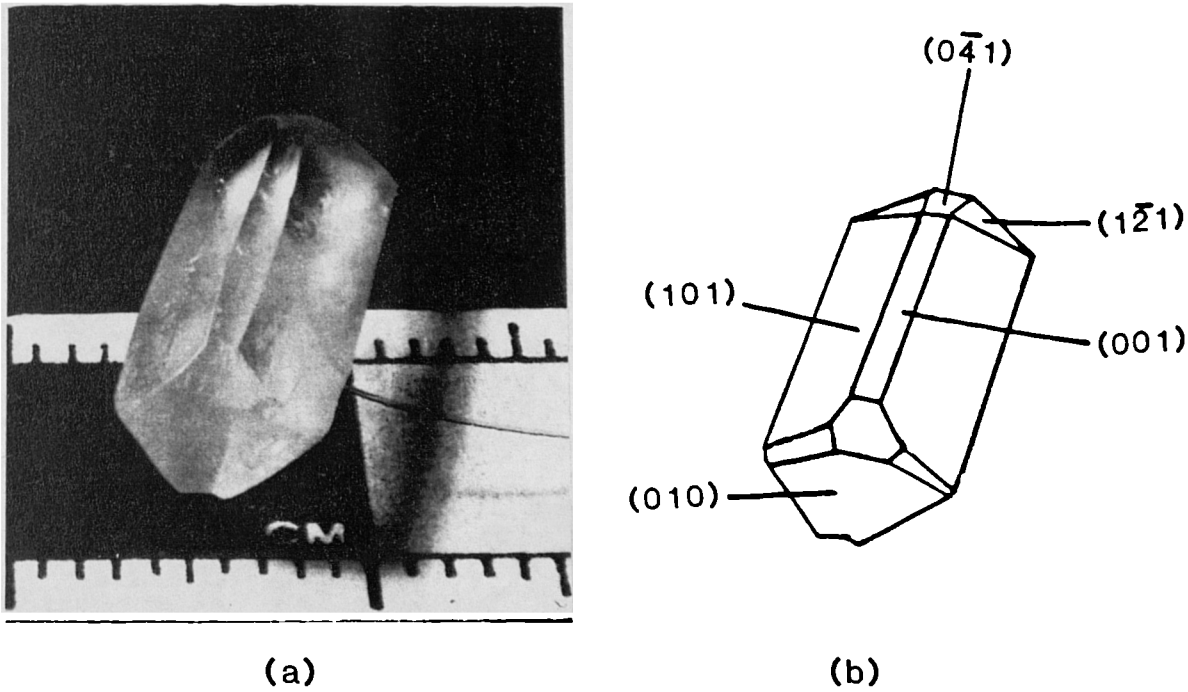

Figure 3.10: a) Typical crystal of $Na_2CO_3.H_2O$ observed in current study. b) Schematic of crystal morphology of $Na_2CO_3.H_2O$.

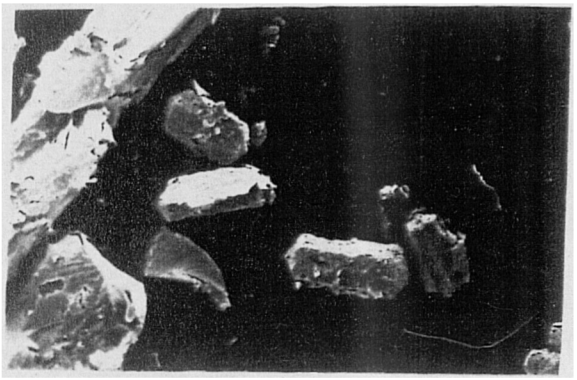

(a)

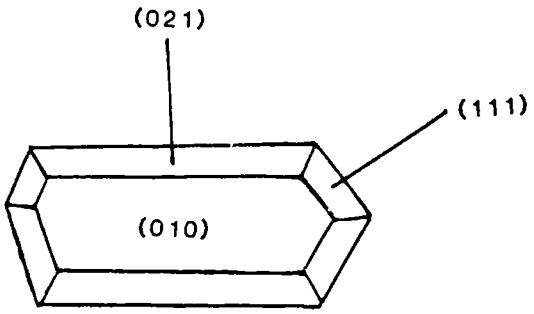

(b)

Figure 3.11: Typical crystal of $Na_2CO_3.7H_2O$ observed in current study. b) Schematic of crystal morphology of $Na_2CO_3.7H_2O$.

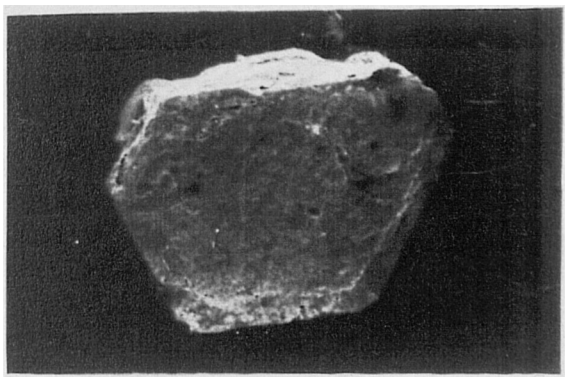

(a)

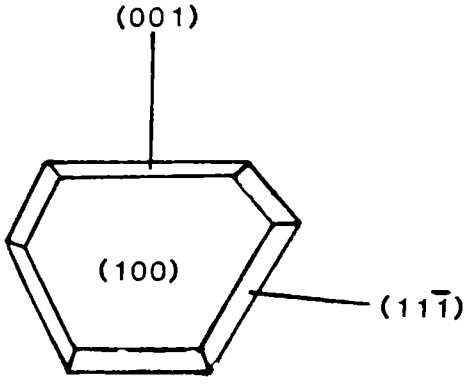

(b)

Figure 3.12: Typical crystal of $Na_2CO_3.10H_2O$ observed in current study. b) Schematic of crystal morphology of $Na_2CO_3.10H_2O$.

dicted and observed interfacial angles. The predicted interfacial angles as obtained from the BFDH model are compared and contrasted to observed interfacial angles for $Na_2CO_3.H_2O$, $Na_2CO_3.7H_2O$ and $Na_2CO_3.10H_2O$ in tables 3.3-3.5 respectively.

Forms H K L	Predicted Interfacial Angles (°)	Observed Interfacial Angles (°) [15]
1 1 0 : 1 $\bar{1}$ 0	69.22	79.17
1 0 0 : 1 0 1	50.90	63.93
1 0 0 : 1 2 1	59.10	69.33
0 0 1 : 1 2 1	52.22	43.63
1 1 0 : 1 2 1	41.70	49.53

Table 3.3: Predicted and Observed Interfacial Angles For $Na_2CO_3.H_2O$.

Forms H K L	Predicted Interfacial Angle (°)	Observed Interfacial Angle (°) [15]
0 1 0 : 2 1 0	69.61	69.50
0 2 1 : 0 $\bar{2}$ 1	71.51	71.57
0 1 0 : 1 1 1	72.05	72.10
1 0 0 : 1 1 1	65.51	65.70
0 1 0 : 2 3 3	71.09	71.15
1 0 0 : 2 3 3	73.11	73.25

Table 3.4: Predicted and Observed Interfacial Angles For $Na_2CO_3.7H_2O$.

Forms H K L	Predicted Interfacial Angle (°)	Observed Interfacial Angle (°) [11]
1 1 0 : 1 $\bar{1}$ 0	100.02	100.31
1 0 $\bar{1}$: 1 0 0	59.05	58.87
1 1 $\bar{1}$: 1 $\bar{1}$ $\bar{1}$	103.87	103.53
1 1 $\bar{1}$: 1 0 0	71.51	71.33
1 1 $\bar{1}$: 1 1 0	36.20	36.08

Table 3.5: Predicted and Observed Interfacial Angles For $Na_2CO_3.10H_2O$.

Although reasonable agreement was observed between the predicted and observed morphologies for $Na_2CO_3.H_2O$ there is a lack of agreement between the predicted and observed interfacial angles; however the good correlation noted for $Na_2CO_3.7H_2O$ and $Na_2CO_3.10H_2O$, highlights that in general, the BFDH model may be employed for accurate morphology simulation.

3.2.5 Sodium Sulphate And Sodium Sulphate Decahydrate

The predicted morphologies based on the BFDH model and the observed morphologies for $Na_2SO_4.10H_2O$ and Na_2SO_4 observed in previous studies and in the present study are shown in figures 3.13-3.18. Major differences can be observed between the predicted morphology of $Na_2SO_4.10H_2O$ (figure 3.13) and Na_2SO_4 (figure 3.14). In the case of Na_2SO_4, the main forms are of $\{1\bar{1}\ \bar{1}\}$ type, the morphology resembling a rhombic bipyramid whereas in $Na_2SO_4.10H_2O$ the morphology resembles a faceted "plate-like" morphology, with {100} as the most predominant form.

In previous studies [15] on the growth morphology of $Na_2SO_4.10H_2O$ (figure 3.15) the following forms were observed: {100}, {001}, {010}, {110}, {120}, {011}, $\{11\bar{1}\}$, {111}, $\{11\bar{2}\}$, {102}, $\{10\bar{1}\}$, $\{10\bar{2}\}$, {021}. A typical crystal of $Na_2SO_4.10H_2O$ obtained during the current study (figure 3.17) exhibits {100}, {010}, {001}, {110}, {111}, {011} and {102} forms, showing good correlation to previous studies. However, certain forms previously observed, e.g. $\{10\bar{1}\}$ and {021}, were not

observed in the current study. Other features may be noted: The {010} and {110} forms tend to have greater importance in the crystals grown during the present study, with a corresponding decrease in morphological importance of the {011} forms. Crystals grown in this study were typically less elongated along the "b" direction than in previous studies. Both these growth morphologies show excellent agreement with the predicted morphology, although certain observed small forms, e.g. {021} and {010} are not predicted.

The following growth forms have been observed during previous studies [15] on the growth of Na_2SO_4 (figure 3.16): {111}, {110}, {113} and {010} forms. This shows excellent agreement with crystals grown during this study (figure 3.18), which exhibit {111}, {110} and {113} forms. The {010} forms previously observed have not been observed during this study. Both these observed growth morphologies are in excellent agreement with the predicted morphology (figure 3.14); the previously observed {010} forms not being predicted.

A comparison of predicted and observed interfacial angles for both $Na_2SO_4.10H_2O$ and Na_2SO_4 is shown in tables 3.6 and 3.7 respectively. Excellent agreement is noted throughout for all the faces observed and when taken in correlation with the morphological observations emphasises the excellent correlation between predicted and observed growth morphologies.

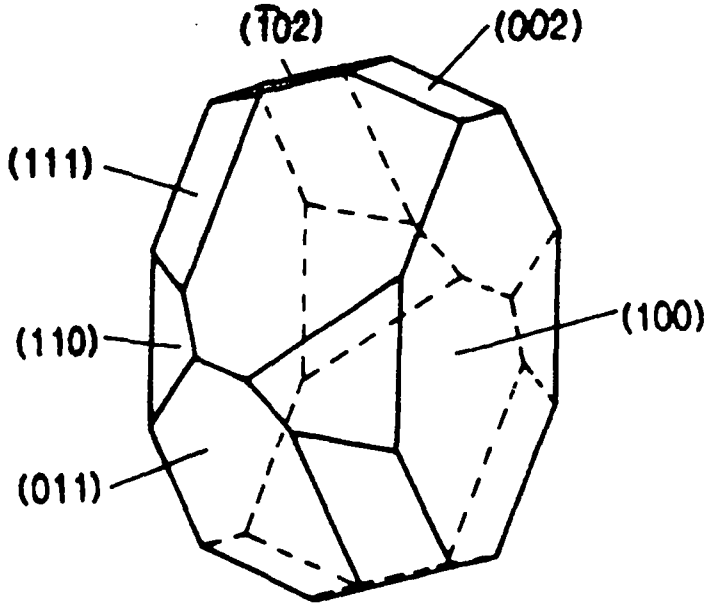

Figure 3.13: Predicted morphology of $Na_2SO_4.10H_2O$ based on the BFDH laws.

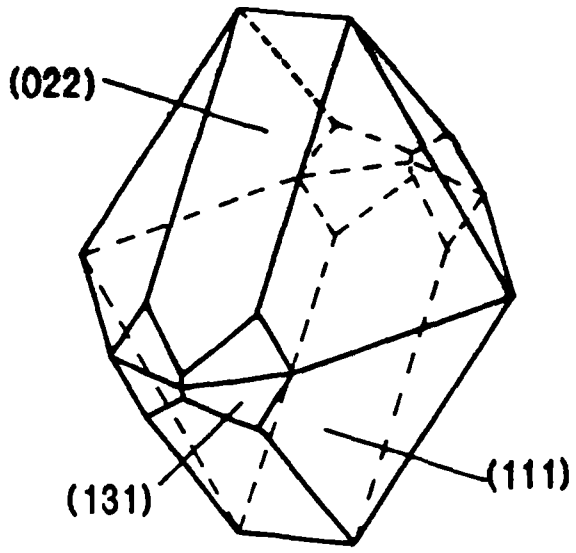

Figure 3.14: Predicted morphology of Na_2SO_4 based on the BFDH laws.

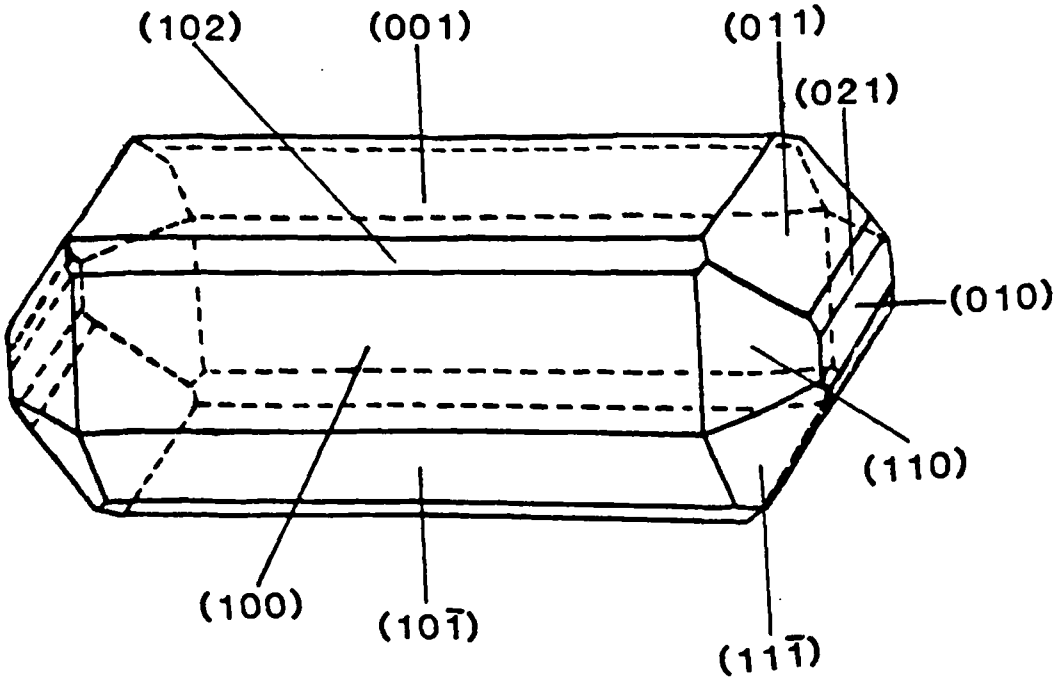

Figure 3.15: Previously reported morphology of $Na_2SO_4.10H_2O$ [15].

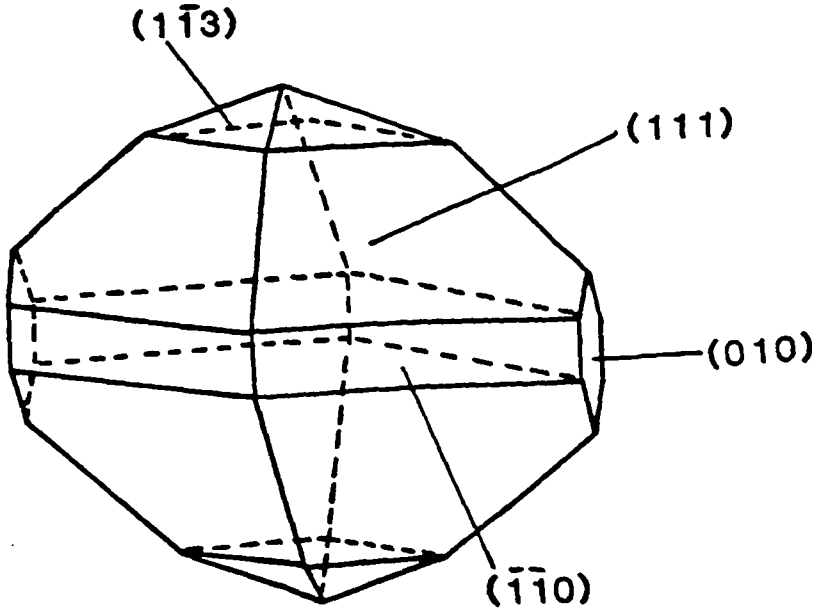

Figure 3.16: Previously reported morphology of Na_2SO_4 [15].

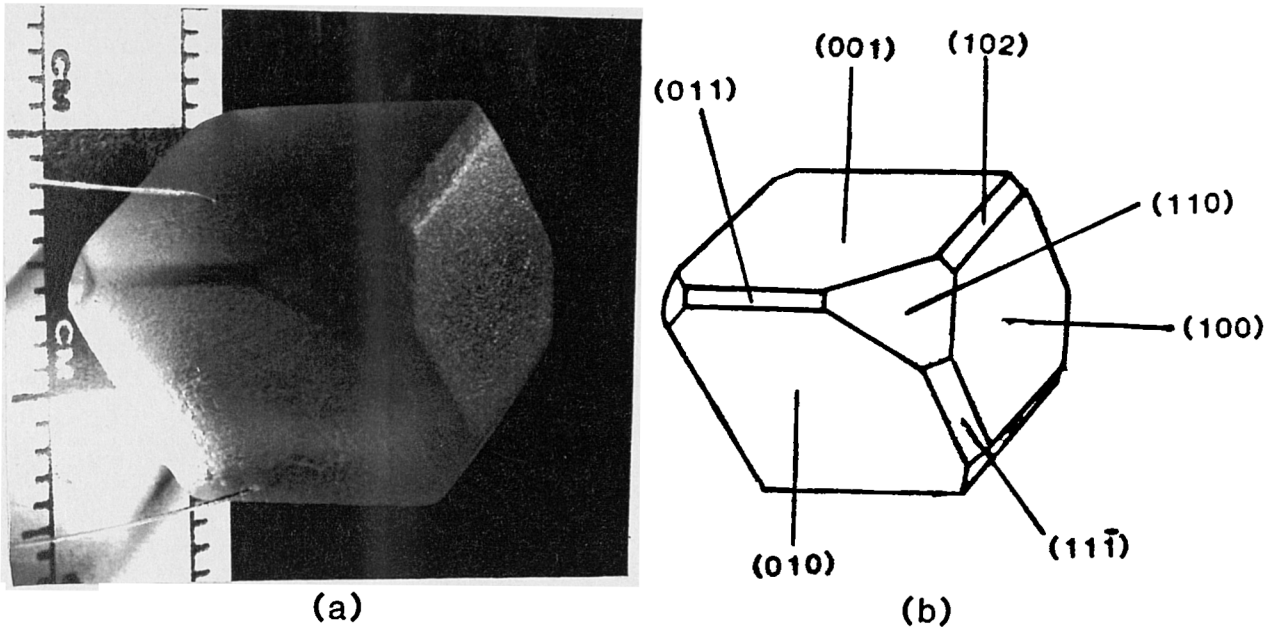

Figure 3.17: a) Typical crystal of $Na_2SO_4.10H_2O$ observed in current study b) Schematic of crystal morphology of $Na_2SO_4.10H_2O$.

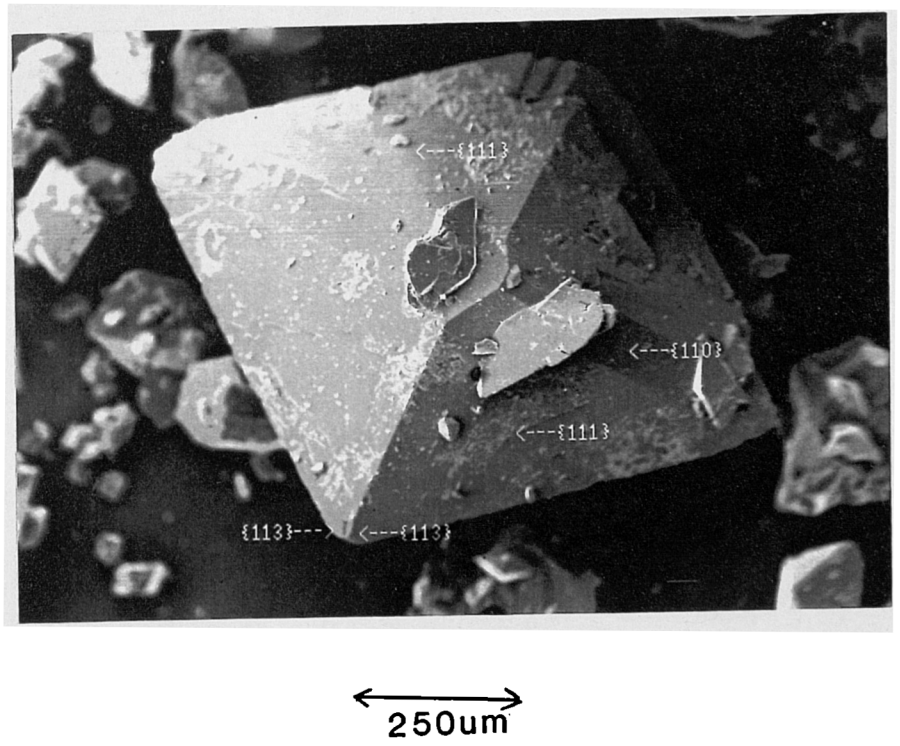

Figure 3.18: Typical crystal of Na_2SO_4 observed in current study.

Forms H K L	Predicted Interfacial Angle (°)	Observed Interfacial Angle (°) [15]
1 1 0 : $\bar{1}$ 1 0	86.83	86.56
0 1 1 : 0 1 $\bar{1}$	80.58	80.50
0 1 2 : 0 1 1	19.18	17.35
1 1 1 : 1 $\bar{1}$ 1	69.16	69.30
1 1 $\bar{1}$: 1 $\bar{1}$ $\bar{1}$	86.67	86.80
1 2 0 : $\bar{1}$ 2 0	50.63	50.40
0 0 1 : 1 1 0	77.87	77.72
0 0 1 : 1 0 0	72.20	72.29
0 0 1 : $\bar{1}$ 1 1	67.46	67.48
0 0 1 : 1 0 2	24.41	32.55
1 0 0 : 1 0 $\bar{2}$	75.16	75.82
1 0 0 : 1 0 $\bar{1}$	49.60	49.64
1 0 0 : 0 1 1	78.60	78.65

Table 3.6: Predicted and Observed Interfacial Angles For $Na_2SO_4.10H_2O$.

Forms H K L	Predicted Interfacial Angle (°)	Observed Interfacial Angle (°) [15]
1 1 1 : 1 $\bar{1}$ 1	44.48	44.32
1 1 1 : 1 1 $\bar{1}$	56.64	56.28
1 1 1 : $\bar{1}$ 1 1	105.27	105.70
1 1 0 : 1 $\bar{1}$ 0	30.93	50.63
1 1 3 : 1 1 0	58.26	57.43

Table 3.7: Predicted and Observed Interfacial Angles For Na_2SO_4.

3.2.6 Burkeite - A Mixed Sodium Sulphate/Carbonate Double Salt

Burkeite [13] - $Na_2CO_3(Na_2SO_4)_2$ is the name given to the mineral discovered in 1935 by Foshag [17] with the formula $Na_2CO_3(Na_2SO_4)_2$. It is a comparatively rare material occurring mainly in natural evaporite situations. Recent work [13] has indicated that the stoichiometry of this compound can be variable and that the more general formulae of $Na_4SO_4(CO_3)_T(SO_4)_{(1-T)}$ would be more appropriate for this material.

Burkeite crystallises in an orthorhombic structure (space group Pmnm) and cell parameters of a=5.17Å b=9.217Å c=7.05814Å [13]. However the crystal structure shows substantial positional disorder which in turn can give rise to structural modulations associated with a larger unit cell. Ramsdell [18] deduced the presence of a supercell containing 12 formula units of burkeite; the "b" and "c" lattice parameters being tripled. Giuseppetti et al [13] have classified 2X and 6X superstructures (see table 3.8) in Burkeite with the variation in superstructure apparently being due to carbonate content.

The equilibrium morphology simulated on the basis of the subcell is shown in figure 3.19 and it can be seen that the {010} forms predominate in the morphology, with the $\{10\bar{1}\}$ forms giving distinct corner facets. The overall morphology could be described as being "plate-like" with distinct side and corner facets and sharply contrasts with the predicted morphologies of the other phases present in the Na_2CO_3-Na_2SO_4-H_2O system. The morphologies simulated on the basis of the 2X and 6X supercells are highlighted in figures 3.20-21. It is immediately observed that the predicted morphologies are more prismatic than the predicted morphology based on the subcell. The predicted morphology based on the 2X supercell is very similar to that of the predicted morphology based on the subcell; e.g. in each case the main form is of a {010} type, with the 2X supercell having $\{02\bar{1}\}$ and the additional $\{1\bar{1}1\}$ forms rather than the $\{01\bar{1}\}$ forms. The predicted morphology based on the 6X supercell is substantially different from that of the subcell and 2X supercell: the {002} forms appear as the predominant form rather than the {010} forms, as in the 2X and the

subcell and the $\{1\bar{1}1\}$ forms are also more predominant in the 6X supercell.

Information on the observed morphology of $Na_2CO_3(Na_2SO_4)_2$ is limited. Pemberton [15] describes burkeite crystals as having tabular {100} forms and narrow {010}, {110} and {001} forms present. Ramsdell [14] described burkeite crystals as being twinned, with {110} and {111} forms being present. In each case, no precise drawings of single crystals are available, the individual crystals and twins described as being "rough, uneven and rarely exceeding 4mm in diameter". Pemberton also describes "small pea-shaped crystals of burkeite, with a surface comprising of relatively bright faces of {010} forms". These observations indicate that the predicted morphology of burkeite possesses the majority of the observed forms, but not the tabular {100} forms.

A typical crystal of $Na_2CO_3(Na_2SO_4)_2$ obtained in the present study is shown in figure 3.22. The habit is rather dendritic, with predominant {010} forms and

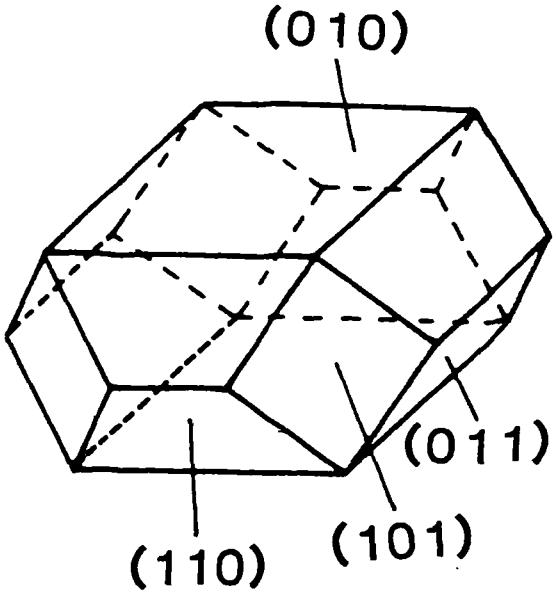

Figure 3.19: Predicted morphology of the $Na_2CO_3(Na_2SO_4)_2$ subcell, based on the BFDH laws.

{101}, {011} and {110} side facets. This is in excellent agreement with the predicted morphology based on the subcell, although the predicted morphology is more tabular in nature, with slight underestimation and overestimation of the {101} and {110}

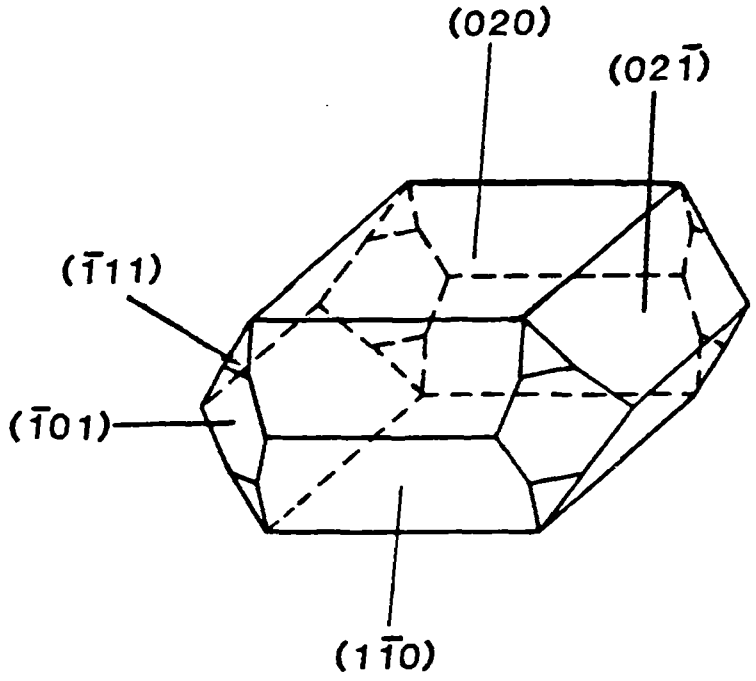

Figure 3.20: Predicted morphology of the 2X $Na_2CO_3(Na_2SO_4)_2$ supercell, based on the BFDH laws.

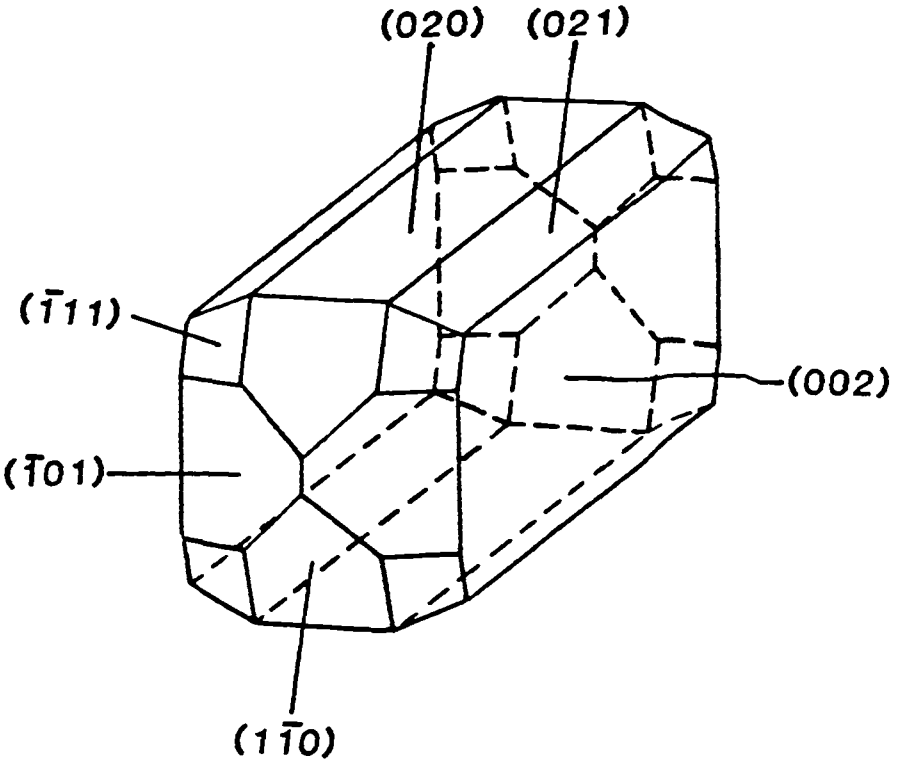

Figure 3.21: Predicted morphology of the 6X $Na_2CO_3(Na_2SO_4)_2$ supercell, based on the BFDH laws.

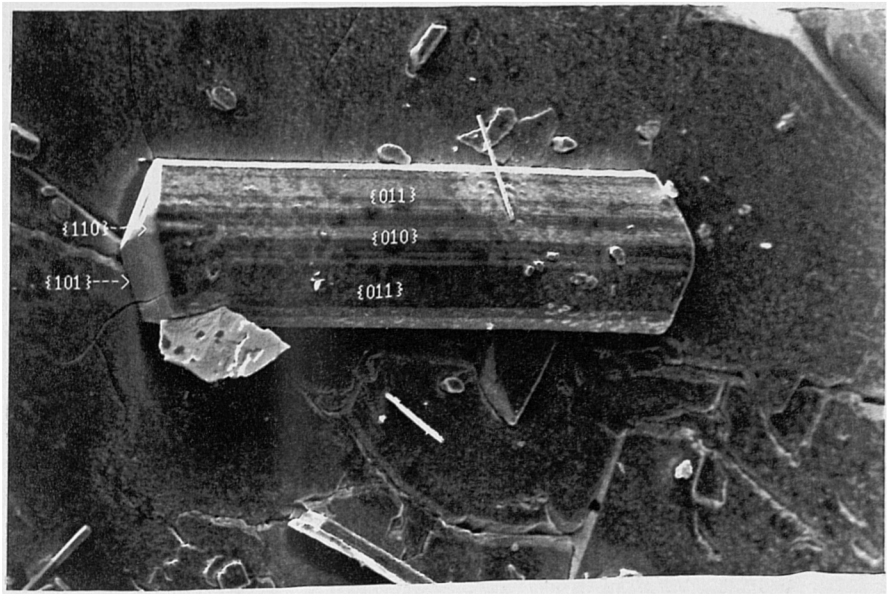

Figure 3.22: Observed Morphology of $Na_2CO_3(Na_2SO_4)_2$.

forms respectively.

A:6X subcell	B:6X subcell	C:2X subcell
Pbnm	Pbnm	Pbnm
a=5.17Å	a=5.177Å	a=5.195Å
b= 18.433Å	b= 18.447Å	b= 7.085Å
c= 21.173Å	c= 21.199Å	c= 7.085Å
Z=12	Z=12	Z=4

Table 3.8: Supercell Formation of Burkeite As Determined by Giuseppetti [13].

In summary, it may be said that the BFDH laws can be used to predict the crystal morphologies of a variety of inorganic materials accurately. In both the carbonate and sulphate systems investigated, the complexity of the resultant morphology mirrors the complexity of the crystal structure. For the hydrates the symmetry tends to be low as the structural packing in the unit cell has to accommodate the water molecules. Structures with the higher hydration levels tend to crystallise in monoclinic rather than orthorhombic structures. The predicted interfacial angles in general show excellent agreement with experimentally determined angles, indicating the high degree

of accuracy of the BFDH model for morphological prediction. Predicted forms may be over- or underestimated in importance, accounting for discrepancies between the predicted and observed morphologies.

3.3 Assessment Of The Role Played By Crystal Chemistry In Habit Modification

The materials that have been examined in this study have exhibited largely prismatic morphologies. However, for any of these materials to be employed as builder materials in the detergent industry, the morphology must be modified from prismatic to dendritic, since dendritic morphologies are preferable for detergent builder materials as these crystallise in a highly porous matrix which allow for the efficient uptake of the various required additives.

Habit modifiers are tailor-made additives which adsorb on specific crystal faces. Mechanistically, it is thought that this surface adsorption blocks surface terraces and steps, thus reducing the growth rate of the modified face. As the crystal morphology is dominated by the slowest growing faces a habit modifier can thus change the polyhedral shape of a crystal by slowing and hence enlarging specific crystal faces. The electrostatic interaction between modifier and substrate effectively determines whether the additive will adsorb. As a close topotactic relationship between adsorbate and substrate is needed for adsorption, ionic crystal surfaces which exhibit a mixed cation/anion environment are hence difficult to modify. Thus modification usually takes place by adsorption onto crystal faces which are either anion or cation rich, for which the requirement to "lattice match" the additive to the crystal surface is not so strict. Polymeric additives are especially attractive for product modification, due to their ease of formulation and dispersion. Polymers containing at least three carboxylate groups, such as polyacrylates, have been found to have habit modifying properties on detergent builders [20]. Such a habit modification process is shown schematically in figure 3.23, which shows the COO^- groups in the polyacrylate to be coulombically attracted to the cation rich surfaces, rather than those which have a mixed ionic environment. This face-specific adsorption changes the morphology (see

figure 3.23 insert) from "plate-like" to "needle-like".

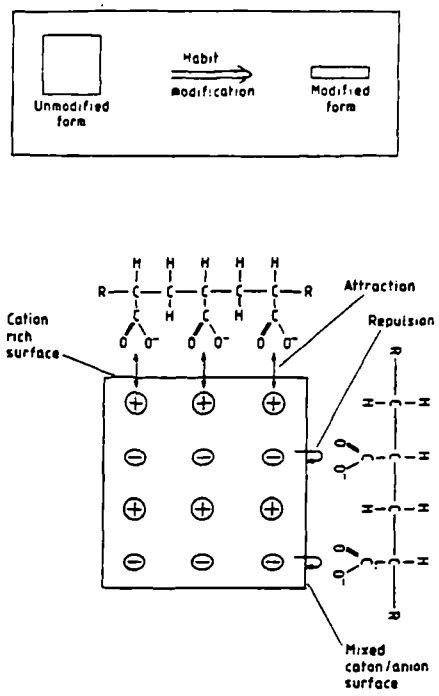

Figure 3.23: Schematic showing the interaction of a habit-modifying polyacrylate with a crystal surface; the insert shows the effect on morphology.

3.3.1 Methodology

The selection of a suitable habit modifier can be greatly aided by examining the crystallographic structure of the material, with the aid of molecular packing projections down the principle crystal axes using computer programs such as ORTEP [21]. In this way the surface chemistry of the crystal faces predicted from the BFDH law can be examined and the chemical nature of the required additive considered. The surface chemistries of the salts $Na_5P_3O_{10}.6H_2O$ and $Na_2CO_3.H_2O$ were predicted using a combination of the predicted crystals forms (From the BFDH law) and the crystal structure drawing program ORTEP.

3.3.2 Sodium Tripolyphosphate Hexahydrate

Figure 3.24 shows a molecular packing projection down the "c" crystallographic axis with the BFDH predicted crystal morphology superimposed. It can be seen that the surfaces chemistries of {100} and {010} faces are quite distinct.

- on the {010} surfaces PO_3 groups of the anions lie parallel to the surface and thus this growth surface comprising alternating layers of anions followed by cations and water.
- The {100} surfaces in contrast reveal both ionic types in the surface.

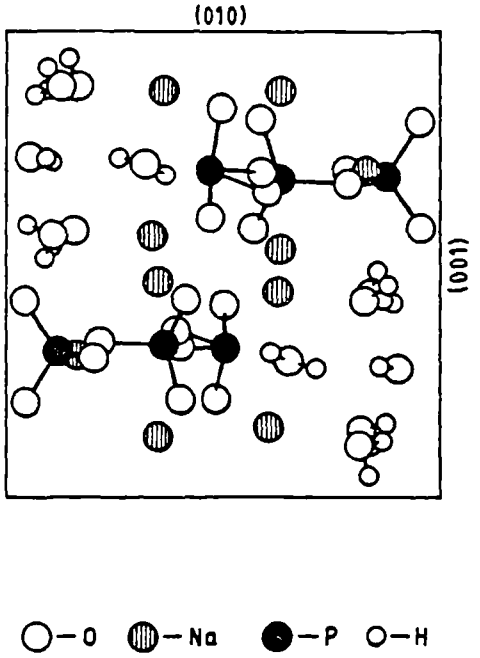

Figure 3.24: Crystal structure/morphology superposition of $Na_5P_3O_{10}(H_2O)_6$ viewed along the a-axis, thus illustrating the surface chemistry of the {010} and {100} forms.

This charge difference between the two forms offers the possibility of habit modification. Polyacrylates have been found to modify STP and one can presume that the COO^- groups in a polyacrylate will be coulombically attracted to the cation rich {010} forms, rather than the {100} forms which display a mixed ionic environment. Growth inhibition on the {010} forms will result in the formation of needles-like morphology with the needle axis presumably along the {100} growth normal.

3.3.3 Sodium Carbonate Monohydrate

The molecular packing of $Na_2CO_3.H_2O$ projected down onto the crystallographic a-axis is shown in figure 3.25 overlaid with its BFDH morphology. From this figure the distinct surface chemistry of the {020}, {011} and {001} forms are clear:

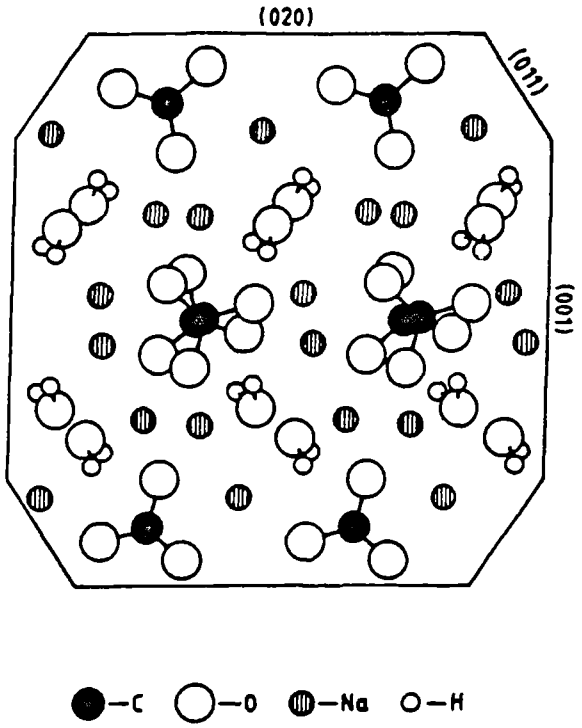

Figure 3.25: Crystal structure/morphology superposition of $Na_2CO_3.H_2O$ as viewed down the a-axis, thus illustrating the surface chemistries of the {001}, {020} and $\{01\bar{1}\}$ forms.

- the {020} surface comprises alternative layers; the first comprising anions and cations followed by the remaining cations together with the water of crystallisation,
- the {011} surface contains anions, cations and water molecules in a repeating structure,
- the {001} surface is similar to that of the {020} but with the separation of the two layers less well defined.

Polyacrylates will also habit modify $Na_2CO_3.H_2O$ with the COO^- groups on the modifier being more likely to bond with forms rich in cations, e.g. {001} and {200},

than the more structurally homogeneous {011}. The better segregated cation structure of the {020} surface contrasts with that of the {001} where the cations appear to be "buried" in between the surface anions. Coulombic repulsion and problems associated with steric hindrance between the COO^- and the CO_3^{2-} anions, seem to preclude adsorption of the modifier on or close to anionic lattice sites.

Examination of crystal chemistry along a single crystallographic axis allows a two dimensional model of a habit modification mechanism to be postulated; however for a more realistic examination of habit modification, an examination of crystal forms along a different crystallographic axis must be conducted, to allow a three dimensional model of habit modification to be formulated.

The molecular packing of $Na_2CO_3.H_2O$ projected down onto the crystallographic b-axis is shown in figure 3.26 overlaid with its BFDH morphology. Thus, the surface chemistries of the {001}, {200} and {11$\bar{1}$} may be elucidated.

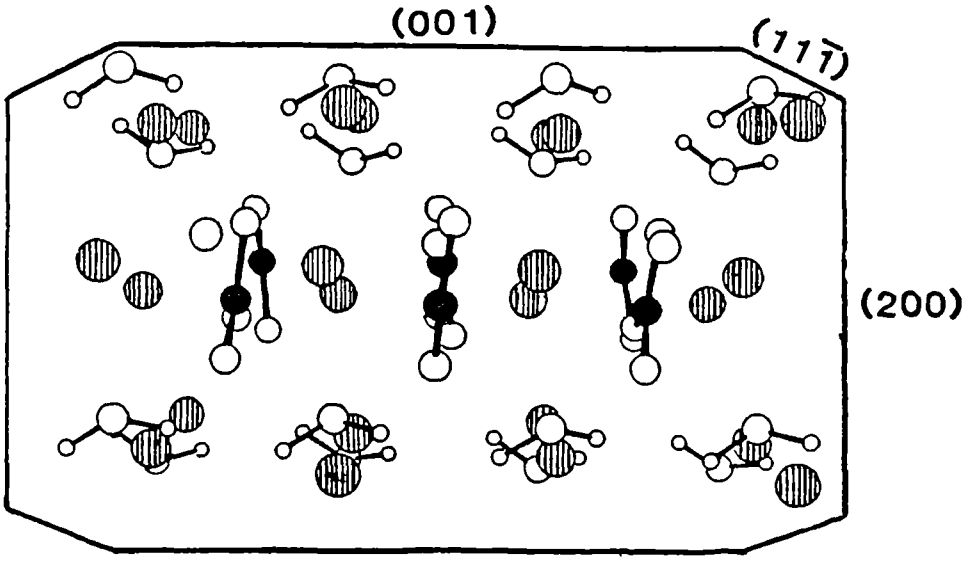

Figure 3.26: Crystal structure/morphology superposition of $Na_2CO_3.H_2O$ as viewed down the b-axis, thus illustrating the surface chemistries of the {200}, {001} and {11$\bar{1}$} forms.

- The {001} surface is as described previously; i.e. alternating layers of sodium cations and waters of hydration, followed by the remaining sodium cations and

carbonate anions.

- The {200} surface is similar to {001}, containing alternating layers of cations and waters of hydration followed by anions, cations and waters of hydration.

- The $\{11\bar{1}\}$ surface contains cations and waters of hydration, followed by sodium cations, carbonate anions and water molecules in a repeating structure. However, there is less segregation between the layers, leading to a more homogeneous surface environment.

The better layer segregation of the {001} and {200} forms indicates that polyacrylate adsorption is more likely to occur on these forms than on the more homogeneos $\{11\bar{1}\}$ forms. Thus, when examined in a three dimensional model, polyacrylate adsorption will occur along the "a" and c" crystallographic directions and thus can be expected to give rise to a needle-like morphology along the {020} plane normal.

In conclusion, it may be said that the predicted crystal morphology of ionic materials when employed in conjunction with crystal structure may be used to deduce the crystal chemistry of a system and thus possible habit modification mechanisms may be postulated.

3.4 Observations Of the Effects Of Habit Modification On The Morphology Of $Na_2CO_3.H_2O$ And $Na_2CO_3.10H_2O$

Alterations in crystal habit, whether desirable or undesirable, is of fundamental importance in any crystallisation study. There are many parameters that can contribute to habit modification, e.g. choice of solvent, pH, supersaturation levels and especially the presence of impurities within a system. The effects of impurities on crystallisation have been extensively documented for a vast number of materials by a variety of authors [e.g. 22,23] and are an integral component of industrial crystallisation; the ability to modify and control morphology for optimum performance being a primary attraction. There are many examples of habit modification in diverse fields:

the anti-caking and habit modifying properties of ferrocyanide ions in sodium chloride [24] production, the use of additives to prevent platelet crystallisation of n-alkanes in diesel fuels [25], and scale prevention [26,27]. Choosing a habit modifier for a particular system is fraught with difficulties, often the choice being made on a trial and error basis. The resultant scale-up to plant levels may provide problems, since processing conditions can effect habit modification and varies considerably between plant and laboratory scale. Garrett [28] has outlined general requirements that normally have to be fulfilled for a material to be employed as a possible habit modifier on an industrial scale:

1) The levels of modifier employed should not be so excessive that the mother liquor becomes contaminated for subsequent processing.

2) The ease of formulation of the modifier plays a major factor, as well as possible prohibitive factors, such as degree of toxicity, etc.

3) The modifier employed should only alter the crystal morphology; normally crystal properties and purity levels should not be altered by the presence of the modifier. One aspect of this is the strength of bonding between the modifier and the crystal surface - the modifier may be adsorbed onto the surface to the extent that it becomes an impurity, which may alter the desired crystal properties.

There are many examples of morphologies being tailored for optimum processing conditions and certain examples relevant to this study may be quoted: Polyacrylates are employed [20] in the detergent industry to modify the prismatic morphologies of carbonate and sulphate based materials, e.g. sodium carbonate monohydrate $Na_2CO_3.H_2O$, and burkeite $Na_2CO_3(Na_2SO_4)_2$ to dendrites. This allows the optimum pore size distribution for liquid uptake and greater packing densities to be obtained. Polymer based additives are also employed to alter the morphology of carbonate and sulphate based materials during the kraft process in the pulp industry, where burkeite $Na_2CO_3(Na_2SO_4)_2$, often produces unwanted scaling, consequently fouling processing. Klaessig [26,27] advocates the use of polyacrylic acids and copolymers to act as soft scale inhibitors for the reduction of this problem. The crystallisation of sodium carbonate monohydrate also provides examples of habit modification:

Melder [29] has claimed that crystallisation of this material at 60^0C normally leads to the formation of brittle hexagonal platelets; but in the presence of small amounts of SO_4^{2-} anions, a low surface area/weight ratio may be obtained and the crystals grown in hexagonal columns; thus the resultant crystals can be easily washed of mother liquor, have better flow characteristics, and are less subject to crystal breakage. Crystals of sodium carbonate monohydrate grown in this study at 60^0C tended to be more "prismatic" in nature (figure 3.10); other assessments on the morphology of sodium carbonate monohydrate [15] (figure 3.7) are also not in good agreement with Melder's description of the crystal morphology of sodium carbonate monohydrate.

The effects of trace amounts of organic impurities on the crystallisation of sodium carbonate monohydrate may possibly have not been taken into account by Melder. The effects of these impurities have proved to be a major problem in the bulk manufacture of high quality crystals of this material. The presence of trace amounts of these impurities (mainly organic acids, or sodium salts of organic acids) alters the crystal morphology from the desirable "block-like" morphology (figure 3.27) to elongated fragile crystals (figure 3.28) that are easily broken, causing dust problems. In bulk production of sodium carbonate monohydrate a variety of techniques have been employed to alleviate this problem, e.g. the use of activated carbon to remove the organic impurities [30]. Walden [31] has deduced that the presence of a combination of Mg^{2+} ions and sodium dodecylbenzenesulphonate during the crystallisation of sodium carbonate monohydrate leads to the formation of "blocky" crystals of a high bulky density.

Low concentrations of sodium sulphate may be employed for habit modification of sodium carbonate monohydrate [26,29,32]; however, at higher concentrations the crystallisation of the double salt burkeite $Na_2CO_3(Na_2SO_4)_2$ occurs.

There are other reports of habit modification of sodium carbonate monohydrate using organic and inorganic modifiers [33]. In all these cases no mechanisms of modification were detailed; it is not known whether the reported modifier materials act by directly adsorbing onto the surface of sodium carbonate monohydrate crystals or whether they act by blocking adsorption of the undesirable organic impurities.

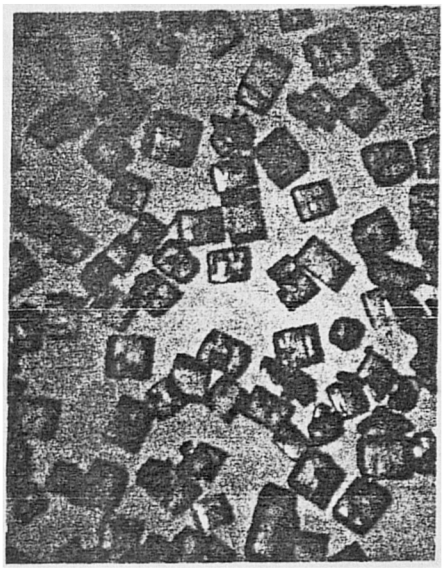

Figure 3.27: Modified morphology of $Na_2CO_3.H_2O$, showing the desired "block" morphology for bulk production [31].

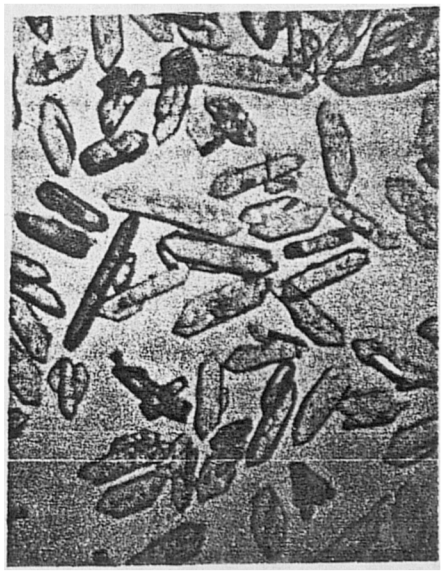

Figure 3.28: Crystals of $Na_2CO_3.H_2O$ obtained in the presence of organic impurities [31].

A contrast may be drawn to the different desired morphologies of sodium carbonate monohydrate required for different processes. For the specific production of bulk sodium carbonate monohydrate, the objective of habit modification is to produce crystals of high packing densities and good flow characteristics, i.e. "blocky" crystals; however this contrasts sharply to the use of sodium carbonate monohydrate in the detergent industry, where the production of sodium carbonate monohydrate of a dendritic habit is the prime consideration.

3.4.1 Methodology

It has been previously stated that polyacrylates containing at least three carboxylate groups can modify the morphology of sodium carbonate monohydrate. Based on this premise, a habit modification mechanism was proposed for sodium carbonate monohydrate. The mechanism was based on the existence of cation rich areas within the crystal structure, which coulombically attract the carboxylate groups in a polyacrylate habit modifier, thus inhibition of the approach of growth units to the crystal surface and alteration of growth rates occurs. An assumption was made that there will also exist in the crystal structure of $Na_2CO_3.10H_2O$ cation rich regions that will also permit habit modification. In order to ascertain the validity of these proposals, a systematic study of the effects on the crystal morphology of sodium carbonate monohydrate and sodium carbonate decahydrate was carried out, using carboxylate based compounds of differing structural complexity. The materials tested for modifying properties are highlighted in figure 3.29.

The impurity level concentration for each system were 5000 and 50,000 μg acid/g anhydrous Na_2CO_3. Crystals of $Na_2CO_3.H_2O$ were obtained by controlled solvent evaporation at constant temperature (50^0C) of solutions of Na_2CO_3 and the impurities. The solutions (approx. $80cm^3$) were kept at constant temperature in a thermostatted water bath in $100cm^3$ conical flasks until crystallisation was seen to have occurred. Crystals of $Na_2CO_3.10H_2O$ were obtained by the slow cooling (0.5^0C/hour) of solutions (approx $80cm^3$) containing the impurities from 30^0C to room temperature. In either case the solutions were allowed to crystallise whilest unstirred. The resultant crystals were washed in n-hexane and stored in paraffin oil

Organic Diacids - $HOOC(CH_2)_a(CHX)_bCOOH$

Oxalic acid - a=0 b=0

malonic acid - a=0 b=1 X=H

Phenylmalonic acid - a=0 b=1 X=C_6H_5

Succinic acid - a=1 b=1 X=H

Phenylsuccinic acid - a=1 b=1 X=C_6H_5

Glutaric acid - a =1 b=2 X=H

Adipic acid - a=1 b=3 X=H

Pimelic acid - a=1 b=4 X=H

Suberic acid - a=1 b=5 X=H

Homophthalic acid - a=1 b=6 X=H

Polyacids

Citric acid - $C(OH)COOH(CH_2COOH)_2.H_2O$

Polyacrylates

"Sokalan" polyacrylate - $(CH_2=CHCOOH)_n$

"Narlex" polyacrylate - $(CH_2=CHCOOH)_n$

"Versicol" polyacrylate - $(CH_2=CHCOOH)_n$

Note: More detailed structural information on these polyacrylates has so far been unavailable.

Other Impurites Tested

Ethane dihydroxyphosphonic acid (EHDP) - $CH_3C(OH)(PO_3H_2)$

Disodium Ethylene diamine tetra-acetic acid

(EDTANa_2) - $[CH_2N(CH_2COOH)CH_2COONa]_2.2H_2O$

Figure 3.29: Structural summary of materials tested for habit modifying properties on $Na_2CO_3.H_2O$ and $Na_2CO_3.10H_2O$.

to prevent any possible sample degradation. The morphologies of the crystals were examined by Scanning Electron Microscopy (SEM). This technique is now briefly detailed.

3.4.2.1 Scanning Electron Microscopy

Scanning Electron Microscopy (SEM) is a relatively new technique, the first microscope employing such a technique appearing only 60 years ago. Essentially electrons are fired at a specimen which consequently emits secondary electrons and x-rays. The secondary electrons are detected, processed and can be consequently viewed as a plot of detected intensity versus detector position. This plot is viewed on-screen as an image of the sample.

Physical characteristics must also be taken into account in the preparation of samples for SEM analysis. The specimen must be initially coated with a film of gold or carbon, depending on the analysis desired to allow conduction of the specimen. The coating and the resultant examination of the specimen take place under vacuum; hence the specimen to be examined has to be stable to vacuum conditions. The electronic conduction of the specimen leads to an increase in temperature; hence problems may arise if the sample is temperature sensitive. Further information on these factors and on SEM in general may be found elsewhere [34].

Tables 3.9 - 3.10 summarise the observations of the effects of impurities on the crystal morphology of $Na_2CO_3.H_2O$ and $Na_2CO_3.10H_2O$ respectively.

Additive Material	Additive Concentration $\mu g/gNa_2CO_3$	Effect Observed	Additive Concentration $\mu g/gNa_2CO_3$	Effect Observed
oxalic acid	5000^{Yes}	b	50000^{Yes}	b
malonic acid	5000^{No}	a	50000^{Yes}	b
succinic acid	5000^{No}	a	50000^{Yes}	b
glutaric acid	5000^{No}	a	50000^{No}	a
adipic acid	5000^{No}	a	50000^{No}	a
pimelic acid	5000^{No}	a	50000^{Yes}	b
suberic acid	5000^{No}	a	50000^{Yes}	b
citric acid	5000^{No}	a	50000^{Yes}	b
homophthalic acid	5000^{No}	a	50000^{No}	a
phenylmalonic acid	5000^{No}	a	50000^{Yes}	b
phenylsuccinic acid	5000^{No}	a	50000^{Yes}	b
EDTA.Na_2	5000^{No}	a	50000^{Yes}	b
"Sokalan" polyacrylate	5000^{Yes}	c	50000^{Yes}	c
"Narlex" polyacrylate	5000^{Yes}	c	50000^{Yes}	c
"Versicol" polyacrylate	5000^{Yes}	c	50000^{Yes}	c
EHDP	5000^{Yes}	b	50000^{Yes}	b

(a) Prismatic morphology retained (b) Dendritic morphology obtained - macroscopic level (c) Dendritic morphology obtained - microscopic level

Table 3.9: Summary of the effects of various impurities on the crystal morphology of $Na_2CO_3.H_2O$.

Additive Material	Additive Concentration $\mu g/gNa_2CO_3$	Effect Observed	Additive Concentration $\mu g/gNa_2CO_3$	Effect Observed
oxalic acid	5000^{Yes}	b	50000^{Yes}	b
malonic acid	5000^{Yes}	b	50000^{Yes}	b
succinic acid	5000^{No}	a	50000^{No}	a
glutaric acid	5000^{No}	a	50000^{No}	a
adipic acid	5000^{No}	a	50000^{Yes}	b
pimelic acid	5000^{No}	a	50000^{Yes}	b
suberic acid	5000^{No}	a	50000^{Yes}	b
citric acid	5000^{No}	a	50000^{Yes}	b
homophthalic acid	5000^{No}	a	50000^{No}	a
phenylmalonic acid	5000^{No}	a	50000^{Yes}	b
phenylsuccinic acid	5000^{No}	a	50000^{Yes}	b
$EDTA.Na_2$	5000^{No}	a	50000^{Yes}	b
"Sokalan" polyacrylate	5000^{Yes}	c	50000^{Yes}	c
"Narlex" polyacrylate	5000^{Yes}	c	50000^{No}	a
"Versicol" polyacrylate	5000^{No}	a	50000^{Yes}	c
EHDP	5000^{Yes}	b	50000^{Yes}	b

(a) Prismatic morphology retained (b) Dendritic morphology obtained - macroscopic level (c) Dendritic morphology obtained - microscopic level

Table 3.10: Summary of the effects of impurities on the crystal morphology of $Na_2CO_3.10H_2O$.

3.4.2 Sodium Carbonate Monohydrate, $Na_2CO_3.H_2O$

The impurities studied do have an influence of the crystallisation of $Na_2CO_3.H_2O$, forming dendrites as postulated by the theoretical mechanism. The change in morphology cannot be attributed to supersaturation effects, as crystallising solutions of $Na_2CO_3.H_2O$ have been evaporated to dryness, with no discernable alteration of

morphology. Upon examination of table 3.9, oxalic acid is the only impurity amongst the di- and polyacids to exhibit modification properties at the lower concentration of 5000μg/gNa_2CO_3. This may possibly be attributed to the lack of any carbon chain length between the carboxylate groups in oxalic acid, the overall effect being a small molecule with a concentrated zone of carboxylate anions being attracted to the cation rich zones on the crystal surface, contrasting to those molecules which have an increasing carbon length between the carboxylate groupings, leading to a greater dispersion between the carboxylate groups and thus coulombic attraction. In general, the trend is of habit modification at the higher concentration of 50000μg impurity/g Na_2CO_3. This impurity concentration is significantly higher than typical concentrations of inorganic impurities required for modification of inorganic systems, e.g., levels of 150ppm Fe^{3+} anions are sufficient to habit modify the morphology of $NH_4H_2PO_4$ [35]. Comparison of the modification effects of succinic acid and phenylsuccinic acid, malonic acid and phenylmalonic acid reveals that the presence of a large side grouping such as a phenyl group does not adversely effect the trends noted - modification is again observed at the higher concentrations of impurity. The dendrites formed are typically of macroscopic levels. Figures 3.30 and 3.31 highlight a typical unmodified morphology of $Na_2CO_3.H_2O$ and the resultant dendrites obtained by the influence of the addition of 50000μg malonic acid/g Na_2CO_3 to crystallising $Na_2CO_3.H_2O$. The presence of many carboxylate groups such as in polyacrylates, seems to have a fundamental effect on the crystallisation of $Na_2CO_3.H_2O$. The crystals obtained (figure 3.32) are of much smaller dimensions (approx. 10 μm levels), to the extent of forming a white powdered material to the naked eye.

Thus it would appear for these carbon based impurities that increasing the carbon chain length whilest keeping the number of carboxylate groups present constant leads to no observable alteration in the modification of $Na_2CO_3.H_2O$. Increasing the concentration of the modifier is a significant factor in the modification; the greater the concentration of impurity present, the greater the subsequent bonding and surface coverage, ultimately leading to habit modification. Small increases in the carboxylate content does not increase the modification powers of the impurity to any great extent. It is only when a large increase in carbon chain length coupled with the large increase

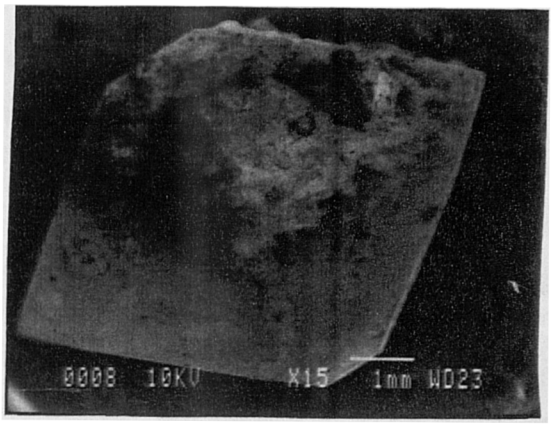

Figure 3.30: Unmodified morphology of $Na_2CO_3.H_2O$, obtained after addition of 5000μg phenylmalonic acid/gNa_2CO_3 to crystallising $Na_2CO_3.H_2O$.

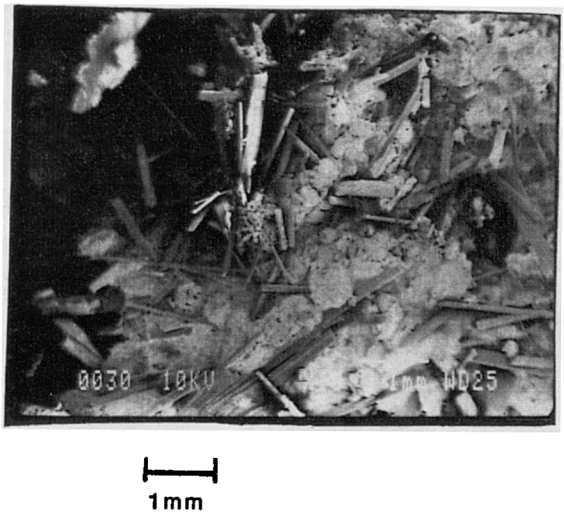

Figure 3.31: Macroscopic dendrites of $Na_2CO_3.H_2O$ obtained after addition of 50000μg malonic acid/gNa_2CO_3 to crystallising $Na_2CO_3.H_2O$.

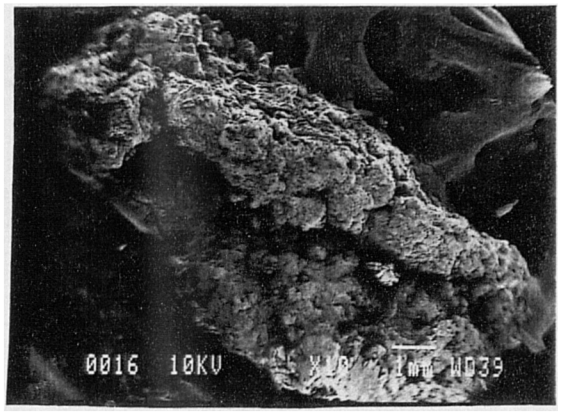

1mm

100um

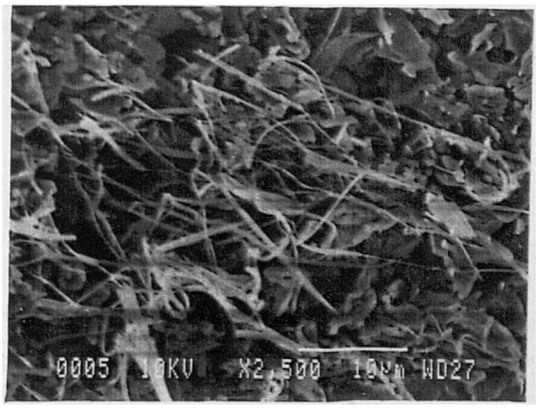

10um

Figure 3.32: Microscopic dendrites of $Na_2CO_3.H_2O$ obtained, after addition of 50000μg Narlex/gNa_2CO_3 to crystallising $Na_2CO_3.H_2O$.

in the number of carboxylate groups leads to very much increased coulombic attraction and surface coverage of $Na_2CO_3.H_2O$, when compared to much smaller impurity molecules, leading to modification occurring at lower concentrations of impurity. The presence of ethanedihydroxyphosphonic acid during crystallisation of $Na_2CO_3.H_2O$ leads to habit modification at both levels of impurity concentration studied. The structure of EHDP (figure 3.29) is analogous to oxalic acid, i.e. in solution a relatively small molecule with a concentrated zone of PO_3^{2-} anions is formed, which will be strongly attracted to the cation zones in $Na_2CO_3.H_2O$.

3.4.3 Sodium Carbonate Decahydrate, $Na_2CO_3.10H_2O$

Examination of the effects of impurities on the crystallisation of $Na_2CO_3.10H_2O$ (table 3.10) leads to similar conclusions being drawn. Carboxylate based impurities modify the morphology from prismatic (figure 3.33) to dendrites, either at the macroscopic level (figure 3.34) or at the microscopic level (figure 3.35); depending on whether the impurity contains a small or large number of carboxylate groups respectively.

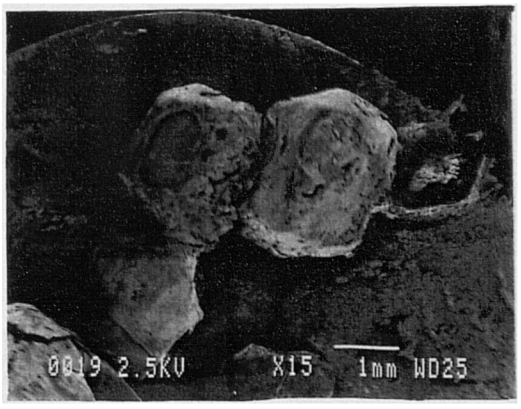

Figure 3.33: Unmodified morphology of $Na_2CO_3.10H_2O$ obtained after addition of 5000μg phenylmalonic acid/g Na_2CO_3 to crystallising $Na_2CO_3.10H_2O$.

Figure 3.34: Macroscopic dendrites of $Na_2CO_3.10H_2O$ obtained after addition of 50000μg phenylmalonic acid/gNa_2CO_3 to crystallising $Na_2CO_3.10H_2O$.

The trend of habit modification becoming apparent at higher additive concentration for the di- and poly-acids investigated is obvious. As for $Na_2CO_3.H_2O$, when the carbon chain length between carboxylate groups is increased, then the relative zone of carboxylate anions is dispersed, hence there is less attraction and subsequent bonding to the crystal surface. Modification only occurs when the concentration of impurity is increased, thus providing a greater carboxylate concentration to counteract this dispersion. The presence of a bulky group, e.g. a phenyl group does not seem to significantly inhibit habit modification - habit modification is still observed to occur at the higher impurity concentration. Although the modification trend is not as apparent in table 3.10 than table 3.9, polyacrylates have similar effects on the morphology of $Na_2CO.10H_2O$ as on $Na_2CO_3.H_2O$, i.e. the presence of significantly more carboxylate groups greatly enhances the habit modification, so that microscopic (figure 3.34) rather than macroscopic (figure 3.35) $Na_2CO_3.10H_2O$ dendrites crystallise. Again as for $Na_2CO_3.H_2O$, EHDP modifies at both impurity concentrations.

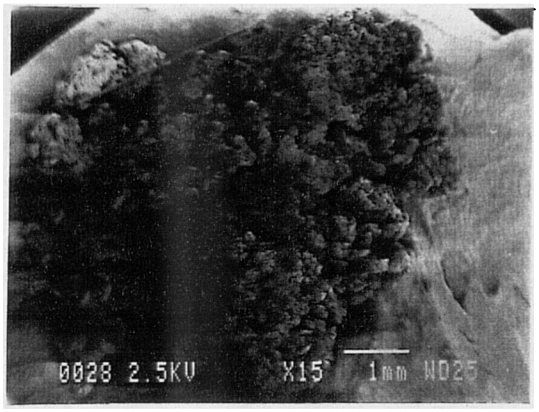

Figure 3.35: Microscopic dendrites of $Na_2CO_3.10H_2O$ obtained after addition of 5000μg Narlex/gNa_2CO_3 to crystallising $Na_2CO_3.10H_2O$.

3.5 Conclusions

It has been shown that the use of simple rules based on crystal lattice geometry and symmetry can be used to predict the morphology of some ionic salts. Predicted morphologies of components within the Na_2CO_3-Na_2SO_4-H_2O system and of $Na_5P_3O_{10}(H_2O)_6$ show reasonable agreement to observed morphologies, with some differences noted between the predicted and observed orders of morphological importance. In general, good correlation is noted between predicted and observed interfacial angles, confirming the accuracy of the BFDH model for morphological prediction.

A mechanism for habit modification of sodium carbonate monohydrate was presented, based on a combination of crystal structure and crystal morphology. This was dependent on the existence of cation rich regions within the crystal structure, coulombically attracting anions in an impurity, e.g. carboxylate groups in polyacrylates. Thus surface coverage occurs, inhibiting crystallising entities approaching the surface. Adsorption was postulated to occur along the {001} and {200} axis, leading to needle growth along the "b" plane normal.

The presence of carboxylate groups in an impurity can lead to habit modification of both $Na_2CO_3.H_2O$ and $Na_2CO_3.10H_2O$. The concentration of modifier present is a major factor in deciding whether the impurity can function as a habit modifier. If the impurity is a very small molecule , a concentrated carboxylate anion zone may be formed, thus modification can occur at lower levels of impurity concentration. If this zone is dispersed by an increasing carbon chain length, then habit modification can only occur at a higher level of impurity concentration. The resultant modified morphologies are macroscopic (mm) dendrites. The presence of large number of carboxylate groups enhances modification of both systems, hence modification can occur at lower levels of impurity concentration. Due to the vastly increased carboxylate concentration, greater modification of the crystal morphologies occur, microscopic (approx. $10\mu m$) dendrites being formed.

3.6 References

1. A. Bravais; Etudes Crystallographiques, Paris (1913)

2. J.D.H. Donnay & D. Harker; Amer. Miner. **22** (1937) 463

3. R. Docherty, K.J. Roberts & E. Dowty; Comp. Phys. Commun. **51** (1988) 423-429

4. E. Dowty; Amer. Miner. **65** (1980) 465-471

5. D.M. Weinch, M. Jansen and R. Hoppe; Zeischrift Fuer Anorganische und Allgemenie Chemie **488** (1982) 80

6. S. Troost; PhD Thesis, University of Groningen, (1969)

7. W. Caspari; J. Chem. Soc. **125** (1924) 2381-2387

8. K.K. Wu & I.D. Brown; Acta Cryst. **B31** (1975) 890

9. C. Betzel, W. Saenger & D. Loewus; Acta Cryst. **B38** (1982) 2802-2804

10. T. Taga; Acta Cryst. **B25** (1969) 2656

11. A.G. Nord; Acta Chemica Scandinavia **27** (1973) 814-822

12. H.A. Levy & G.C. Lisensky; Acta Cryst **B34** (1978) 3502-3510

13. G. Giuseppetti, F. Mazzi & C. Tadini; Neues. Jahrb. Mineral., Monatsch **5** (1988) 203-21

14. N. Rolfe; private communication; 15. P. Groth; "Chemische Krystallographie" Verlag, Leipzig, (1908)

16. R.J. Hauy; J. Phys. **19** (1792) 366

17. W.F. Foshag; Amer. Miner. **20** (1935) 50-56

18. L.S. Ramsdell; Amer. Miner. **27** (1942) 230-231

19. H.E. Pemberton; The Mineralogical Board, (1975)

20. C. Atkinson, M.J.H. Heybourne, W.J. Iley, P.C. Russell, T. Taylor & D.P. Jones Eur. Pat. EP221776A (1987) 37pp

21. C.K. Johnson; Oak Ridge National Laboratory (1976)

22. J.W. Mullin; "Crystallisation", Butterworths, London (1972)

23. H.E. Buckley; "Crystal Growth", Chapman and Hall, London (1952)

24. N.V. Koninklijke Nederlandesche Zoutindustrie; U.K. Pat. GB752852 (1954) 15pp

25. K. Lewtas, R. Tack, & J.W. Mullin; "Advances in Industrial Crystallisation" (1991)

26. F.C. Klaessig & D.F. Jacques; U.S. Pat. US4263092 (1981) 5pp

27. F.C. Klaessig & D.F. Jacques; U.S. Pat. US4255309 (1981) 7pp

28. D.E. Garret; Chem. Eng. Prog. **54** no. 12 (1958) 65-69

29. G.J. Melder; U.K. Pat. GB1208416 (1970) 14pp

30. H. Hellmers & J. Wiseman; U.S. Pat. US3260567 (1966) 5pp

31. J. Walden; U.S. Pat. US3975499 (1976) 10pp

32. P. Johnson; U.S. Pat. US3486844 (1975) 13pp

33. D. Tabler; U.S. Pat. US3459477 (1969) 8pp

34. J. Goldstein; "Scanning Electron Microscopy and X-ray Microanalysis: A Text for Biologists, Materials Scientists And Geologists" (1981) New York, London Plenum.

35. J.W. Mullin, A. Amatavivadhana & M. Chakraborty; J. Appl. Chem., **20** (1970) 153-158

Chapter 4

Determination Of Intermolecular Force Potentials With A View To Their Potential Application In Morphological Studies Of Alkali Sulphates

Contents

4.1 Introduction

Chapter three highlighted morphological simulations based on lattice geometry models. The Bravais/Friedel/Donnay/Harker (BFDH) laws enabled the relative morphological importance of a specific face to be related to the crystal structure. The resultant predicted morphologies of the various components in the Na_2CO_3-Na_2SO_4-H_2O system showed excellent correlation to observed growth morphologies. However, predicted crystal morphologies based on intermolecular force calculations are normally considered more accurate than those based on geometrical models. Morphologies of various organic materials are now routinely predicted in this way, with great success [1,2,3]. In order for morphological predictions based on intermolecular force calculations to be extended for inorganic systems, interionic potentials describing all the interactions are required. Such potentials may be derived empirically or by direct calculation.

This chapter presents the empirical determination of interionic potentials describing the interactions of β-potassium sulphate. Predicted and observed solid state properties are compared and contrasted. Intermolecular force calculations employing these interionic potentials are described. Attempts at obtaining attachment energies for morphological prediction from lattice energy calculations are outlined.

Finally, the derived potentials are transferred to sodium sulphate. The determined solid state properties are compared and contrasted to experimental observations.

4.2 Morphological Prediction Based On Energetic Considerations

4.2.1 Predicting Growth From Attachment Energy And Its Application To Morphological modelling

A further refinement to morphological modelling based on lattice geometry considerations was introduced by Hartman and Perdok [4,5] that accounted for bonding within

the crystal structure. They identified chains of bonds within the crystal structure known as Periodic Bond Chains (PBC's). The weakest bond within the PBC's is the rate determining step and governs the rate of growth along the direction of the chain. Three categories of crystal faces could be defined depending on the geometry of the PBC chains (see figure 4.1).

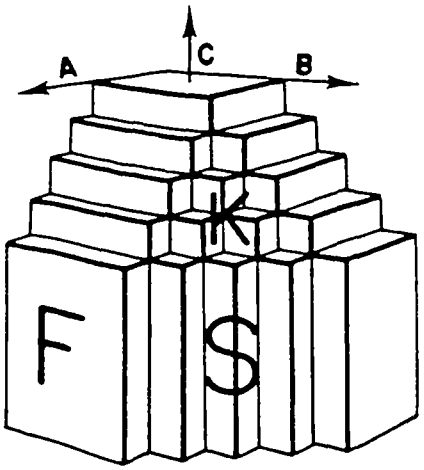

Figure 4.1: "F", "S" and "K" faces corresponding to PBC's parallel to A,B and C respectively.

It can be seen that a flat (F) face contains two or more PBC's in a layer d_{hkl}, a stepped (S) face contains one PBC in a layer d_{hkl} and a kinked (K) face contains no PBC's within a layer d_{hkl}. These categories grow by different mechanisms: "F" faces are grown according to a layer mechanism, are slow growing and hence are important faces on a morphology. "S" faces grow according to one dimensional nucleation, whereas "K" faces need no nucleation, grow fast and are not normally found on crystals. The fundamentals of slice and attachment energy are developed from this theory. The slice energy (E_{slice}) is defined as the energy released upon the formation of a slice of thickness d_{hkl}. The attachment energy (E_{att}) can be defined as the fraction of the lattice energy released upon attachment of a slice of thickness d_{hkl} to

a crystal surface. Thus, the total lattice energy (E_{cr}) may be defined as:

$$E_{cr} = E_{slice} + E_{att} \tag{4.1}$$

The assumption is made that the attachment energy is proportional to the growth rate and that the larger the attachment energy (E_{att}) the larger the growth rate and hence the less important the corresponding form within the morphology. This assumption has been shown to be valid for a number of growth theories [6].

Such a calculation of attachment energies forms the basis of the computer program HABIT [3], a computer program designed to calculate lattice, slice and attachment energies for morphological simulation. This program was principally written to compute energies for organic molecular crystals, and the resultant predicted morphologies from these calculations have proved highly successful for a variety of organic materials. Essentially, the program takes an inputted unit cell and generates a three dimensional sphere of unit cells to simulate the crystal structure; the sphere radius being user defined. The interaction energies between the crystallising entities must be evaluated, and can be described for two non-bonded atoms by the Buckingham 6-exp potential (see equation 4.2) or the Lennard Jones 6-12 potential (see equation 4.3):

$$V_{ij} = -A/r_{ij}^6 + Bexp^{-r/\rho} \tag{4.2}$$

$$V_{ij} = -A/r_{ij}^6 + B/r_{ij}^{12} \tag{4.3}$$

where the first two components in each equation describe the repulsive and attractive van der Waals interactions respectively; "A","B" and "ρ" are parameters specific to particular atom-atom interactions. Summing the interactions between a central molecule and each of the surrounding molecules within the crystal yields the lattice energy (E_{cr}). Slice and attachment energies may be calculated from the summation of the interatomic interactions outwith and within the interplanar spacing. This can easily be illustrated in figure 4.2. It can be seen from figure 4.2 that interactions between a central molecule "A" and molecule "B" are within the slice d_{hkl}, hence the resultant interaction energy will contribute to the slice energy. Molecule "B" lies outside the slice , thus interactions will contribute to the attachment energy. However

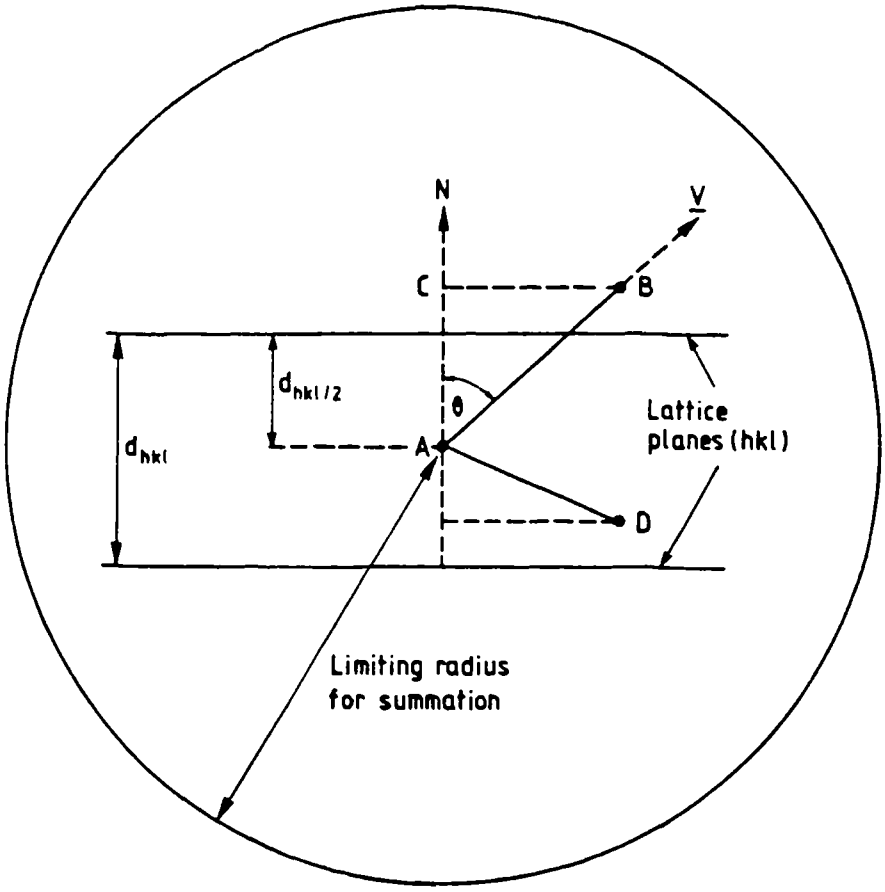

"A" is the central molecule, "B" is a molecule outside the slice, "D" is a molecule in the slice, "N" is the growth normal parallel to the planes (hkl), "AB" and "AD" are 'bonding vectors', "d_{hkl}" is the interplanar spacing, "θ" is the angle between the growth normal and the bonding vector, "AC" is the component of the vector "AB" parallel to "N" the growth normal.

Figure 4.2: Schematic diagram showing the partition of slice and attachment energies

the component of the energy parallel to the growth normal "N" must be obtained, i.e. ABcosθ.

Calculations of attachment energies and their consequent use in crystal habit prediction have been used for a variety of organic materials [1-3]. A variety of intermolecular potentials are readily available for the calculation of the interactions required for derivation of a lattice energy. For inorganic systems however, there are a lack of suitable intermolecular potentials for molecular ions such as phosphates, carbonates and sulphates and their interaction, often, with water of crystallisation. This, in conjunction with the predominance of long range forces which are not as important in organic systems, hinders such calculations. The methodology and theory behind obtaining these potentials is now detailed:

4.2.2 Empirical Derivation Of Interionic Potentials For Inorganic Systems

Computer simulation studies of inorganic materials have been becoming increasingly more important in many areas in recent years. A class of catalytic materials that have particularly benefited from this field of study are zeolites [7], since reaction paths and adsorption/de-adsorption of reactants and products may be predicted. In the photographic industry, simulation studies of defects in silver halide crystals are invaluable[8], the defect structures being necessary to the photographic processes. Much work has been carried out on oxides - from nuclear ceramics, e.g. UO_2/PO_2 [9] where experimental studies are normally limited, to the rapidly expanding field of high T_c superconductors, e.g. La_2CuO_4 [10-12]. Initially studies were hindered by the large amounts of c.p.u. time that the calculations required. However, advances in computational architecture have made calculations increasingly more complex and are being handled with greater ease.

Currently, several models exist for solid state simulation. These range from the classical "point charge" model in which each ion is treated as a point ion, with interactions via potential energy functions, to more complex models in which each atom is treated via quantum mechanics [13]. Whatever method is chosen is dependent

upon the problem in question: for a simple study of a ionic system, then the point charge model provides an adequate description; however for a more complex situation, e.g. the study of electronic defects then a quantum mechanical approach is necessary to fully describe the system.

For the ionic systems under consideration in this study, a classical approach based on the Born model was applied. In this model it is postulated that the total energy of a system can be separated into two areas, e.g. the lattice energy (E_{cr}) of a two-bodied system may be described as follows:

$$E_{cr} = \sum_{i>j} [q_i q_j / D r_{ij} + \phi_{ij}(r_{ij})] \tag{4.4}$$

The first term represents the standard electrostatic interaction based on Coulomb's Law, where "q_i", "q_j", are the charges on the ions "i", "j", "D" is the dielectric constant and r_{ij} is the separation distance. Where the coulombic part of this potential is dominant (i.e. for ionic systems) this series is slowly convergent in real space; i.e. long range forces can play quite a significant role in bonding in the solid state. In order to converge the coulombic series quicker, the Ewald method is used. This method expresses a slowly convergent sum in real space as a sum of two rapidly converging sums, one in real space, one in reciprocal space. Details of this method can be found elsewhere [7,14]. The second term represents two body central force atomic interactions and can either be a Buckingham (see equation 4.2) or Lennard-Jones (see equation 4.3) potential form.

The Born model may be further enhanced by the inclusion of 3 bodied interaction potentials, such as in bond bending:

$$E_B = 1/2 k_b (\theta - \theta_o)^2 \tag{4.5}$$

In the above "k_b" is the bond bending constant and describes the deviation from the equilibrium coordinate angle. In the case of a tetrahedrally coordinated system the equilibrium angle $\theta_o = 109.47°$. The inclusion of this parameter is a major factor in improving the degree of accuracy of simulation of a system which contains a significant degree of covalency. Other multi-bodied parameters that may be included in a simulation are e.g. four-bodied torsional terms.

For any system, the terms "A", "ρ" and "C" must be determined, usually by empirical fitting or by direct calculation. One must also establish whether a "rigid ion" model or a "shell" model is employed, depending on whether polarisability is a factor in the calculation. The "shell model" treats polarisable ions as a core and shell system linked via a harmonic spring, with the ionic mass at the core and charge divided between the core and the shell. The polarisability "α", is given by "Y^2/k", where "k" is a spring constant and "Y" the shell charge. The shell model has frequently been used with great success and is most applicable to calculations involving electronic defects. Although a simpler model, the rigid ion model has been used to great effect to simulate a variety of systems [15].

4.2.3 Calculation Of Solid State Properties For Inorganic Systems

In order for equilibrium crystal properties to be calculated, it is first necessary to obtain the equilibrium configuration. This is achieved by minimising the total energy of a system, comprising the short range and coulombic interactions with respect to the lattice ion positions. The theory behind the energy minimisation and the calculation of lattice properties may be found elsewhere [16,17].

Minimisation of the lattice energy can occur in two ways:

- The energy minimum can be found with respect to lattice positions only, which corresponds to minimising the structure at constant volume, or
- the energy minimum can be found with respect to lattice positions and lattice parameters, corresponding to minimising the structure at constant pressure.

Elastic, dielectric and piezoelectric constants may be calculated [17] from strain derivatives of the lattice energy. The programs THBFIT [18] and THBREL [19] were used to simulate the structure and lattice properties and are described as follows:

4.3.1.1 The Computer Program THBFIT

Program THBFIT, empirically fits potentials for ionic, semi-ionic and molecular solids to their experimentally determined lattice properties. These include elastic constants, dielectric constants, phonon frequencies and structure (the requirement that the potential should reproduce both the atom positions and the unit cell constants). A wide range of potential forms may be fitted, depending on the field of interest. They include Buckingham and Lennard-Jones forms for non-bonded interactions, with Morse and spring constant potentials for bonded interactions. Three body interactions, for example bond bending terms, may also be fitted, as may four body torsional terms.

4.3.1.1 The Computer Program THBREL

Program THBREL, is a lattice energy minimisation program. Starting with a crystal structure and a set of interatomic potentials, the program adjusts the structure until the lattice energy mininum is reached. This can be done in two ways: Constant Volume minimisation adjusts only the atomic positions; whereas Constant Pressure minimisation additionally adjusts the lattice parameters. A wide range of potentials may be used in THBREL as in THBFIT. As well as the minimised structure, the program calculates lattice properties, including elastic and dielectric constants.

Predicted morphologies based on lattice energy calculations are normally considered to be more accurate than those based on the BFDH model. However, in order to obtain an estimation of the morphologically most important forms due to energetic considerations, interionic potentials must be obtained that simulate the structure and properties of the material in question. The determination of these interionic potentials is highlighted for β potassium sulphate.

4.3 Results Of Studies On β-K_2SO_4

4.3.1 Determination Of Interionic Potentials And Crystal Properties - Beta Potassium Sulphate

Potassium sulphate can exist in a variety of forms [20,21,22,23], for example a phase change from the orthorhombic β-low temperature phase to the high temperature α-hexagonal phase occuring at 860K. The low temperature orthorhombic phase was investigated in this study, which crystallises in a Pnam space group with four molecules per unit cell and unit cell dimensions a= 7.476Å, b=10.071Åand c= 5.763Å, $\alpha = \beta = \gamma = 90^0$ [23].

The crystal structure is illustrated in figure 4.3 and can be seen to consist of packing of monomeric anions and potassium cations, with two crystallographic mirror planes (z=1/4, z=3/4) present in the unit cell. All the atoms with the exception of O(3) lie within these planes. The K^+ cations are arranged in a "zig-zag" fashion along the "c"-axis and the SO_4^{2-} tetrahedron has one orientation, with one apice of the adjacent tetrahedron pointing alternately up and down along the "c"-axis. In order to simulate β-K_2SO_4 it was assumed that the predominant interactions

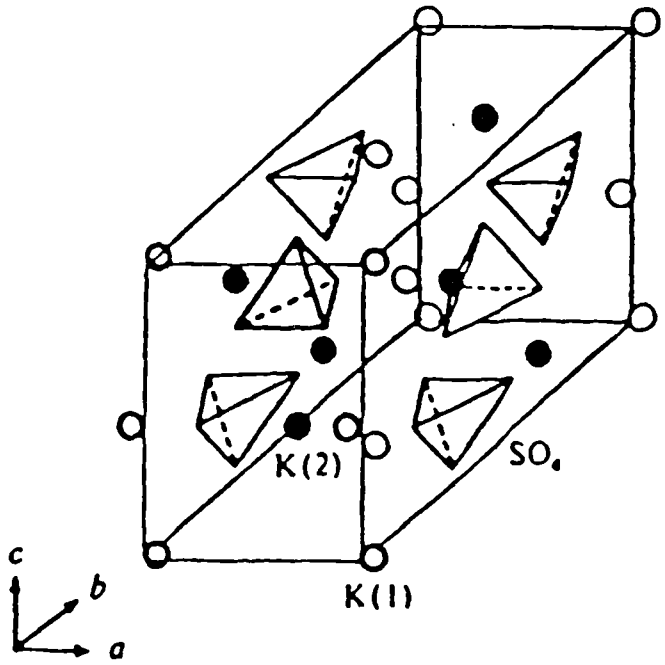

Figure 4.3: Crystal structure of β-K_2SO_4 .

would be attractive interactions occuring between the K^+ cations and the SO_4^{2-} anions, with both attractive and repulsive interactions occuring within the SO_4^{2-} tetrahedron. The following potentials were employed to simulate the interactions: Buckingham potentials were used to simulate sulphur-oxygen, potassium-oxygen and oxygen-oxygen interactions; a bond-bending potential between sulphur-oxygen was included to simulate the tetrahedral sulphate environment. A standard coulombic interaction was also included for the potassium-oxygen environment.

Using THBFIT, these interactions were simulated, with the resultant structure and lattice properties minimised until the closest correlation with a perfect lattice was achieved. The interionic potential parameters that gave the closest correlation are highlighted in Table 4.1.

The best predicted structure obtained by THBFIT was then "relaxed" using THBREL, until the internal and external strain components (i.e. lattice and atom strains) were reduced to zero. The lattice properties thus obtained are shown in Tables 4.2.

Final Ionic Charges Obtained By Empirical Potential Fitting			
K	S	O	
+1.00	+1.72	-0.93	
Final Buckingham Potential Parameters Obtained By Empirical Potential Fitting			
Bond Type	A(eV)	ρ	C(eVT^{-6})
K....O	5151.8	0.2549	0.0
O....O	66465.0	0.1838	27.88
S....O	1827.9	0.1991	0.0
Final Bond Bending Constant and Bond Angle Derived By Empirical Potential Fitting			
	k_b	θ	
	2.0	109.47°	

Table 4.1: Summary of Final Potential Parameters Obtained During Empirical Potential Fitting For Beta-Potassium Sulphate.

Lattice Energy = -182.83eV			
ELASTIC CONSTANT TENSOR(10^{11}dynecm^{-2})			
Predicted		Literature [24]	
C_{11}	= 6.61	C_{11}	= 5.52
C_{12}	= 1.79	C_{12}	= 2.05
C_{13}	= 2.05	C_{13}	= 2.05
C_{22}	= 5.38	C_{22}	= 5.36
C_{23}	= 2.00	C_{23}	= 2.05
C_{33}	= 6.28	C_{33}	= 5.65
C_{44}	= -5.13	C_{44}	= 1.42
C_{55}	= 2.17	C_{55}	= 1.95
C_{66}	= 1.65	C_{66}	= 1.88
Static Dielectric Constant			
2.81	0.00	0.00	
0.00	5.90	0.00	
0.00	0.00	4.32	

Table 4.2: Predicted Crystal Properties For β-K_2SO_4.

Since all strains have been reduced to zero, the lattice structure can be assumed to be perfect. Reasonable agreement is noted between the predicted and observed elastic constants, with the exception of C_{44}. No literature data is available for a comparison of the predicted lattice energy and static dielectric constants.

Thus it may be concluded that empirically derived interionic potentials can be employed to simulate accurately the structure and solid state properties of β-K_2SO_4, although there is a lack of experimental data for complete correlation of the predicted and observed solid state properties. These potentials may be further employed in the calculation of interionic interactions for the prediction of crystal morphology based on energetic considerations.

4.3.2 Simulation Of Equilbrium Morphology Of Beta Potassium Sulphate

As outlined in chapter three, the Bravais/Friedel/Donnay/Harker (BFDH) rules may be used to relate crystal structure to crystal morphology and thus accurate simulations may be obtained of crystal morphology. The BFDH rules were employed to simulate the crystal morphology of beta potassium sulphate. The resultant predicted morphology is highlighted in figure 4.4.

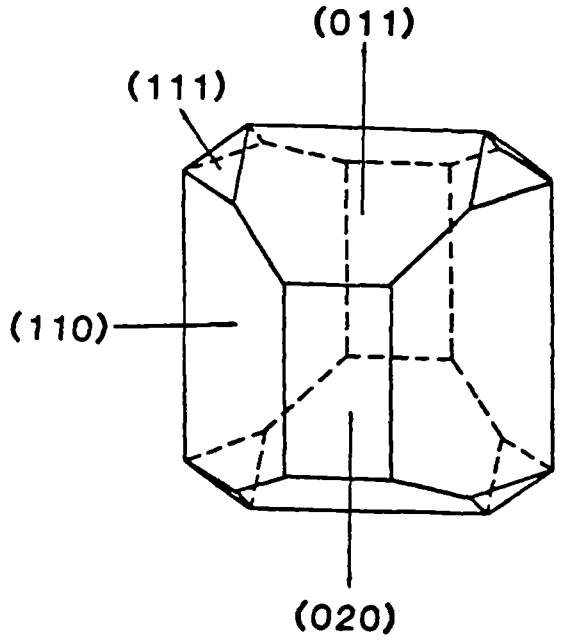

Figure 4.4: Predicted morphology of β K_2SO_4 based on the BFDH laws.

The morphology may be described as prismatic and quite "blocky", with predominant $\{1\bar{1}0\}$, $\{01\bar{1}\}$ forms, with $\{020\}$ and $\{11\bar{1}\}$ forms present to a lesser extent.

Beta potassium sulphate tends to grow forming a variety of differing morphologies, e.g. (figure 4.5) [25] which complicates the task of comparison between predicted and observed morphologies. A typical morphology of β-K_2SO_4 grown from solution at low supersaturation is shown in figure 4.6 [26] and may be taken as a test case for comparison to the predicted morphology based on the BFDH model. Agreement is noted between this observed morphology and the morphology based on the BFDH model; however the predicted morphology is somewhat bulkier along the "b" axis, with the inclusion of $\{01\bar{1}\}$ forms rather than the observed (021) forms.

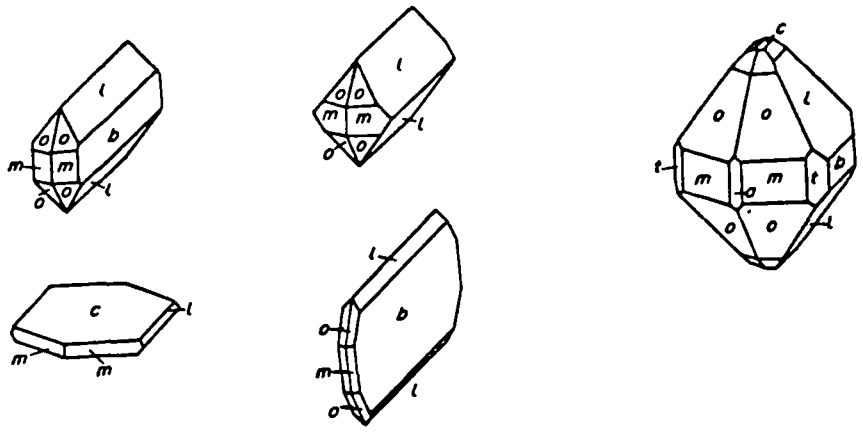

Figure 4.5: Literature observed morphologies for potassium sulphate [25]. a={100}, b={010}, c={011}, l={021}, m={110}, o={111}, t={130}

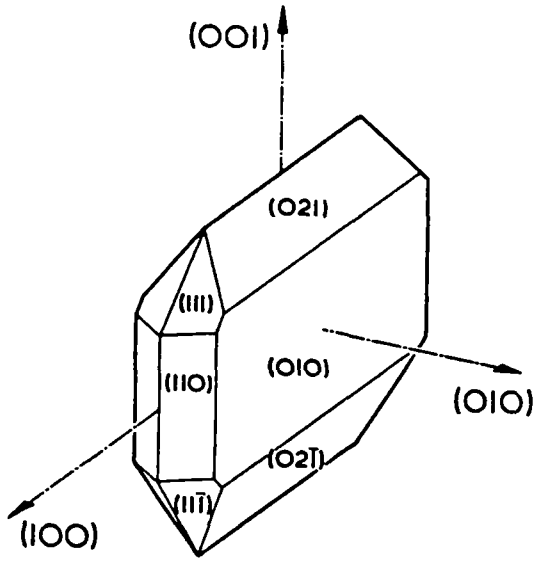

Figure 4.6: Typical morphology of potassium sulphate, grown at from solution at low supersaturation [26].

A predicted morphology based on attachment energy calculations has been obtained by Vogels [27]; However, this calculations has been based on the interactions being modelled as point charge interactions and neglects the interionic interactions within the sulphate grouping. The current study has derived potentials that accounts for all interionic interactions within the system; thus the attachment energies obtained in the current study should be in better agreement with the true attachment energy. The predicted morphology obtained by Vogels is shown in figure 4.7 and shows reasonable agreement to the observed growth morphology and the predicted morphology based on the BFDH laws; i.e. the {101} and {110} forms predominate, with {111} and {200} facets.

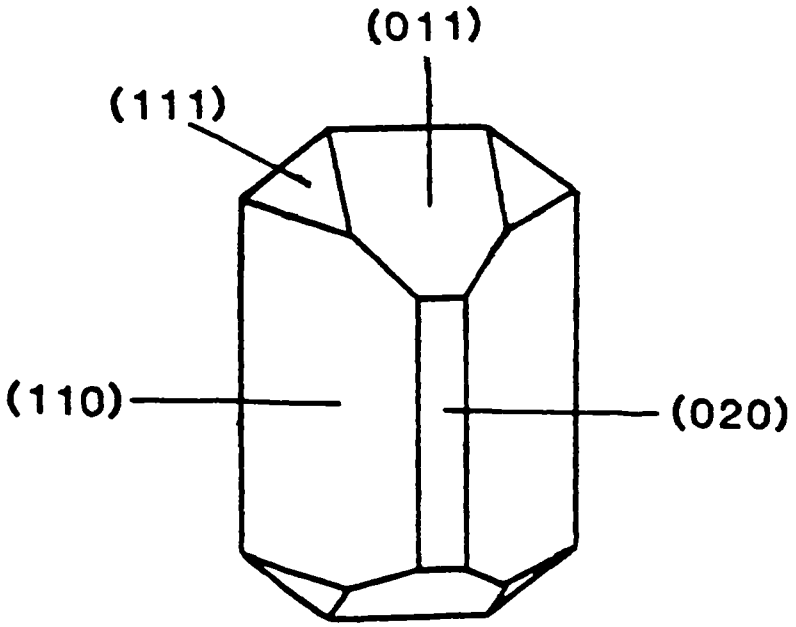

Figure 4.7: Predicted morphology of β-KSO_4 based on attachment energy calculations [27].

Figures 4.8 and 4.9 show the typical dependence of lattice energy upon summation radius for some typical organic materials [28] and for beta potassium sulphate respectively. In the case of an organic material, the lattice energy quickly rises (within 10-15Å summation distance) to a constant value, and may be attributed to the predominance of two bodied interactions within these systems except when there is significant hydrogen bonding present; the coulombic contribution to the lat-

tice energy for an organic system is small (typically 1-5%). Two bodied interactions are short range interactions that are dramatically reduced in influence with increasing summation distance; coulombic interactions tend to have greater influence over longer distances. For an inorganic material (e.g. β K_2SO_4), coulombic interactions predominate in the system (98-99%) and the lattice energy summation distance must be greatly increased for convergence to occur. Lattice energy calculations employing HABIT during the current study have not been successful due to the slow convergence of the lattice energy sum to an extent beyond reasonable computational limits. Thus partitioning the lattice energy into slice and attachment energies (equation 4.1) led to the attainment of unrealistic attachment energies (table 4.3).

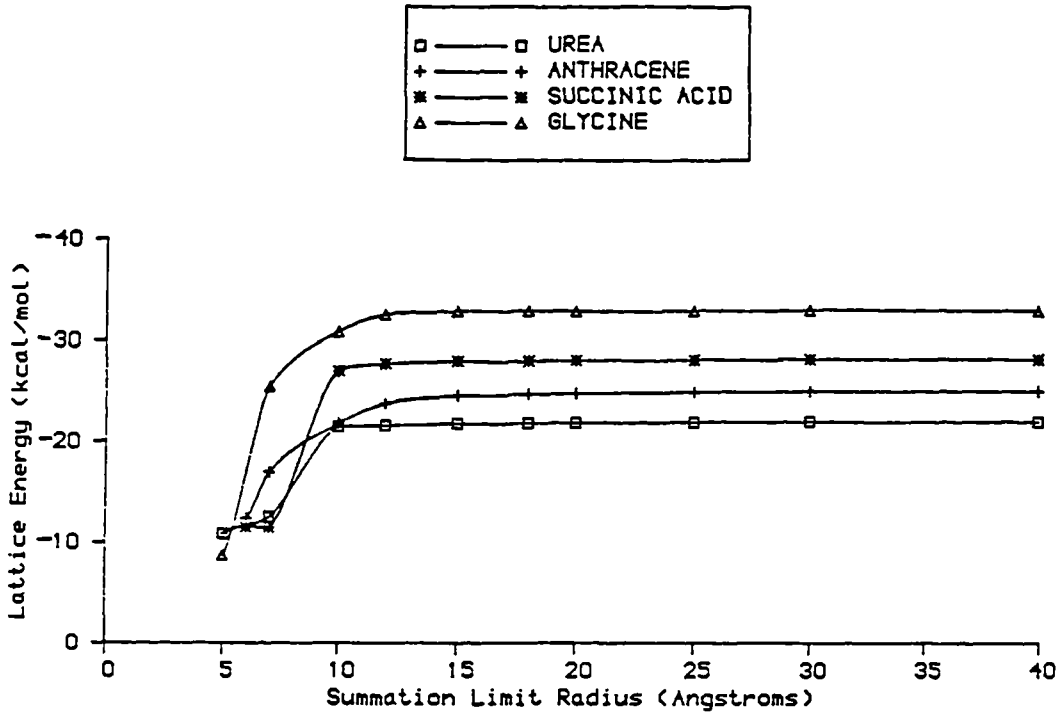

Figure 4.8: Plot of calculated lattice energy versus summation radius for typical organic materials [28]

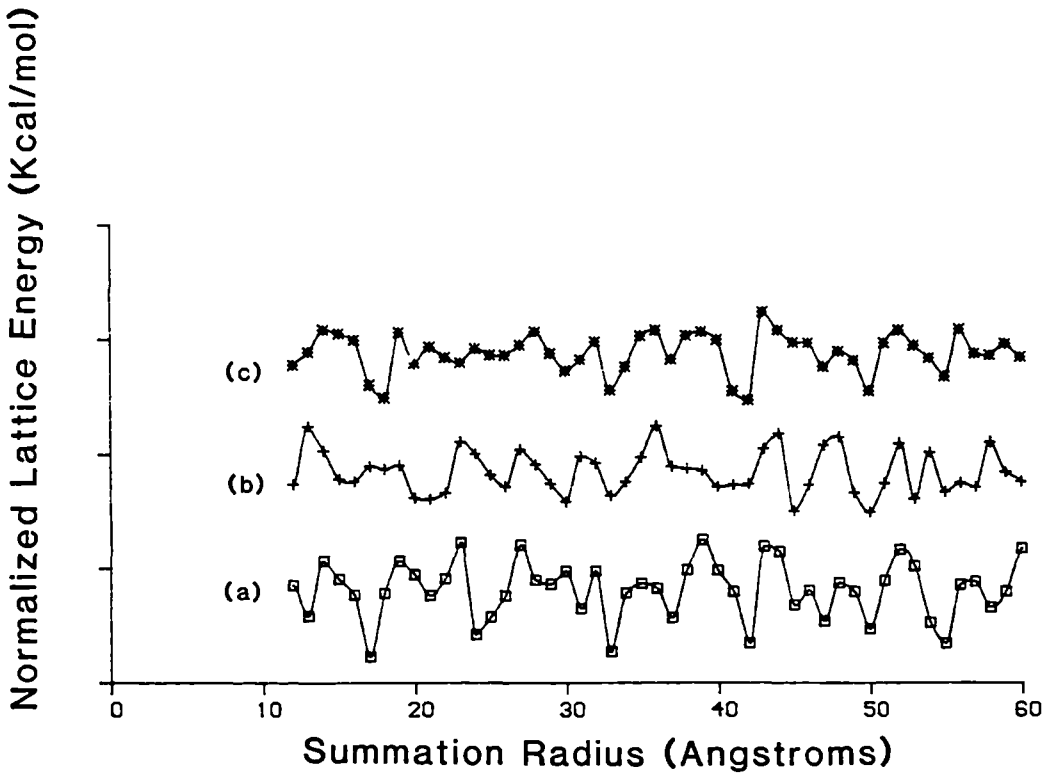

a)Lattice summation from K_1, b) Lattice summation from K_2, c) Lattice summation from SO_4^{2-}

Figure 4.9: Plot of calculated lattice energy versus summation radius for β-K_2SO_4.

Form H K L	Attachment Energy (E_{att}) ($Kcalmol^{-1}$)
1 $\bar{1}$ 0	128.80
0 2 0	-1568.08
0 1 $\bar{1}$	111.47
1 $\bar{2}$ 0	105.56
1 1 $\bar{1}$	119.78
2 0 0	4437.29
2 $\bar{1}$ 0	156.33
1 $\bar{2}$ 1	-101.17
2 0 $\bar{1}$	102.02
1 $\bar{3}$ 0	156.04

Table 4.3: Morphological importance based on calculation of attachment energies for β-K_2SO_4.

4.4 Results Of Studies On Na_2SO_4

4.4.1 Potential Transferability Between β-K_2SO_4 And Na_2SO_4

An investigation was conducted to determine whether the potentials derived for β-K_2SO_4 could be successfully applied to another molecular sulphate system. This methodology of potential transferability has previously been applied to zeolite systems successfully, but has not been attempted for molecular ion systems.

To test the transferability of the potentials describing the SO_4^{2-} interactions in β-K_2SO_4, a simulation of the structure and solid state properties of sodium sulphate was conducted. This system is another Group 1 orthorhombic sulphate, that exists in a variety of different phases [29]. The phase investigated in this study was the low temperature (V) phase. This phase crystallises in a Fddd space group, with 4 molecules per unit cell and unit cell dimensions a= 5.860Å, b=12.304Å and c= 9.817Å, $\alpha = \beta = \gamma = 90^o$ [30]. As for β-potassium sulphate, it was assumed that

the predominant interactions would be attractive and repulsive interactions within the SO_4^{2-} tetrahedra and attractive interactions between the Na^+ cations and the SO_4^{2-} anions.

The program THBFIT was employed to model these interactions using the Buckingham interionic potentials derived describing the sulphur-oxygen and oxygen-oxygen interactions for potassium sulphate and a sodium-oxygen potential that has been previously employed in zeolite simulation [7]. Using THBFIT, all interactions were simulated and the structure and predicted solid state properties minimised until the closest correlation to a perfect lattice was obtained. The final potential parameters obtained by the fitting are highlighted in table 4.4. The structure was then relaxed to a perfect lattice by reduction of the internal and external strain components. The solid state properties obtained for the perfect lattice structure are highlighted in table 4.5.

Final Ionic Charges Obtained By Empirical Potential Fitting			
Na	S	O	
+1.00	+1.72	-0.91	
Final Potential Parameters Obtained By Empirical Potential Fitting			
Bond Type	A(eV)	ρ	C(eVT^{-6})
Na....O	5151.8	0.2549	0.0
O....O	66465.0	0.1838	27.88
S....O	1827.9	0.1991	0.0
Final Bond Bending Constant and Bond Angle Derived By Empirical Potential Fitting			
	k_b	θ	
	2.0	109.47°	

Table 4.4: Summary of final potential parameters obtained during empirical potential fitting for sodium sulphate.

Lattice Energy = -89.71eV					
ELASTIC CONSTANT TENSOR(10^{11}dynecm^{-2})					
Predicted			Literature [31]		
C_{11}	=	5.54	C_{11}	=	8.04
C_{12}	=	1.61	C_{12}	=	2.98
C_{13}	=	1.57	C_{13}	=	2.56
C_{22}	=	7.23	C_{22}	=	10.54
C_{23}	=	0.82	C_{23}	=	1.67
C_{33}	=	4.41	C_{33}	=	6.74
C_{44}	=	0.62	C_{44}	=	1.48
C_{55}	=	0.93	C_{55}	=	1.80
C_{66}	=	1.65	C_{66}	=	2.35
Static Dielectric Constant					
3.72		0.00		0.00	
0.00		2.75		0.00	
0.00		0.00		4.29	

Table 4.5: Predicted Crystal Properties For Na_2SO_4.

As for β-K_2SO_4, experimental lattice energy and static dielectric constant data is not available, thus a complete correlation between predicted and observed solid state properties is not possible. The predicted elastic constants are in reasonable agreement with Von Bayhs' results [31].

Reasonable correlation between the predicted and observed elastic constants is noted ; the predicted elastic constants for sodium sulphate being in general somewhat lower than those experimentally determined.

Thus it may be concluded that the interionic potentials derived for the sulphur-oxygen and the oxygen-oxygen interactions in the simulation of beta-potassium sulphate have been transferred and employed to simulate successfully the low temperature (V) phase of sodium sulphate. A perfect lattice structure has been achieved and

the predicted solid state properties are in reasonable agreement with experimental observation.

4.5 Conclusions

Interionic potentials have been empirically derived to simulate accurately the structure and solid state properties of beta-potassium sulphate. The potentials are based on a Buckingham potential form, describing the potassium-oxygen, sulphur-oxygen and oxygen-oxygen interactions within the system. Three bodied interactions are simulated using a bond bending term. The structure has been relaxed to a perfect lattice, and the resultant calculated solid state properties have shown to be in reasonable agreement with experimental studies.

Attempts at partitioning a lattice energy sum into slice and attachment energies for morphological modelling have so far proved unsuccessful, due to the slow convergence of the coulombic attractions within the system.

The potentials derived describing the sulphate interactions in beta potassium sulphate have been successfully transferred to another group one system, i.e. sodium sulphate. The crystal structure of sodium sulphate was relaxed to a perfect lattice structure, with reasonable correlation noted between predicted and solid state properties.

Further work should center on the inclusion of an accelarated convergence routine (e.g. based on the Ewald method), which will allow rapid convergence of coulombic lattice sums. A lattice energy may then be partitioned into slice and attachment energies, for resultant morphological modelling.

The potential describing the sulphate interactions should be further tested for transferability, e.g. application to more complex sulphate systems e.g. $(NH_4)_2SO_4$ is a salt with a molecular cation, would enable the determination of the portability of the potentials describing the sulphate grouping.

4.6 References

1. R. Docherty, G. Clydesdale, K.J. Roberts & P. Bennema; J. Phys. D: App. Phys. **24** (1991) 89-99

2. R. Docherty & K.J. Roberts; J. Crystal Growth, **88**, 1988, 159-168

3. G. Clydesdale, R. Docherty & K.J. Roberts; Comp. Phys. Comm. **64** (1991) 311-328

4. P. Hartman & W.G. Perdok; Acta Cryst. 8 (1955) 49-52

5. P. Hartman; "Crystal Growth: An Introduction" ed. P. Hartman (North Holland, Amsterdam, 1973), 637

6. P. Bennema & P. Hartman; J. Cryst. Growth **49** (1980) 145-156

7. R.A. Jackson & C.R.A. Catlow; Molecular Simulation **1** (1988) 207-224.

8. R. Baetzold, C.R.A. Catlow, J. Corish, F.M. Healy, P.W.M. Jacobs & Y. Tan; Submitted to J. Phys. Chem. Solids

9. R.A. Jackson, A.D. Murray, J.H. Harding & C.R.A. Catlow, Phil. Mag. **53** 1986 27-50

10. B. Von Grande, D. Muller-Buschbaum & W. Schweizer; Z. Anorg. (Allg.) Chem., **428** (1977) 120-124.

11. M.S. Islam, M. Leslie, S.M. Tomlinson & C.R.A. Catlow; J. Phys. C., **21** (1988). L109-L117

12. R.J. Birgeneau, C.Y. Chen, D.R. Gabbe, H.P. Jennsen, M. Kastner, C.J. Peters, P.J. Picone, T. Thio, T.R. Thurston, H.L. Tuller, J.D. Axe, P. Boni & G. Shirane, G; Phys. Rev. Lett., **59** (1987) 1329-1332

13. C. Pisani & R. Dovesi; Int. J. Quant. Chem., **17** (1970) 501-514

14. B.J. Dick & A.W. Overhauser; Phys. Rev. **B112** (1958) 90-103.

15. R. Jackson, Proceedings of NATO Conference on Simulation Studies - in press

16. C.R.A. Catlow & M.J. Norgett; AERE Harwell Report **M.2673** 1978 1-53

17. C.R.A. Catlow & W.C. Mackrodt; "Computer Simulation of Solids:Lecture Notes in Physics", Berlin, Pub. Springer-Verlag, Vol. 166 (1982) Chap. 1 3-20

18. M. Leslie; SERC Daresbury Laboratory Report - in preparation.

19. M. Leslie; SERC Daresbury Laboratory Report - in preparation.

20. M.A. Bredig; J. Phys. Chem. 46 (1942) 747-764.

21. M. Bernard & R. Hocart; R. Bull. Soc. Fr. Mineral. Cristallogr. 84 (1961) 396-399.

22. H.F. Fischmeister; 93 420-434 1962 420-434.

23. J.A. McGinnnety; Acta Cryst. B28 (1972) 2845-2852

24. Von S. Hasshuhl; Acta Cryst. 18 (1965) 839-841

25. J.W. Mullin "Crystallisation" Pub. Butterworths, second ed. 19-20

26. J.W. Mullin & C. Gaska; J. Chem. Eng. Data 18 (1973) 217-220

27. L. Vogels; PhD Thesis, University of Nijmegen; Ch. 3, 1991, 49-68

28. R. Docherty; PhD Thesis, University of Strathclyde (1989)

29. Gmelin; Handbuch der Anorganischen Chemie 21 (1966) 1091-1095

30. A. Nord; Acta Chem. Scand. 27 (1973) 814-822

31. Von W. Bayh; Acta Cryst. 20 (1966) 931-932

Chapter 5

The Role Of Carbonate In The Precipitation And Agglomeration In The Na_2CO_3-Na_2SO_4-H_2O System

Contents

5.1 Introduction

Crystallisation is currently the dominant technique for particle separation and purification in use in the industrial community during the last twenty years. One of the many reasons for the dominance of this technique is the high purity levels that may be obtained using a relatively low energy input.

The morphology of precipitated products can play an important role in particulate processing, e.g. the efficiency of tablet production in the pharmaceutical industry, the separation of particulates from mother liquor and the dust/toxicity problems associated with crystal attrition and fragmentation during processing.

Crystallisation of high surface area agglomerated crystallite matrices are used as an aid in the dispersion of high value added effect chemicals, such as detergent surfactants etc. Components within the Na_2CO_3-Na_2SO_4-H_2O system are employed to crystallise such matrices. In order to optimise surface area properties such as porosity etc, it is desirable to have the crystallite matrix composed of dendrites. This chapter presents a reexamination of the Na_2CO_3-Na_2SO_4-H_2O system. This system has been previously examined by various authors, ranging from low temperature solution studies [1-4] to high temperature studies concerning melt crystallisation [5-8]. However, studies of the system at low temperatures have been limited in the temperature range observed. A typical phase diagram [2] based on low temperature solution studies is shown in figure 5.1 and the following phases have been identified:

- sodium carbonate monohydrate, $Na_2CO_3.H_2O$ [9]
- sodium carbonate heptahydrate, $Na_2CO_3.7H_2O$ [10]
- sodium carbonate decahydrate, $Na_2CO_3.10H_2O$ [11]
- sodium sulphate, Na_2SO_4 [12]
- sodium sulphate decahydrate, $Na_2SO_4.10H_2O$ [13]
- burkeite, $Na_2CO_3(Na_2SO_4)_2$ [14]

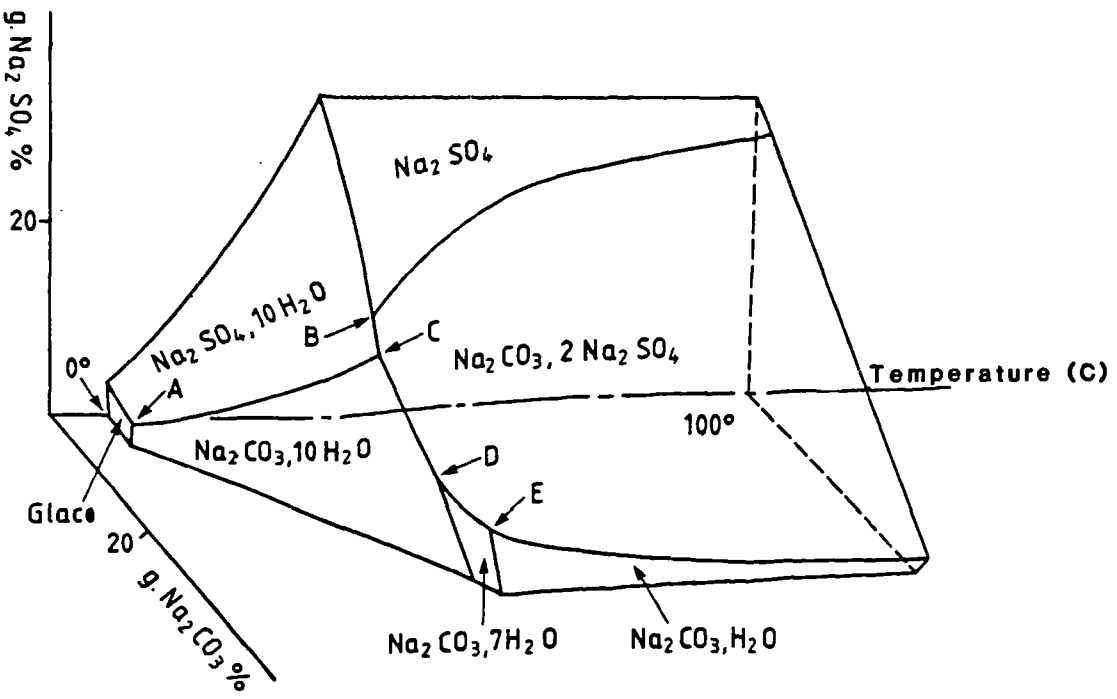

Figure 5.1: Typical phase diagram of the Na_2CO_3-Na_2SO_4-H_2O system [2]

The current study focussed on the particular region of the Na_2CO_3-Na_2SO_4-H_2O system stable in the temperature range $(30\text{-}90)^0C$, this temperature region is desirable for the crystallisation of dendrites for the detergent industry. The precipitated crystalline particulates are studied to examine the inter-relationship between solution composition, precipitation temperature and crystal morphology.

5.2 Methodology

Crystalline samples were obtained by the controlled solvent evaporation at constant temperature of solutions containing molar ratios of Na_2CO_3:Na_2SO_4 ranging from (5:1) to (1:5) (Na_2CO_3:Na_2SO_4) in the temperature range $(30\text{-}90)^0C$. The solutions (approx. $80cm^3$) were held unstirred in $100cm^3$ conical flasks in a thermostatted water bath at constant temperature, until crystallisation occurred. The resultant crystalline samples were washed and stored under an inert medium to remove the possibility of sample hydration from the environment. The phases present were identified and analysed using X-ray powder diffraction, Scanning Electron Microscopy (SEM) and

Energy Dispersive X-ray Microanalysis (EDX). Chemical analysis was employed to determine the carbonate and sulphate concentration of each sample. Each analysis method is briefly summarised.

5.2.1 X-ray Powder Diffraction

A combination of both conventional x-ray sources and synchroton radiation was employed to determine the unknown phases present. Powder diffraction may be employed to determine the various phases as each of these phases has a distinguisable x-ray powder pattern (figure 5.2), hence the various phases that may be present in a mixture can readily be identified by powder diffraction.

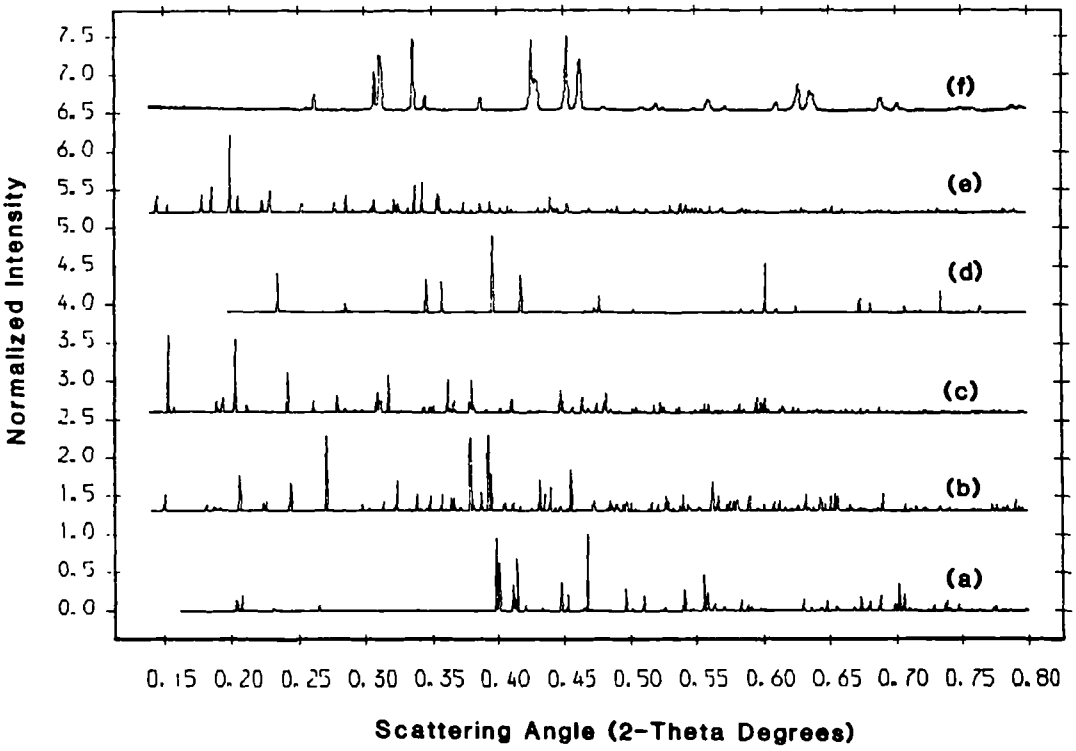

(a) $Na_2CO_3.H_2O$, (b) $Na_2CO_3.7H_2O$, (c) $Na_2CO_3.10H_2O$, (d) Na_2SO_4 (e) $Na_2SO_4.10H_2O$, (f) $Na_2CO_3(Na_2SO_4)_2$

Figure 5.2: Powder diffraction spectra for all phases present in the Na_2CO_3-Na_2SO_4-H_2O system.

Synchroton radiation holds many advantages over conventional x-ray sources, e.g. a tunable wavelength source affording significantly greater intensities (up to 10^6 times greater), with the ability to obtain low angle spectra that can allow the determination of supercell formation. The samples analysed using synchroton radiation were taken on station 8.3 at the SERC Daresbury SRS and were consequently indexed by Vissers method [15], from which the lattice parameters were determined.

Samples obtained using a conventional source were analysed [16] by matching peak positions and intensities to standard data in the JCPDS database.

5.2.2 Scanning Electron Microscopy And Energy Dispersive X-ray Microanalysis

The basics of Scanning Electron Microscopy (SEM) have been reviewed in section 3.4.2.1. As previously stated electrons are fired at a specimen which consequently emits secondary electrons and x-rays. The secondary electrons are detected, processed and can be consequently viewed as an image of the sample. The emitted x-rays radiation may be employed in Energy Dispersive X-ray Microanalysis (EDX). The emitted radiation will have characteristic energies dependent on the elemental constituents of the specimen and these energies may be analysed to obtain an elemental mapping of the specimen. Further details of these techniques may be found elsewhere [17].

The EDX spectra associated with these phases are shown in figure 5.3. As observed in figure 5.2, the spectra for each phase differs; the major point to be noted is the increasing intensity of the oxygen peak with respect to the sodium peak, as the hydration content is increased. This raises the point that EDX parallels x-ray powder diffraction, in the ability to distinguish between samples of different hydration content. Although there are underlying factors that make EDX a less attractive analysis technique than x-ray powder diffraction, e.g. sample sensitivity to vacuum conditions etc, a major advantage is that it is a mobile scanning technique, i.e. it can be used to identify and differentiate between particles of different composition within a specimen, whereas powder diffraction is a bulk analysis technique, detailing only the presence of different compositions within a specimen. Thus EDX may be

employed in the analysis of mixtures where there exists extensive agglomeration, to identify the chemical nature of the agglomerates.

5.2.3 Determination Of Carbonate Ion Concentration

The carbonate anion concentration can be determined potentiametrically, from a titration with hydrochloric acid (equation 5.1). A sharp change in the solution potential is observed upon reaching the end point. Carbonate ion concentrations can be determined by this method with an accuracy of $\pm$0.5wt%

$$Na_2CO_3 + 2HCl \longrightarrow 2NaCl + CO_2 + H_2O \tag{5.1}$$

5.2.4 Determination Of Sulphate Ion Concentration

The sulphate anion concentration can be determined by titration with lead nitrate to form insoluble lead sulphate (equation 5.2):

$$Na_2SO_4 + PbNO_3 \longrightarrow PbSO_4 + 2NaNO_3 \tag{5.2}$$

Bromophenol blue is used as an indicator, changing colour from green $\longrightarrow$ purple upon reaching the end point. Sulphate ion concentrations can be determined to within $\pm$0.5wt% by this method.

5.3 Results And Discussion

5.3.1 Redetermination Of The Phase Diagram Of The Na_2CO_3-Na_2SO_4-H_2O System

The reexamination of the Na_2CO_3-Na_2SO_4-H_2O system based on x-ray powder diffraction studies is shown in table 5.1.

On examination of table 5.1, the hydration content of the crystallising phase increases as crystallising temperature decreases. The general trend noted are phase changes from predominantly carbonate based materials $\longrightarrow$ burkeite $\longrightarrow$ sulphate based materials. Burkeite is observed to be the dominant crystallising phase within

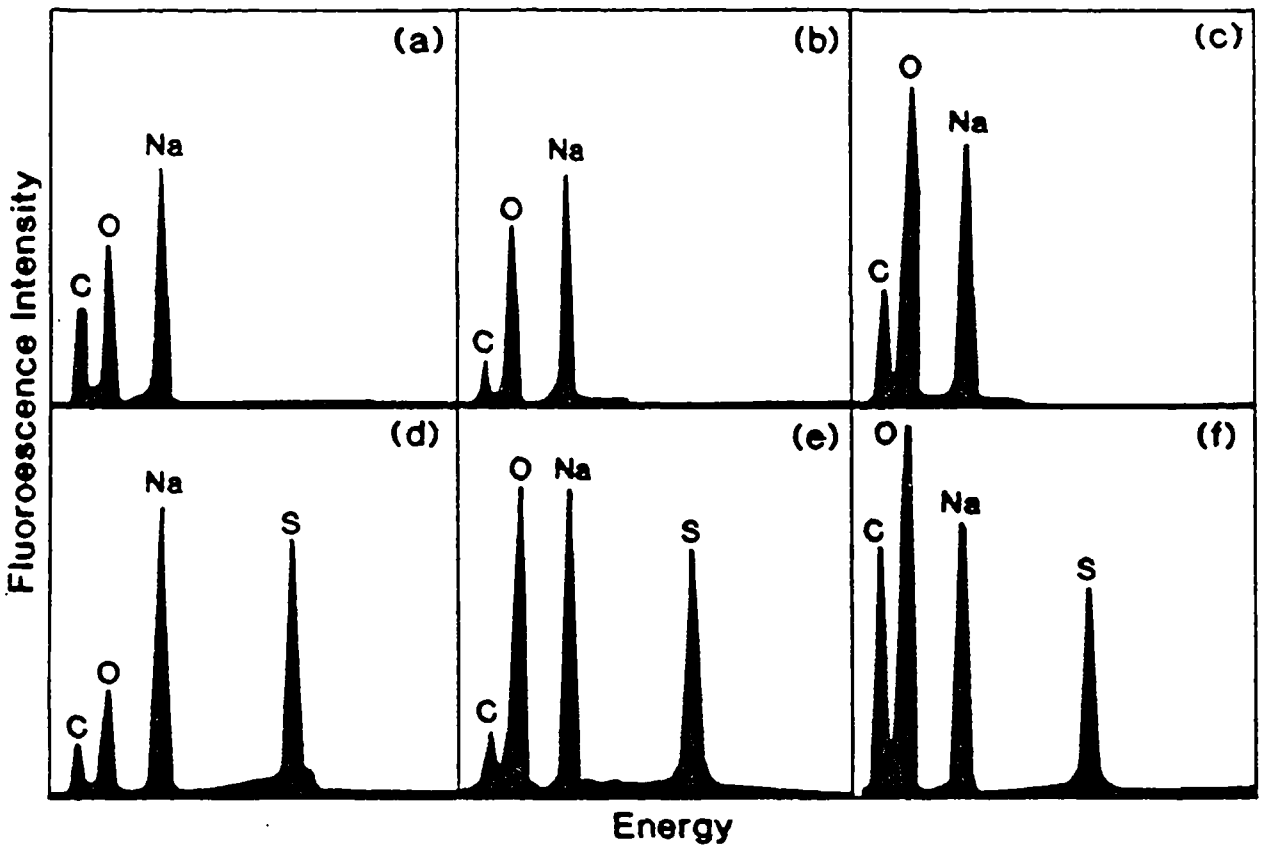

(a) $Na_2CO_3.H_2O$ (b) $Na_2CO_3.7H_2O$ (c) $Na_2CO_3.10H_2O$ (d) Na_2SO_4 (e) $Na_2SO_4.10H_2O$ (f) $Na_2CO_3.H_2Na_2CO_3(Na_2SO_4)_2$

Figure 5.3: EDX spectra associated with the various components of the Na_2CO_3-Na_2SO_4-H_2O.

TEMP°C \ RATIO Na_2CO_3: Na_2SO_4	5:1	4:1	3:1	2:1	1:1	1:2	1:3	1:4	1:5
90	Maj B • Min C1	Maj B* • Min C1	Maj B* • Min C1	Maj B* • Min C1	B • tr S	Maj B • Min S	Maj B • Min S	Maj B* • Min S	S
80	B*	B*	B*	B*	B*	B*	B*	S	S
70	Maj C1 • Min BS	Maj C1 • Min B	B* • tr X	B* • tr X	B* • tr X	Maj S • MinB	Maj S • tr X	Maj S • tr X	Maj S • tr X
60	Maj B • Min C1	B*	B	B	B*	Maj S • Min B	S	S	S
50	C1 • tr B	C1	Maj B • Min C1	B*	B	S	S • tr C1	S • tr C1	S • trC1,B
40	Maj B • Min C1	B*	B*	B*	B*	Maj B • tr S,X	S	S	S
30	Maj B* • trC1,C7,S	Maj C7 • tr S10	Maj B* • tr S10,X	Maj B* • Min X	Maj B • Min X	Maj S10 • trB,C10X	Maj S10 • trB,C10X	Maj S10 • tr X	Maj S10 • tr X

KEY

B- BURKEITE S- Na_2SO_4 S10- $Na_2SO_4.10H_2O$ C1- $Na_2CO_3H_2O$ C7- $Na_2CO_3.7H_2O$

C10- $Na_2CO_3.10H_2O$ Maj- MAJOR PHASE Min- MINOR PHASE tr- TRACE AMOUNT

X- UNIDENTIFIED PHASE DUE TO PREFERRED ORIENTATION.

*- PRESENCE OF LOW ANGLE PEAKS,POSSIBLY INDICATING SUPERCELL FORMATION

Table 5.1: Re-determined phase diagram of the Na_2CO_3-Na_2SO_4-H_2O system.

the region (3:1-1:1) (Na_2CO_3:Na_2SO_4) throughout the temperature range investigated. This region of preferential burkeite formation increases at temperatures greater than 70^0C. Some discrepancies with previous author's findings [14] are noted: Burkeite was observed to be the crystallising phase at 30°C in the region (1:1 - 1:5) (Na_2CO_3:Na_2SO_4) [14]; with the exception of the equimolar 1:1 Na_2CO_3:Na_2SO_4, the current study indicates that the predominant crystallising phase within this region is $Na_2SO_4.10H_2O$. A possible reason for this difference could be that the crystallising phase is a function of supersaturation, i.e. different crystallising compounds at different supersaturations, although this observation requires further investigation.

Although powder diffraction and EDX can be employed to identify and distinguish between different components in a mixture, problems such as preferred orientation effects normally inhibit the determination of the relative concentrations of each component with any degree of accuracy. Thus techniques based on chemical analysis have to be employed for such a determination. If in the case of the Na_2CO_3-Na_2SO_4-H_2O system the carbonate and sulphate anion concentrations for a specimen are calculated, then the relative concentrations of the components in the crystallised mixture may be obtained. Attempts were made to determine the carbonate and sulphate anion concentrations of the samples obtained for the redetermination of the Na_2CO_3-Na_2SO_4-H_2O system, using the methods described in section 5.2. However, the combination of sample fluroescence and the lack of reproducibility meant that the sulphate anion concentration could not be determined with any degree of reliability, e.g. levels of 140wt% SO_4^{2-} concentration being recorded for certain samples. However, determination of the carbonate anion concentration was reproducible and showed good correlation to the approximate concentrations obtained from powder diffraction data. The theoretical carbonate concentration for every possible component of the Na_2CO_3-Na_2SO_4-H_2O system and the resultant determined carbonate concentrations for the mixtures shown in table 5.1 are highlighted in tables 5.2 and 5.3 respectively. In general the trends in table 5.3 are similar to those observed in table 5.1; i.e. a decreasing carbonate content in the crystallising system as the sulphate content is increased. The expansion of the burkeite $Na_2CO_3(Na_2SO_4)_2$ region with increasing crystallisation temperature is again noted.

Component	Concentration (wt%)
$Na_2CO_3.H_2O$	48.39
$Na_2CO_3.7H_2O$	25.85
$Na_2CO_3.10H_2O$	20.97
$Na_2CO_3(Na_2CO_3)_2$	15.38
Na_2SO_4	0
$Na_2SO_4.10H_2O$	0

Table 5.2: Theoretical carbonate anion concentration of all components in the Na_2CO_3-Na_2SO_4-H_2O system.

Temperature	Na_2CO_3:Na_2SO_4 (moles)								
(^{0}C)	5:1	4:1	3:1	2:1	1:1	1:2	1:3	1:4	1:5
90	30.52	24.85	19.41	27.68	16.30	12.11	11.15	10.36	0.62
80	38.30	27.40	12.23	21.28	15.73	10.41	11.32	1.25	0.90
70	43.57	27.00	18.40	16.13	14.08	3.97	0.48	0.20	0.21
60	13.08	17.49	16.73	15.88	14.29	12.74	0.38	0.09	0.14
50	36.51	46.00	27.90	14.68	13.24	3.53	0	0	0.50
40	18.62	16.20	14.78	14.61	13.00	6.25	0.14	0.10	0.10
30	22.93	23.75	15.34	15.19	13.00	1.41	0.45	0.28	0.18

Table 5.3: Determined carbonate anion concentration for the redetermined Na_2CO_3-Na_2SO_4-H_2O system.

The existence of low angle peaks, e.g. ($2\theta < 15°$), in a powder diffraction spectra can indicate the formation of supercells. Burkeite has been known to form a variety of supercells, ranging from 2X and 6X [14] to 12X [18] superstructures. This superstructure formation is due to anionic positional disorder within the crystal structure, leading to structural modulations associated with a larger unit cell. Possible burkeite superstructure reflections were noted at a variety of Na_2CO_3:Na_2SO_4 ratios

and temperatures, although no obvious trend could be discerned for superstructure formation as a function of temperature or Na_2CO_3:Na_2SO_4 ratio. An example of burkeite powder diffraction spectra (taken at the Daresbury SRS) both with and without supercell reflections is shown in figure 5.4.

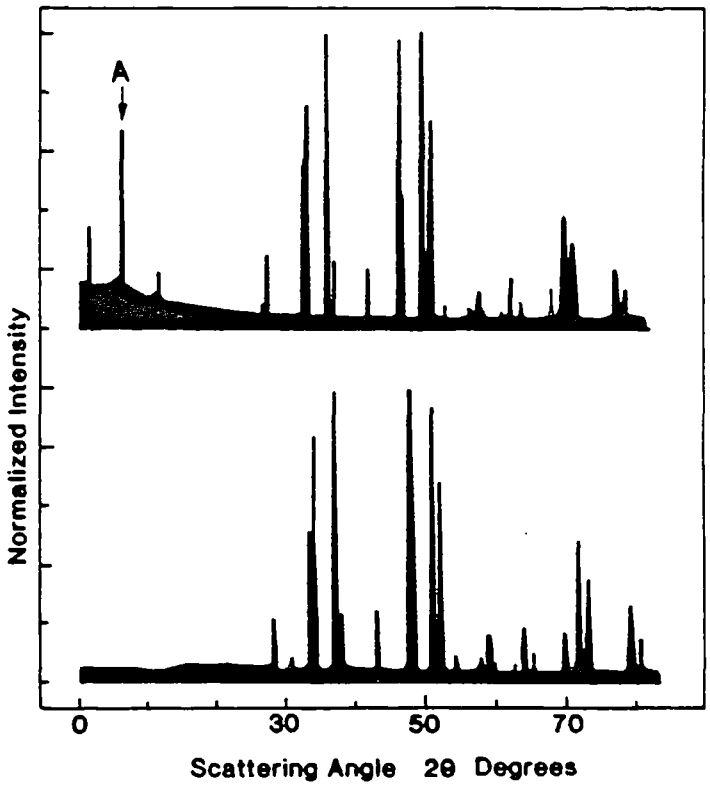

Figure 5.4: High resolution powder X-ray diffraction spectra of burkeite taken on station 8.3 at the Daresbury Synchroton Radiation source showing the characteristic low angle peaks (labelled A) associated with the formation of a modulated supercell

5.3.2 Particulate Morphology As A Function Of Precipitation Temperature And Phase Composition

When a series of components crystallise from solution interesting inter-relationships between the various components are observed. The series (5:1-1:5) Na_2CO_3:Na_2SO_4 crystallised at 70^0C are shown in figure 5.5(a-h). The high degree of agglomeration present provides difficulties in identification of the various components present using the morphology predictions highlighted in chapter 3; thus EDX provides an essential identifying technique for phase identification. The phase changes noted for this region are from predominantly $Na_2CO_3.H_2O \longrightarrow Na_2CO_3(Na_2SO_4)_2 \longrightarrow Na_2SO_4$. Extensive agglomeration is exhibited for the carbonate-based materials (figure 5.5(a-f)), with a tendency to form spheroidal particulates approximately (100-200 μm) in diameter. A definite change in the degree of agglomeration is noted when there is a phase change from predominantly carbonate based materials (figure 5.5(a-f)) to sulphate based materials (figure 5.5(g-h)). It is also observed that the burkeite particles (typically 10-30 μm) in general are much smaller in size than the larger sodium carbonate monohydrate (50-105 μm) and sodium sulphate (40-270 μm) particles and tend to act as an "agglomerating nucleator", binding particles together.

This tendency for burkeite to act as an agglomerating nucleator is also noted at other precipitation temperatures. Figures 5.6(a-c), 5.7(a-c) and 5.8(a-c) show the crystallised morphologies obtained from solutions containing (5:1),(1:1) and (1:4) Na_2CO_3:Na_2SO_4 mole ratios at 90^0C, 50^0C and 30^0C respectively. In figure 5.6(a) thin platelets (30-180μm) of $Na_2CO_3.H_2O$ are observed, coated in much smaller particles (3-10μm) of $Na_2CO_3(Na_2SO_4)_2$ with extensive agglomeration between particulates. Extensive agglomeration is also noted when a solution containing 1:1 Na_2CO_3:Na_2SO_4 is crystallised at 90^0C (figure 5.7(b)), although much larger crystals (30-60μm) of $Na_2CO_3(Na_2SO_4)_2$ are observed. This contrasts with figure 5.7(c), which illustrates the resultant major phase $Na_2CO_3(Na_2SO_4)_2$ and minor phase Na_2SO_4 obtained when a solution of ratio of (1:4) Na_2CO_3:Na_2SO_4 also crystallises at 90^0C. In this case much lower agglomeration is observed, with larger (20-40μm), more distinctive burkeite dendrites formed, which tend to agglomerate together rather

than to form the larger (100-160μm) Na_2SO_4 particles. At lower temperatures the $Na_2CO_3.H_2O$ platelets are replaced by more "block-like" morphologies (40-200μm), e.g. figure 5.7(a) which illustrates the resultant major phase $Na_2CO_3.H_2O$ and minor phase $Na_2CO_3(Na_2SO_4)_2$ obtained when a solution of a (5:1) mole ratio of Na_2CO_3:Na_2SO_4 crystallises at 50^0C. However small $Na_2CO_3(Na_2SO_4)_2$ particles (10-30μm) are still observed on the surface of the $Na_2CO_3.H_2O$ blocks and again appears to act as agglomeration nucleators. This agglomeration tendency of $Na_2CO_3(Na_2SO_4)_2$ is clearly highlighted in figure 5.8(b), where $Na_2CO_3(Na_2SO_4)_2$ is the single phase crystallised at 50^0C from a solution of ratio 1:1 Na_2CO_3:Na_2SO_4. Small (10-30μm) particles of $Na_2CO_3(Na_2SO_4)_2$ again exhibit a high degree of agglomeration, forming a larger (650 μm) particulate. The significantly larger (200-500μm) Na_2SO_4 particles crystallised from a solution of ratio (1:4) Na_2CO_3:Na_2SO_4 (figure 5.7(c))show little agglomeration and clearly contrasts to the extensive agglomeration exhibited in figure 5.7(a) and (b).

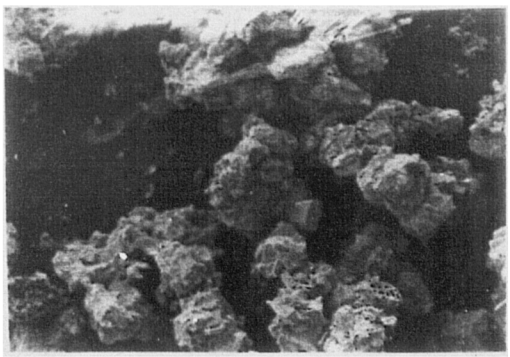

(a)

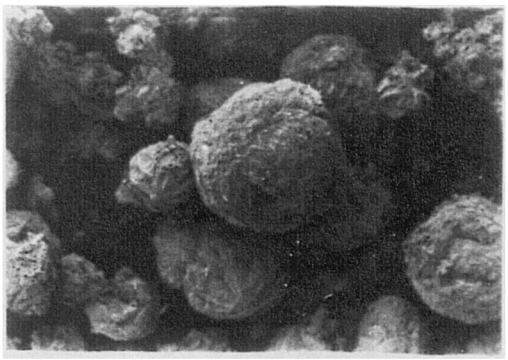

(b)

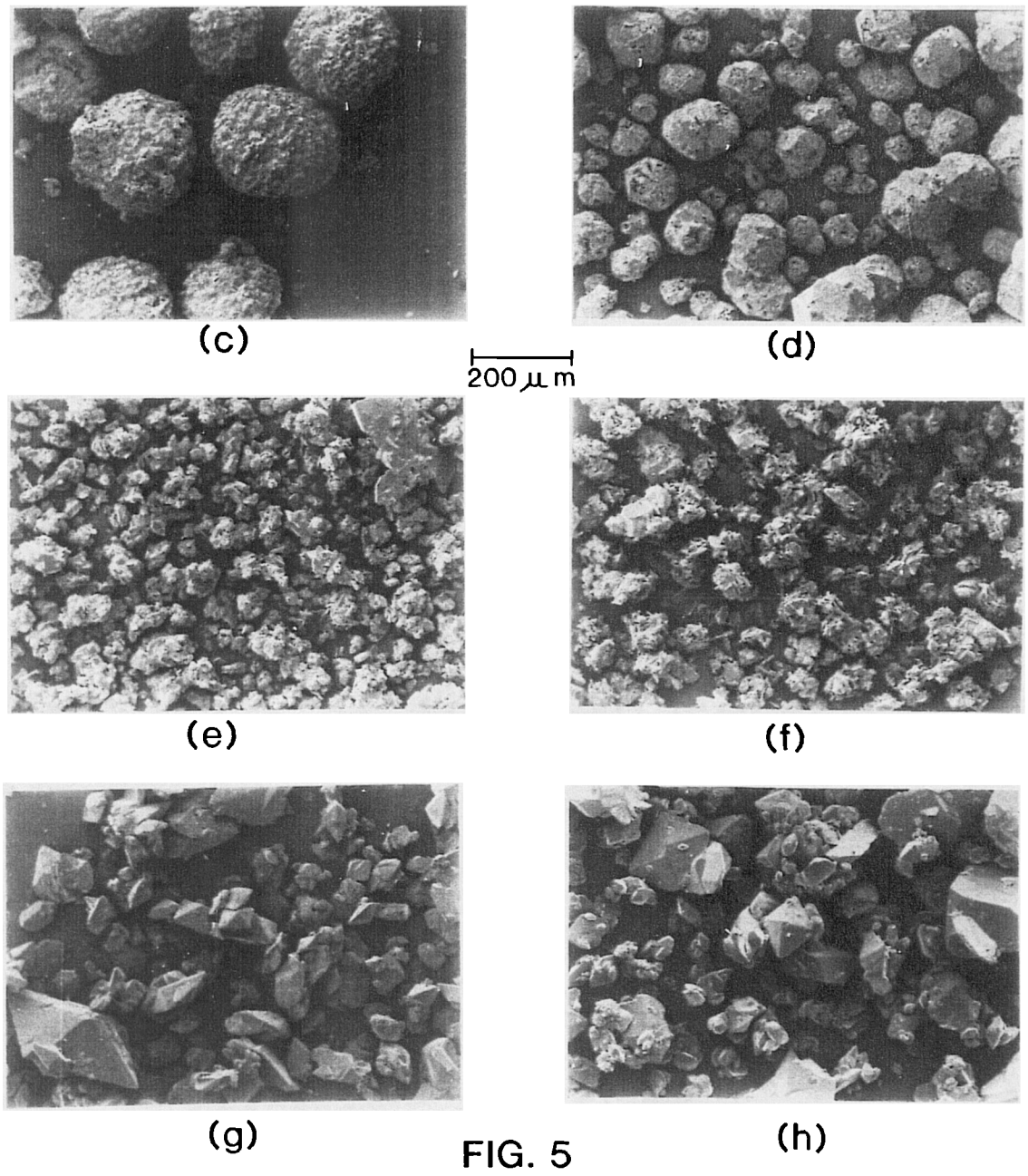

FIG. 5

(a) 5:1 Na_2CO_3:Na_2SO_4 (b) 4:1 Na_2CO_3:Na_2SO_4 (c) 3:1 Na_2CO_3:Na_2SO_4 (d) 2:1 Na_2CO_3:Na_2SO_4 (e) 1:1 Na_2CO_3:Na_2SO_4 (f) 1:2 Na_2CO_3:Na_2SO_4 (g) 1:4 Na_2CO_3:Na_2SO_4 (h) 1:5 Na_2CO_3:Na_2SO_4

Figure 5.5: Observed morphologies crystallised at 70°C in the (5:1)-(1:5) Na_2CO_3:Na_2SO_4 region.

Decreasing the precipitation temperature from $90^0C \longrightarrow 70^0C \longrightarrow 50^0C$ seems to lead to an increase in the size of the $Na_2CO_3.H_2O$ and Na_2SO_4 crystallites, but does not significantly influence the size of the $Na_2CO_3(Na_2SO_4)_2$ crystallites. This behaviour is significantly altered for precipitates crystallised at 30^0C. Figures 5.8 (a-c) highlight the obtained morphologies of solutions containing 5:1, 1:1 and 1:4 moles Na_2CO_3:Na_2SO_4 crystallised at 30^0C respectively. The predominant precipitate in the (5:1) (figure 5.8(a)) and (1:1) (figure 5.8(b)) Na_2CO_3:Na_2SO_4 systems are large burkeite crystals (200-850μm), that are extensively agglomerated. This contrasts with a solution of 1:4 Na_2CO_3:Na_2SO_4 crystallised at the same temperature. From powder diffraction studies, the predominant precipitate has been identified as sodium sulphate decahydrate ($Na_2SO_4.10H_2O$) and a trace amount of a material that could not identified due to preferred orientation problems. Figure 5.8(c) highlights the precipitated morphologies obtained from this solution. The large $Na_2SO_4.10H_2O$ crystals (200-600μm) are clearly observed, as are small (20-50μm) crystallites of $Na_2CO_3(Na_2SO_4)_2$ that are extensively bonded to the surface of the $Na_2SO_4.10H_2O$ crystallites. Thus SEM can provide a complementary technique to x-ray powder diffraction in the identification of samples where preferred orientation problems exist and inhibit the identification of the phases present. If a material has charge rich crystal surfaces, then crystallites of the material will not readily agglomerate due to repulsion effects. It was highlighted in chapter 3 that the habit modification of $Na_2CO_3.H_2O$ occured due to the presence of ionic layers in the structure, which lead to cation rich surfaces; hence it would be expected that $Na_2CO_3.H_2O$ will not easily agglomerate. It may be postulated that the lack of agglomeration noted when Na_2SO_4 and $Na_2SO_4.10H_2O$ are the crystallisation materials indicate the presence of charged crystal surfaces in these systems. However from figures 5.5-5.8, $Na_2CO_3(Na_2SO_4)_2$ seems to act as an agglomeration nucleator, extensively binding both to sulphate and carbonate based materials. Burkeite has a complex disordered crystal structure [17] and this structural disorder may lead to the formation of homogeneous rather than charged layers in the crystal structure. Hence the resultant lack of charge rich crystal surfaces may be the reason why $Na_2CO_3(Na_2SO_4)_2$ can agglomerate much more readily than either pure carbonate or sulphate based materials.

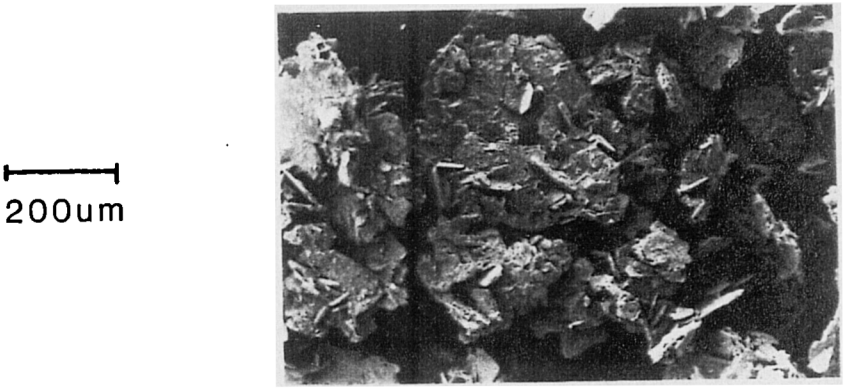

(a)

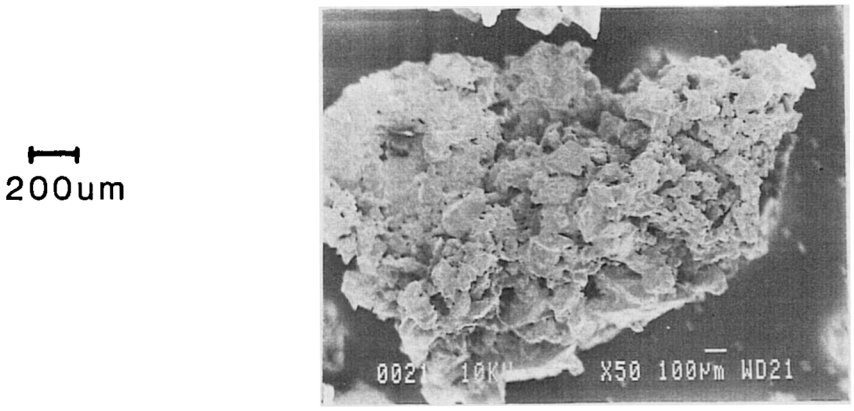

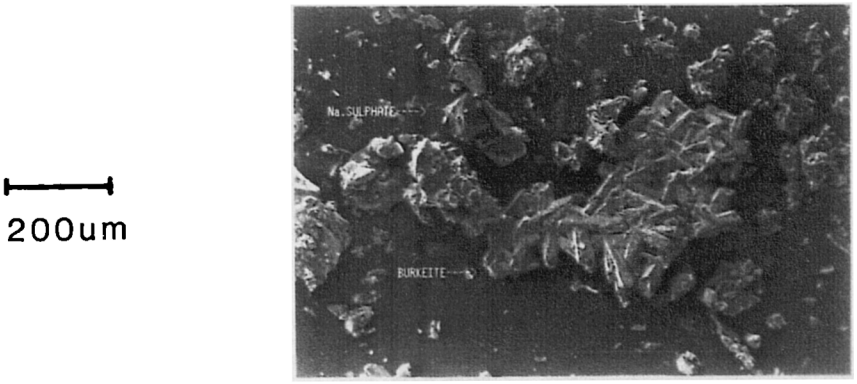

(a) 5:1 Na_2CO_3:Na_2SO_4; major phase $Na_2CO_3(Na_2SO_4)_2$, minor phase $Na_2CO_3.H_2O$. (b) 1:1 Na_2CO_3:Na_2SO_4; major phase $Na_2CO_3(Na_2SO_4)_2$, minor phase Na_2SO_4. (c) 1:4 Na_2CO_3:Na_2SO_4; major phase $Na_2CO_3(Na_2SO_4)_2$, minor phase Na_2SO_4.

Figure 5.6: Crystallisation at 90^0C of various Na_2CO_3:Na_2SO_4 ratios within the Na_2CO_3-Na_2SO_4-H_2O system

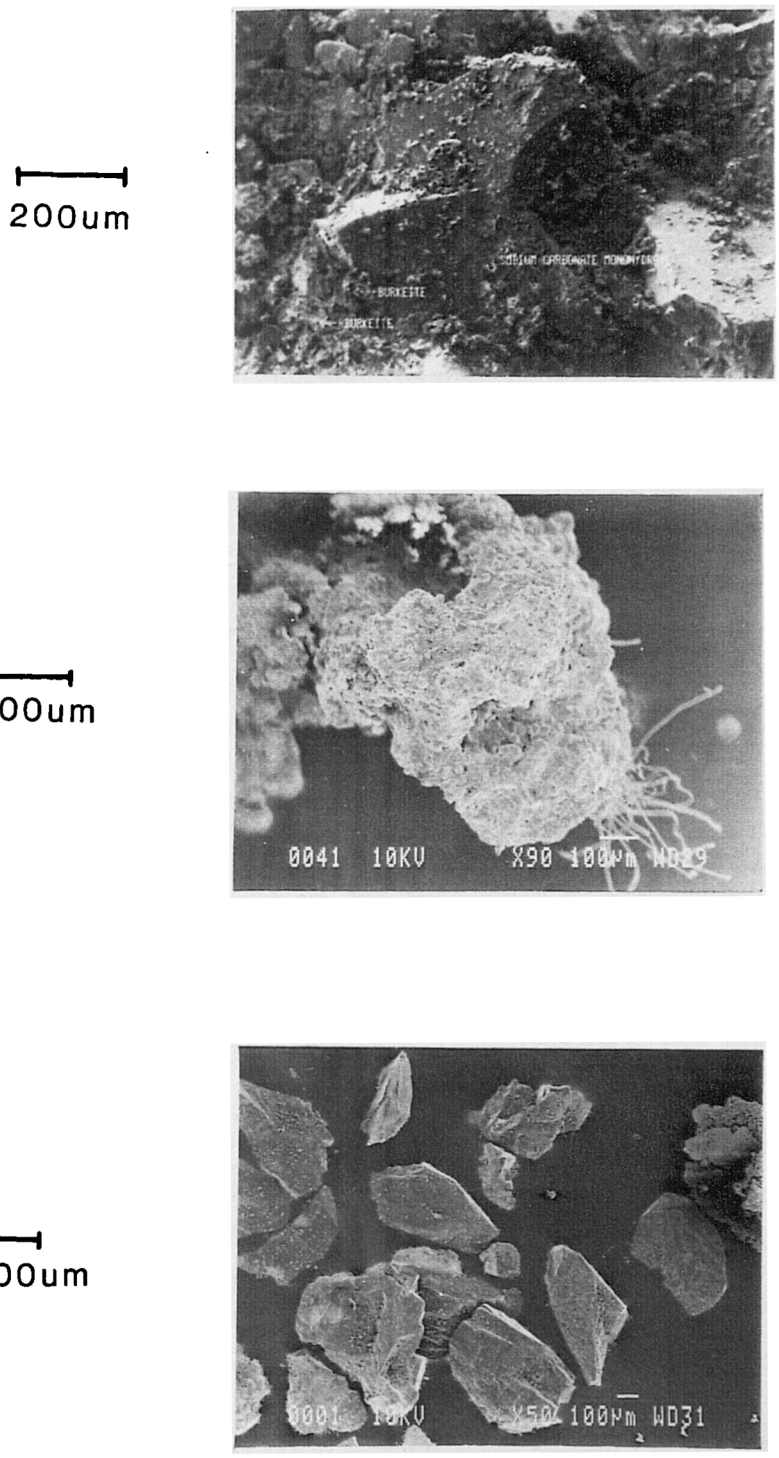

(a) 5:1 Na_2CO_3:Na_2SO_4; major phase $Na_2CO_3.H_2O$, minor phase $Na_2CO_3(Na_2SO_4)_2$ (b) 1:1 Na_2CO_3:Na_2SO_4; single phase $Na_2CO_3(Na_2SO_4)_2$ (c) 1:4 Na_2CO_3:Na_2SO_4; major phase Na_2SO_4, minor phase $Na_2CO_3.H_2O$.

Figure 5.7: Crystallisation at 50^0C of various Na_2CO_3:Na_2SO_4 ratios within the Na_2CO_3-Na_2SO_4 system

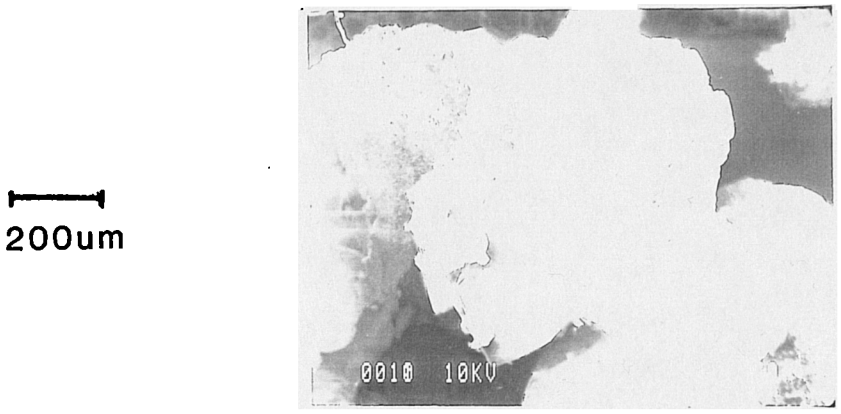

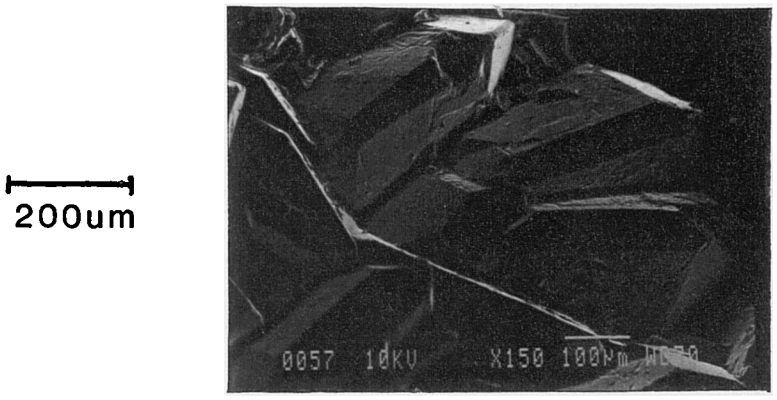

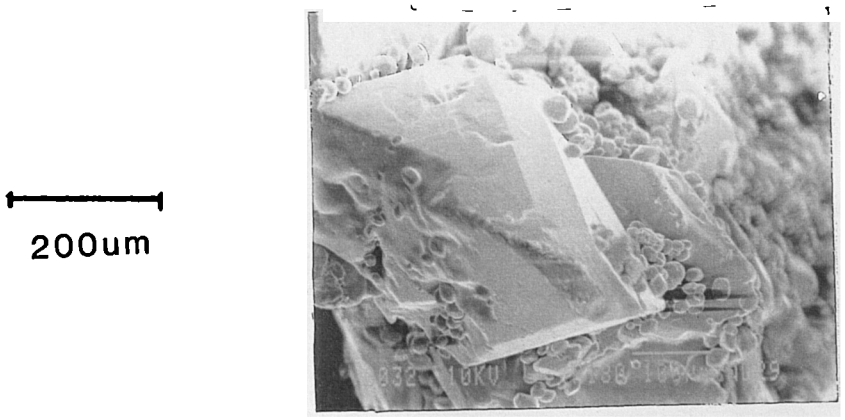

(a) 5:1 Na_2CO_3:Na_2SO_4; major phase $Na_2CO_3(Na_2SO_4)_2$, minor phase $Na_2CO_3.H_2O$, and $Na_2CO_3.7H_2O$. (b) 1:1 Na_2CO_3:Na_2SO_4; major phase $Na_2CO_3(Na_2SO_4)_2$, unidentified minor phase. (c) 1:4 Na_2CO_3:Na_2SO_4; major phase $Na_2SO_4.10H_2O$, unidentified minor phase.

Figure 5.8: Crystallisation at 30^0C of various Na_2CO_3:Na_2SO_4 ratios in the Na_2CO_3-Na_2SO_4-H_2O system

5.4 Conclusions

The Na_2CO_3-Na_2SO_4-H_2O system has been reexamined by x-ray powder diffraction, Scanning Electron Microscopy (SEM), Energy Dispersive X-ray Microanalysis (EDX) and chemical analysis. The x-ray studies were employed to determine the bulk phases present in a specimen, whereas SEM and EDX acted as complementary techniques, allowing the resolution of particles of different compositions within a specimen and allowing the identification of particles that may have otherwise been hindered by fluoroescence problems. The presence of low angle peaks in the powder diffraction spectra of burkeite ($Na_2CO_3(Na_2SO_4)_2$) indicated the formation of supercells. These low angle peaks were noted over a wide composition and temperature range, although no relationship between the existence of these supercells and solution temperature/composition could be discerned.

As the ratio of Na_2CO_3:Na_2SO_4 in the crystallising solution is decreased, the the resultant crystallised components changed from being carbonate based (e.g. $Na_2CO_3.H_2O$, $Na_2CO_3.7H_2O$ $\longrightarrow$ to burkeite ($Na_2CO_3(Na_2SO_4)_2$) $\longrightarrow$ to sulphate based (e.g. Na_2SO_4, $Na_2SO_4.10H_2O$)). As the sulphate content in the crystallising solution is increased, the degree of agglomeration observed is decreased. Burkeite seems to act as an agglomerating nucleator, extensively binding to $Na_2CO_3.H_2O$, Na_2SO_4 and $Na_2SO_4.10H_2O$. This may possibly be attributed to the disordered crystal structure of burkeite, which leads to the formation of homogeneous rather than charged surfaces that exist for the other components in the Na_2CO_3-Na_2SO_4-H_2O system.

Variation in precipitation temperature influences the size of the crystallites obtained. A high precipitation temperature implies a higher nucleation rate and the resultant crystallites obtained are relatively small. As the precipiation temperature is lowered, then the nucleation rate will be progressively lowered, which is reflected in the larger crystallites obtained.

Future studies could concentrate on further examination of the low angle peaks that imply supercell formation for burkeite ($Na_2CO_3(Na_2SO_4)_2$). These peaks should be examined to ascertain all possible supercells that may be formed by burkeite.

The crystal structure of burkeite should also be studied, to investigate whether the high degree of agglomeration exhibited by this material is due to the presence of homogeneous rather than charged surfaces, caused by the disordered crystal structure.

5.5 References

1. A.E. Dawkins; J. Chem. Soc. **121** (1922) 776-781

2. W. Caspari; J. Chem. Soc **125** (1924) 2381-2387

3. N.S. Kurnakov & S.Z. Makarov; Ann. Inst. Anal. Phys. Chem. **4/2** (1930) 307-363

4. L.S. Itkina; J. Appl. Chem., **26** (1953) 457-461

5. C. Bale & A. Pelton; CALPHAD **6** (1982) 255-278

6. B. Mehrotra; Phase Transitions **16/17** (1989) 431-436

7. A.N. Khlapova & E.E. Burvaya; Zh. Neorg. Khim., **2** (1957) 1864-1882

8. P. Pascal; Noveau Traite De Chemie Minerale, **2** (1966) 894-895

9. K.K. Wu & I.D. Brown; Acta Cryst. **B31** (1975) 890-895

10. C. Betzel, W. Saenger & D. Loewus; Acta Cryst. **B38** (1982) 2802-2804

11. T. Taga; Acta Cryst. **B25** (1969) 2656-2660

12. A.G. Nord; Acta Chemica Scandinavia **27** (1973) 814-822

13. H.A. Levy & G.C. Lisensky; Acta Cryst **B34** (1978) 3502-3510

14. G. Giuseppetti, F. Mazzi & C. Tadini; Neues. Jahrb. Mineral. Monatsch **5** (1988) 203-21

15. J. M. Visser; J. Appl. Cryst. **2** (1969) 89-95

16. I. Tucker; COMPARE, Unilever Research Port Sunlight Laboratory

17. J. Goldstein; "Scanning Electron And X-ray Microanalysis: A Text For Biologists, Materials Scientists And Geologists" (1981) London, New York Plenum

18. W.F. Foshag; Amer. Miner. **20** (1935) 50-56

Chapter 6

Studies Of The Nucleation Kinetics Of Some Carbonates, Phosphates And Sulphates

Contents

6.1 Introduction

In chapter two the relationships between supersaturation, nucleation and resultant crystal growth were examined. This chapter will examine in detail nucleation kinetics for a variety of inorganic systems using different detection techniques to register the onset of nucleation. Previous nucleation kinetic studies have employed a variety of detection techniques, e.g. visual [1,2], differential scanning calorimetry [3], light transmittance [3,4], conductivity [5] and actual counting of the number of crystallising particles [2]. In a study of the crystallisation of n-alkane systems Stewart [3] concluded that turbidometry was the most sensitive technique for the detection of nucleation. A large spread in results obtained under the same experimental conditions were also noted in this study; a feature observed in many different systems using different detection techniques. Thus experiments must be repeated under identical conditions for complete impartiality and for valid comparison and discussion of the results obtained. An automated crystallisation instrument was designed by Gerson [4], that allowed the computer controlled repetition of experiments under identical conditions to be conducted, with the onset of nucleation detected by turbidometry measurements. This instrument has been further extended by the inclusion of conductivity measurements, thus allowing each detection system to be compared and contrasted for the systems studied.

This chapter presents an examination of the crystallisation kinetics of some carbonates, sulphates and phosphates. The initial section describes in detail the crystallisation cell employed in all studies and the methodologies for determining saturation curves, metastable zonewidths and interfacial energies. A study was conducted of the crystallisation kinetics of two model systems, potash alum ($AlK(SO_4)_2.12H_2O$) and ammonium dihydrogen orthophosphate ($NH_2H_2PO_4$). The influences of preheating time and temperature on the determined crystallisation parameters are discussed and solution turbidometry, conductivity and temperature are compared and contrasted as methods of detecting nucleation.

The final section examines the crystallisation kinetics of sodium sulphate decahydrate ($Na_2SO_4.10H_2O$) and sodium carbonate decahydrate

($Na_2CO_3.10H_2O$), as determined by this instrument. A study of the influence of carbonate on the crystallisation of $Na_2SO_4.10H_2O$ is discussed; a solution containing a 50:50 molar ratio of Na_2SO_4:Na_2CO_3 crystallised and the resultant interfacial energy compared and contrasted to determined interfacial energies for $Na_2SO_4.10H_2O$ and $Na_2CO_3.10H_2O$.

6.2 Methodology

The basic methodology that was employed for any system to be studied was the initial determination of the saturation curve and the maximum metastable zonewidth by the slow cooling and heating of a solution at three different concentrations. Fast cooling of the solution into the metastable zonewidth provides information on induction times, nucleation rates and interfacial energies. During the course of this study, certain points became apparent. The experimental spread of results varied considerably, depending on factors such as the positioning of the probes in solution and the number of probes present in the solution. Hence the results derived cannot be taken as absolute values; the kinetic parameters derived can only be employed in comparative studies.

6.2.1 Instrumentation

Schematics of the automated system and the crystallisation cell that was employed throughout all the studies are shown in figure 6.1 (a) and (b) respectively. The basic objectives of the instrumentation is to induce supersaturation and resultant nucleation by controlled temperature lowering, with crystallisation observed by changes in solution transmittance and conductivity. The system to be studied is prepared in the form of a solution (approx. $80cm^3$) and placed in a glass cylinder containing a plastic magnetic flea. Each system studied was doubly recrystallised and the resultant solution to be studied prefiltered. Three probes were inserted into the solution; a platinum resistance thermometer, a Sybron Brinkman stainless steel fibre optic turbidometric probe and an EDT A5002 platinum plate polymer dip conductivity probe. The turbidometric probe functions by light transmittance through a 2cm path length in the

solution, employing 180^0 light scattering by reflectance via a mirror. A reduction in light transmittance is noted with the formation of nuclei in the supersaturated solution, which is observed on a Brinkman PC700 colorimeter. The same principles apply to conductivity: a drop in solution conductivity is noted on an EDT Alpha 800 conductivity meter due to the formation of nuclei in the supersaturated solution. The change in resistance in the platinum resistance thermometer due to temperature changes in the solution can be interpreted as a difference in voltage. Voltages corresponding to the detection and temperature readings are converted to digital signals via an OASIS MADA 12 bit analogue to digital interface and sent to a BBC-B microcomputer for subsequent processing. The BBC microcomputer provides temperature control for the system, controlling the temperature of a HAAKE F3 water bath into which the glass cylinder has been placed, via the digital to analogue converter. The temperature of the solution to be studied is assumed to be equivalent to that of the water bath. Stirring of the solution is provided by the magnetic flea, which is in turn rotated at constant speed by a turbo-jet magnetic stirrer (approx. 180 rpm); controlled by a water pump within the bath. The conductivity probe is precalibrated for a standard solution of conductivity $2000\mu Scm^{-1}$. Accuracy of conductivity measurement is $\pm$ 0.5% for a measurement range of (0-200,000)μScm^{-1}. The turbidometric setting for a solution is arbitrary and is not absolute, a solution with a measured transmittance of 100% is not totally transparent, and 0% does not represent total opacity. Similarly, accuracy of the turbidometric probe is $\pm$ 0.4% for a measurement range of (0-100)% The glass cylinder, magnetic flea, and the probes that were inserted into solution were washed in doubly distilled water, dried and inspected for obvious dust contamination to try and minimise the possibility of heterogeneous nucleation, although realistically this is almost impossible. It has been estimated that a solution may contain up to 10^8 heterogeneous particles per cm^3 of solution [6], which may be reduced to $< 10^3$ particles upon careful filtration. Thus, although the experiments determined are based on the assumption that homogeneous nucleation occurs, it is almost certain that heteronuclei will be present and will influence the nucleation mechanisms. At the beginning of each cycle the temperature of the solution is raised to a point so that any crystallites of the material that are present are completely dissolved. Con-

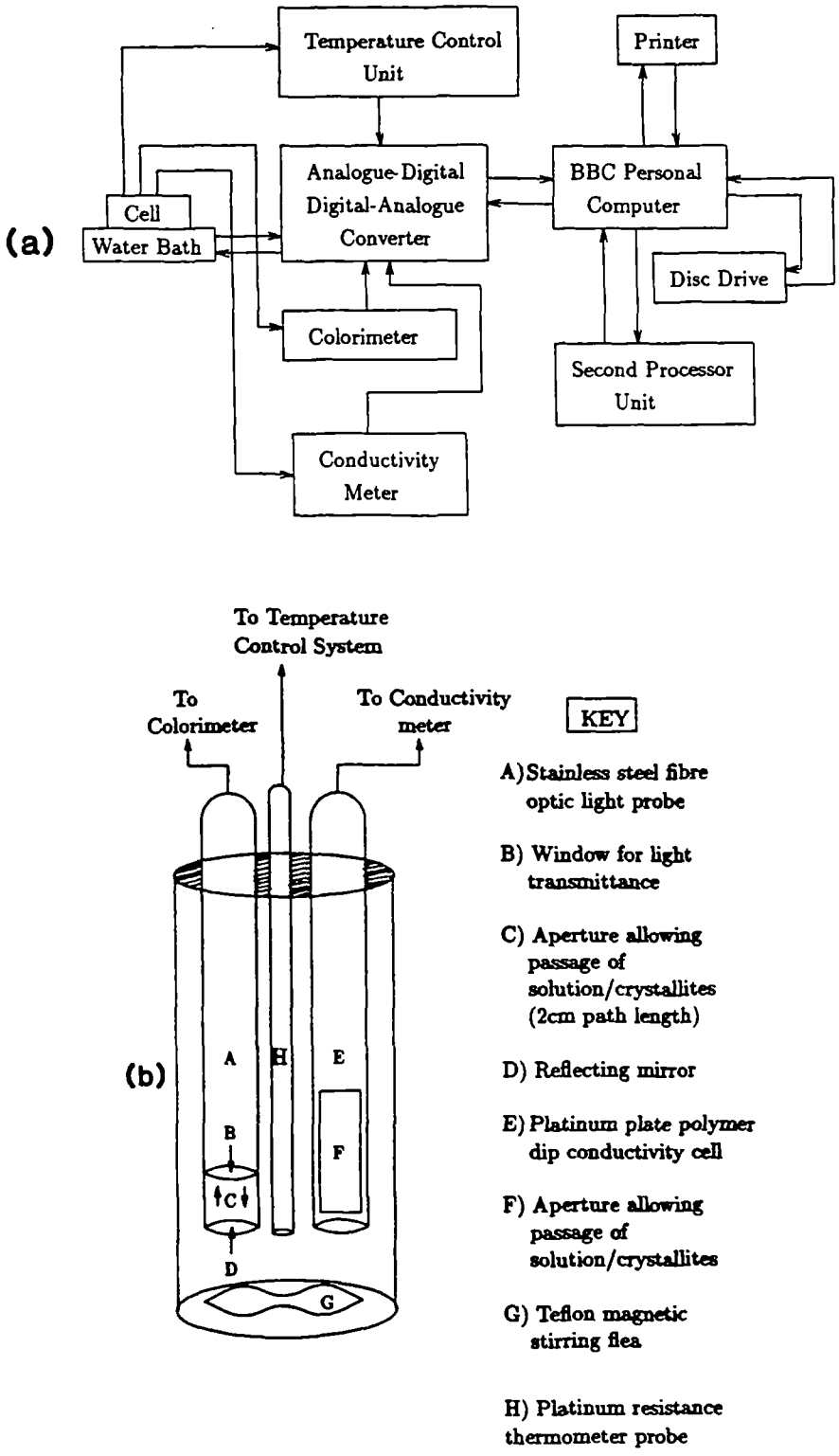

Figure 6.1: Schematic of a) the instrumentation employed for study of nucleation kinetics, b) the crystallisation cell as employed in the automated crystallisation cell.

ductivity and turbidometric readings at this point are assumed to be for a "clear" solution. The temperature and the time of heating is dependent on the system to be studied. During an experiment, readings of the temperature, turbidity and conductivity were taken approximately every 10 seconds. At each reading, the signals for the temperature, turbidity and conductivity were measured and averaged over a period of 10 seconds to reduce the effects of electronic noise. Crystallisation is said to have occurred when the observed solution conductivity and transmittance readings drop by certain predefined factors from those recorded for a clear solution. Similarly, when a crystallised solution is heated, dissolution is said to have occurred when the solution transmittance and conductivity are raised to within certain predefined factors from those recorded for a clear solution.

6.2.2 Saturation Curve And Maximum Metastable Zone-width Determination For A System

Essentially, the experiment comprises of the slow cooling and heating of a system. The system is first preheated for a period of time to a certain temperature above the saturation temperature, in order to remove any crystallites and possible solution structure present. Upon controlled slow cooling, crystallisation will occur and the crystallisation temperature (T_{cryst}) may be determined. Crystallisation is defined as a drop in turbidity and conductivity with respect to that recorded for a clear solution. Upon crystallisation the solution is cooled further to ensure complete crystallisation. Slow heating at the same rate is then applied until dissolution occurs, the temperature of dissolution (T_{diss}) being defined as the temperature where the transmittance and conductivity of the solution come within a percentage of that recorded for a clear solution. The saturation temperature (T_{sat}) may be defined as the point where dissolution occurs at an infinitely slow rate of heating and is equivalent to the "y" axis intercept of a plot of dissolution temperatures versus heating rate.

The metastable zone width is defined as the difference between the saturation temperature and the crystallisation temperature, i.e. (T_{sat}-T_{cryst}). Idealized examples are shown of controlled slow cooling with resultant crystallisation (figure 6.2)

and slow heating with resultant dissolution (figure 6.3) recorded by turbidometry and conductivity.

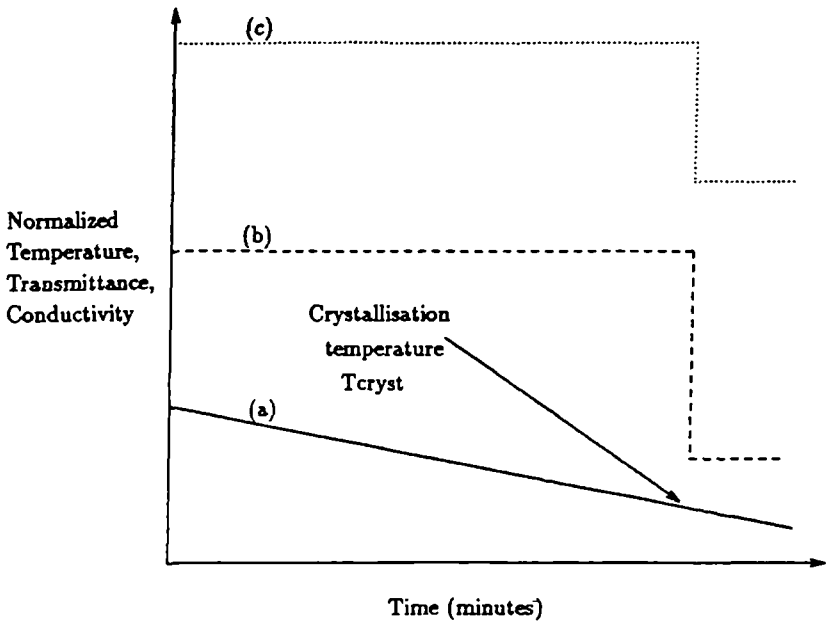

Figure 6.2: Idealized slow cooling with resultant crystallisation.

Obviously different concentrations of solute will have correspondingly different saturation temperatures. A mininum of three different saturation temperatures are required to define the saturation curve. Using the Van Hoff isotherm the saturation curve may be defined by:

$$ln(x) = \Delta S_d/R - \Delta H_d/RT \tag{6.1}$$

where "ΔS_d" is the entropy of dissolution, "ΔH_d", the enthalpy of dissolution, "T" the saturation temperature and "x" the mole fraction of solute in solution. This equation may be also used to assess the ideality of solution behaviour.

The order of reaction of the nucleation process, e.g. ("m" in equation 2.26) may be obtained from a plot of the logarithm of cooling rate versus the logarithm of the metastable zone width.

In each case a linear regression method was used to derive the lines of best fit for the determination of saturation temperatures and orders of reaction.

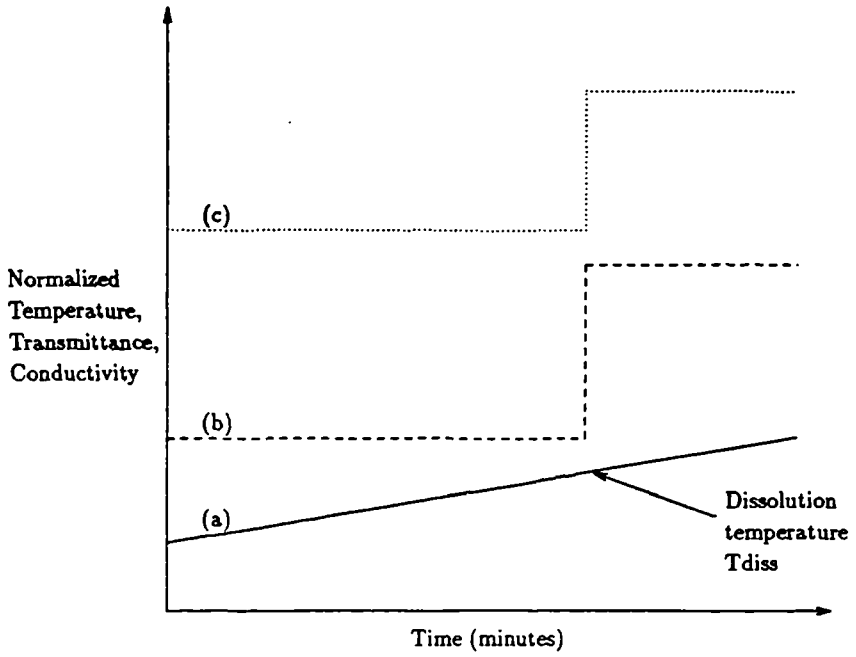

Figure 6.3: Idealized slow heating with resultant dissolution.

6.2.3 Interfacial Energy Determination For A System

If a solution is quickly cooled to within the metastable zone, a period of time will elapse before the onset of nucleation, which is known as the induction time. The rate of change of solution transmittance or conductivity with respect to time may be measured, however this cannot be equated to the classic definition of nucleation rate which is equivalent to the number of particles produced with respect to time, per unit volume. Further conversion factors would have to be introduced in each case in order to equate the rate of change of solution transmittance and conductivity to the nucleation rate. It is envisaged that future studies will enable the determination of interfacial energies from measurements of the rate of change of solution transmittance and conductivity.

For a system, the solution is preheated a given amount above the saturation temperature for a period of time, until all nuclei and possible solution structure are removed. The solution is then cooled at the fastest controlled cooling rate possible for the water bath in question. Since a variety of water baths were used during these studies, a cooling rate of 0.35°C/min was employed, this rate being within the capabilities of all baths employed. This deviates from theory in which an instantaneous

temperature drop to the desired level within the metastable zone occurs, although this is in practice impossible. The point at which crystallisation occurs is noted by a predefined drop in both the turbidity and conductivity of the solution. The crystallisation temperature "T_{cryst}" is defined as the temperature at which a predefined drop in solution conductivity and transmittance occurs. The induction time "τ" is the period of time elapsed before nucleation occurs. Upon crystallisation the solution transmittance and conductivity are recorded at twenty second intervals, this representing the mininum repeat time for recording of solution temperature, transmittance and conductivity. The rate of change of solution transmittance and conductivity (J) is recorded within the initial twenty second period.

From equation 2.20 a plot of $\ln(\tau)$ versus $T^{-3}\ \ln(S)^{-2}$ will yield a straight line of slope (γ^3constant), from which the interfacial energy "γ" may be determined. A plot of $\ln(J)$ versus $T^{-3}\ln(S)^{-2}$ in this case, will yield a parameter related to (γ^3constant) as previously explained, thus a parameter related to the actual interfacial energy "γ" is obtained. An idealized example of a crash cool is shown in figure 6.4.

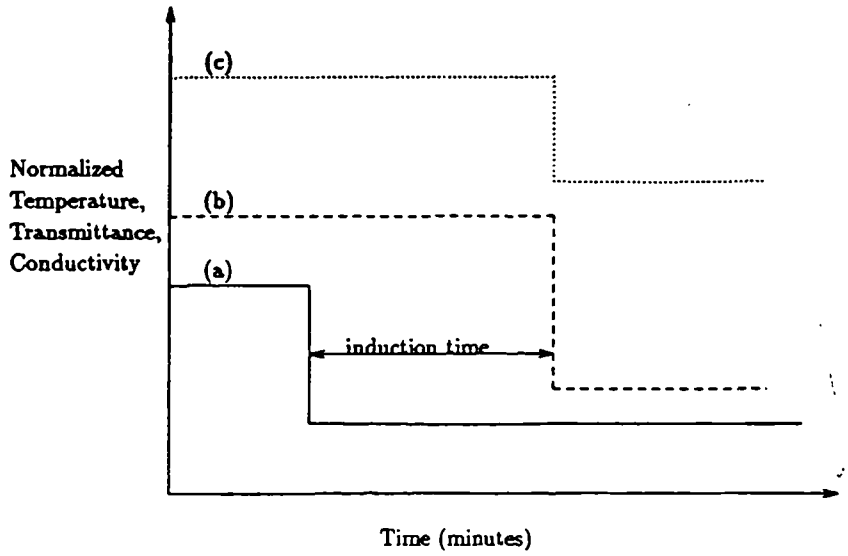

Figure 6.4: Idealized example of a crash cool as recorded by conductivity and turbidometry, highlighting the induction period before the onset of nucleation.

6.3 Studies Of Model Systems

6.3.1 Potash Alum, $AlK(SO_4)_2.12H_2O$

6.3.1.1 Saturation Curve And Metastable Zonewidth Determination

Potash alum has been well studied over the years and has advantageous crystallisation characteristics, e.g. the formation of large, discrete crystals that do not agglomerate readily, that are easily grown from solution. A solubility curve [7] for potash alum is shown in figure 6.5. The effects of the magnitude and time of preheating on the

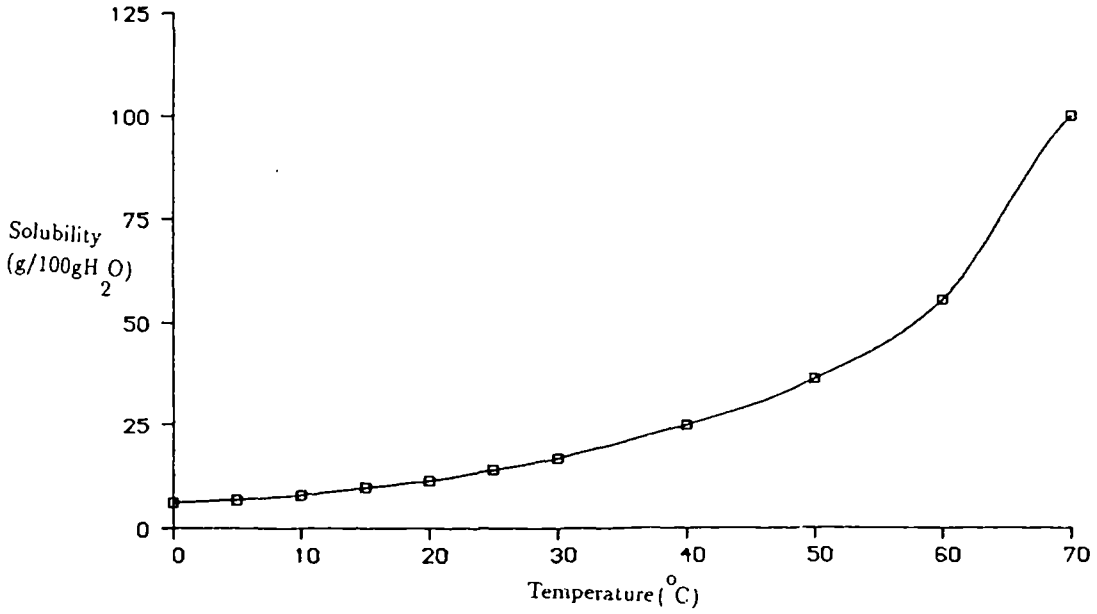

Figure 6.5: Solubility curve for potash alum [7].

determination of a saturation temperature for a particular solute concentration were initially investigated. A solution of potash alum was prepared, using a concentration of 12g $AlK(SO_4)_2.12H_2O/100gH_2O$, this corresponding to an approximate saturation temperature of 21^0C. Differences of 5% and $1\mu Scm^{-1}$ in turbidometry and conductivity respectively from the values recorded for a clear solution were chosen to represent the detection parameters at which crystallisation and dissolution occur. These parameters seemed to represent the mininum values that could be employed for this particular system, as attempts employing smaller detection parameters lead to erroneous results due to the effects of electronic noise for this system. The solution was

preheated for 60 minutes and 120 minutes at 10^0C and 20^0C respectively, above the approximate saturation temperature, before a slow cooling/heating cycle was initiated. The cooling/heating rates employed were 0.30^0C/min, 0.25^0C/min, 0.20^0C/min and 0.15^0C/min, with 4 repeats carried at each cooling rate. The resultant precipitation and dissolution temperatures ($\pm$ standard deviations) obtained at each rate for the experimental conditions studied are shown in Tables 6.1 and 6.3. A schematic of the typical crystallisation/dissolution processes are shown in figures 6.6 and 6.7.

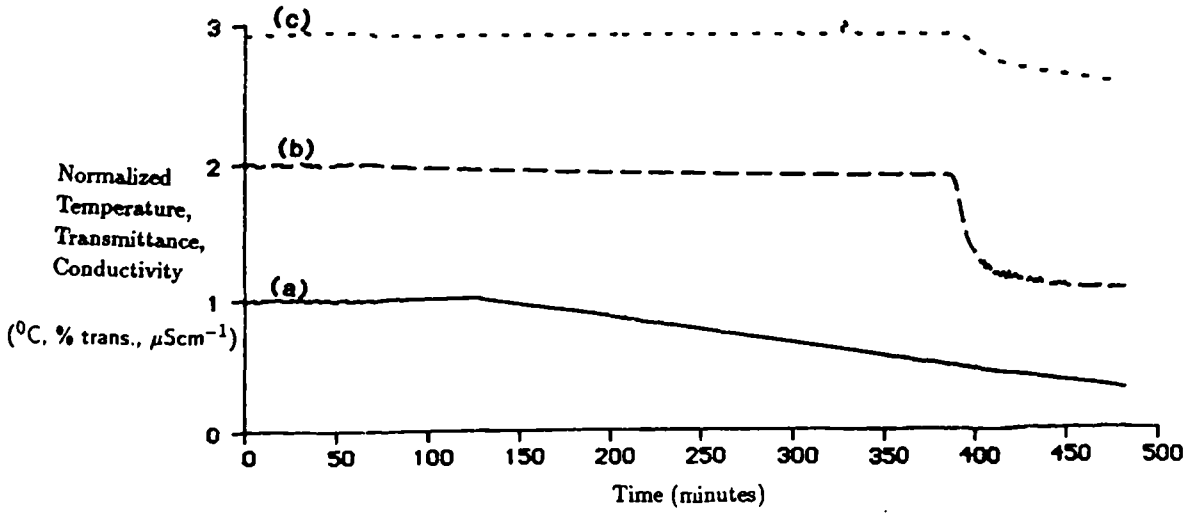

a) temperature b) transmittance c) conductivity

Figure 6.6: Schematic of crystallisation as detected by turbidometry and conductivity that occurs during slow cooling of $AlK(SO_4)_2.12H_2O$.

What is apparent in figure 6.6 is the sudden drop in turbidity (approx. 60%) and conductivity (dropping from 35.04μScm^{-1} to 18μScm^{-1})) upon crystallisation. No deviation in the rate of temperature change was noted when crystallisation occurred, implying that monitoring temperature as a means of detecting crystallisation is inappropriate for $AlK(SO_4)_2.12H_2O$, since it is apparent that the heat of crystallisation is not great enough to significantly alter the temperature of the system.

As explained previously, the "y" axis intercept of a plot of dissolution temperature versus heating rate yields the saturation temperature for a given solute concentration.

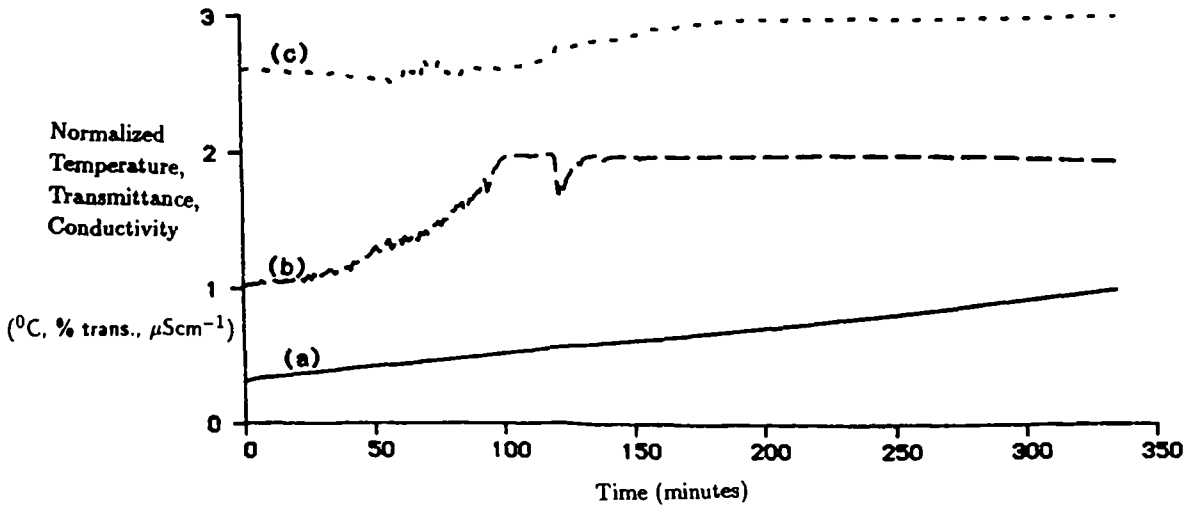

a) temperature b) transmittance c) conductivity

Figure 6.7: Schematic of dissolution as detected by turbidometry and conductivity that occurs during slow heating of $AlK(SO_4)_2.12H_2O$.

Plots of dissolution temperatures versus heating rates as determined by each detection technique are shown in figures 6.8 and 6.9. The determined saturation temperatures ($\pm$ standard deviation) for each technique, the maximum metastable zonewidth and the orders of reaction ($\pm$ standard deviation) as calculated from equation 2.26 are highlighted in Tables 6.2 and 6.4.

Over-temperature Employed (^{0}C)	Over-heating Time (mins)	Heating/ cooling Rate (^{0}C/min)	Average Precipitation Temperature (^{0}C)	Average Dissolution Temperature (^{0}C)
10	60	0.30	$19.50_{10.75}$	$20.12_{0.23}$
10	60	0.25	$16.18_{14.08}$	$20.11_{0.07}$
10	60	0.20	$20.98_{9.35}$	$20.04_{0.06}$
10	60	0.15	$17.14_{13.2}$	$20.01_{0.12}$
10	120	0.30	$11.74_{0.38}$	$21.43_{0.06}$
10	120	0.25	$12.58_{1.01}$	$21.32_{0.12}$
10	120	0.20	$13.35_{0.68}$	$21.48_{0.18}$
10	120	0.15	$14.10_{1.07}$	$21.31_{0.12}$
20	60	0.30	$11.38_{1.66}$	$20.98_{0.22}$
20	60	0.25	$18.70_{21.46}$	$20.48_{0.25}$
20	60	0.20	$18.82_{0.74}$	$20.62_{0.11}$
20	60	0.15	$13.31_{0.30}$	$20.43_{0.13}$
20	120	0.30	$12.62_{3.32}$	$22.03_{0.12}$
20	120	0.25	$13.75_{0.65}$	$21.94_{0.08}$
20	120	0.20	$14.34_{0.31}$	$21.80_{0.06}$
20	120	0.15	$14.78_{0.54}$	$21.69_{0.06}$

Table 6.1: Determined crystallisation data based on turbidometric measurements for $AlK(SO_4)_2.12H_2O$.

Over-Temperature Employed (^0C)	Over-Temperature Time (mins)	Saturation Temperature Obtained (^0C)	Max. Metastable Zone Width (^0C)	Order Of Reaction
10	60	$19.88_{0.35}$	12.15	-
10	120	$21.30_{0.35}$	10.42	$1.82_{0.19}$
20	60	$19.95_{0.62}$	12.98	-
20	120	$21.34_{0.20}$	12.74	$1.26_{0.22}$

Table 6.2: Saturation data obtained using different initial overheating conditions, employing turbidity as the crystallisation detection technique for $AlK(SO_4)_2.12H_2O$.

Over-temperature Employed (^{0}C)	Over-temperature Time (mins)	Heating/ cooling Rate (^{0}C/min)	Average Precipitation Temperature (^{0}C)	Average Dissolution Temperature (^{0}C)
10	60	0.30	$9.24_{2.15}$	$16.96_{0.56}$
10	60	0.25	$10.26_{0.41}$	$17.03_{0.07}$
10	60	0.20	$11.01_{0.48}$	$17.08_{0.31}$
10	60	0.15	$11.74_{0.43}$	$17.00_{0.10}$
10	120	0.30	$24.02_{12.06}$	$13.39_{4.56}$
10	120	0.25	$12.31_{0.22}$	$18.40_{0.16}$
10	120	0.20	$21.52_{8.79}$	$18.15_{3.96}$
10	120	0.15	$17.93_{4.41}$	$17.14_{1.63}$
20	60	0.30	$10.53_{0.42}$	$16.48_{0.17}$
20	60	0.25	$10.36_{0.51}$	$16.53_{0.70}$
20	60	0.20	$11.57_{0.48}$	$16.98_{0.34}$
20	60	0.15	$12.12_{0.19}$	$16.87_{0.27}$
20	120	0.30	$10.25_{0.60}$	$16.78_{0.06}$
20	120	0.25	$11.09_{0.37}$	$16.95_{0.15}$
20	120	0.20	$11.88_{0.19}$	$17.11_{0.07}$
20	120	0.15	$12.66_{0.50}$	$17.22_{0.12}$

Table 6.3: Determined crystallisation data based on conductivity measurements for $AlK(SO_4)_2.12H_2O$.

Over-Temperature Employed (^{0}C)	Over-Temperature Time (mins)	Saturation Temperature Obtained (^{0}C)	Max. Metastable Zone Width (^{0}C)	Order Of Reaction
10	60	$17.10_{0.70}$	9.89	$1.36_{0.16}$
10	120	$21.73_{10.44}$	9.77	-
20	60	$17.44_{0.90}$	6.95	$1.71_{0.25}$
20	120	$17.69_{0.33}$	7.14	$1.70_{0.12}$

Table 6.4: Saturation data obtained using different initial overheating conditions, employing conductivity as the crystallisation detection technique for $AlK(SO_4)_2.12H_2O$.

It is immediately noted that the determined saturation temperatures obtained using turbidometry as the method of detecting crystallisation are higher and show better correlation to the actual saturation temperature of 21^{0}C, than the determined saturation temperatures obtained using conductivity as the method of detecting crystallisation. There is a large spread in the precipitation temperatures obtained (tables 6.2 and 6.4), which can be attributed to the presence of heteronuclei in the solution, which cannot be totally eradicated. These nuclei will act as centres for nucleation, significantly influencing crystallisation characteristics, e.g. the temperature of crystallisation and the metastable zonewidth. This can be seen in the extent of the variation in standard deviations of the precipitation temperatures and the metastable zonewidths. The heteronuclei do not significantly influence the dissolution process, as can be seen from the small standard deviations in the dissolution temperatures from each detection technique. The heterogeneous particles are trapped within the crystal during crystallisation and are thus unable to exert any great influence upon dissolution. Increasing the length of preheating time significantly reduces the degree of experimental scatter in the determined precipitation temperatures using both detection methods. Visually it was noted that during an experimental cooling/heating cycle, turbidometry provided a more sensitive technique than conductivity to detect crystallisation and dissolution. In general, the greater the preheating time, the lower

the standard deviation of the resultant saturation temperature; these results being improved if a greater preheating temperature is also employed. The implication is that employing the longer preheating time in combination with the greater preheating leads to the smallest experimental scatter in the resultant data. There is a significant variation in the determined saturation temperatures using turbidometry with preheating time that is not observed to the same extent in the data determined by conductivity. Orders of reaction (equation 2.26) based on turbidometric measurements for an preheating time of 60 minutes at each overtemperature could not be obtained, due to erroneous determined crystallisation temperatures that implied the existence of negative metastable zonewidths; a feature also observed for measurements based on conductivity employing an preheating of 10^0C for 120 minutes preheating time. A visual inspection of the solution during these cycles did not reveal the presence of any nuclei. A possible reason for this data trend is the presence of a degree of structuring within the solution, which the longer preheating time disrupts, creating a completely homogeneous solution. Another possible reason is the formation of very small clusters of $AlK(SO_4)_2.12H_2O$ nuclei which can be detected by the more sensitive turbidometric technique and not by the less sensitive conductivity technique or by visual detection.

Thus it may be concluded that increasing the degree of preheating and time of preheating leads to a decrease in the degree of experimental scatter. It was noted that determined saturation data based on turbidity rather than conductivity measurements were more comparable to literature saturation data. Obviously the correlation between the determined saturation temperatures and the literature temperatures is dependent on what detection values are assigned to the turbidometric and conductivity measurements to detect crystallisation and dissolution. The preheating parameters of 120 minutes preheating time and 20^0C overtemperature were determined to be the parameters at which the least experimental scatter of data occurred. These parameters were employed in all subsequent studies.

A saturation curve was determined for three different concentrations of potash alum, using both turbidometric and conductivity measurements. The resultant determined saturation temperatures, maximum metastable zonewidths and orders of

reaction (from equation 2.26) are highlighted in tables 6.5 and 6.6. The determined dissolution temperatures are plotted versus heating rate for each detection technique in figures 6.8 and 6.9. Better correlation is observed between saturation temperatures determined from turbidometric rather than conductivity measurements, and saturation temperatures determined in previous studies. There are significant variations in the determined maximum metastable zonewidths; in general, the determined metastable zonewidths based on turbidometric measurements are larger than the corresponding conductivity based measurements. This would imply that conductivity is more sensitive to the onset of nucleation than turbidometry. However it was visually observed during a slow cooling/heating cycle that turbidometry was more sensitive to the onset of nucleation than conductivity. Thus the choice of detection limit is the factor deciding the validity of the determined maximum metastable zonewidths and saturation temperatures. Since the saturation temperatures determined from turbidometry measurements show better correlation to previous studies than those determined from conductivity measurements, the implication is that turbidometry is more sensitive to the processes of crystallisation/dissolution and therefore the determined metastable zonewidths for turbidometric measurements are more likely to show better correlation to the actual maximum metastable zonewidth than measurements based on conductivity. There are major difficulties in obtaining any fundamental information from the determined orders of reaction, since this term is dependent on crystal growth kinetics as well as nucleation [2]. The orders of reaction determined in this study are in the range (1.11-3.49) and are in reasonable agreement with a previous study [2], which reported values ranging from 2.6-3.2, depending on the detection technique employed.

By employing the Van Hoff isotherm (equation 5.21), enthalpies and entropies relating to dissolution based on each detection technique may be obtained. A plot of ln (mole fraction of solute in solution) versus 1/(saturation temperature) for the data based on turbidometric measurements, conductivity measurements and literature data is shown in figure 6.10. From this, the determined enthalpies and entropies of dissolution are compared and contrasted to calculated enthalpies and entropies of dissolution based on previous studies in table 6.7.

The high degree of linearity of the three plots in figure 6.10 is indicative of the high degree of ideal solution behaviour. For the detection values assigned, the determined entropies and enthalpies of dissolution are in reasonable agreement with those determined from literature saturation data, with the measurements based on turbidometric measurements showing slightly better correlation to the literature data than the measurements based on conductivity.

g $AlK(SO_4)_2.12H_2O$ per 100g H_2O	Saturation Temperature (K) [7]	Saturation Temperature (^0C)	Max. M.S.Z.W. (^0C)	Order of Reaction
9.5	15	$14.22_{2.83}$	10.69	$1.64_{0.22}$
11.2	20	$20.34_{0.20}$	12.74	$1.26_{0.22}$
14.0	25	$27.30_{0.41}$	8.58	$3.49_{0.35}$

Table 6.5: Comparison of determined saturation temperatures, maximum metastable zonewidths and orders of reaction based on turbidometry to previous studies.

g $AlK(SO_4)_2.12H_2O$ per 100g H_2O	Saturation Temperature (^0C) [7]	Saturation Temperature (^0C)	Max. M.S.Z.W. (^0C)	Order of Reaction
9.5	15	$10.29_{0.56}$	8.04	$1.11_{0.18}$
11.2	20	$17.69_{0.33}$	7.14	$1.70_{0.12}$
14.0	25	$23.68_{0.37}$	6.54	$1.37_{0.11}$

Table 6.6: Comparison of determined saturation temperatures, maximum metastable zonewidths and orders of reaction based on conductivity to previous studies.

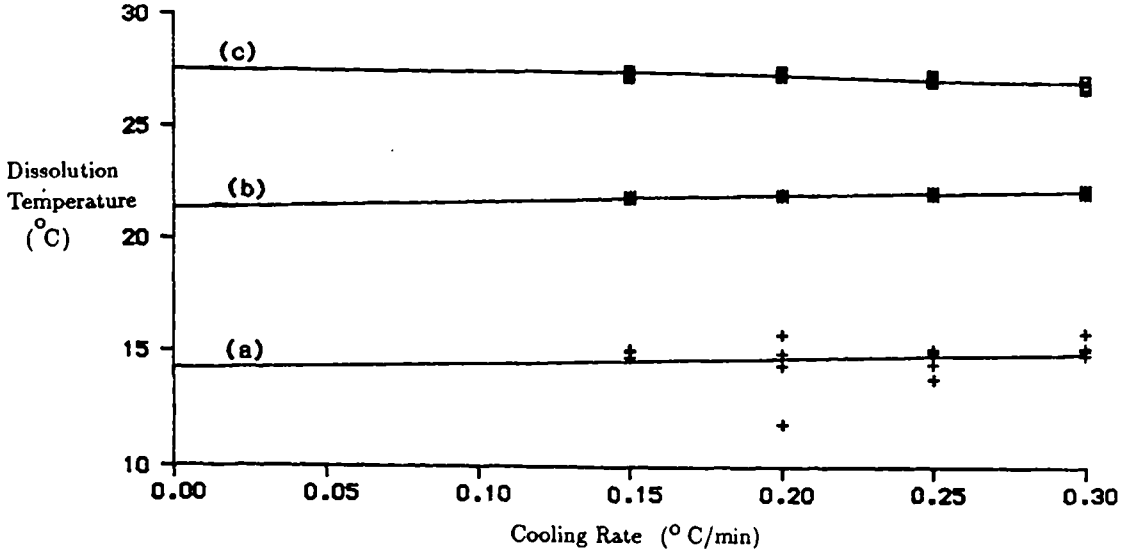

Correlation coefficients: a) 76 %, b) 90 %, c) 15 %

Figure 6.8: Plot of determined dissolution temperatures (based on turbidometric measurements) versus heating rate at a) 9.5g, b) 11.2g, c) 14.0g $AlK(SO_4)_2.12H_2O$/100g H_2O repectively.

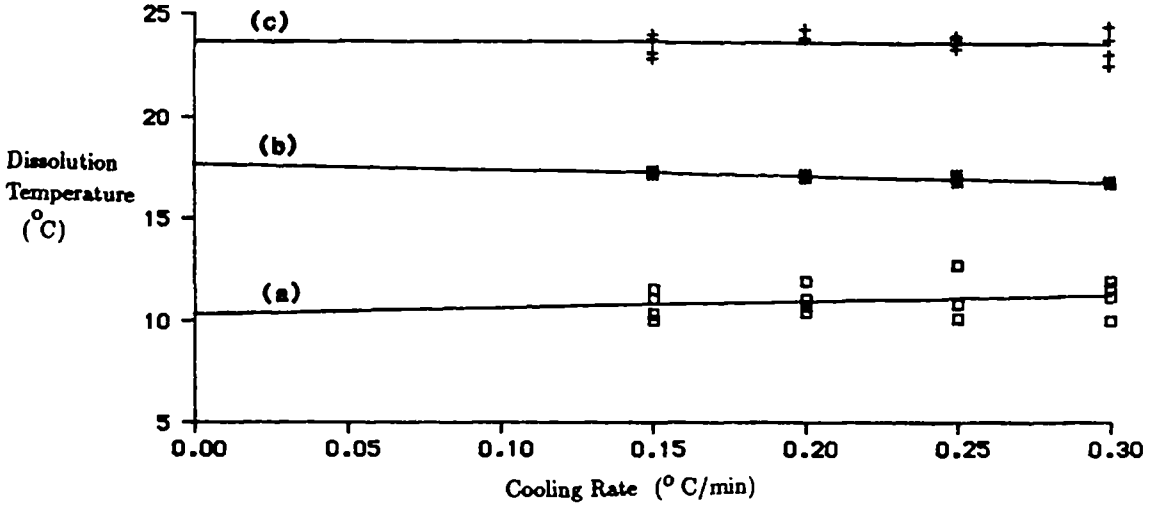

Correlation coefficients: a) 24 %, b) 85 %, c) 10 %

Figure 6.9: Plot of determined dissolution temperatures (based on conductivity measurements) versus heating rate at a) 9.5g, b) 11.2g, c)14.0g $AlK(SO_4)_2.12H_2O$/100g H_2O respectively.

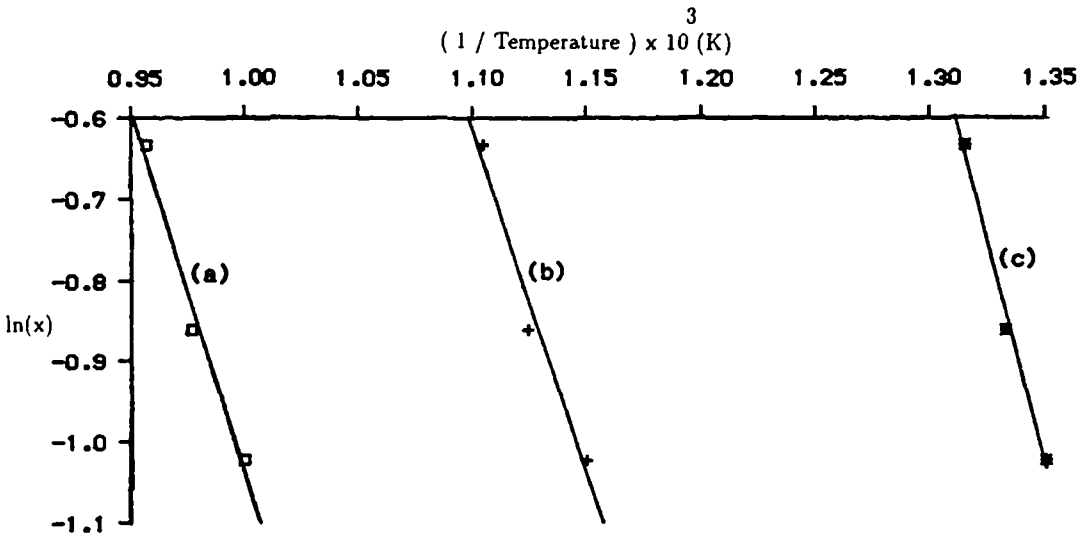

Correlation coefficients: a) 99 %, b) 99 %, c) 99 %

Figure 6.10: Plot of ln(mole fraction) versus 1/saturation temperature a) based on turbidometric measurements, b) based on conductivity measurements, c) based on literature data.

Type	Enthalpy of Dissolution (J/mol*K)	Entropy of Dissolution (J/mol)	Correlation Coefficient
Literature	$2.77x10^4$	$8.7x10^1$	-0.99
Turbidity	$2.11x10^4$	$6.5x10^1$	-0.99
Conductivity	$2.00x10^4$	$6.2x10^1$	-0.98

Table 6.7: Comparison of predicted enthalpies and entropies of dissolution to observed values.

6.3.1.2 Interfacial Energy Determination

Crash cooling a solution enables the determination of induction times and rates of change of solution transmittance and conductivity, thus allowing calculation of the interfacial energy (equation 2.20). A typical crash cool is shown in figure 6.11. A crash cool was carried out at each concentration of potash alum (as defined in tables 6.5 and 6.6). From the resultant induction times, interfacial energies may be estimated. The measured rates of change of solution transmittance will yield a parameter related to the interfacial energy. Some typical measurements of induction times and nucleation rates recorded are shown in table 6.8. As previously defined, "τ" is the recorded induction time, "J^t" and "J^c" are the recorded rates of change of solution trasnmittance and conductivity respectively. The parameter "ΔT" is the degree of undercooling and is equivalent to ($T_{saturation-crystallisation}$). The superscript "t" refers to turbidometric measurements, the superscript "c" refers to conductivity measurements.

Upon examination of table 6.8, the trend of increasing undercooling leads to a decrease in induction time and an increase in the rates of change of solution transmittance and conductivity is clearly observed. Much higher undercoolings would seem to be obtained during crash cool experiments using turbidometry than conductivity; however the determined saturation temperature based on conductivity at this particular concentration (23.66^0C) is significantly lower than that determined from

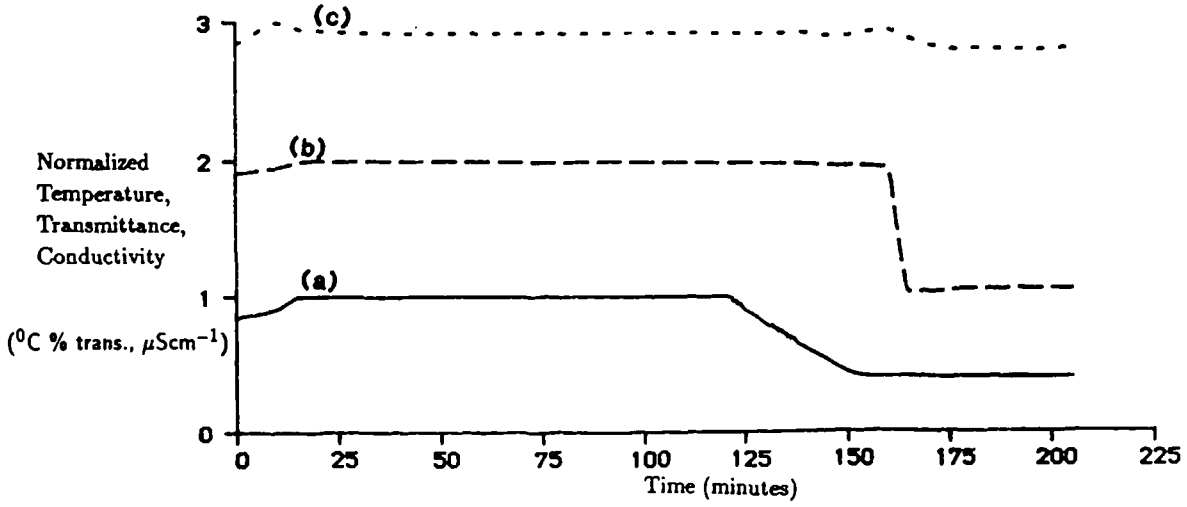

a) temperature b) transmittance c) conductivity

Figure 6.11: Typical crash cool as recorded by turbidometry and conductivity for $AlK(SO_4)_2.12H_2O$.

turbidometric measurements (27.30^0C). The rates of change of solution transmittance are notably greater than the rates of change of solution conductivity, implying that during crystallisation the solution transmittance changes much more rapidly than the solution conductivity and thus, turbidometry would seem to be more sensitive to crystallisation than conductivity.

Plots of ln (J) vs $T^{-3}ln(S)^{-2}$ and ln (τ) vs $T^{-3}ln(S)^{-2}$ at each concentration are highlighted in figures 6.12 - 6.15. The resultant determined induction time based interfacial energies and rate based interfacial energy related parameters ($\pm$ standard deviations) are highlighted in table 6.9. As previously defined, the superscripts "t" and "c" are representative of turbidometric and conductivity measurements respectively. The subscript in each case is the standard deviation.

Large variations in the determined induction times and the rates of change of solution transmittance and conductivity at each supersaturation are observed, which is reflected in the low correlation coefficients of the fitted lines in figures 6.12-6.15. This may be attributed to the influence of heterogeneous nuclei upon the crystallising

solution. Obviously crystallisation parameters such as nucleation rates, induction times and thus the derived interfacial energies are significantly influenced by the presence of these heterogeneous nuclei. This can be illustrated by the positive slope obtained for the plot of ln(rate of change of solution conductivity) vs $T^{-3}ln(S)^{-2}$ obtained from conductivity measurements, which implies the existence of a factor related to a negative interfacial energy. It is apparent that there is greater variation in the determined rate data for than the induction time data for each technique, implying that the subsequently determined energy parameter (related to the actual interfacial energy) is less reliable than the corresponding interfacial energy determined from induction time measurements. No significant differences can be distinguished between interfacial energies based on turbidometry and the corresponding measurements based on conductivity.

ΔT^t (^0C)	τ^t (mins)	J^t (%trans./min)	ΔT^c (^0C)	τ^c (mins)	J^c ($\mu S/cm^{-1}/min$)
8.87	27.78	$1.46x10^5$	4.30	11.89	$2.18x10^3$
6.96	25.74	$0.88x10^5$	2.56	20.61	$2.00x10^3$
4.97	45.29	$0.47x10^5$	1.35	25.36	$1.56x10^3$
2.94	58.29	$0.06x10^5$	1.43	37.37	$1.22x10^3$
0.92	210.98	$0.53x10^5$	0.41	28.12	$1.52x10^3$

Table 6.8: Typical induction time and rate of change of solution conductivity/ transmittance measurements for $AlK(SO_4)_2.12H_2O$, based on turbidometric and conductivity measurements.

Various aspects of the crystallisation kinetics of potash alum have been studied [1,8]. If supersaturation is obtained by conventional solution cooling, it was found that the nucleation rates increased with increases in supersaturation, agitation and temperature, with supersaturation dominating the processes as predicted by classic nucleation theory [8]. A plot of ln (induction time) versus $T^{-3}ln(S)^{-2}$ was determined for agitated and nonagitated systems (figure 6.16).

It was concluded in this study that non-agitated solutions appear to nucleate following classic homogeneous behaviour and agitated solutions appear to nucleate

following a heterogeneous mechanism. The data in the current study has been determined from agitated systems and although does show a large degree of variation, does not follow the trend shown in figure 6.16(b). The degree of agitation used in Mullin's study was approximately 400rpm; the degree of agitation in this system is significantly less (approx. 180rpm) and is more analogous to the unagitated than the agitated system. The range of interfacial energies obtained from Mullin's study followed a linear dependence on temperature, the values obtained ranging from ($3.14x10^{-3}Jm^{-2}$) at 15^0C to ($2.03x10^{-3}Jm^{-2}$) at 35^0C. These values are much less than the interfacial energy ($50x10^{-3}Jm^{-2}$) predicted by the Nielson-Söhnel empirical relationship, which is based on equilibrium solubility. It was concluded that this relationship which has been successfully applied to sparingly soluble salts, needed further refinement for successful application to soluble salts. The interfacial energies obtained in the current study are approximately a factor of ten smaller than those obtained by Mullin. This difference may be possibly attributed to various parameters, such as the degree of agitation and the presence of heterogeneous nuclei in the system. By plotting the logarithim of the determined interfacial energies versus 1/temperature (figure 6.17), the linear dependence of the interfacial energy upon temperature may be noted.

Concentration (g per 100g/H_2O)	Induction Time Based Interfacial Energy^t ($10^{-4}Jm^{-2}$)	Rate Based Interfacial Energy Related Parameter^t ($10^{-4}Jm^{-2}$)	Induction Time Based Interfacial Energy^c (10 Jm^{-2})	Rate Based Interfacial Energy Related Parameter^c ($10^{-4}Jm^{-2}$)
9.5	$9.68_{0.31}$	$12.61_{1.84}$	$6.76_{0.01}$	$5.85_{1.44}$
11.2	$8.09_{0.34}$	$9.42_{0.77}$	$6.02_{0.85}$	$6.99_{3.0}$
14.0	$2.95_{0.01}$	$2.77_{0.20}$	$2.28_{0.17}$	$-0.01_{4.23}$

Table 6.9: Summary of interfacial energies and related parameters determined from induction time and rate measurements, based on turbidometric and conductivity data for $AlK(SO_4)_2.12H_2O$.

The addition of a second solvent to a crystallisation system (i.e. "drowning out") may be employed to achieve much higher degrees of supersaturation than can be achieved with conventional solution cooling. When applied to $AlK(SO_4)_2.12H_2O$ [1], it was concluded that primary heterogeneous nucleation predominates with homogeneous nucleation becoming significant at supersaturation ratios ("S") greater than 4.5 and a calculated interfacial energy of $39mJm^{-2}$ was reported. This interfacial energy is in better agreement with the predicted interfacial energy of $50mJm^{-2}$ than the energies determined by Mullin or in the current study. As the levels of supersaturation achieved during the current study (1.01-1.41) and in Mullin's study ($S \leq 2.68$) are notably lower than a supersaturation ratio of 4.5 and thus fall into the region of heterogeneous nucleation indicated by Mylardz et al [1], the implication is that the resultant determined interfacial energies in these studies are lowered by the significant influence of the heteronuclei present. Thus for a very soluble salt such as $AlK(SO_4)_2.12H_2O$, in order to determine true interfacial energies based on homogeneous nucleation, higher supersaturations must be obtained to override nucleation occuring on any heteronuclei present in the system.

Hence, it may be concluded for $AlK(SO_4)_2.12H_2O$ that turbidometry provides a more sensitive technique for detecting crystallisation than conductivity. Monitoring temperature as a means for detecting crystallisation is inappropriate, due to the small heat of crystallisation. Employing an preheating temperature of 20^0C and 120 minutes preheating time above the approximate saturation point seems to provide the least experimental scatter. This represented the highest preheating temperature and longest preheating time tested. It was observed that variation in the overheating time critically influenced the subsequent parameters determined. The combination of the aforementioned parameters may represent the conditions where any possible solution structure present is completely disrupted, creating a completely homogeneous solution. The determined crystallisation temperatures, induction times and nucleation rates were much more subject to variation than the dissolution temperatures, due to the influence of heterogeneous nuclei. The resultant determined saturation temperatures were found to be in reasonable agreement with previous studies. Greater variations were observed in the determined rates of change of solution transmittance

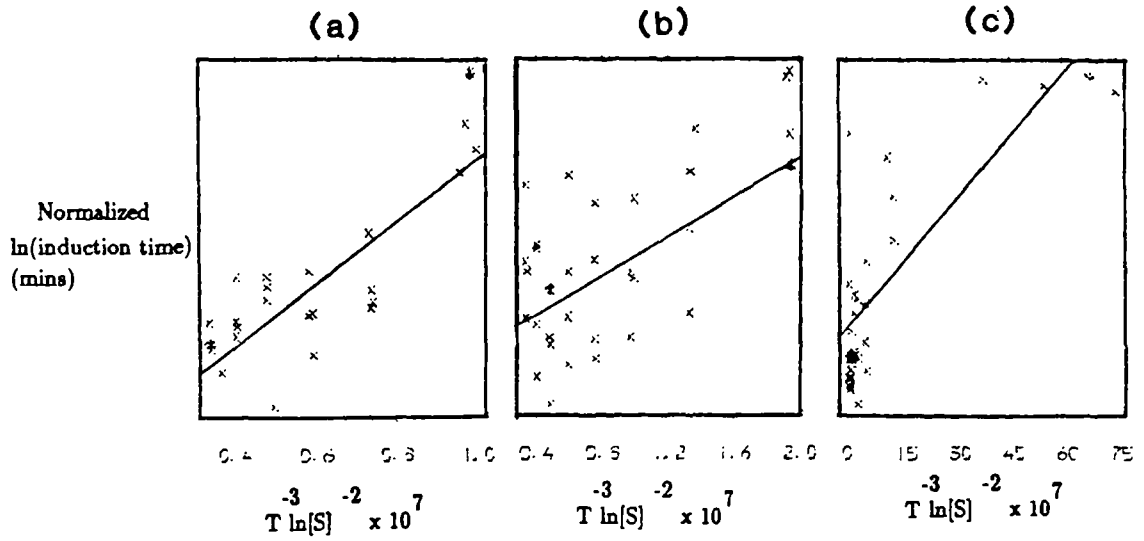

Correlation coefficients: a) 81 %, b) 68 % c) 82 %

Figure 6.12: Plot of normalised $\ln(\tau)$ vs $T^{-3}\ln(S)^{-2}$ based on turbidometric measurements for a) 9.5g, b) 11.2g, c) 14.0g $AlK(SO_4)_2.12H_2O/100gH_2O$ respectively.

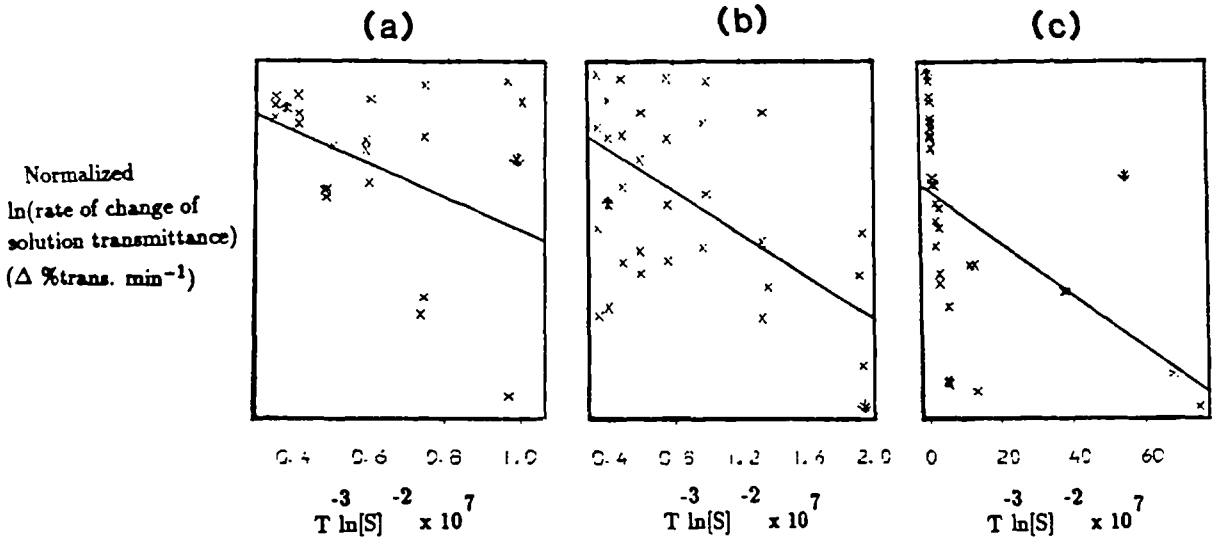

Correlation coefficients: a) 49%, b) 48%, c) 36%

Figure 6.13: Plot of normalised $\ln(J)$ vs $T^{-3}\ln(S)^{-2}$ based on turbidometric measurements, for a) 9.5g, b) 11.2g, c) 14.0g $AlK(SO_4)_2.12H_2O/100g\ H_2O$ respectively.

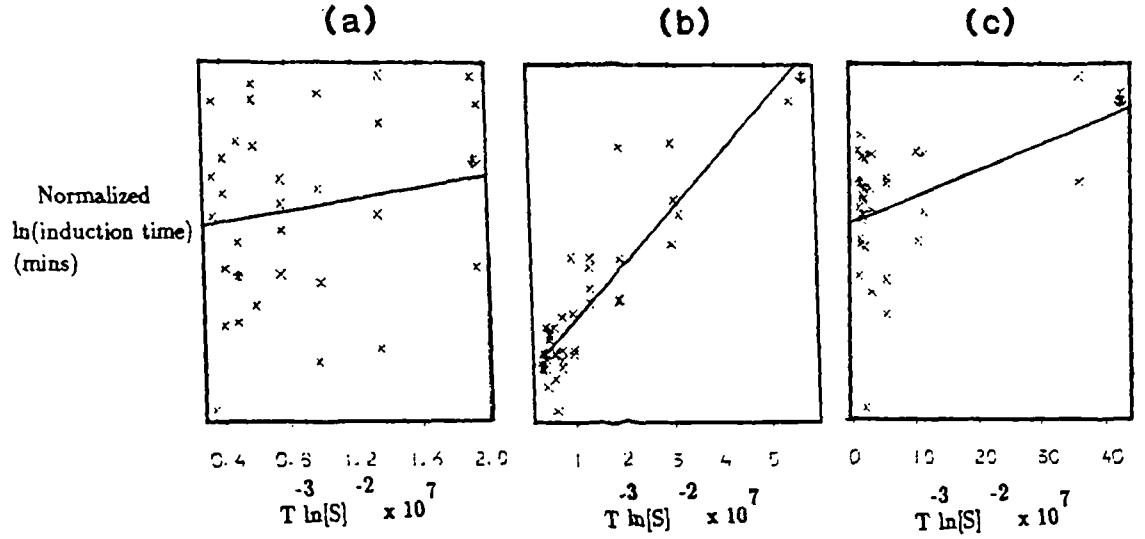

Correlation coefficients: a) 25%, b) 90%, c) 53%

Figure 6.14: Plot of normalised $\ln(\tau)$ vs $T^{-3}\ln(S)^{-2}$ based on conductivity measurements, for a) 9.5g, b) 11.2g, c) 14.0g $AlK(SO_4)_2.12H_2O$/100g H_2O respectively.

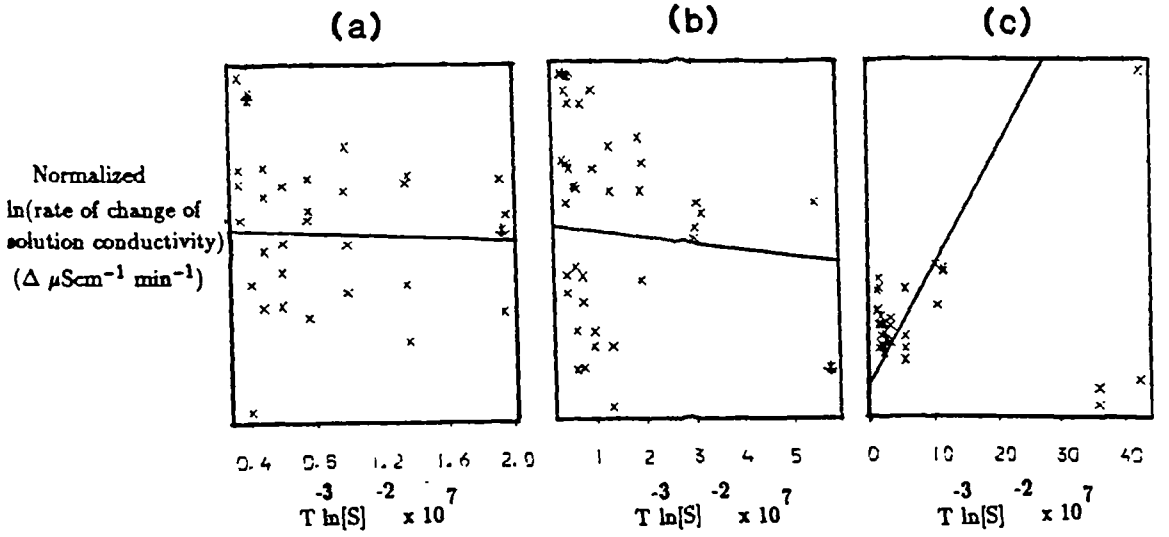

Correlation coefficients: a) 25 %, b) 15%, c) 19%

Figure 6.15: Plot of normalised $\ln(J)$ vs $T^{-3}\ln(S)^{-2}$ based on conductivity measurements for a) 9.5g, b) 11.2g, c) 14.0g $AlK(SO_4)_2.12H_2O$/100g H_2O respectively.

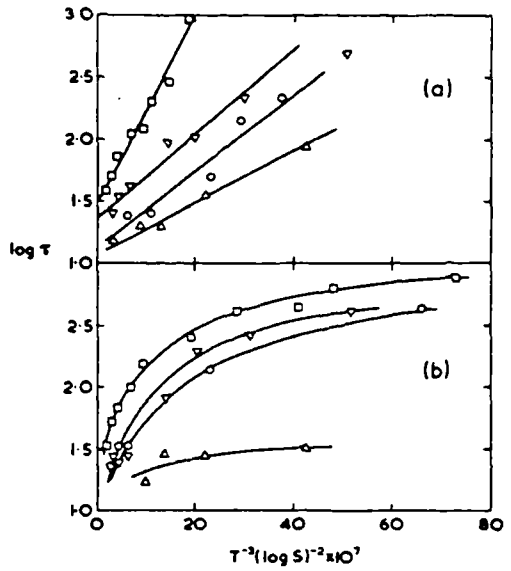

Figure 6.16: Plot of ln (induction time) versus $T^{-3}\ln(S)^{-2}$ for a) non-agitated potash alum system and b) agitated potash alum system. [8]
(□15°C), (▽20°C), (O 25°C), (Δ 35°C)

and conductivity than the determined induction times.The derived interfacial energies are significantly lower than those determined by Mullin [8] but show the same dependence on temperature. The determined interfacial energies by Mullin and in the current study are based on the conventional method of obtaining supersaturations by lowering of the solution temperature, however the supersaturations achieved by this method for $AlK(SO_4)_2.12H_2O$ are relatively low. Higher degrees of supersaturation may be achieved by "drowning out" experiments and have been employed [1] to determine that above the threshold supersaturation ratio of S=4.5 primary homogeneous occurs; below this value primary heterogeneous nucleation occurs. The determined interfacial energy at these higher supersaturations shows better correlation to the predicted interfacial energy, thus implying that the influence of heteronuclei in the solution significantly lowers the determined values of interfacial energies.

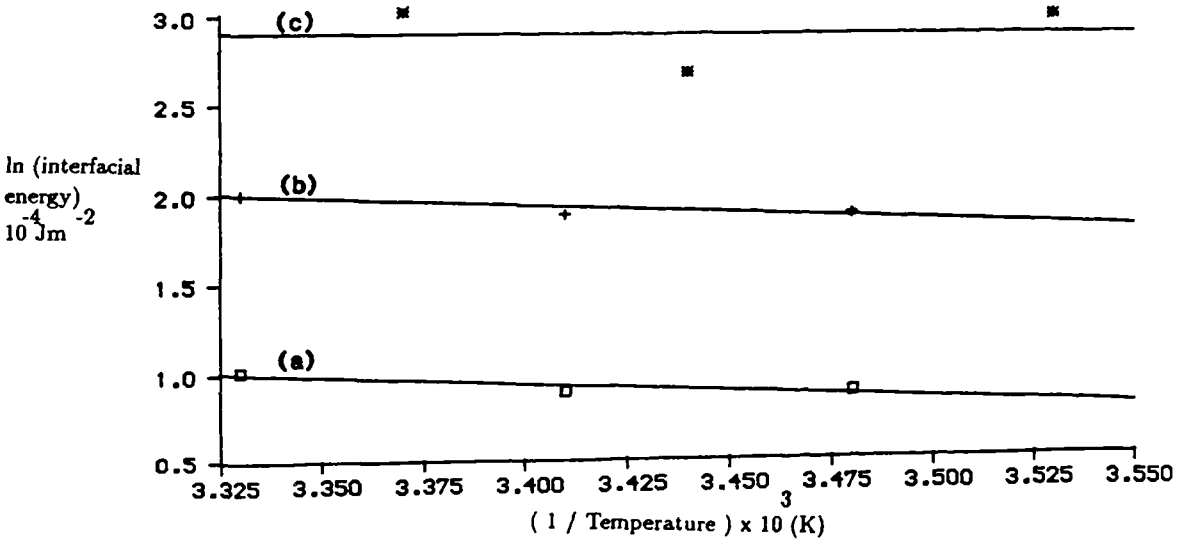

Correlation coefficients: a) 94 %, b) 95 %, c) 47 %

Figure 6.17: Plot of ln(interfacial energy) vs 1/temperature for $AlK(SO_4)_2.12H_2O$, determined from a) induction times^t based interfacial energies, b) rate based ^{t} interfacial energy related parameters, c) induction times^c based interfacial energies. The superscripts "t" and "c" represent turbidometric and conductivity based measurements respectively.

6.3.2 Ammonium Dihydrogen Orthophosphate, $NH_4H_2PO_4$

6.3.2.1 Saturation Curve And Metastable Zonewidth Determination

Ammonium dihydrogen orthophosphate ($NH_4H_2PO_4$) is another system that has advantageous crystallisation properties, e.g. forming large discrete crystals of a single phase. The solubility curve [7] for this material is shown in figure 6.18.

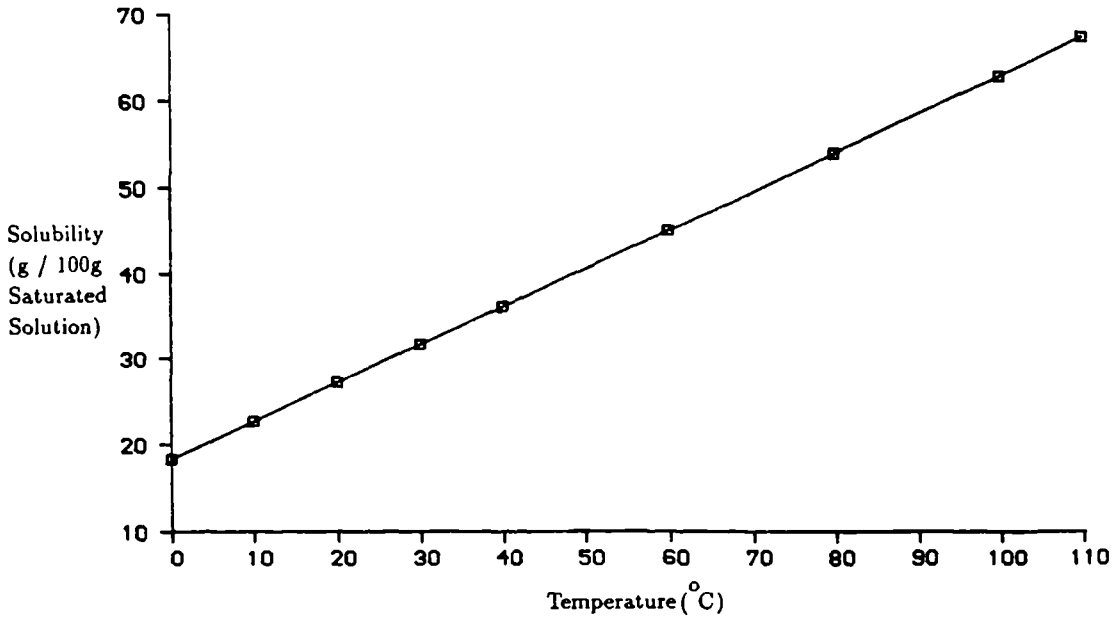

Figure 6.18: Solubility curve for $NH_4H_2PO_4$ [7].

Again, a comparison between literature saturation data and the determined saturation temperatures based on conductivity and turbidometry measurements may be employed, to determine which technique is the most sensitive for detection of nucleation. Three different solution concentrations of $NH_4H_2PO_4$ were examined, with the same initial conditions as those determined for $AlK(SO_4)_2.12H_2O$ employed, i.e. 120 minutes preheating time and 20^0C preheating temperature. An example of the slow cooling with resultant crystallisation and the slow heating with resultant dissolution at a low and high solute concentration respectively, are shown in figures 6.19 and 6.22.

Different detection limits were chosen to those employed for $AlK(SO_4)_2.12H_2O$, due to the different crystallisation characteristics for this material, and the greater fluctuations noted in the solution conductivity and transmittance during the initial

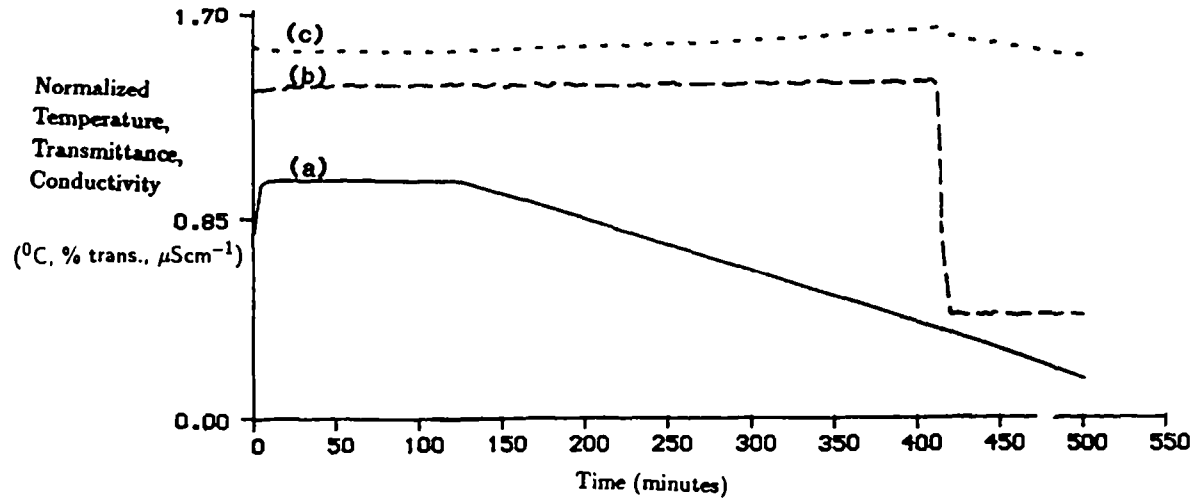

a) temperature b) transmittance c) conductivity

Figure 6.19: Slow cooling of $NH_4H_2PO_4$ observed at low solute concentrations, monitored by temperature, turbidometry and conductivity, with resultant crystallisation.

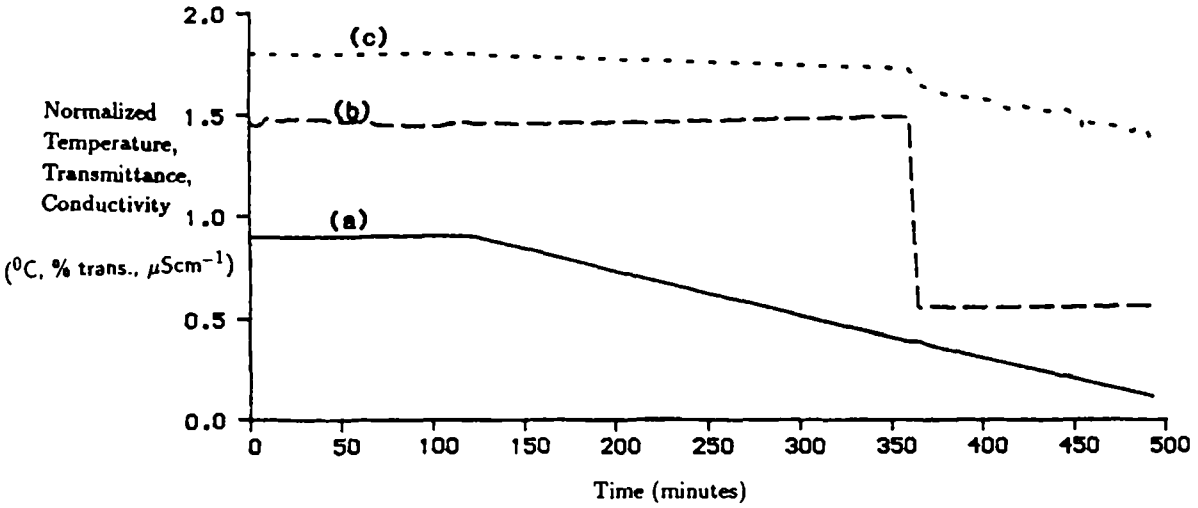

a) temperature b) transmittance c) conductivity

Figure 6.20: Slow cooling of $NH_4H_2PO_4$ observed at higher solute concentrations, monitored by temperature, turbidometry and conductivity, with resultant crystallisation

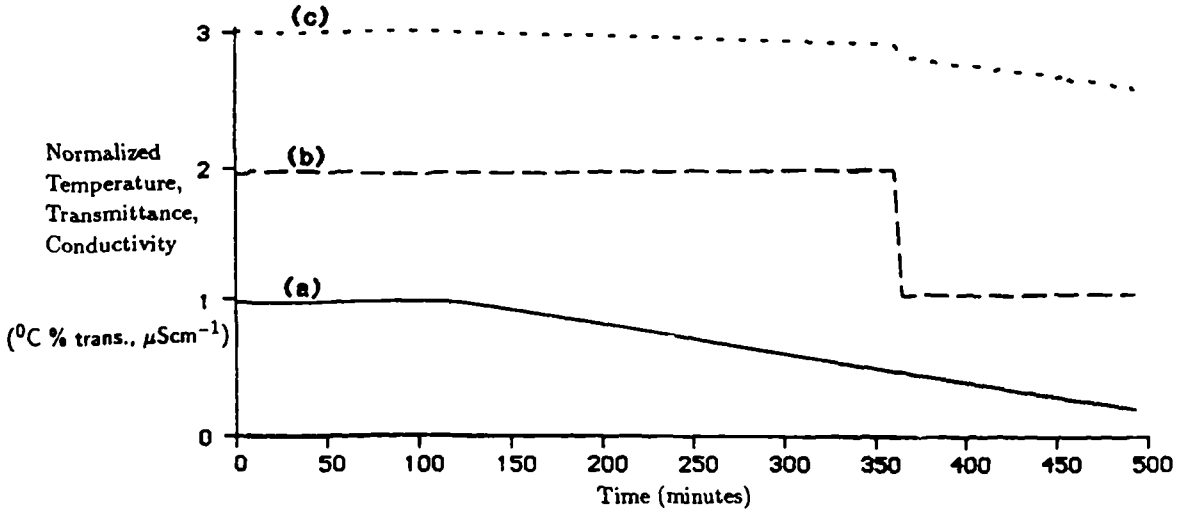

a) temperature b) transmittance c) conductivity

Figure 6.21: Slow heating of $NH_4H_2PO_4$ at low solute concentrations, monitored by temperature, turbidometry and conductivity, with resultant dissolution.

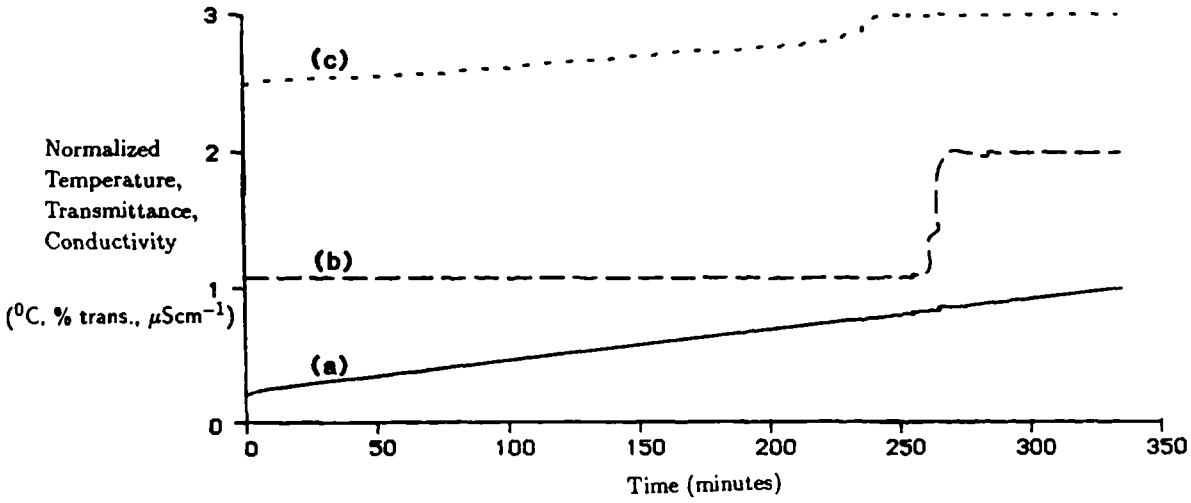

a) temperature b) transmittance c) conductivity

Figure 6.22: Slow heating of $NH_4H_2PO_4$ at higher solute concentrations, monitored by temperature, turbidometry and conductivity, with resultant dissolution.

preheating cycle. The solution conductivity was much higher than that recorded for $AlK(SO_4)_2.12H_2O$, typically a solution containing 27.50g $NH_4H_2PO_4$/100g saturated solution (equivalent to a saturation temperature of 20^0C) having a measured solution conductivity of 159μScm^{-1}. The detection parameters chosen were a drop of 10% transmittance and 3μScm^{-1} conductance from that recorded for a clear solution representing the points at which crystallisation occurs and dissolution to have occurred when the solution transmittance and conductivity come within 10% and 3μScm^{-1} respectively, of that recorded for a clear solution.

The resultant determined saturation temperatures, maximum metastable zone-widths and orders of reaction are compared and contrasted to previous studies in tables 6.10 and 6.11.

Figures 6.19 and 6.21 indicate that there is no dependence of solution conductivity upon temperature; the change in solution conductivity during crystallisation and dissolution is extremely small (approx. 9μScm^{-1}) compared to the change in solution transmittance (approx. 70% transmittance) during these processes. However, figures 6.20 and 6.22 are those recorded for 31.79g $NH_4H_2PO_4$/100g saturated solution, corresponding to a literature saturation temperature of 30^0C. The temperature dependence of the solution conductivity is clear; this temperature dependence is not observed for solution concentrations representing 10^0C and 20^0C respectively. The change in solution conductivity during crystallisation and dissolution is slightly greater (11μScm^{-1}) than that noted at lower solute concentrations. Hence, the detection parameters were accordingly altered from $\pm$ 3% to $\pm$ 25%. The resultant saturation temperatures determined at this concentration show excellent correlation to previous studies [7]. At the lower solute concentrations, the determined saturation temperatures based on conductivity measurements are lower than those determined from turbidometry and are also lower than those determined in previous studies. In general, the saturation temperatures derived from turbidometric measurements showed better correlation to literature saturation data than the saturation temperatures determined from conductivity measurements, especially at the solute concentration of 22.77g $NH_4H_2PO_4$/100g saturated solution. At this concentration, the determined saturation temperature significantly differs from that determined in previous studies.

The determined orders of reaction show reasonable correlation, with relatively low standard deviations indicating little variation in the determined precipitation temperatures.

A factor that should be taken into account in the interpretation of this data is the presence of hydrogen bonding both in solution and in the solid state of $NH_4H_2PO_4$. The hydrogen bonding will obviously have an effect on the mobility of the ionic species in solution, which will consequently influence conductivity based kinetic data measurements. It is also obvious from table 6.11 that the conductivity based saturation temperature for the solute concentration equivalent to a 30^0C saturation temperature [7] shows better correlation to previous studies than the determined saturation temperatures for solute concentrations equivalent to 10^0C and 20^0C. It may be possible to tentatively conclude that the better correlation noted at this higher saturation temperature is due to the disruption of the solution hydrogen bonding, creating a homogeneous solution.

Measurement of the solution transmittance is not influenced by the presence of hydrogen bonding; thus the determined saturation parameters based on turbidometric measurements show somewhat better correlation to previous studies than parameters based on conductivity measurements.

The determined enthalpy and entropy of dissolution based on each technique can be compared and contrasted to dissolution parameters determined from previous studies. The poor agreement between the determined saturation temperatures from previous studies and those based on conductivity measurements in the current study is reflected in the resultant determined enthalpies and entropies of dissolution. In each case the determined saturation curve exhibits a high degree of linearity, indicating ideal solution behaviour. However, reasonable correlation is observed between the dissolution enthalpies and entropies determined from previous studies and turbidometry. Thus the $NH_4H_2PO_4$ system would seem to be a parallel to $AlK(SO_4)_2.12H_2O$, with the implication that turbidometry provides a better technique than conductivity for the determination of crystallisation parameters.

g $NH_4H_2PO_4$ per 100g Saturated Solution [7]	Saturation Temperature (^{0}C)	Saturation Temperature (^{0}C)	Max. M.S.Z.W. (^{0}C)	Order of Reaction
22.77	10	$7.61_{0.52}$	21.68	$1.49_{0.16}$
27.50	20	$22.05_{0.29}$	15.17	$0.61_{0.44}$
31.79	30	$33.24_{1.64}$	24.04	$1.69_{0.18}$

Table 6.10: Comparison of determined saturation temperatures, maximum metastable zonewidths and orders of reaction based on turbidometry to previous studies for $NH_4H_2PO_4$.

g $NH_4H_2PO_4$ per 100g Saturated Solution [7]	Saturation Temperature (^{0}C)	Saturation Temperature (^{0}C)	Max. M.S.Z.W. (^{0}C)	Order of Reaction
22.77	10	$-0.20_{1.11}$	21.33	$0.86_{0.50}$
27.50	20	$15.60_{0.41}$	9.85	$1.55_{0.12}$
31.79	30	$29.73_{2.71}$	9.07	$0.76_{0.03}$

Table 6.11: Comparison of determined saturation temperatures, maximum metastable zonewiths and orders of reaction based on conductivity to previous studies for $NH_4H_2PO_4$.

Type	Enthalpy of Dissolution (J/mol*K)	Entropy of Dissolution (J/mol)	Correlation Coefficient
Literature	$1.54x10^4$	$6.7x10^1$	0.99
Turbidity	$1.25x10^4$	$5.7x10^1$	0.99
Conductivity	$0.99x10^4$	$4.9x10^1$	0.99

Table 6.12: Comparison of predicted enthalpies and entropies of dissolution derived from turbidometric and conductivity measurements to previous studies, for $NH_4H_2PO_4$.

6.3.2.2 Interfacial Energy Determination

A solution containing 27.5g $NH_4H_2PO_4$/100g saturated solution (corresponding to a literature saturation temperature of 20^0C) was crash cooled through a variety of supersaturations, with the resultant induction times and rates of change of solution conductivity/transmittance recorded. Some typical undercoolings (ΔT), induction times and rates recorded are highlighted in table 6.13. As defined for $AlK(SO_4)_2.12H_2O$, "τ" is defined as the induction time, "J" is defined as the rate of change and the superscripts "t" and "c" define turbidometric and conductivity measurements respectively.

The expected trend would be an increase in undercooling leading to an increase in rate of change of solution transmittance/conductivity and a corresponding decrease in induction time. Significant deviations from this trend are noted in table 6.13 and are much more obvious than the corresponding measurements for $AlK(SO_4)_2.12H_2O$. The determined rates of change of solution transmittance are notably higher than the rates of change based on conductivity measurements, implying that turbidometry is more sensitive to the onset of nucleation than conductivity; a point which was also observed for $AlK(SO_4)_2.12H_2O$. Plotting $ln(\tau)$ vs $T^{-3}(ln(S)^{-2})$ (figure 6.23) and ln (J) vs $T^{-3}(ln(S)^{-2})$ (figure 6.24) allows the crystal-solution interfacial energy to be determined. Deviations from the expected linear relationship are notable in each case,

especially for measurements based on the determination of solution rate parameters; again attributable to the presence of heterogeneous nuclei in the system. Based on these measurements, the resultant determined interfacial energies ($\pm$standard deviations) are highlighted in table 6.14.

ΔT^t (^0C)	τ^t (mins)	J^t (%trans./min)	ΔT^c (K)	τ^c (mins)	J^c ($\mu S/cm^{-1}/min$)
24.03	27.60	$0.61x10^5$	21.34	31.52	$0.01x10^4$
22.96	47.28	$0.01x10^5$	20.35	27.61	$0.13x10^4$
22.23	25.10	$0.37x10^5$	19.19	23.84	$0.10x10^4$
19.43	63.06	$0.22x10^5$	18.72	25.10	$1.65x10^4$
18.55	36.39	$1.15x10^5$	17.70	25.10	$0.63x10^4$

Table 6.13: Typical induction time and nucleation rate measurements for $NH_4H_2PO_4$, based on turbidometric and conductivity measurements.

Induction Time Based Interfacial Energy^t ($10^{-4}Jm^{-2}$)	Rate Based Interfacial Energy Related Parameter^t ($10^{-4}Jm^{-2}$)	Induction Time Based Interfacial Energy^c ($10^{-4}Jm^{-2}$)	Rate Based Interfacial Energy Related Parameter^c ($10^{-4}Jm^{-2}$)
$9.69_{3.05}$	$15.98_{5.91}$	$-9.59_{2.04}$	$14.77_{4.75}$

Table 6.14: Interfacial energies determined from induction time and nucleation rate measurements, based on turbidometric and conductivity data for $NH_4H_2PO_4$.

The determined interfacial energies in this study are of the same order of magnitude as those determined for $AlK(SO_4)_2.12H_2O$. The large degree of experimental scatter is highlighted, with a negative interfacial energy being deduced from conductivity based induction time measurements. These values are in poor agreement with a value of $4mJm^{-2}$ determined by Söhnel [9] and are notably lower than a calculated interfacial energy of $20mJm^{-2}$ [9], which was based on dissolution enthalpy considerations:

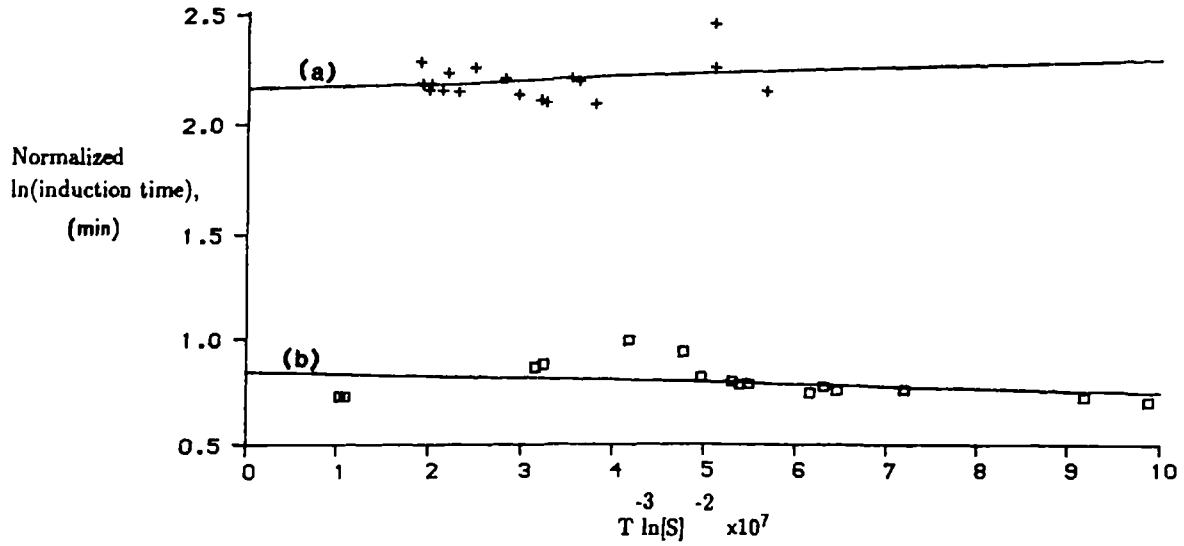

correlation coefficients: a) 31%, b) 78%

Figure 6.23: Plot of normalised $\ln(\tau)$ vs $T^{-3}\ln(S)^{-2}$ based on a) turbidometric and b) conductivity measurements for $NH_4H_2PO_4$.

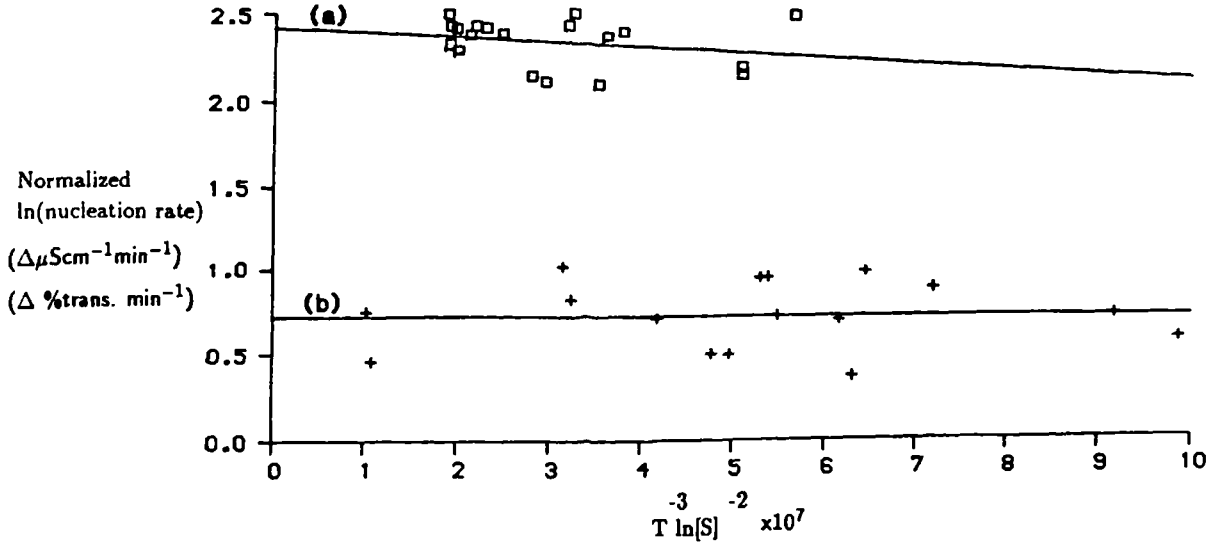

Correlation coefficients: a) 25%, b) 32%

Figure 6.24: Plot of normalised $\ln(J)$ vs $T^{-3}\ln(S)^{-2}$ based on a) turbidometric and b) conductivity measurements for $NH_4H_2PO_4$.

$$\gamma = 1.8x10^9 \Delta H_c/(V_m^2 N_A)^{1/3} \quad (6.2)$$

where "γ is the interfacial energy, "ΔH_c" is the heat of crystallisation, "V_m" the molar volume and "N_A" Avogadro's number.

Söhnel concluded that for well-soluble and slightly soluble materials conventional techniques such as solution cooling cannot ensure the establishment of a high enough supersaturation required for overriding the birth of crystals on the heteronuclei already present in the solution. Thus the resultant interfacial energies determined are too low, being equivalent to a "heterogeneous based interfacial energy" ("$\gamma.f(\varphi)$" in equation 2.24) rather than a "homogeneous based interfacial energy" ("γ" in equation 2.20). Hence, the relatively low interfacial energies determined in the current study can be attributed to the presence of heteronuclei in the crystallising solution, lowering the interfacial energy. However, Söhnel also noted that the model upon which the calculated interfacial energies are based needed further refinement, before successful application to soluble systems.

6.3.3 Summary

For the model systems tested it was noted that parameters dependent upon crystallisation, eg. induction times and precipitation temperatures were much more subject to experimental scatter than dissolution based parameters, e.g. dissolution temperatures. This may be attributed to the presence of heteronuclei, which cannot be totally removed. During crystallisation and dissolution of both $AlK(SO_4)_2.12H_2O$ and $NH_4H_2PO_4$, the changes in solution transmittance were much greater than the changes in solution conductivity. The smaller changes in conductivity measured in conjunction with possible temperature dependence effects and the influence of hyrogen bonding in the solution (noted for $NH_4H_2PO_4$), implied that accurate assessment of the crystallisation and dissolution of a system was more likely to be obtained when based on turbidometric rather than conductivity data. This was confirmed by saturation data measurements, where data based on turbidometric measurements showed better correlation to previous studies than corresponding data based on conductivity

measurements. Solution temperature measurement as a means of determining the crystallisation of a system was inappropiate for $AlK(SO_4)_2.12H_2O$ and $NH_4H_2PO_4$, no change in solution temperature upon crystallisation being detected for either system.

The rates of change of solution transmittance were significantly higher than the corresponding rates of change of solution conductivity for $AlK(SO_4)_2.12H_2O$ and $NH_4H_2PO_4$, implying that turbidometry is more sensitive to nucleation than conductivity. However it was determined that the measured rates of change for both solution transmittance and conductivity were much more sensitive to experimental scatter than measured induction times. As the rates of change of solution transmittance and conductivity are not equivalent to the nucleation rate, the interfacial energy may only be estimated from induction time measurements. A further conversion is required before interfacial energies may be determined from rates of change of solution transmittance and conductivity data. The determined interfacial energies were significantly lower than the predicted value, due to the influence of heteronuclei on the crystallising solution.

It may be concluded that crystallisation kinetic parameters may be more accurately determined from turbidometric measurements than conductivity measurements. In order to remove any solution structure present, the system to be studied should be preheated for 120 minutes for a preheating temperature of 20^0C.

6.4 Studies Of Sodium Sulphate/Carbonate Salts

Potash alum and ammonium dihydrogen orthophosphate are favourable for crystallisation studies, forming large discrete crystals of a single phase. However, many systems crystallise forming a variety of different phases. Systems of interest in this study that fall into this group are the Na_2SO_4-H_2O and Na_2CO_3-H_2O systems. Within these systems, compounds of varying degrees of hydration exist, which are formed depending on the crystallising temperature. A study was carried out on the nucleation characteristics of a specific compound from each system, i.e. $Na_2SO_4.10H_2O$ and

$Na_2CO_3.10H_2O$ was carried out. The effect of the influence of carbonate addition on the crystallisation kinetics of $Na_2SO_4.10H_2O$ was investigated by examination of the crystallisation of a solution containing a 1:1 molar ratio of (Na_2CO_3:Na_2SO_4).

The conclusions reached from examination of $AlK(SO_4)_2.12H_2O$ and $NH_4H_2PO_4$ were applied to the studies of these sodium carbonate/sulphate salts, i.e. turbidometric data was considered solely for the measurement of precipitation and dissolution based parameters. Induction time, rather than nucleation measurements were considered for the determination of interfacial energies. It was felt that these conditions provided the most reliable data measurements.

6.4.1 Sodium Sulphate Decahydrate, $Na_2SO_4.10H_2O$

6.4.1.1 Saturation Curve And Maximum Metastable ZoneWidth Determination

Crystallisation of sodium sulphate from solution may lead to a variety of different phases, depending on the temperature of the crystallising solution. A typical solubility curve [7] of the Na_2SO_4-H_2O system is shown in figure 6.25. Three sodium sulphate based phases may be noted: (a) sodium sulphate decahydrate ($Na_2SO_4.10H_2O$), (b) a metastable sodium sulphate heptahydrate ($Na_2SO_4.7H_2O$) phase and(c) sodium sulphate (Na_2SO_4). The phase transition between the equilibrium phases $Na_2SO_4.10H_2O$ and Na_2SO_4 occurs at 32.4^{0}C and the phase transition between the metastable $Na_2SO_4.7H_2O$ phase and Na_2SO_4 occurs at 23.7^{0}C [7].

Sodium sulphate decahydrate was chosen to be the material of study in this system. This was due to the problems of trying to study a metastable phase ($Na_2SO_4.7H_2O$) and the almost horizontal negative solubility of Na_2SO_4, which indicated that upon controlled heating, the degree of supersaturation obtained is not sufficient for precipitation to be detected by turbidometry.

A typical slow cooling/slow heating cycle, using turbidity to detect crystallisation and dissolution is shown in figures 6.26 and 6.27. The crystallising phase in each case is $Na_2SO_4.10H_2O$.

What is apparent from figure 6.26 is the sharp increase in temperature upon

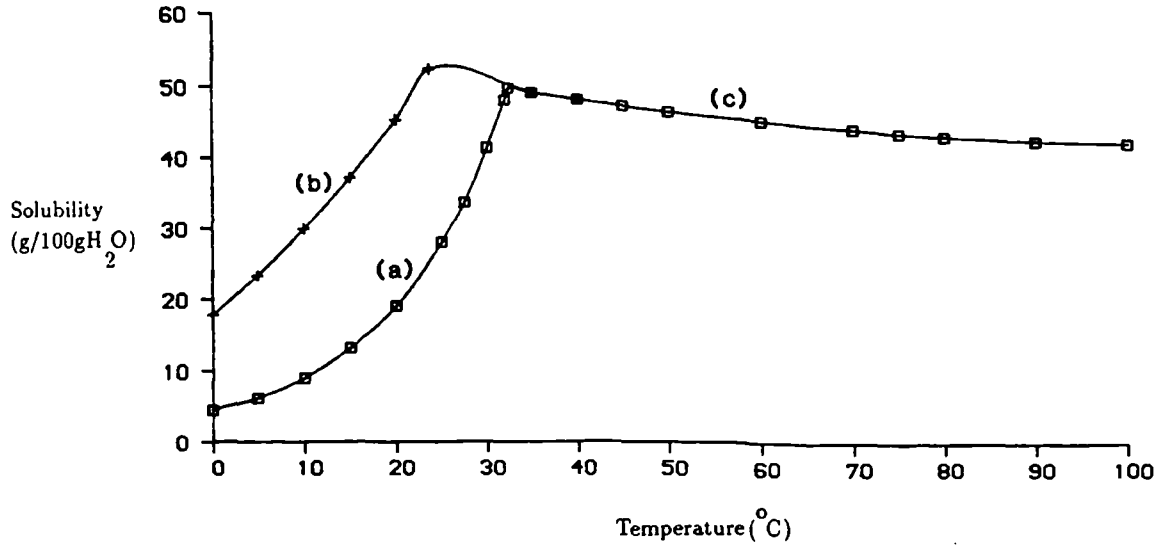

Figure 6.25: Solubility curve for the Na_2SO_4-H_2O system [7]

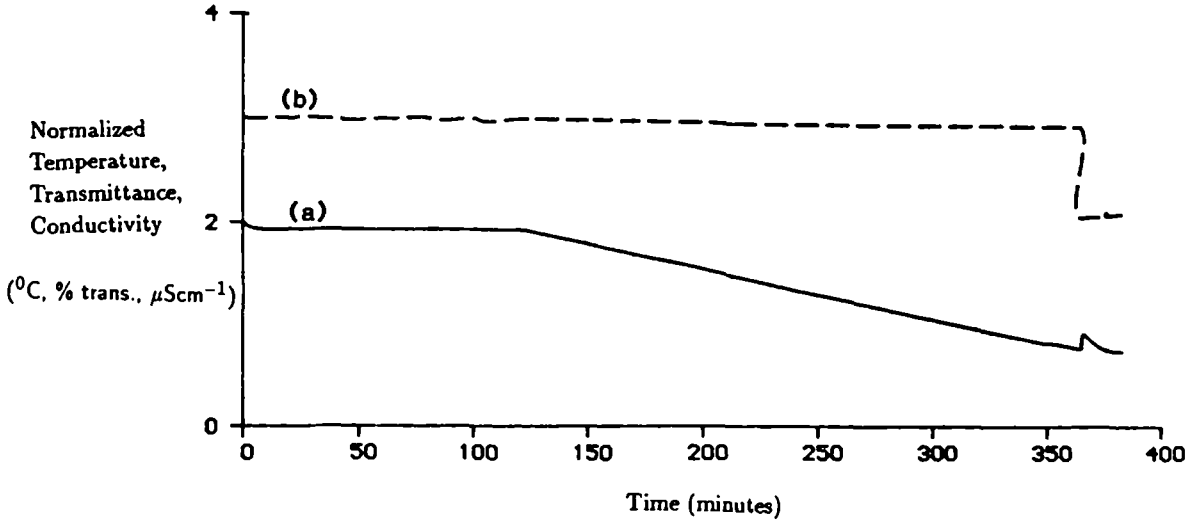

a) temperature b) transmittance

Figure 6.26: Schematic of the crystallisation of $Na_2SO_4.10H_2O$ that occurs during the slow cooling of a solution, as detected by turbidometry.

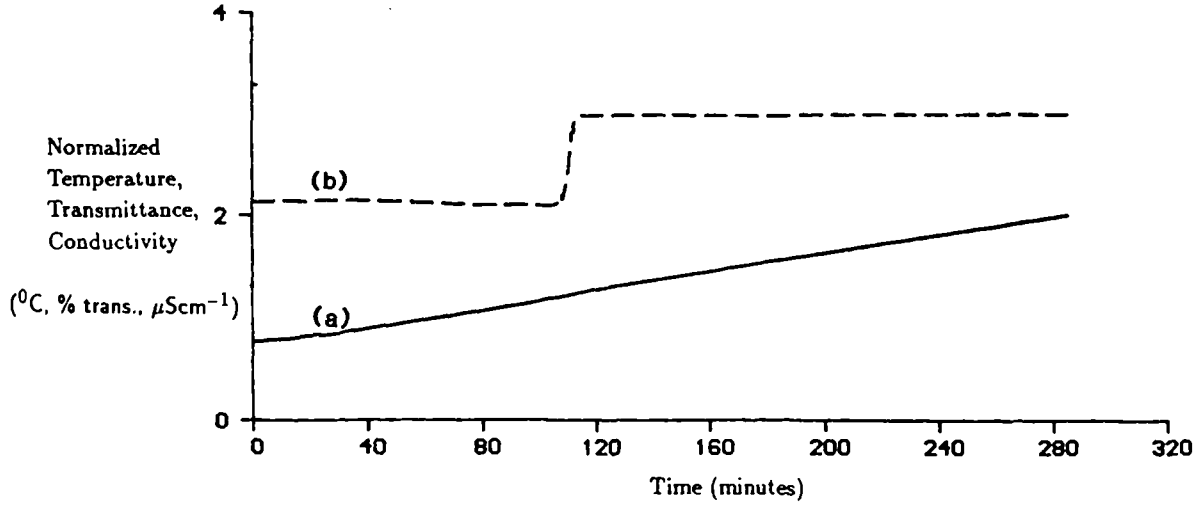

a) temperature b) transmittance

Figure 6.27: Schematic of the dissolution of $Na_2SO_4.10H_2O$ that occurs during the slow heating of a crystallised solution, as detected by turbidometry.

crystallisation which was not observed for $AlK(SO_4)_2.12H_2O$ and $NH_4H_2PO_4$, which would imply that the heat of crystallisation for $Na_2SO_4.10H_2O$ is of a sufficient magnitude to alter the solution temperature noticably and thus solution temperature may be monitored and employed as a means of detecting crystallisation.

A saturation curve was determined by the examination of crystallisation and dissolution at 3 different solution concentrations. A preheating time and temperature of 120 minutes and 20^0C above the approximate saturation point were employed. Since the solubility of $Na_2SO_4.10H_2O$ is significantly different from that of $AlK(SO_4)_2.12H_2O$ and $NH_4H_2PO_4$ (see figure 6.28 for comparison), different detection limits have to be employed to register the onset of crystallisation and dissolution of $Na_2SO_4.10H_2O$. A difference of 20% solution transmittance from the values recorded for a clear solution were chosen to represent the points at which crystallisation and dissolution had occurred, respectively.

The resultant determined saturation temperatures, maximum metastable zone-widths and orders of reaction are compared and contrasted to literature data in table

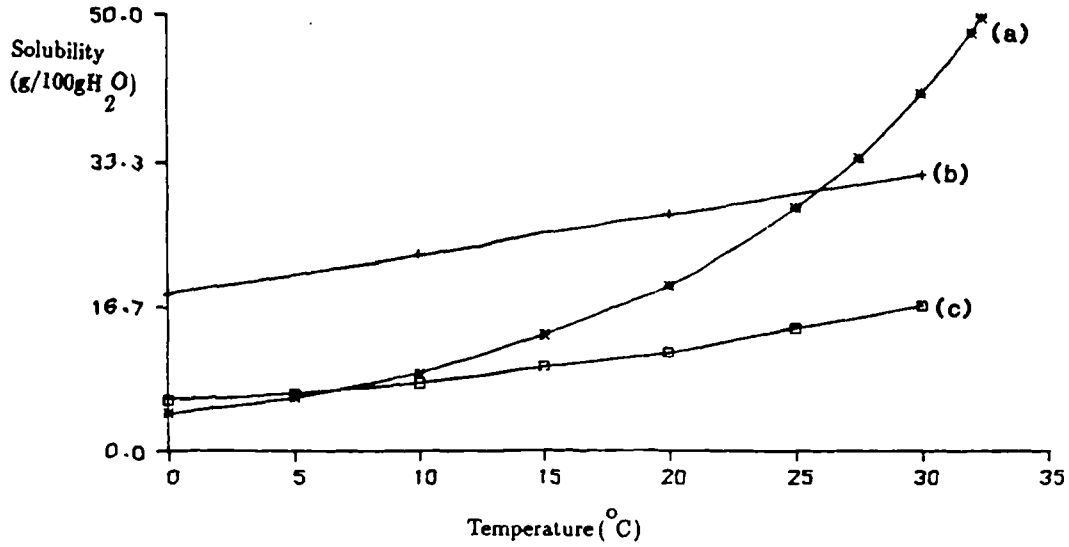

Figure 6.28: Plot illustrating the combined solubility curves of (a) $Na_2SO_4.10H_2O$, (b) $NH_4H_2PO_4$ and (c) $AlK(SO_4)_2.12H_2O$.

6.15. The subscript in each case is the standard deviation.

The determined metastable zone widths are significantly larger than those recorded for $AlK(SO_4)_2.12H_2O$ and $NH_4H_2PO_4$, implying that greater supersaturations can be achieved with $Na_2SO_4.10H_2O$ than $AlK(SO_4)_2.12H_2O$ and $NH_4H_2PO_4$ before the onset of nucleation. Previous nucleation studies on $Na_2SO_4.10H_2O$ [10] have not been able to determine the metastable zonewidth due to instrument constraints. The measured metastable zonewidth during seeded nucleation has been observed [11], ranging from 0.29^0C to 0.60^0C, depending on the rate of cooling employed. The determined saturation temperatures are in reasonable agreement with the literature data; the saturation temperatures determined by turbidometry showing slightly better agreement than those based on conductivity. The determined orders of reaction for techniques show significant variations, ranging from 3.68 to 6.98 and may be attributed to the variations in determined crystallisation temperatures observed during this study. These determined orders of reaction are in reasonable agreement with a previous study [11], which reported an order of reaction of 2.55 for $Na_2SO_4.10H_2O$.

The entropies and enthalpies relating to the dissolution process can be calculated

from the Van Hoff isotherm using equation 6.1. The determined values are compared and contrasted to calculated values based on literature saturation temperatures in table 6.16.

g Na_2SO_4 per 100g H_2O	Saturation Temperature (^0C) [7]	Saturation Temperature (^0C)	Max. M.S.Z.W. (^0C)	Order of Reaction
10.9	20	$21.76_{2.43}$	33.20	$6.25_{3.25}$
28.0	25	$26.07_{2.80}$	31.13	$3.68_{1.29}$
41.2	30	$29.10_{3.41}$	17.76	$6.98_{1.92}$

Table 6.15: Comparison of determined saturation temperatures, maximum metastable zonewidths and orders of reaction based on turbidity to literature saturation data.

Type	Enthalpy of Dissolution (J/mol*K)	Entropy of Dissolution (J/mol)	Correlation Coefficient
Literature	$5.54x10^4$	$1.97x10^3$	-0.99
Turbidity	$7.50x10^4$	$2.62x10^3$	-0.99

Table 6.16: Comparison of determined enthalpies and entropies of dissolution for $Na_2SO_4.10H_2O$ to literature data.

The high degree of ideal solution behaviour predicted (illustrated by the correlation coefficient) and the predicted enthalpies and entropies of dissolution is comparable to that predicted from literature data.

It was observed during a slow cooling/heating cycle that if very slow rates of cooling were employed, e.g. of the order of ^0C/hour rather than ^0C/minute, then different behaviour of the solution turbidometry were observed. Upon very slow cooling, the solution transmittance drops gradually, rather than the sudden drop that would be expected upon encountering the metastable zone edge. A typical example of this slow

decrease in solution transmittance is shown in figure 6.29. The temperature and turbidity curves are compared and contrasted to the solubility curves of the two possible phases that can be present at this solution temperature range, i.e. $Na_2SO_4.10H_2O$ and $Na_2SO_4.7H_2O$ [7]. Table 6.17 highlights the slopes, intercepts and correlation coefficients of the best fitting lines through each of these data sets.

What is immediately apparent from table 6.17 and figure 6.29 is that there is agreement between the data derived from turbidity measurements and the solubility curve for $Na_2SO_4.7H_2O$. This is immediately apparent upon comparison of the slopes of each of these lines in table 6.17. Comparison of a number of runs reproduces this behaviour and seems to confirm these findings. Visual inspection of the solution during this slow cooling cycle did not reveal the presence of any nuclei and filtration of the solution did not yield any crystallites. Hence it would appear that fast cooling of a solution of Na_2SO_4 allows $Na_2SO_4.10H_2O$ to crystallise whereas upon very slow cooling, the metastable $Na_2SO_4.7H_2O$ phase slowly crystallises, which can be observed by turbidometry.

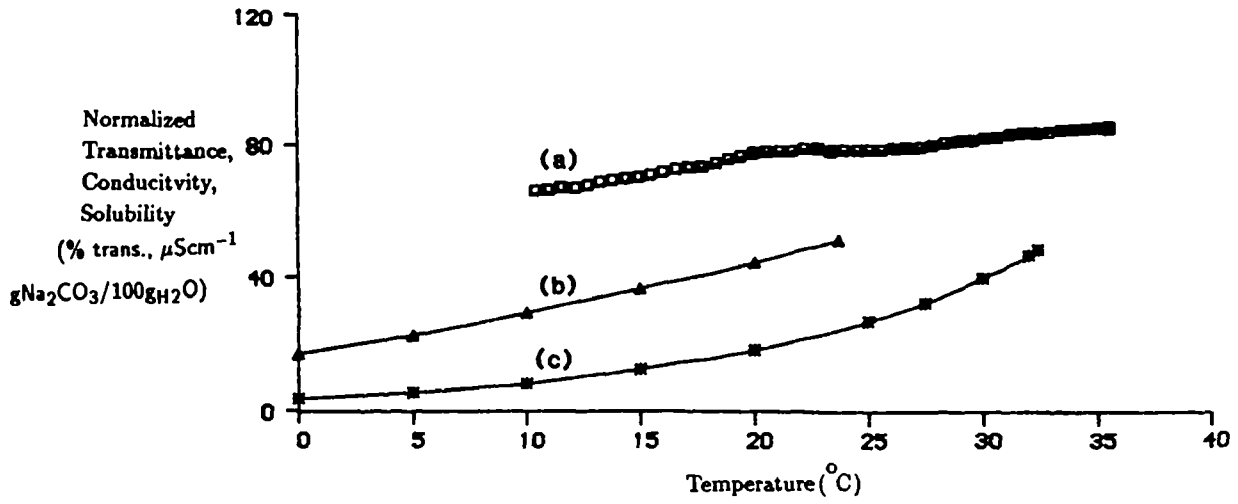

Figure 6.29: Comparison of measured solution (a) transmittance to solubility curves for (b) $Na_2SO_4.7H_2O$ and (c) $Na_2SO_4.10H_2O$.

Data Set Type	Slope of Best Fitting Straight Line	Intercept of Best Fitting Straight Line	Correlation Coefficient
$Na_2SO_4.10H_2O$	0.13	1.23	-0.97
$Na_2SO_4.7H_2O$	0.82	22.57	0.97
Solution Transmittance Data	0.81	59.21	-0.98

Table 6.17: Comparison of solubility curves for $Na_2SO_4.10H_2O$ and $Na_2SO_4.7H_2O$ to turbidity and conductivity measurements for a Na_2SO_4 based solution cooled in the order of ^0C/hour.

6.4.1.2 Interfacial Energy Determination

A solution containing 41.2g Na_2SO_4 per 100g H_2O (this corresponding to a saturation temperature of 30^0C) was crash cooled into the metastable zone indicated in table 6.15. Typical undercooling and induction time and measurements obtained are highlighted in table 6.18. The recorded undercoolings and induction times are represented by "ΔT" and "τ" respectively.

The expected trend of increasing undercooling leading to decreasing induction times cannot be discerned due to the high degree of scatter in the determined crystallisation temperatures and induction times, which are reflected in the low correlation coefficient obtained in figure 6.30 where $\ln(\tau)$ vs $T^{-3}\ln(S)^{-2}$ is plotted. The resultant determined interfacial energy is highlighted in table 6.20.

The large variations in induction time measurements are reflected in the large standard deviation obtained for the resultant determined interfacial energy. The measured interfacial energy is significantly greater than the corresponding energies obtained for $AlK(SO_4)_2.12H_2O$ and $NH_4H_2PO_4$, falling in the mJm^{-2} range.

An interfacial energy may be calculated using the relationship derived by Söhnel (equation 6.2). If the heat of crystallisation (ΔH_c) and the molar volume are taken to be $78.30KJmol^{-1}$ and $9.73x10^7m^3$ respectively [6], then the interfacial energy γ is calculated to be as $78.90mJm^{-2}$. This value is somewhat higher than the values

determined, however as previously mentioned [8,9], the relationship highlighted in equation 5.24 needs further refinement before successful application to soluble salts.

ΔT^t (K)	τ (mins)
18.49	16.31
14.53	11.29
13.72	13.80
12.22	165.56
11.88	262.13

Table 6.18: Typical induction time measurements for $Na_2SO_4.10H_2O$, based on turbidometric measurements.

Interfacial Energy ($10^{-4}Jm^{-2}$)	$37.54_{9.76}$

Table 6.19: Induction time based interfacial energy, determined from turbidometric measurements for $Na_2SO_4.10H_2O$.

Thus it may be summarised for the nucleation of $Na_2SO_4.10H_2O$, that crystallisation temperatures are much more susceptible to the influence of heterogeneous nuclei than dissolution temperatures. This was reflected in the determined saturation temperatures which showed good correlation to previous studies. The determined crystallisation temperatures showed a large experimental spread and thus significant variations in the maximum metastable zonewidth were obtained. If cooling a solution was of the order of ^0C/min, then the resultant precipitate was $Na_2SO_4.10H_2O$. When a cooling rate of the order of ^0C/hour was employed, then slow crystallisation of the metastable phase $Na_2SO_4.7H_2O$ was observed. Measured induction times were again prone to the influence of heteronuclei, leading to large fluctuations in the measured induction times and consequently a large standard deviation in the measured interfacial energy.

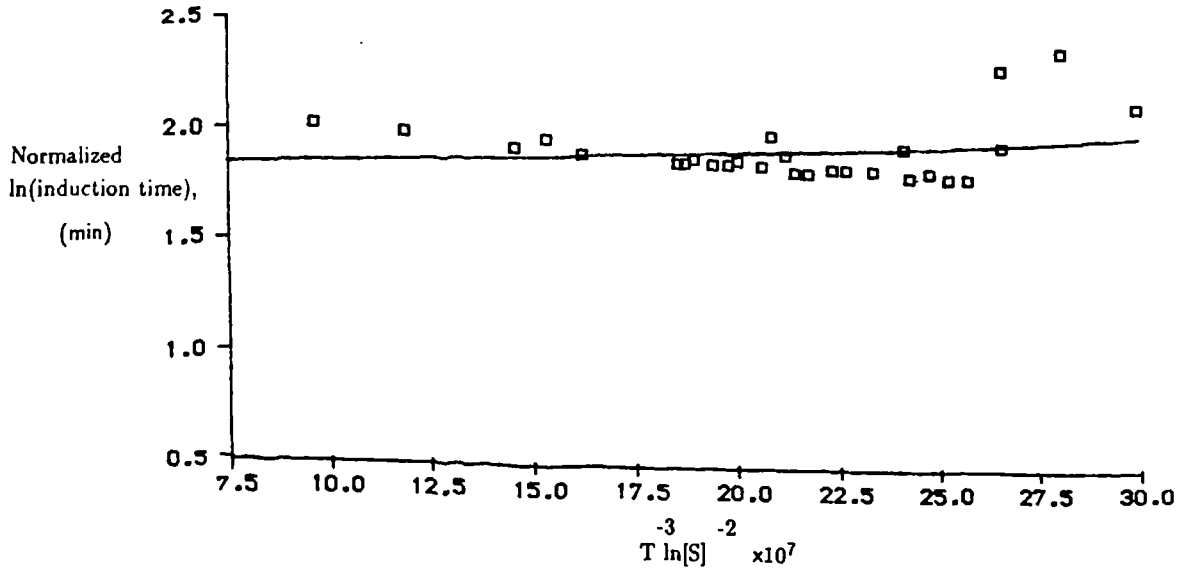

correlation coefficient: a) 38%

Figure 6.30: Plot of ln (τ) versus $T^{-3}ln(S)^{-2}$ based on turbidometric measurements for $Na_2SO_4.10H_2O$.

The determined interfacial energy was significantly greater than those obtained for $AlK(SO_4)_2.12H_2O$ and $NH_4H_2PO_4$, but is also somewhat lower than the predicted interfacial energy, following the pattern observed for $AlK(SO_4)_2.12H_2O$ and $NH_4H_2PO_4$. This may be accounted for by the presence of heteronuclei and the need for further refinement of the model which the prediction is based on, for successful application to soluble systems.

6.4.2 Sodium carbonate decahydrate, $Na_2CO_3.10H_2O$

6.4.2.1 Saturation curve And Metastable Zonewidth Determination

Sodium carbonate (Na_2CO_3) displays similar crystallisation characteristics to sodium sulphate, with the formation of a variety of hydrated phases, depending on the the temperature of crystallisation. The solubility of the Na_2CO_3-H_2O system [7] is highlighted in figure 6.31. The hydrated phases (a) sodium carbonate decahydrate ($Na_2CO_3.10H_2O$), (b) sodium carbonate heptahydrate ($Na_2CO_3.7H_2O$) and (c) sodium carbonate monohydrate ($Na_2CO_3.H_2O$) are all observed. Sodium carbonate decahy-

drate was chosen for this study. A typical slow cooling/heating cycle are shown in figures 6.32 and 6.33.

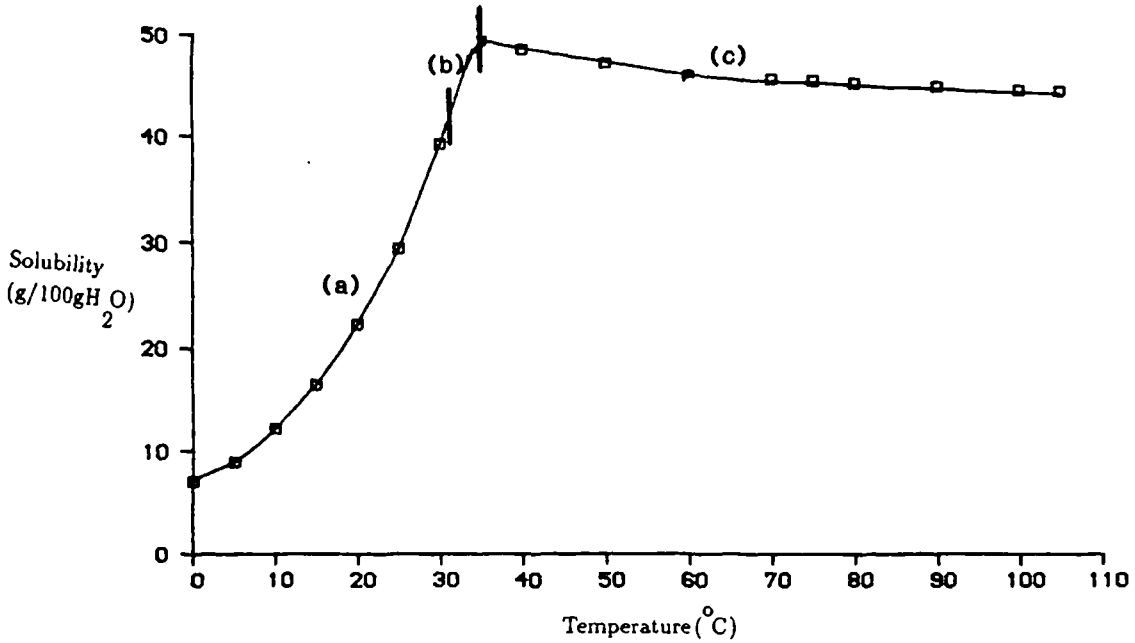

Figure 6.31: Solubility curve of the Na_2CO_3-H_2O system [7].

Similar crystallisation characteristics to $Na_2SO_4.10H_2O$ can be seen in figures 6.32 and 6.33; i.e. the large changes in solution transmittance during crystallisation and dissolution. As for $Na_2SO_4.10H_2O$, a significant increase in solution temperature occurs upon crystallisation. This sharp increase may be readily detected and thus as for $Na_2SO_4.10H_2O$, temperature may be employed as a means of detecting the onset of nucleation in a solution.

Saturation curve determination followed the same procedures adopted for $AlK(SO_4)_2.12H_2O$, $NH_4H_2PO_4$ and $Na_2SO_4.10H_2O$; i.e. 120 minutes preheating time and 20^0C preheating temperature. It was assumed that a 10% drop in solution transmittance from those recorded for a clear solution was representative of the nucleation process. Similarly, when the solution transmittance came within 10% of that recorded for a clear solution, then dissolution is said to have occurred.

Three concentrations of sodium carbonate, known to crystallise as sodium carbonate decahydrate were studied in order to determine the saturation curve. Table 6.20 compares and contrasts the determined saturation temperatures, maximum

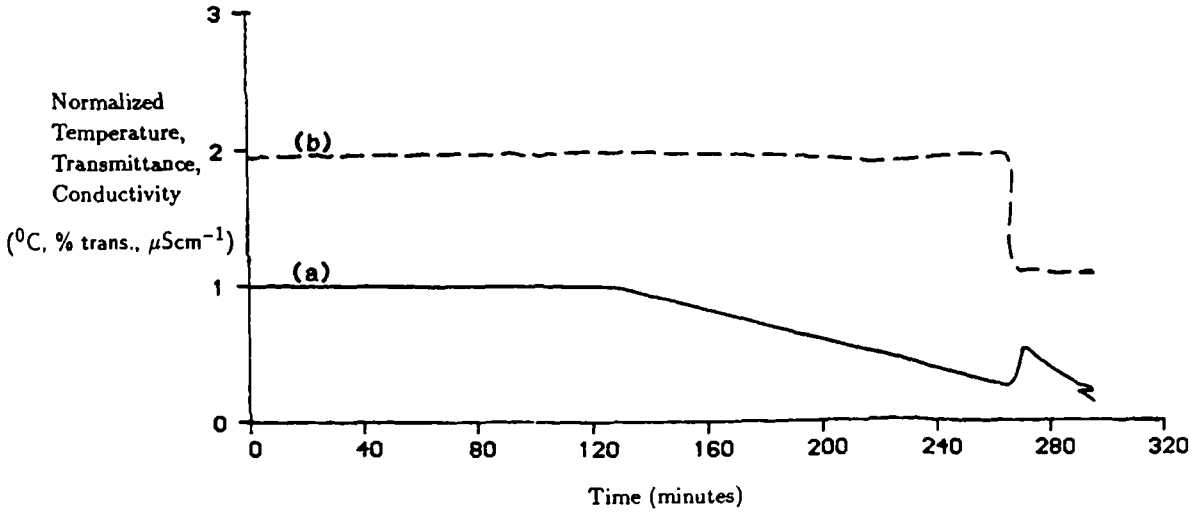

a) temperature b) transmittance

Figure 6.32: Schematic of the crystallisation of $Na_2CO_3.10H_2O$ that occurs during the slow cooling of a solution, as detected by turbidometry.

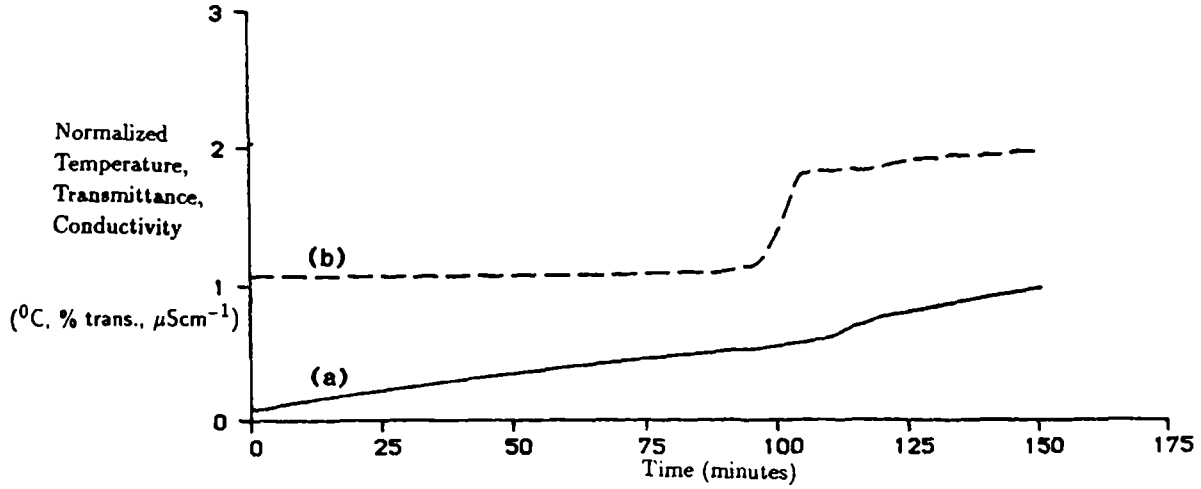

a) temperature b) transmittance

Figure 6.33: Schematic of the dissolution of $Na_2CO_3.10H_2O$ that occurs during the slow heating of a crystallised solution, as detected by turbidometry.

metastable zonewidths and orders of reaction with literature saturation data. In general, good agreement is noted between the determined saturation temperatures and the saturation temperatures determined from previous studies. The determined metastable zonewidths are not as large as those determined for $Na_2SO_4.10H_2O$, hence the degree of supersaturation obtained before the onset of nucleation is less for $Na_2CO_3.10H_2O$ than $Na_2SO_4.10H_2O$. In terms of determined maximum undercooling for all four systems studied, the system with the maximum allowable undercooling was $Na_2SO_4.10H_2O$ followed by $Na_2CO_3.10H_2O$, $NH_4H_2PO_4$ and $AlK(SO_4)_2.12H_2O$.

Based on these determined saturation temperatures, enthalpies and entropies of dissolution may be calculated and compared (table 6.21) to those determined from previous studies.

The same trends are noted in this case as were noted for the other systems: the determined enthalpy and entropy of dissolution determined show reasonable correlation to the enthalpy and entropy of dissolution determined, and a high degree of solution ideality comparable to previous studies is indicated.

g Na_2CO_3 per 100g H_2O	Saturation Temperature (^{0}C) [7]	Saturation Temperature (^{0}C)	Max. M.S.Z.W. (^{0}C)	Order of Reaction
22.2	20	$22.67_{2.28}$	21.99	$0.10_{0.47}$
29.4	25	$27.14_{1.08}$	23.23	$1.13_{1.01}$
39.2	30	$31.61_{1.02}$	20.64	$6.31_{1.36}$

Table 6.20: Comparison of determined saturation temperatures, maximum metastable zonewidths and orders of reaction based on solution transmittance, to literature saturation data.

Type	Enthalpy of Dissolution (J/mol*K)	Entropy of Dissolution (J/mol)	Correlation Coefficient
Literature	$4.00x10^4$	$1.47x10^3$	1.00
Turbidity	$4.54x10^4$	$1.64x10^3$	1.00

Table 6.21: Comparison of determined enthalpies and entropies of dissolution based on turbidometry to determined values based on previous studies, for $Na_2CO_3.10H_2O$.

6.4.2.2 Interfacial Energy Determination

A solution of $29.4gNa_2CO_3/100gH_2O$ was crash cooled into the metastable zone indicated in table 6.20. Some typical undercoolings (ΔT) and induction times (τ) determined during crash cooling are highlighted in table 6.22.

ΔT (^0C)	τ (mins)
18.50	45.15
17.44	272.19
16.40	20.07
14.84	22.58
13.34	28.75

Table 6.22: Typical induction time measurements for $Na_2CO_3.10H_2O$, based on turbidometric measurements.

The significant variations in determined induction times for each detection technique means that no relationship between undercooling and measured induction times can easily be discerned. The plot of log (τ) versus $T^{-3}ln(S)^{-2}$ (figure 6.34) highlights the degree of experimental scatter present.

The resultant determined interfacial $energy_{standarddeviation}$ is shown in table 6.23. The relatively large standard deviation is indicative of the large degree of scatter in the determined induction times. The determined interfacial energy again falls

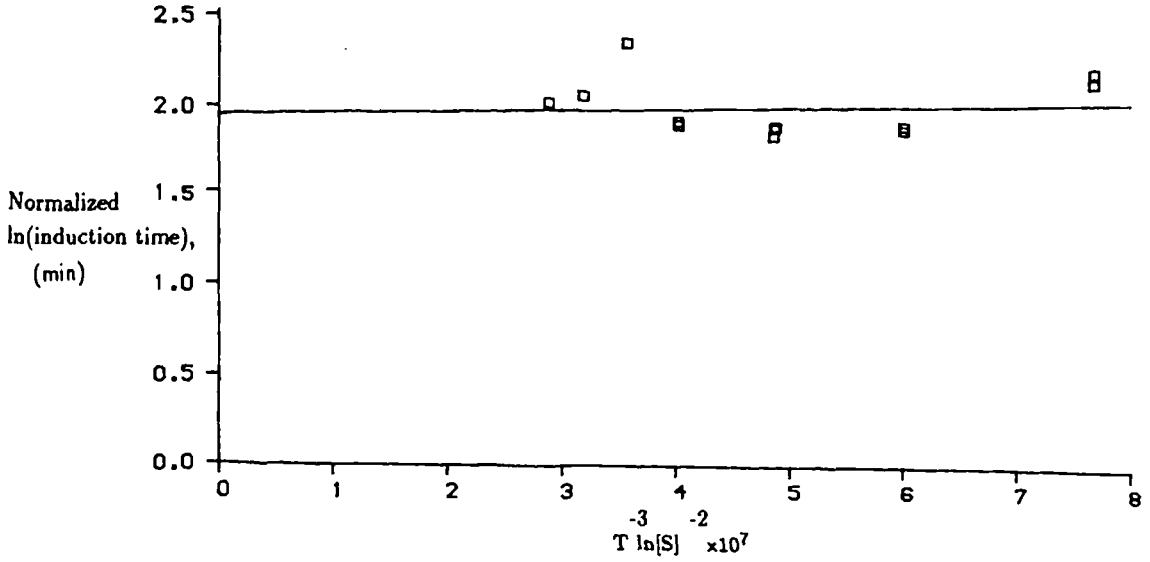

Correlation coefficient: a) 57%

Figure 6.34: Plot of ln (τ) versus $T^{-3}ln(S)^{-2}$ based on turbidometric and measurements for $Na_2SO_4.10H_2O$.

into the mJm^{-2} range, but is significantly smaller than the corresponding interfacial energy determined for $Na_2SO_4.10H_2O$.

As for $Na_2SO_4.10H_2O$ (6.4.1.2), an interfacial energy may be calculated using the Söhnel relationship. If the heat of crystallisation (ΔH_c) and the molar volume (V_m) are assumed to be $67.83KJmol^{-1}$ and $7.36x10^7m^3$ [6], then from equation 5.24, the interfacial energy "γ" may be calculated to be $82.3mJm^{-2}$. As noted for all the systems studied, the determined interfacial energy is notably lower than the predicted energy, for reasons highlighted earlier.

Interfacial Energy ($10^{-4}Jm^{-2}$)	$26.94_{8.53}$

Table 6.23: Induction time based interfacial energy determined from turbidometric measurements, for $Na_2CO_3.10H_2O$.

6.4.3 Crystallisation of Na_2CO_3-Na_2SO_4 mixed systems

In chapter five, the role of sodium carbonate in the agglomeration of the various phases crystallised in the Na_2CO_3-Na_2SO_4-H_2O system was investigated. A possible parallel in this study would be an investigation of the role and influence of Na_2CO_3 on the nucleation of Na_2SO_4. As in chapter four a series of Na_2CO_3:Na_2SO_4 ratios covering a range from predominantly carbonate based to predominantly sulphate based, e.g. 5:1 - 1:5 molar ratio Na_2CO_3:Na_2SO_4 could be studied. Determination of saturation temperatures and induction times and resultant interfacial energies may allow the elucidation of the influence of the addition of sodium carbonate on the nucleation of $Na_2SO_4.10H_2O$.

As an example, a crash cool has been carried out on a 1:1 mole ratio Na_2CO_3:Na_2SO_4. Saturation data was assumed to be equivalent to previously studies [1]. The resultant determined interfacial energy is highlighted in table 5.26.

Although there are again significant variations in the determined induction time measurements due to the influence of heteronuclei, the determined interfacial energy for a precipitated solution of 1:1 mole ratio Na_2SO_4:Na_2CO_3 shows good correlation to the determined interfacial energy for $Na_2SO_4.10H_2O$. However from chapter five (section 5.3.1), the crystallising phase at this Na_2SO_4:Na_2CO_3 concentration was determined to be burkeite $Na_2CO_3(Na_2SO_4)_2$. Thus it may be tentatively concluded that the interfacial energy for $Na_2CO_3(Na_2SO_4)_2$ is approximately $36.72 \times 10^{-4} Jm^{-2}$; and is similar to the interfacial energy determined for $Na_2SO_4.10H_2O$. Hence, a plot of determined interfacial energy versus Na_2CO_3:Na_2SO_4 ratio may be obtained (figure 6.38), showing the interfacial energy progression from $Na_2SO_4.10H_2O \longrightarrow Na_2CO_3(Na_2SO_4)_2 \longrightarrow Na_2CO_3.10H_2O$.

Interfacial Tension ($10^{-4} Jm^{-2}$)	$36.72_{11.57}$

Table 6.24: Induction time based interfacial energy determined from induction turbidometric measurements, for a 1:1 mole ratio of Na_2CO_3:Na_2SO_4.

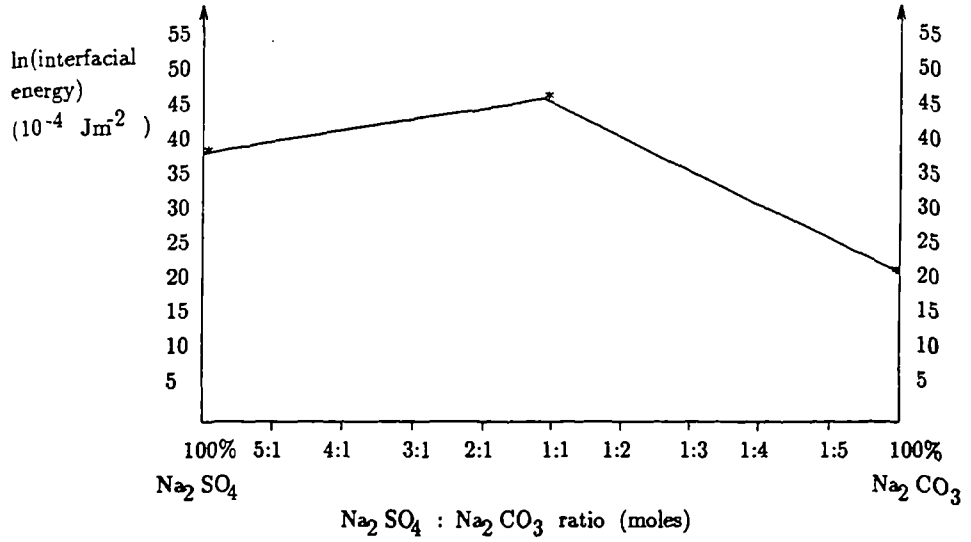

Figure 6.35: Interfacial energy versus Na_2CO_3:Na_2SO_4 ratio.

6.4.4 Summary

In general, the same trends noted for the model systems $AlK(SO_4)_2.12H_2O$ and $NH_4H_2PO_4$ are noted for the sodium carbonate/sulphate systems; i.e. less experimental scatter for dissolution based parameters than for precipitation based parameters. The determined saturation curves for both $Na_2CO_3.10H_2O$ and $Na_2SO_4.10H_2O$ show good correlation to previous studies, with the determined metastable zonewidths for these two systems significantly higher than those determined for $AlK(SO_4)_2.12H_2O$ and $NH_4H_2PO_4$, implying that greater supersaturations can be obtained for $Na_2SO_4.10H_2O$ and $Na_2CO_3.10H_2O$ before the onset of nucleation. Upon crystallisation of either system, a significant increase in solution temperature was detected, inidicating that temperature may be monitored to detect the onset of nucleation.

Based on observations of $AlK(SO_4)_2.12H_2O$ and $NH_4H_2PO_4$, determined interfacial energies were obtained from turbidometric induction time measurements. However, significant experimental scatter due to the influence of heteronuclei was still observed. The subsequently derived interfacial energies were significantly higher than those determined for $AlK(SO_4)_2.12H_2O$ and $NH_4H_2PO_4$, with the interfacial energy for $Na_2SO_4.10H_2O$ greater than that of $Na_2CO_3.10H_2O$, but were notably

lower than predicted interfacial energies due to the influence of these heteronuclei.

The interfacial energy of a solution containing a 1:1 molar mixture of Na_2CO_3:Na_2SO_4 (from section 5.3.1 determined to be burkeite ($Na_2CO_3(Na_2SO_4)_2$) was obtained and found to be similar to the interfacial energy determined for $Na_2SO_4.10H_2O$, possibly a reflection of the higher sulphate content of this double salt.

6.5 Conclusions

The use of an automated crystallisation cell can allow impartial measurement of various crystallisation parameters such as precipitation and dissolution temperatures and induction times. Studies were carried out on the crystallisation characteristics of $AlK(SO_4)_2.12H_2O$, $NH_4H_2PO_4$, $Na_2SO_4.10H_2O$ and $Na_2CO_3.10H_2O$. In general it was observed that precipitation based parameters were much more susceptible to the influence of heteronuclei than dissolution based parameters, a higher degree of experimental scatter observed for the former measurements. Thus parameters such as saturation temperatures, enthalpies and entropies of dissolution can be determined with a higher degree of reliability than, e.g. precipitation temperatures and interfacial energies.

When turbidometry, conductivity and temperature are compared as nucleation detection techniques, a number of points became apparent: generally turbidometry was observed to be the more sensitive technique; larger changes occuring in solution transmittance than conductivity during nucleation. Conductivity did not provide as good a means of detecting nucleation as turbidometry; if a system contains hydrogen bonding or it's measured conductivity is temperature dependent, then the the choice of a detection limit is complicated and the measured conductivity cannot be viewed as reliable.

Temperature may be employed as a means of detecting the onset of nucleation in certain cases, e.g. $Na_2SO_4.10H_2O$ and $Na_2CO_3.10H_2O$ but is obviously dependent on the magnitude of the heat of crystallisation. The determined metastable zonewidths were significantly less for $AlK(SO_4)_2.12H_2O$ than for $NH_4H_2PO_4$, $Na_2SO_4.10H_2O$

and $Na_2CO_3.10H_2O$, implying that greater supersaturations may be obtained for the latter three compounds before the onset of nucleation.

The interfacial energies based on induction time measurements for each technique showed significant variations, hence no obvious trend as to what detection technique is the most suitable for interfacial energy calculations could be discerned. During nucleation, the rates of change of solution conductivity were in general significantly less than the corresponding turbidometric measurements, implying that conductivity is less sensitive to the onset of nucleation than turbidometry. The calculated interfacial energies (based on induction time measurements) in all cases were notably smaller than the predicted interfacial energies due to the influence of heteronuclei, which lower the value of the determined interfacial energies. It is also likely that since only low supersaturations can be achieved for soluble systems by conventional temperature lowering, the supersaturations obtained are not of a sufficient magnitude to achieve pure homogeneous nucleation. However, the fact that the predicted interfacial energies are based upon a model that needs further refinement before successful application to soluble systems, must also be taken into account.

Further experimental studies could focus on the influence of Na_2CO_3 addition on the interfacial energy of $Na_2SO_4.10H_2O$. A whole range of Na_2CO_3:Na_2SO_4 ratios could be examined and the resultant plot of interfacial energy versus Na_2CO_3:Na_2SO_4 mole ratio allow the dependence of interfacial energy upon Na_2CO_3 content to be elucidated.

Future developments of this automated cell could include higher rates of stirring and the presence of baffles, to ensure that a greater degree of agitation is present and thus more homogeneous conditions are found throughout the solution. Utilising a more intense light source to measure solution transmittance, e.g. a He-Ne laser may improve the sensitivity of the cell to crystallisation. This in combination with a detector situated at 90^0 to the light source (figure 6.36), will improve further the sensitivity to detect nucleation. This setup has been used previously by Wojciechowski et al [12] in precipitation studies of $BaSO_4$ and can be employed in the measurement of extremely short induction times that exist at very high supersaturations.

Although employing a more intense light source may allow greater sensitivity to

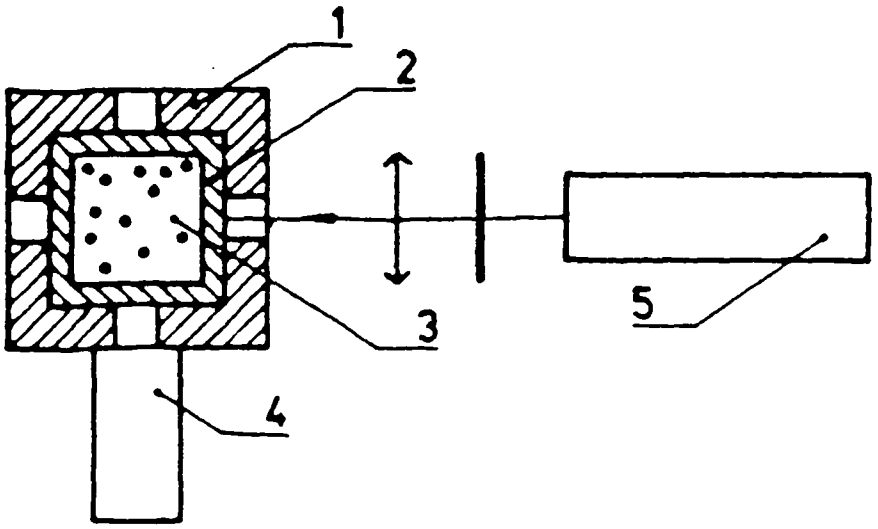

1) thermostat 2) glass cuvette 3) Ba_2SO_4 solution 4) photomultiplier 5) He-Ne laser

Figure 6.36: Crystallisation cell used in the study of $BaSO_4$ precipitation [12].

the onset of nucleation, the crystallising phase cannot be identified without separation and analysis of the crystallites by, e.g. chemical analysis or powder diffraction. An automated cell employing a more sensitive light source in conjunction with an x-ray source [4] (figure 6.37) could be employed, so that in-situ identification of the crystallising phase is obtained. A further comparison may be drawn between turbidometry and x-rays as tools for the detection of the onset of nucleation.

In the study of soluble inorganic salts, it is indicated that a much higher degree of supersaturation is required than can be obtained by conventional temperature lowering in order to achieve primary homogeneous nucleation. The addition of an organic solvent, e.g. acetone to the aqueous solution could be employed for this purpose and could allow more accurate estimations of the interfacial energy.

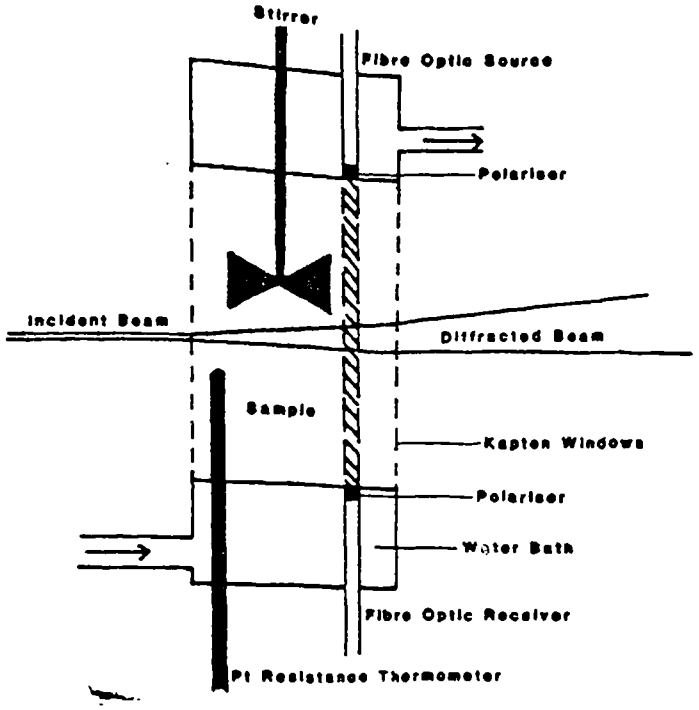

Figure 6.37: Crystallisation cell employing turbidometry and x-rays as tools for the detection of crystallisation and dissolution [4].

6.6 References

1. J. Mylardz and A.G. Jones; Powder Technology, 65 (1991) 187-194

2. J.W. Mullin & J.J. Jancic; Trans. I. ChemE, 57 (1979) 188-193

3. A. Stewart, PhD Thesis, University of Strathclyde, (1988)

4. A. Gerson, PhD Thesis, University of Strathclyde, (1990)

5. O. Söhnel & J.W. Mullin; J. Cryst. Growth 44 (1978) 377-382

6. J.W. Mullin; "Crystallisation" Second Edition, Butterworths, London, (1972)

7. A.L. Seidell; "Solubilities of Inorganic and Metal-Organic Compounds", Van Nostrand Press, (1958-1965)

8. J.W. Mullin & S. Žáček; J. Cryst. Growth 53 (1981) 515-518

9. O. Söhnel; J. Cryst. Growth 57 (1982) 57 101-108

10. J. Nývlt; private communication (1991)

11. J. Nývlt, R. Rychlý, J. Gottfried & J. Wurzelová; J. Cryst. Growth 6 (1970) 151-162

12. K. Wojciechowski & W. Kibalczyc; J. Cryst. Growth 76 (1986) 379-382

Chapter 7

The Influence Of Processing Conditions On The Particulate Properties Of Industrially Crystallised Burkeite

Contents

7.1 Introduction

Carbonate and sulphate based materials can be crystallised to form high surface area, highly porous powders, which can be used for a variety of purposes, e.g. catalysts. One usage of particular interest of these materials are as carrier materials as well as builders in the detergent industry. A carrier material is composed of a crystalline matrix which forms a porous close-packed structure. Pore size is typically of the order (0.1 - 50)μm. However a pore size range of (0.5-3)μm is desirable for detergent operation, allowing efficient uptake and retention of the various liquid components required for washing duty - e.g. surfactants, perfumes etc. For maximum liquid carrying capacity a carrier requires a high internal porosity and a pore size that is significantly smaller than the inter-particle pore size distribution. The optimum method of achieving this is to have the crystallisation and agglomeration of dendrites forming the matrix.

Common detergent builders are phosphates, carbonates and sulphates. Sodium tripolyphosphate hexahydrate $Na_5P_3O_{10}6.H_2O$ was the dominant carrier for many years due to it's ease of formation and ready modification to the optimum dendritic form, as well as being a very effective builder. However, environmental considerations (e.g. eutrification of lakes, etc) have lead to a search for alternative materials that can be utilised as builders. Sodium carbonate monohydrate, $Na_2CO_3.H_2O$ and the double salt, burkeite $Na_2CO_3(Na_2SO_4)_2$ can be, and have been employed as replacement builders/carriers for phosphates, principally because carbonate and sulphate based materials are relatively inexpensive, easy to obtain and are ecologically more acceptable. Both burkeite and sodium carbonate monohydrate were first considered unsuitable as detergent builders/carriers [1,2,3], due to their tendency to form "block-like" agglomerates, with a pore size distribution too large for effective uptake and retention of the various detergent components. However certain polyacrylates allowed both burkeite and sodium carbonate monohydrate to be habit modified sufficiently to be used as effective carriers with the adequate pore size distribution for maximum uptake of the various liquid components [4-12].

This chapter presents a study of the crystallisation and agglomeration of habit

modified burkeite and resultant conversion to a powder suitable for detergent operation. The following points were investigated:

- The optimum porosity has been previously determined for a burkeite builder to occur within the pore size range (0.5-3 μm) [13]. A study was conducted to determine whether this pore size range occurred during the initial crystallisation/agglomeration period or during spray drying.

- The mechanical influences on burkeite crystallisation were investigated by observation of the effects of different impellers on the agglomeration/porosity relationship of a burkeite slurry system.

- Within a saturated slurry, there is a tendency for small particles to dissolve and larger particles to grow larger (known as Ostwald ripening), to minimize the surface energy of the system [14]. Hence, the slurry will tend towards a monosize particle distribution. The possibility of this phenomena existing for burkeite, thus influencing the particle agglomeration/powder porosity was investigated.

- The conditions chosen to spray dry a powder can significantly influence the resultant powder properties. Different drying regimes were employed during the spray drying of a burkeite powder, to investigate the effects on particle agglomeration/powder porosity.

Economically, it is important to have knowledge of the power requirements of an impeller, so that a balance may be struck between the most efficient impeller and that which is most cost effective. Torque measurements for each impeller were obtained, to calculate the power requirements for slurry agitation. From this it should be possible to calculate which impeller is the most desirable for burkeite production.

7.2 Industrial Crystallisation Of High Surface Area Powders

7.2.1 Particle Agglomeration

Previous work has concluded that the degree of agglomeration decreases with increasing intensity of agitation, mean crystal size and solid concentration [15] and increases with supersaturation [16,17] to a maximum plateau. Agglomeration can be separated into two areas:

- where the agglomeration occurs in the sub-micron range with no well developed single crystals [15,18,19].

- where well developed single crystals occur which then agglomerate over a large size range [15,20].

In most crystallising systems the rate of crystallisation is high, leading to small particles within the system. This will maximise the agglomeration [18,19], leading to the former case. The latter case is rarer and usually occurs at low supersaturations. The burkeite systems under consideration have been assumed as being examples of the former case. Different mechanisms have been proposed for agglomeration depending on whether the agglomeration is induced by fluid-mechanical processes, e.g. orthokinetic agglomeration [21] or whether agglomeration is due to particles subjected to collisions during Brownian motion, e.g. perikinetic agglomeration [21]. The effects on agglomeration and crystallisation by choice of impeller have not been thoroughly investigated. Agglomerate breakdown can occur by various processes - collisions between the impeller or vessel walls and the agglomerates, collisions between the aglomerates themselves, or agglomerate breakdown due to stresses induced by fluid motion. There has been controversy over the mechanism of agglomerate breakdown - Shamlou's model [22] proposed the erosion of agglomerates due to fluid induced stresses, rather than the total fragmentation model that has been proposed by DeBoer

and others [23]. The evidence for agglomerate beakdown due to collisions between the agglomerates themselves is rather contradictory and requires further investigation.

When a solid is added to a liquid, the solid will not encounter the liquid as discrete particles, rather, agglomeration of the solid will occur before the solid is dispersed. Hence breakdown of the agglomerates must occur before the solid may be dispersed into solution. It is the function of the impeller to breakdown these particulates and to ensure good dispersion and mixing of liquid and particles. It has been found that large impellers are more effective than small impellers at drawing solids into a liquid, but small impellers were observed to give higher shear rates than larger impellers, and thus were more effective for particle breakdown and efficient mixing [24].

The impellers belonged to either of two classes of influencing fluid flow; either radial or axial flow: Radial flow occurs when liquid is discharged from the impeller by centrifugal forces. Moving liquid impinges on the vessel wall, is split and re-entrained, causing further turbulence and mixing (figure 7.1). The impellers investigated that belonged to this class were the flat paddle and mini anchor impellers. Axial flow occurs when liquid enters the impeller and is discharged parallel to the impeller axis (figure 7.2). The marine propeller, MSPB and turbine impellers are examples of impellers belonging to this class.

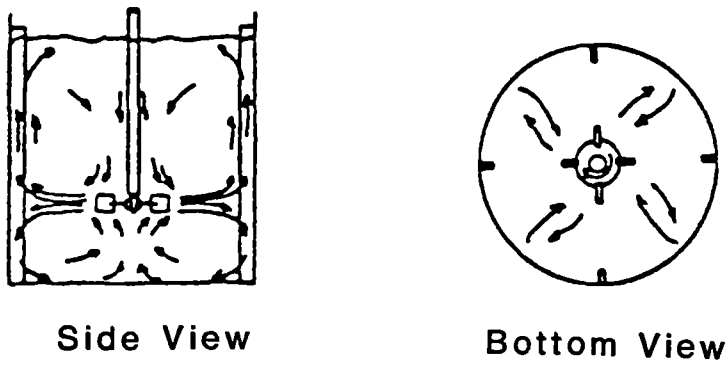

Figure 7.1: Representation of radial flow pattern within a stirred vessel [4].

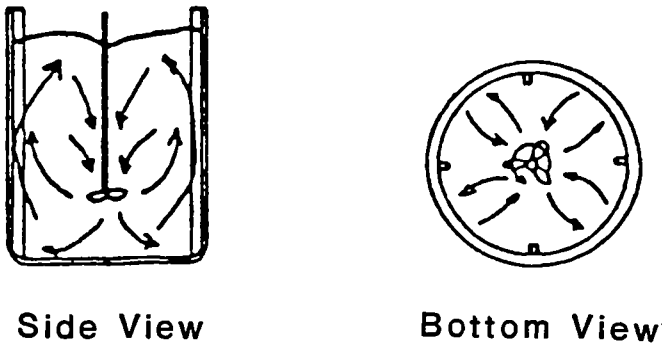

Figure 7.2: Representation of axial flow pattern within a stirred vessel [4].

7.2.2 Particle Formation By Spray Drying

A predominant process step in the production of detergent powders is spray drying. This process is commonly associated with detergent powders but is also a major process in the production of a variety of powders, ranging from food stuffs (e.g. powdered milk) to mineral ores [25]. Spray drying is normally described as the transformation of an initial feed (e.g. solids slurry) to a dried particulate form. This is normally achieved by the atomisation of the feed, which is then sprayed into a hot drying medium (normally air). Atomisation is the production of a fine spray from the feed and is the key process in achieving economic production of top quality products. The atomisation stage must create a spray for optimum evaporation conditions, leading to a dried product of the required characteristics. Atomisers can be split into 2 groups: rotary atomisers and nozzles. Rotary atomisers are used to produce fine grained products (approx. 30 - 120μm). They rely on centrifugal energy to create the spray and function by introducing the feed onto a rotating disc or wheel. The feed flows outward and disintegrates into a spray of droplets. An example of a rotary atomizer is shown in figure 7.3. Nozzle atomisers are used to produce coarser grained products (200-1000μm) and rely on pressure or kinetic energy to create a spray. Since nozzles operate at a lower slurry throughput than rotary atomisers, multiple nozzles are often employed for high throughputs. The feed is made to rotate within the nozzle forming

a cone shaped spray. A common nozzle atomiser is shown in figure 7.4. The position of the atomiser in relation to the drying air inlet position influences drying behaviour and subsequent powder properties. A variety of positions are available, however the three most common are co-current, counter-current and mixed flow systems (figures 7.5a - c). The feed and air flow can enter the spray-drying tower in the same direction (co-current arrangement), opposite directions (counter-current arrangement) or a combination of both arrangements (mixed flow arrangement). The arrangement chosen is dependent on the particles physical properties and the desired particle requirements. Normally if a material is heat sensitive or a fine grained powder is desired then a co-current arrangement is preferred, although scale-up problems may be encountered with this arrangement. Counter-current arrangements are used to produce a coarser powder and is normally used when a powder is not heat sensitive. A coarser powder is produced since there is more air-feed contact, therefore more collisons hence greater agglomeration. A mixed arrangement can also be used to produce a coarse powder, but is normally less economic than a counter-current arrangement.

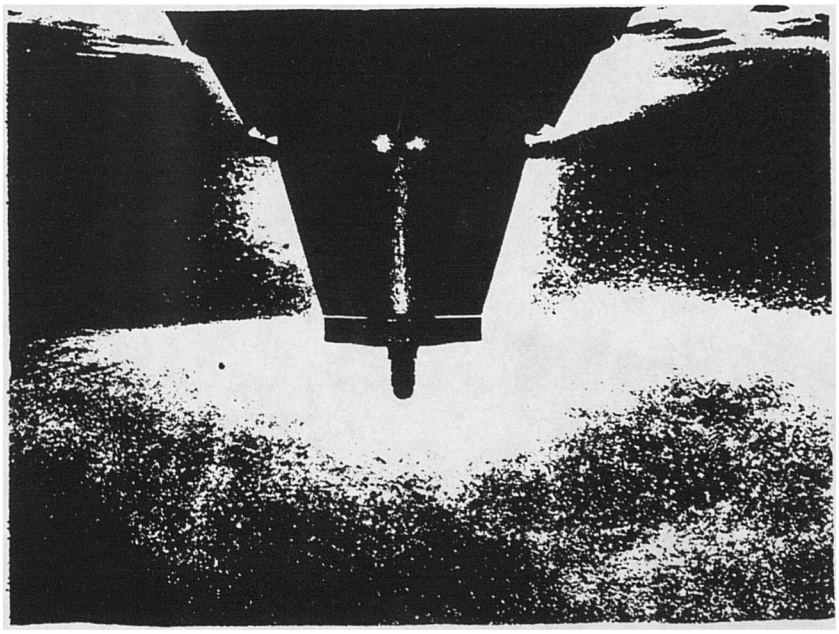

Figure 7.3: Example of a rotary atomiser [25].

Figure 7.6 illustrates a typical detergent powder production process. The initial solids/liquids charge is added to the crystalliser (crutcher). After the initial crystalli-

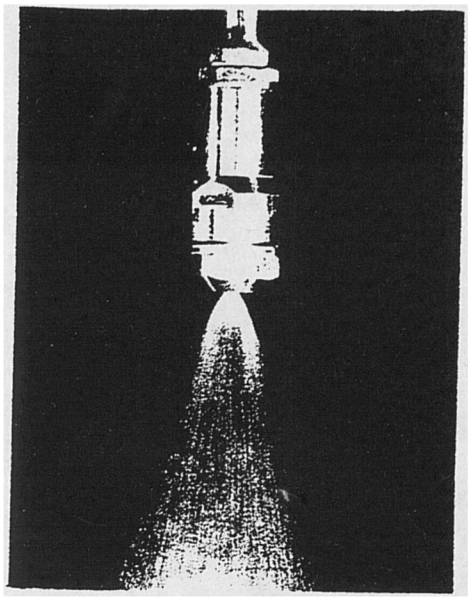

Figure 7.4: Example of a nozzle atomiser [25].

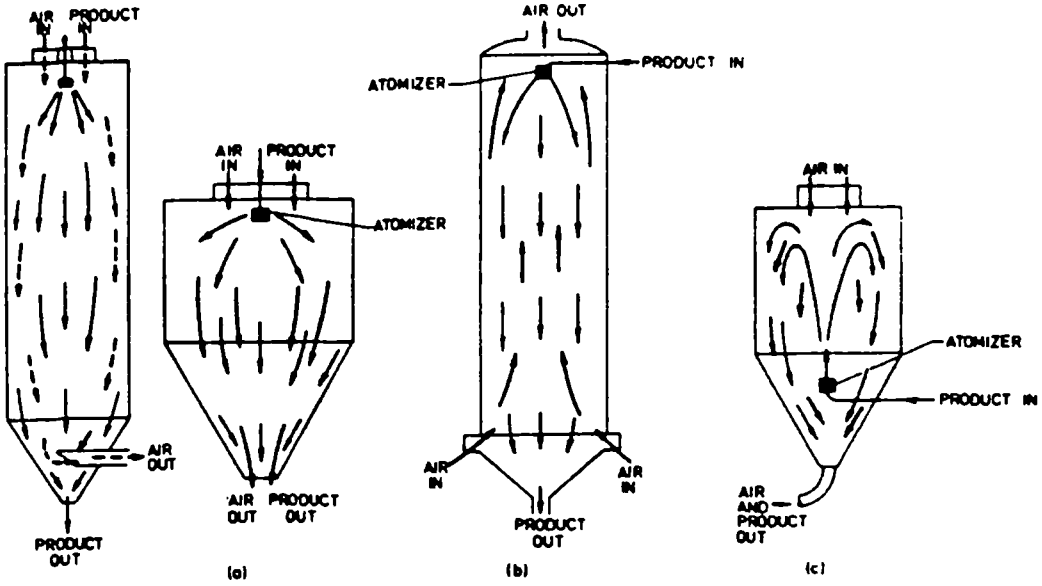

a) Co-current flow arrangment b) Counter-current flow arrangement

c) Mixed flow arrangement

Figure 7.5: Examples of spray drying tower arrangements [25].

sation/reaction period, the resultant solids slurry (typically 80 -100μm) is pumped through a mill (reducing particle size thus preventing atomiser obstruction) then into a spray drying tower. A counter-current spray/air contact arrangement is employed with nozzle atomisers producing a coarse powder (500-600μm). This is normally desired to prevent dusting problems during production and for the consumer. The ratio of nozzle input/output diameters determines the width of the spray cone that develops within the tower and the moisture content of the resultant powder - a large ratio means that the resultant powder is much coarser, due to the longer residence time needed within the tower to reduce moisture to desired levels. The longer the residence time, the greater the number of particle collisions, hence the greater the agglomeration. Obviously the cone width must be controlled so that the spray is not allowed to impact on the tower walls, leading to caking problems. The particulate product is then removed, with the entrained fines (typically 100-120μm) separated from the output air via a cyclone/scrubber, then normally recycled into the feed. The resultant powder is consequently sprayed with various postdoped liquids e.g. perfumes, optical brighteners etc, which are incorporated into the powder pores by capilliary action, before further processing/packaging etc.

7.3 Methodology

7.3.1 Techniques For Particle Characterisation

7.3.1.1 X-Ray Powder Diffraction

The bulk chemical composition of the powder samples obtained was determined by X-ray powder diffraction, on a conventional Phillips PW1050 diffractometer. As described in section 5.2.1, comparison [26] of the obtained spectra to determined standard spectra [JCPDS] allows identification of the phases present.

7.3.1.2 Scanning Electron Microscopy

Scanning Electron Microscopy (SEM) and Energy Dispersive X-Ray Microanalysis (EDX) were employed to identify the chemical nature of the individual particulates

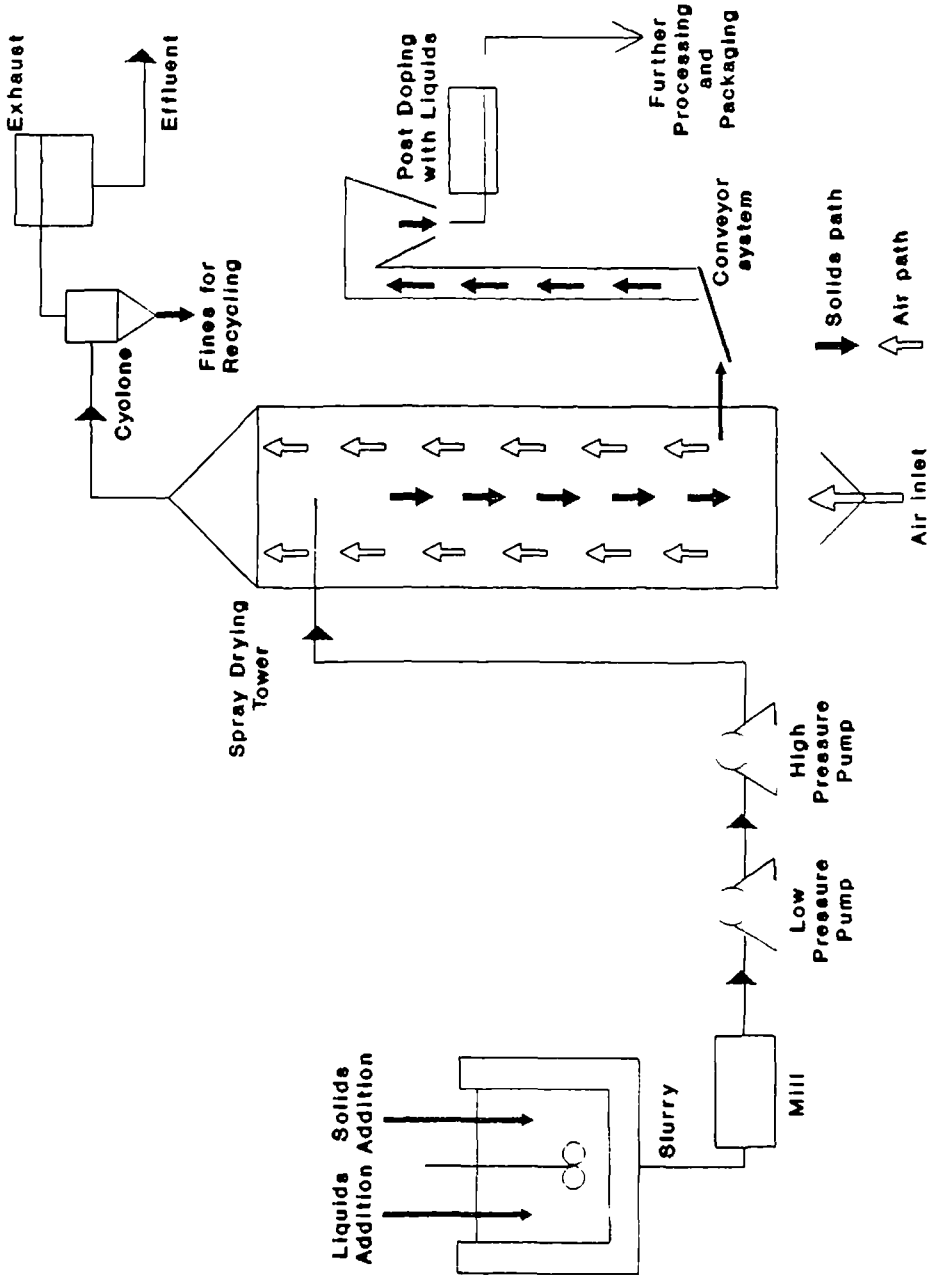

Figure 7.6: Typical detergent powder process.

and to investigate the effects of crystal habit and size on the packing structure of agglomerates and hence the pore size distribution. A brief summary of the techniques can be found in section 5.2.2.

7.3.1.3 Mercury Intrusion Porosimetry

The porosity of the resultant powders obtained during this study were measured using mercury intrusion porosimetry. The theory behind mercury intrusion porosimetry is well known, being based on the equation derived by Young and Laplace, i.e.:

$$\Delta P = (2\gamma \cos \Theta)/r \tag{7.1}$$

ΔP= excess pressure required to force the liquid (in this case mercury) into a capilliary within the solid.

r= radius of capilliary (assumed cylindrical in form)

γ = surface tension of liquid

Θ= contact angle between liquid and solid.

Essentially the data obtained from this technique is a measure of the volume of mercury intruded into the pores of a sample as a function of pressure applied. The smaller the pore diameter, the higher the pressure needed for mercury intrusion. A mercury porosimeter [27-30] can be used to generate high pressures and measure both pressure and volume of mercury taken up by the pores. The change in volume of the bulk mercury is frequently measured by the change in electrical resistance of an immersed wire remote from the solid. The cumulative volume is the volume of mercury intruded into a powder pores and is normally a measure of the liquid uptake capacity of a powder. The pore size distribution as measured by mercury porosimetry may be split into two regions: that of interparticle pore volume distribution and intraparticle pore volume distribution (figure 7.7). The interparticle pore volume distribution is the region where the measured porosity is attributed to pores between particulates (normally 70-100μm), whereas the intraparticle pore volume region is a measure of a particle's internal porosity. Previous studies had assumed that the region between (0.5-7μm) was the region of internal porosity that exhibited good uptake of postdosed liquids [15]. However, this does not show good correlation with studies of powder

uptake capacity. A reassessment showed that in general, the region (0.5-3)μm is the region of intraparticle porosity for burkeite that exhibits good correlation with studies of powder uptake capacity [13]; a typical uptake capacity range for a standard spray dried burkeite powder being (0.4-0.6)ml/g. This figure is significantly reduced by the presence of certain anions, e.g. Ca^{2+} and to a lesser extent Mg^{2+} in a burkeite slurry. These anions lead to a reduction of the intra-particle pores of optimum liquid uptake by modifying the crystal growth and resultant crystal morphology. There is also evidence that mixing and spray drying conditions (e.g. nozzle pressure) can influence porosity [13].

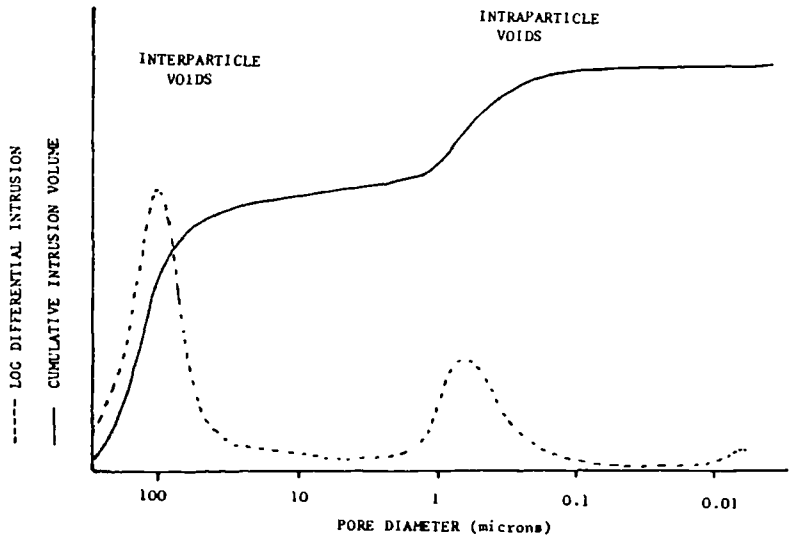

Figure 7.7: Plot of mercury uptake as a function of pore size

7.3.2 Influence Of Stirring On Particle Porosity During Batch Crystallisation

The mechanical aspects of mixing in relation to agglomeration/porosity were investigated by the preparation and agitation of standard burkeite slurry samples (table 7.1) in a 2lb batch crystalliser, using different impellers (table 7.2). Material addition follows the order shown in table 7.1. Characteristics of the impellers are given in table 7.3. Levels of agitation were kept approximately constant by visual evaluation of the level of "vortex" formation within the slurry. Reaction conditions were kept

constant (slurry temperature = 85°C, reaction time = 20 minutes); these conditions having previously been used for burkeite production [10,32,33]. Slurry samples were withdrawn, washed and stored in an inert solvent (e.g. n-hexane) to prevent crystallisation/hydration effects outwith the reaction vessel. The slurry samples were then filtered and oven dried at 80^0C for 12 hours. The resultant powders were consequently analysed using X-ray powder diffraction, mercury porosimetry and Scanning Electron Microscopy.

Component	Mass(Kg)
Water	2.0991
Narlex LD34	0.1465
Sodium Sulphate	1.881
Sodium Carbonate	0.4554
Alkaline Silicate	0.091
Synperionic 7EO	0.0198

Table 7.1: Slurry formulation for burkeite production.

Impeller Used
Marine Propellor
Flat Blade Impeller
Mini-Anchor Impeller
Turbine Impeller
Multi-Stage Pitched Blade (MSPB) Impeller

Table 7.2: Impellers used for slurry agitation.

Impeller Type	Impeller/Vessel Diameter Ratio	R.P.M. During Formulation	Approx. Torque During Formulation (Nm^{-1})
Marine Propellor	0.333	700	-
Flat Paddle	0.333	400	79.00
Mini-Anchor Impeller	0.553	250	54.00
Turbine Impeller	0.633	250	66.00
MSPB	0.800	170	48.94

Table 7.3: Impeller type and characteristics for slurry formulation.

7.3.3 Particle Size Distribution As A Function Of Residence Time During Batch Crystallisation

A slurry was prepared (table 7.4) in a 100lb batch crystalliser and agitated using a MSPB impeller, with an impeller/vessel diameter ratio of 0.82. Samples were withdrawn, washed and stored in n-hexane after the following residence time intervals: 5 mins, 15 mins, 30 mins, 60 mins, 120 mins and 240 mins. The slurry was then milled twice and spray dried. The spray drying parameters are shown in table 7.5. Powder samples were obtained by filtration of the slurry, the solids dried for 12 hours at 80^0C. The resultant powders were analysed using the aforementioned particle characterisation techniques.

Component	Mass (Kg)
Water	23.42
Narlex LD34	1.66
Sodium Sulphate	13.48
Sodium Carbonate	5.17
Alkaline Silicate	1.05
Synperionic 7EO	0.22

Table 7.4: Slurry formulation for investigation of Ostwald Ripening.

Air Inlet Temperature (°C)	350
Nozzle Jet Pressure (Bar)	40
Air Flow Rate (Kg/min)	50
Nozzle Diameter Ratio (inlet/outlet)(mm)	2.54/1.78

Table 7.5: Spray drying conditions for investigation of Ostwald Ripening

7.3.4 Effect Of Processing Conditions On Particle Porosity During Spray Drying.

A slurry was prepared (table 7.6) in a 600lb batch crystalliser and mixed using a turbine impeller, with a impeller/vessel diameter ratio of 0.41. The slurry was allowed to crystallise at 85°C, for 20 minutes. The resultant slurry was then spray dried, whilest varying the air flowrate and nozzle ratio. The spray drying conditions during preparation are presented in table 7.7. A burkeite slurry was spray dried under constant spray drying conditions (as in table 7.5) using 3 different nozzle diameter ratios; 3.05/2.54, 2.54/1.78 & 2.29/1.52mm. In all cases the resultant samples were analysed using mercury intrusion porosimetry, powder diffraction and Scanning Electron Microscopy.

Component	Mass (Kg)
Water	234.17
Narlex LD34	16.63
Sodium Sulphate	134.84
Sodium Carbonate	51.68
Alkaline Silicate	10.51
Synperionic 7EO	2.18

Table 7.6: Slurry formulation for investigation of the effect of tower conditions on burkeite agglomeration/porosity.

Sample Number	Air Inlet Rate (Kg/min)	Slurry Rate (Kg/min)	Inlet Temperature (°C)	Outlet Temperature (°C)	(T_{inlet}-T_{outlet}) (°C)
1#	73.23	7.42	346.81	127.97	218.84
2#	59.14	7.23	348.84	113.92	234.92
3#	49.91	7.38	348.81	100.79	248.02
4#	39.63	7.74	350.21	90.23	259.98
5%	40.37	8.03	349.81	87.26	262.55
6%	39.61	8.26	350.00	81.31	268.69
7%	31.74	8.30	350.21	74.98	275.23
8%	26.55	8.41	350.00	71.05	278.95

#Nozzle diameter ratio 2.29/1.52mm %Nozzle diameter ratio 2.54/1.78mm employed. Air Inlet Temperature and Nozzle Jet Pressure as in Table 8.5

Table 7.7: spray drying conditions for investigation of tower conditions on burkeite agglomeration/porosity.

Nozzle Diameter Ratio (mm)	Air Inlet Rate (Kg/min)	Slurry Rate (Kg/min)	Inlet Temperature (°)	Outlet Temperature (°)
2.29/1.52	49.94	7.48	349.86	95.18
2.54/1.78	49.96	8.27	350.02	89.19
3.05/2.54	49.85	12.93	350.04	84.25

Table 7.8: Spray drying conditions for investigation of nozzle diameter ratio variation on burkeite agglomeration/porosity.

7.4 Results And Discussion

7.4.1 Influence Of Stirring On Particle Porosity During Batch Crystallisation

In the investigation of impeller effect on the agglomeration/porosity relationship, analysis of the powder diffraction data obtained (table 7.9) indicated the presence of phases other than burkeite in the samples examined. Complete burkeite formation was expected to take place, with possible differences in agglomeration, depending on the mixing/shear characteristics imparted by the impeller used. The results obtained from the use of the MSPB, turbine and anchor impellers (table 7.9) suggests two possibilities :

- The level of agitation generated by these impellers was not sufficient to ensure complete burkeite formation, or,

- The use of different impellers may offer the opportunity to influence the final phase crystallised from a slurry.

Impeller Type	Major Phase	Minor Phase
Marine Propellor	Burkeite	—
Flat Paddle Impeller	Burkeite	—
Mini-Anchor Impeller	Burkeite	Sodium Carbonate Monohydrate
Turbine Impeller	Burkeite	Sodium Carbonate Monohydrate
MSPB Impeller	Burkeite	Sodium Carbonate Monohydrate

Table 7.9: Phase analysis for slurries agitated by different impellers.

The impellers studied belonged to two classes of agitation - radial flow and axial flow regimes and can be distinguished as follows:

Axial Flow: Marine propellor, Multi-Stage Pitched Blade (MSPB) and Turbine impellers,

Radial Flow: flat paddle and mini-anchor impellers.

Although the slurries agitated by the flat paddle impeller and marine propeller crystallised with complete burkeite formation, the agitation mechanism in each case is very different; the flat paddle impeller causing agitation by radial flow and the marine propeller by axial flow. The slurries agititated by mini-anchor, turbine and MSPB impellers all crystallised with a mixture of predominantly burkeite with minor phase sodium carbonate monohydrate present, as determined by powder diffraction. Hence it can be seen that neither class of agitation was significant in influencing the extent of burkeite formation.

It has been stated that the level of agitation generated by an impeller may be a factor influencing the extent of burkeite crystallisation. If the order of material addition is examined (table 7.1), sodium carbonate is added after sodium sulphate, which has already dissolved to form an undersaturated solution. It can be assumed that either of two processes will occur:

- Dissolution of sodium carbonate will also occur, leading to the eventual crystallisation of the double salt burkeite, or
- solid phase sodium carbonate will remain and will be hydrated to form sodium carbonate monohydrate.

The greater the intensity of turbulence generated, the greater the degree of mixing/breakdown of particulates and thus the higher the dissolution rate of sodium carbonate. The intensity of turbulence generated is a result of the power input per unit volume, which is equivalent to the torque applied to the system. If the level of agitation is too low, then the mixing/turbulence generated will not be sufficient to ensure complete dissolution of sodium carbonate, which may then hydrate, forming undesirable sodium carbonate monohydrate crystals.

Torque and r.p.m. readings were determined for each impeller (table 7.3), except for the marine propeller, due to mechanical constraints. Although the level of agitation was kept approximately constant throughout, the large variation in r.p.m. readings required for this level of agitation is apparent. Since r.p.m. is proportional to torque (see figure 7.8), it can be deduced that the marine propellor and the flat blade impeller have the highest torque readings during formulation, and therefore are inputting the highest (power/m^3) into the system, torque being defined as the power input per unit volume. Since the power input per unit volume can be taken as a measure of the intensity of turbulence, it may be said that the marine propeller and flat paddle impeller are generating the highest degrees of turbulence for all the impellers investigated. Thus, the implication is that both the marine propeller and the flat blade impeller will maximise particulate breakdown, mixing and dissolution when sodium carbonate is added to the undersaturated sodium sulphate solution, thus leading to complete burkeite formation. The mini-anchor, MSPB and turbine impellers do not generate sufficient agitation for complete dissolution of sodium carbonate, hence hydration of sodium carbonate leading to formation of sodium carbonate monohydrate occurs. It can also be assumed (from r.p.m. readings) that the flat blade impeller has the lower power requirements for complete burkeite formation and hence would be assumed to be the most efficient in burkeite production.

However the powder porosity is the most important factor in carrier production. Mercury intrusion porosimetry has been used previously in the analysis of burkeite [13] and has determined the optimum porosity of burkeite to be the region (0.5-3)μm. On examination of the porosity of the powders agitated by the various impellers, it can be seen (figure 7.9 and table 7.10) that the trend is of decreasing cumulative porosity

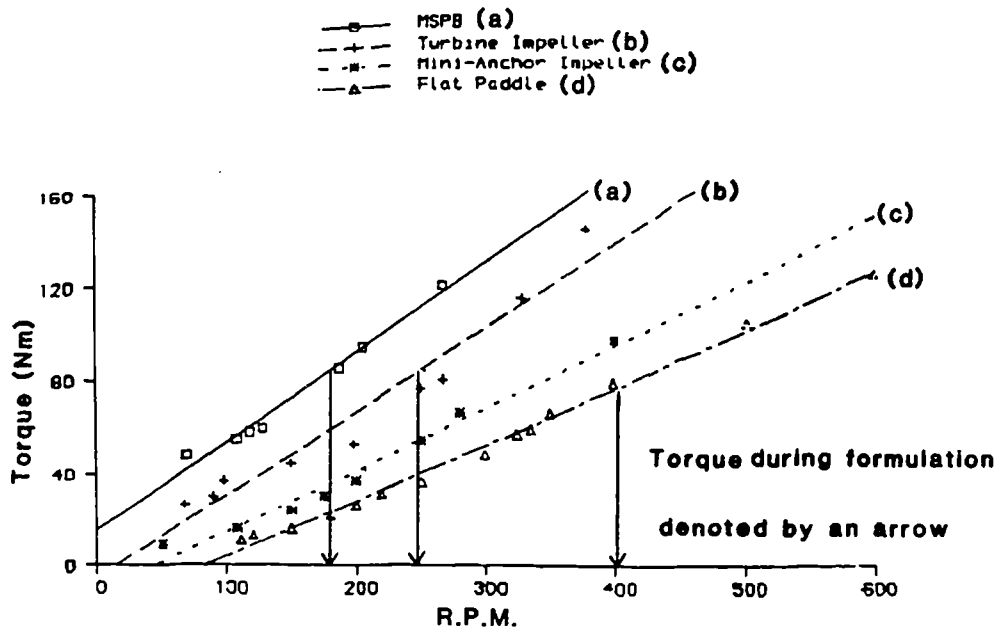

Figure 7.8: Plot of torque readings vs measured R.P.M. for impellers investigated.

with decreasing pore size distribution.

Impeller Type	Inter-particle Pore Size (μm)	Intra-particle Pore Size (μm)	Total Porosity (ml/g)	Internal Porosity (ml/g)
Marine Propellor	70	0.2	0.88	0.28
Flat Paddle Impeller	60	0.2	0.83	0.32
Mini-Anchor Impeller	80	0.6	0.65	0.23
Turbine Impeller	105	2.0	0.46	0.01
MSPB Impeller	70	0.4	0.69	0.12

Table 7.10: Slurry porosities obtained for slurry agitation by various impellers.

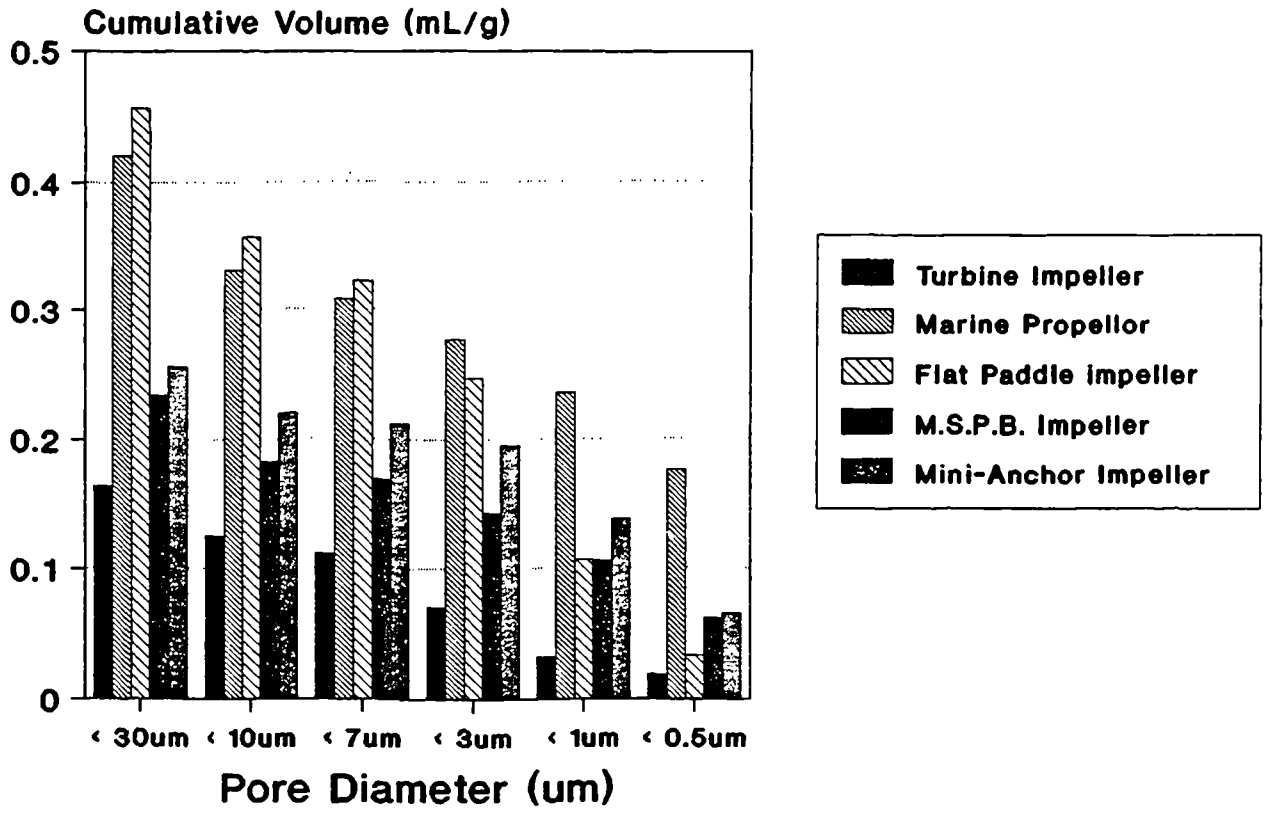

Figure 7.9: Cumulative volume versus pore diameter for impellers investigated.

Throughout the pore range investigated, the cumulative pore volume of the slurry sample agitated by the turbine impeller was significantly lower than the other slurries investigated. The internal porosity was almost negligible, suggesting very poor liquid uptake. This may be attributed to the presence of sodium carbonate monohydrate (table 7.9) and may also account for the lower cumulative pore volumes/internal porosities determined for the slurry samples agitated by the mini-anchor and MSPB impellers. In the interparticle pore volume region (70μm - 100μm), the slurries agitated by the marine and flat paddle impellers provided the highest cumulative volume of those investigated. However, within the intraparticle pore volume region (0.5-3μm), the porosity of the slurry agitated by the flat paddle drops significantly, with respect to the other samples investigated, indicating that the bulk of the porosity of this sample is due to pore formation caused by inter-particle agglomeration, and not particle internal porosity. However, a significant proportion (approx. 70%) of the porosity for the slurry agitated by the marine propeller, is due to particle internal porosity, which would indicate efficient nonionic uptake. Hence, it would appear that although the

flat blade impeller has the lowest power requirements for complete burkeite crystallisation, the marine propeller is the optimum impeller for the impellers investigated, providing the highest proportion of particle internal porosity relating to liquid uptake (approx. 0.28ml/g). It would also appear that flow pattern does not seem to play a significant role in influencing the crystallisation/agglomeration processes, as relating to internal porosity.

The porosity observations obtained can be correlated to particle packing using Scanning Electron Microscopy (SEM). Figures 7.10-7.14 are micrographs representative of the particle structures of the slurry samples investigated. The slurry sample agitated by the marine propeller is highlighted in figure 7.10 and illustrates the particle packing for burkeite. The "plate-like" crystals seem to agglomerate by an "edge to face" mechanism, thus creating the porosity. The crystalline plates have an average longest dimension of approx. 5μm, and the pores created have been determined to be predominantly in the region (0.5-3μm). The same particle packing can be observed for the slurry sample agitated by the flat paddle (figure 7.11), although not as distinct as in figure 7.10. Distinct differences however, may be observed in the particle packing of the slurries agitated by the three remaining impellers. There is evidence on figures 7.12-7.14 of the presence of sodium carbonate monohydrate in the slurry, along with the distinctive burkeite agglomeration noted in figures 7.10 and 7.11. The larger "platelike" sodium carbonate monohydrate crystals (approx. 40μm) disrupt the normal burkeite particle packing, and significantly reduce the predominance of the intraparticle pore range (0.5-3μm) required for efficient liquid uptake. Previous studies have indicated that an uptake of 0.4-0.6ml/g in the pore region (0.5-3μm) is desirable and normally found in spray dried burkeite powders. The porosity measurements obtained for the slurry samples agitated by the different impellers imply that a significant portion (approx. 47-70%) of the optimum porosity occurs during the initial crystallisation/mixing stages. Other factors however, must be taken into account: only spray dried and slurry samples have been subjected to the same mixing conditions should be compared in order to assess where the conditions for optimum porosity occur. The effects of other physical processes on porosity, e.g. milling should also be assessed. Milling is carried out to reduce particulate size, preventing nozzle

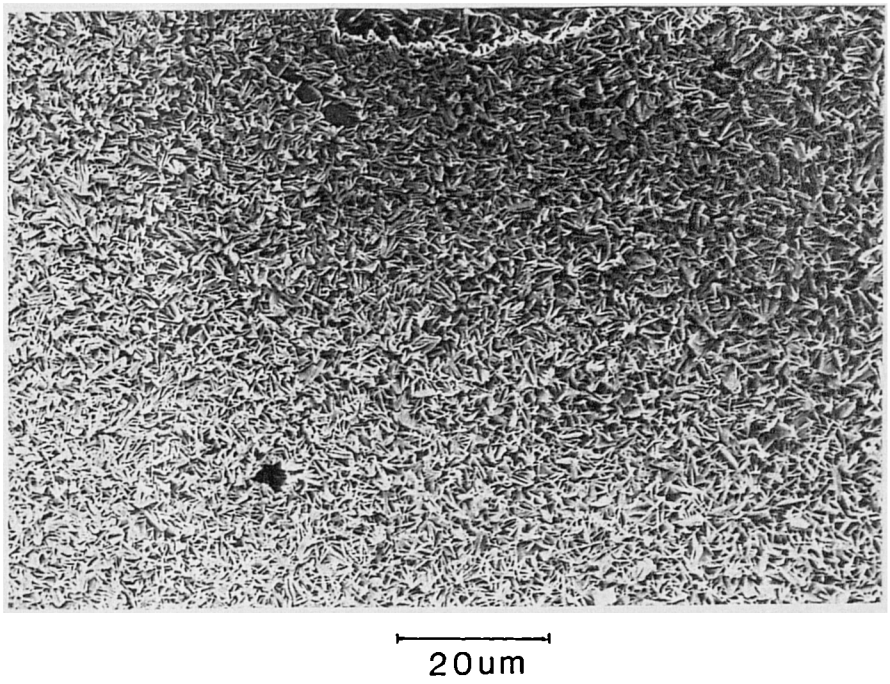

Figure 7.10: Micrograph of slurry agitated by marine propellor.

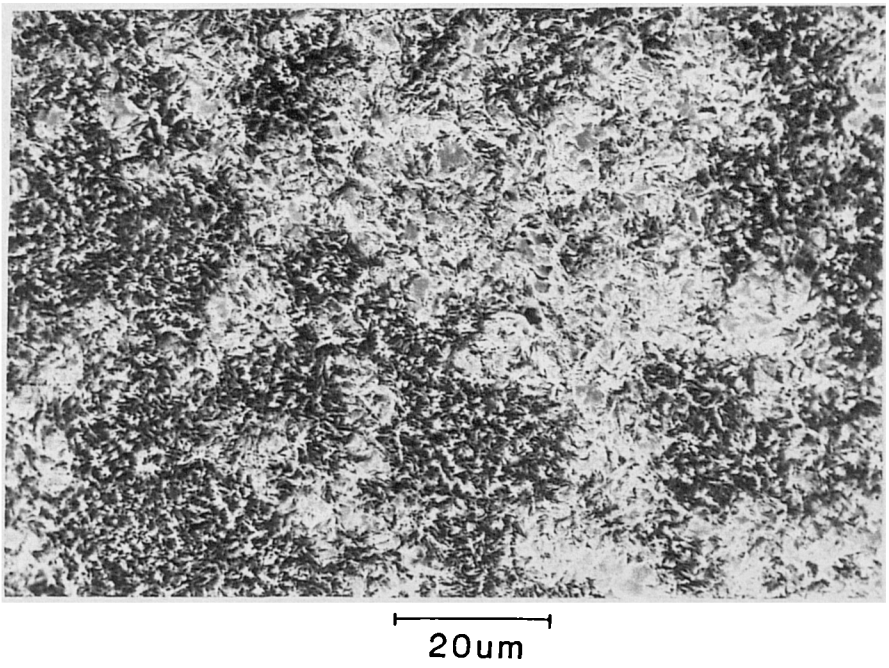

Figure 7.11: Micrograph of slurry agitated by flat paddle impeller.

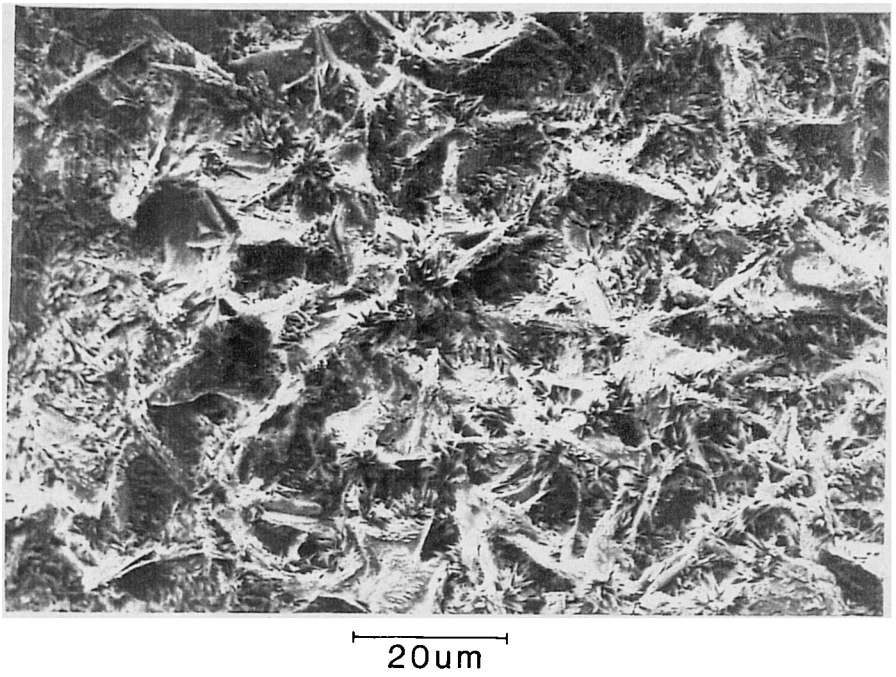

Figure 7.12: Micrograph of slurry agititated by Multi-stage pitched blade impeller.

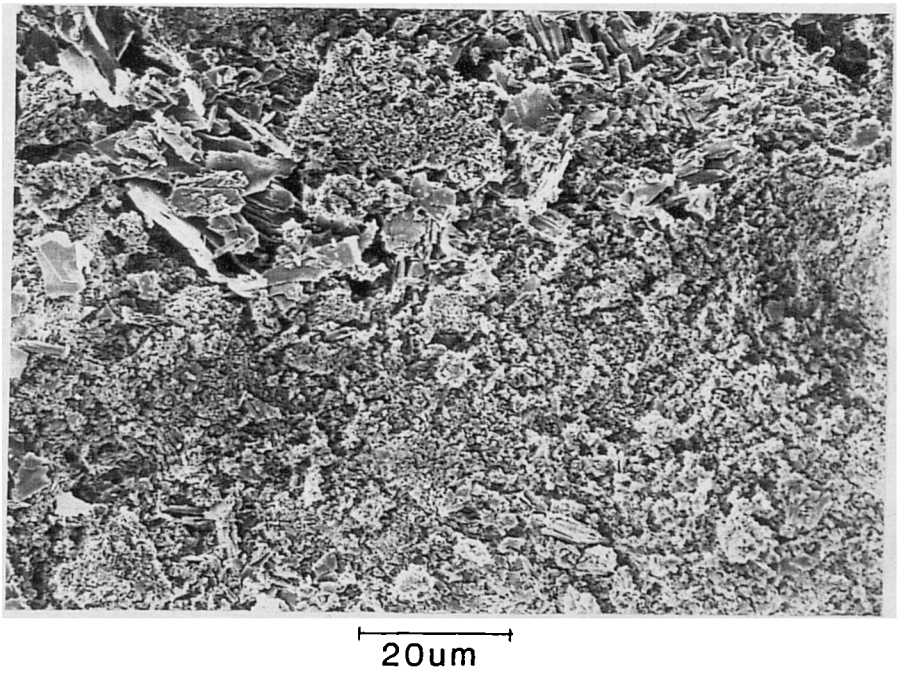

Figure 7.13: Micrograph of slurry agitated by mini-anchor impeller.

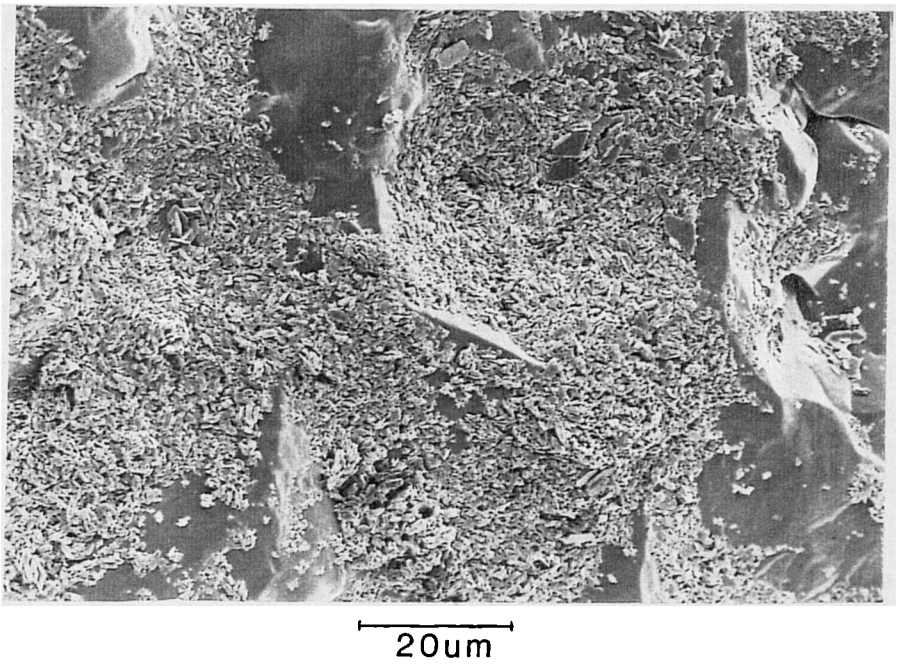

Figure 7.14: Micrograph of slurry agitated by turbine impeller.

blockage during spray drying and has been known to significantly influence powder porosity [32].

7.4.2 Particle Size Distribution AS A Function Of Residence Time During Batch Crystallisation

The development of burkeite as a function of time can be observed using powder diffraction (table 7.11). Burkeite tends to form rapidly after the addition of sodium carbonate, as can be seen from the data of the sample taken after 5 minutes residence time - equal proportions of burkeite and sodium sulphate are observed. The proportion of burkeite gradually increases until complete burkeite formation is observed between 60 and 120 minutes residence time.

Figures 7.15 - 7.22 illustrate the development from large (250 -300μm) low porosity particulates, through to formation of smaller, more porous particles of burkeite. The small pores formed by the "edge to face" mechanism noted previously (figure 7.10) are apparent in figures 7.19-7.21. The porosity measurements obtained from the various slurry samples are illustrated in figure 7.23 and table 7.12. Certain points may be noted: Throughout the pore size investigated there is little difference in porosity between the slurry samples taken after 120 and 240 minutes residence time, figures

7.19 and 7.20 confirming this observation. If Ostwald ripening was occurring, then growth of the larger particles would continue, while the smaller particles would dissolve. These changes would obviously influence the pore size distribution. However, over a 120 minute period (between 120 and 240 minutes residence time) there was no apparent changes in the measured porosity in the pore size investigated; implying that there was no change in the pore size distribution. Hence it may be concluded that no evidence for Ostwald ripening was found for burkeite crystallisation. The changeover to complete burkeite formation is also apparent throughout the pore size range investigated, i.e. within the inter- and intra-porosity range, the cumulative volume is higher throughout for samples taken after 120 minutes and 240 minutes residence time, compared to samples taken after 5,15,30 and 60 minutes residence time. However, the most important factor in this diagram is the dominance of the porosity of the milled sample in the range investigated. The porosity is significantly higher than any other sample, including the spray dried sample. A possible reason for this is that the milling process breaks down large agglomerates, exposing much more of the intraparticle porosity for liquid uptake. An example of this may be seen in figure 7.21, where the internal pores of the particles are clearly exposed for liquid uptake. However, the porosity of the spray dried powder is less than that of the milled sample, especially in the intraporosity range. There may be various reasons for this difference in porosity. One reason may be that when the feed enters the drying medium, the rapid evaporation causes particles to dry, forming an outer "crust". Large holes develop in these particles when moisture beneath the crust is removed, thus disrupting the particle packing and hence porosity/liquid uptake. Another possibility is that solution dries on the surface of the particles thus blocking pores and reducing porosity. The typical spherical particles formed by spray drying are illustrated in figure 7.22.

Residence Time	Phases Determined
5 mins	Burkeite & Sodium Sulphate
15 mins	Burkeite & Sodium Sulphate
30 mins	Burkeite & Sodium Sulphate
60 mins	Burkeite & Sodium Sulphate
120 mins	100% Burkeite
240 mins	100% Burkeite
Milled Slurry	100% Burkeite
Spray Dried Slurry	100% Burkeite

Table 7.11: Powder diffraction analysis of burkeite formation/Ostwald ripening as a function of time.

Residence Time (Mins)	Inter-particle Pore Size (μm)	Intra-particle Pore Size (μm)	Total Porosity (ml/g)	Internal Porosity (ml/g)
5 mins	90	0.5	0.69	0.11
15 mins	85	0.4	0.93	0.19
30 mins	103	0.3	1.03	0.18
60 mins	103	0.38	0.98	0.19
120 mins	70	0.4	1.33	0.28
240 mins	90	0.4	1.19	0.30
Milled Slurry	108	0.45	0.98	0.57
Spray Dried Slurry	90	0.3	1.49	0.37

Table 7.12: Analysis of burkeite formation/Ostwald ripening on resultant powder porosity as a function of time.

A comparison between slurry and spary dried samples agitated under the same conditions can also be made from figure 7.23. Comparison of the sample taken after 240 minutes residence time and the samples taken after spray drying illustrate a number

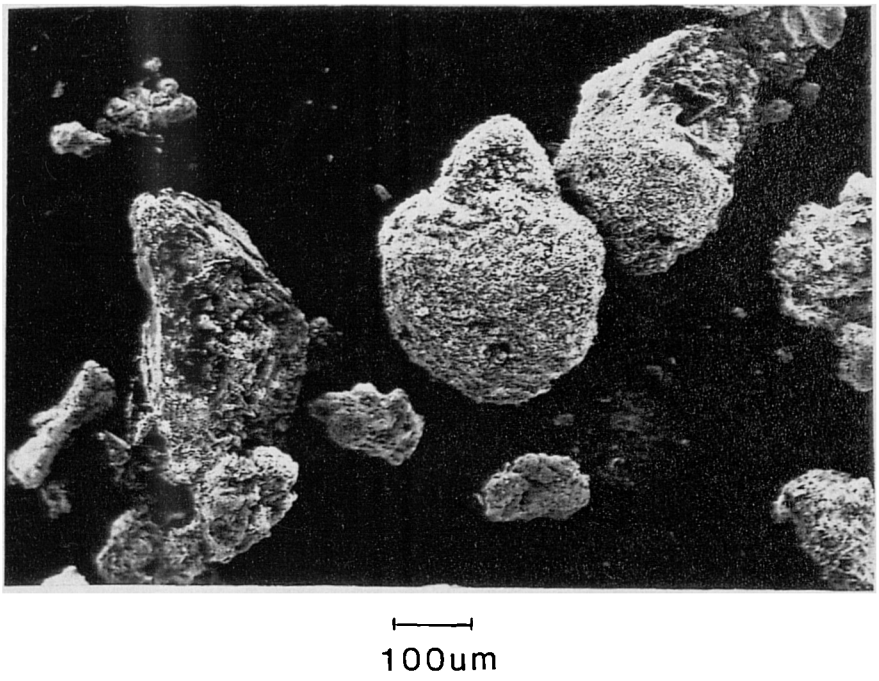

Figure 7.15: Micrograph of slurry after 5 minutes residence time.

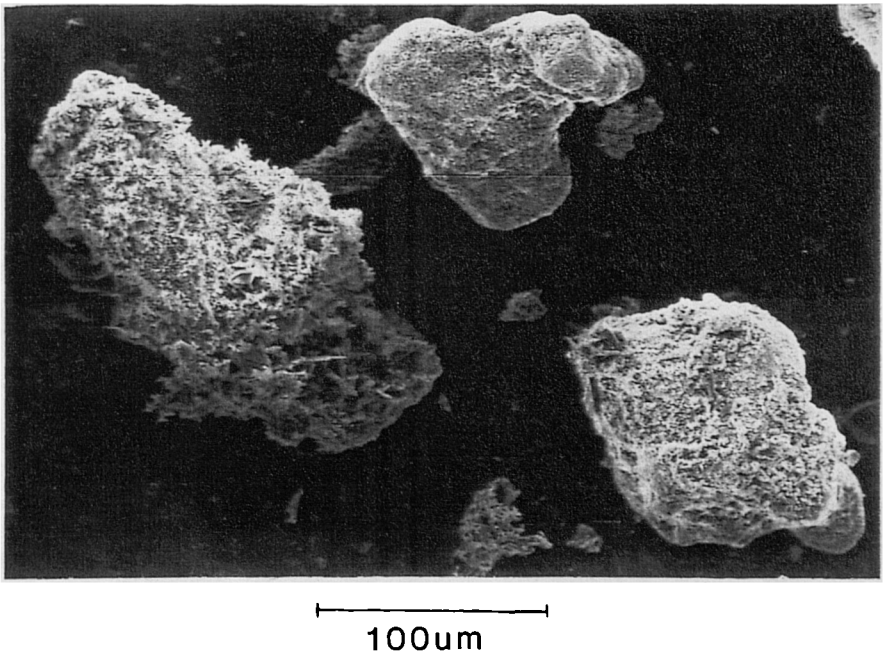

Figure 7.16: Micrograph of slurry after 15 minutes residence time.

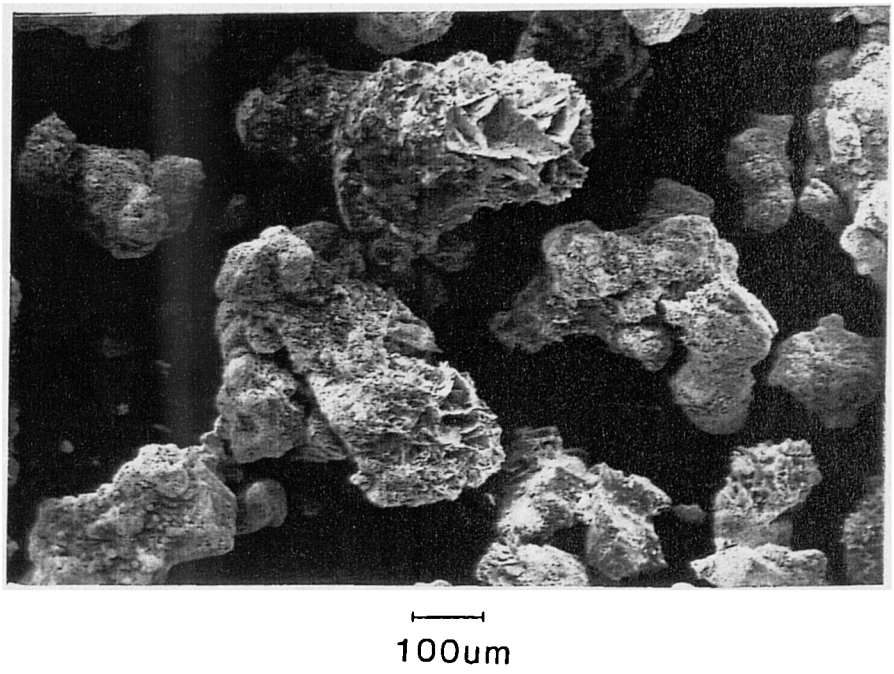

Figure 7.17: Micrograph of slurry after 30 minutes residence time.

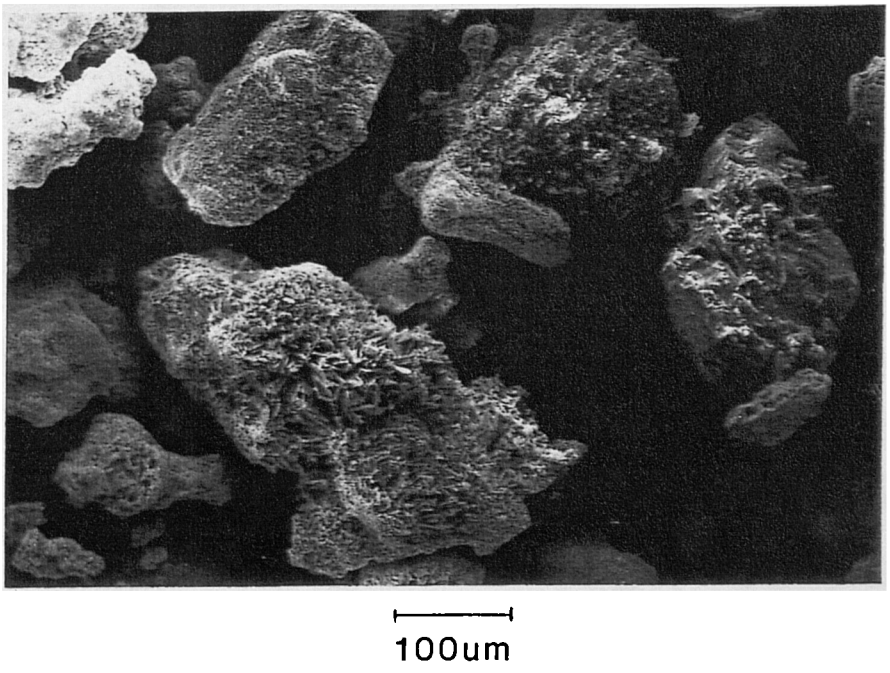

Figure 7.18: Micrograph of slurry after 60 minutes residence time.

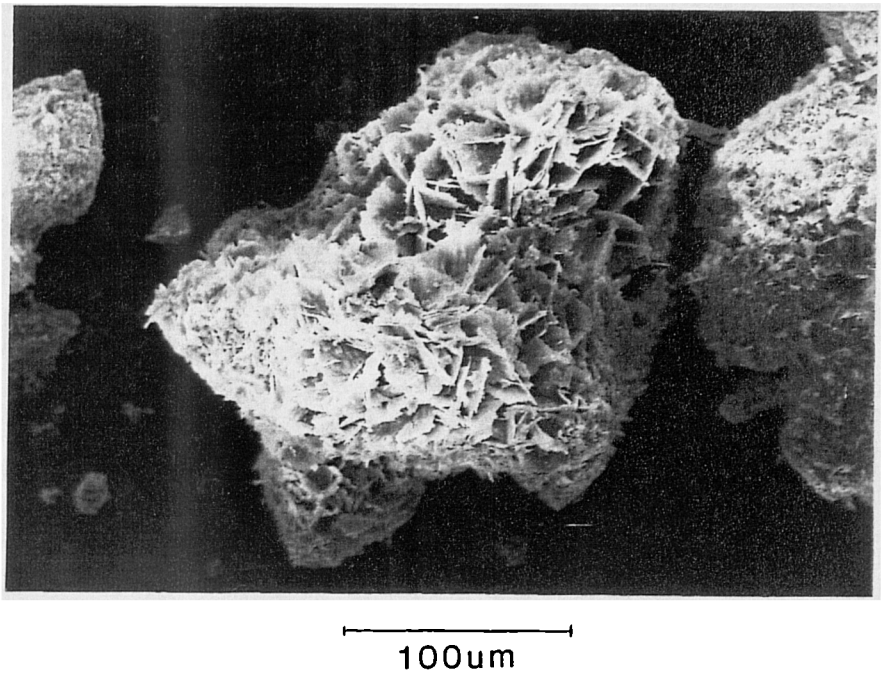

Figure 7.19: Micrograph of slurry after 120 minutes residence time.

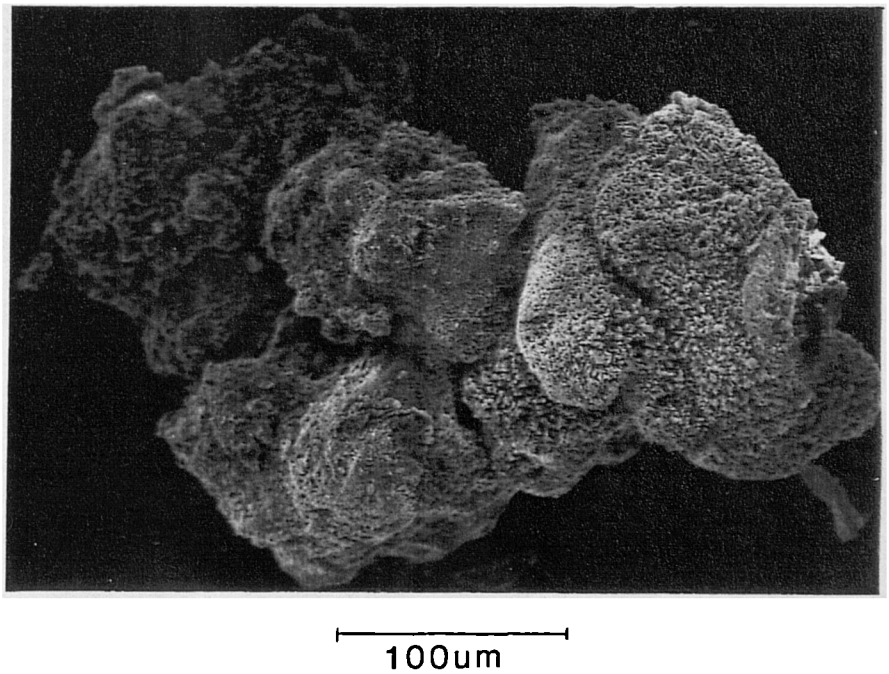

Figure 7.20: Micrograph of slurry after 240 minutes residence time.

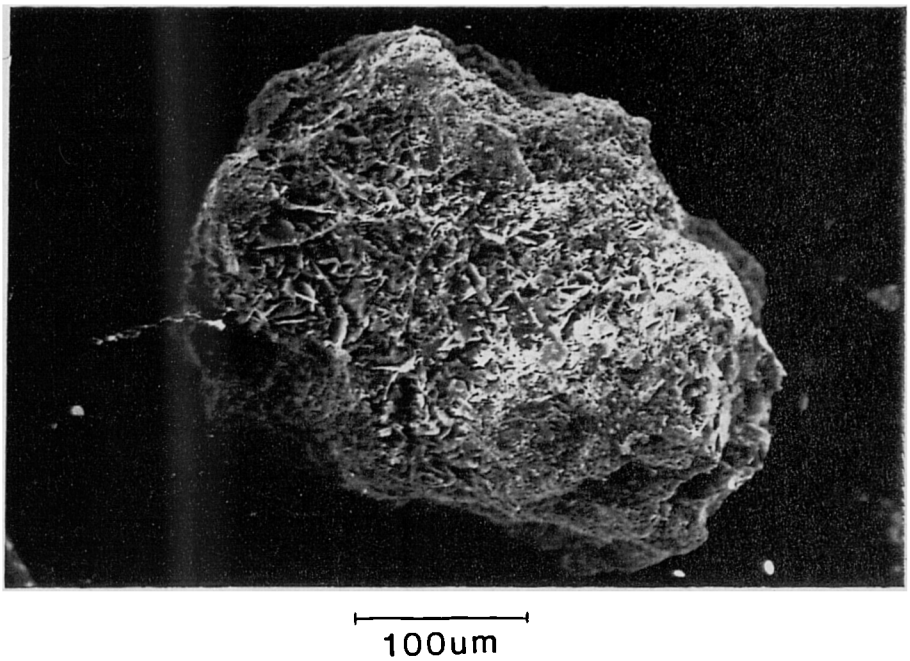

Figure 7.21: Micrograph of slurry after milling.

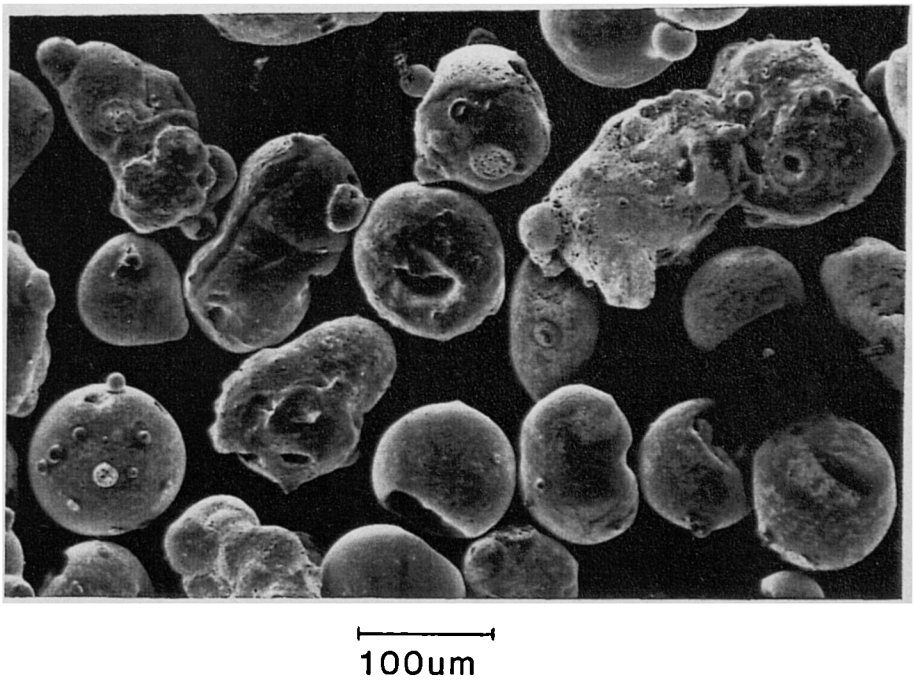

Figure 7.22: Micrograph of resultant spray dried powder.

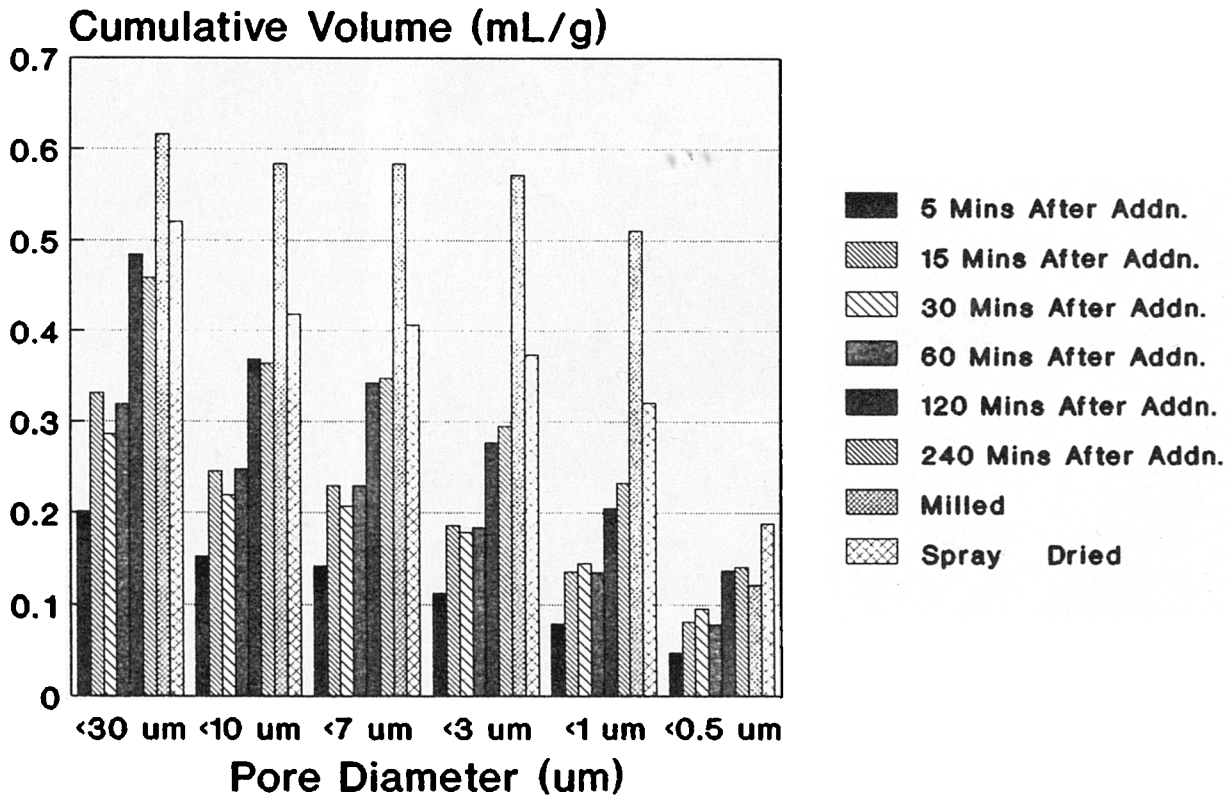

Figure 7.23: Cumulative volume versus pore diameter as a function of material addition

of points: The uptake in the optimum pore range for the slurry sample is (0.30ml/g), whereas the spray dried sample is (0.37ml/g). Hence it may be concluded that from this study, a significant proportion (79%) of the desired porosity occurs during the initial crystallisation/mixing stages as previously implied. The liquid uptake figure obtained from this spray dried sample is rather low: liquid uptakes up to 0.6ml/g are regarded as standard for spray dried burkeite powders, implying that at least 49% of liquid uptake in the desired pore range occurs during the initial mixing/crystallisation stages. The effects of milling on liquid uptake/porosity are significant and should be further investigated.

7.4.3 Effect Of Processing Conditions On Particle Porosity During Spray Drying

Variation of spray drying tower conditions will alter drying rates and hence the residence times required to obtain desired moisture levels. This will obviously influence the resultant powder porosity. If conditions such as air inlet rate, air inlet temperature etc are kept constant and the nozzle inlet/outlet diameter is varied, the effects on powder porosity are illustrated in figure 7.24 and table 7.13. From powder diffraction studies, complete burkeite formation was noted in each case.

An increase in the nozzle diameter ratio will allow a higher feed throughput to enter the drying medium (reflected in the increasing slurry rates in table 7.8), leading to more particle collisions, hence greater inter-particle agglomeration. The removal of water can adversely effect powder porosity, since during the drying process moist particles will dry forming a dry outer skin, whilest water must still remain in the particle interior. The removal of this "inner" water can lead to the formation of "blowholes", which adversely effects particle packing, and hence porosity. The trend of increasing inter-particle porosity with increasing nozzle diameter ratio is clearly observed in figure 7.24. Within the intra-particle porosity region (0.5-3μm) in figure 7.24, the trend of increasing cumulative volume/porosity is not as apparent. The cumulative volume reaches an upper limit (approx. 0.45ml/g) at lower pore sizes, indicating that variation of the nozzle diameter ratio does not significantly influence

particle internal porosity.

It can be assumed that the variation in air inlet rate occurs at an approximately constant slurry rate. Hence, a decrease in air inlet rate leads to progressively milder drying conditions. This avoids flash evaporation, which causes disruption to particle packing and thus porosity. As the nozzle diameter ratio does not significantly influence the internal powder porosity, a whole range of air inlet rates may be studied to observe the effects of drying rate on powder porosity. In order to study a wide variation of air inlet and slurry rates, it is necessary to change the nozzle diameter ratio.

Decreasing the air inlet rate (table 7.14 and figure 7.25) at constant nozzle diameter ratio influences both the inter-and intra-particle porosity. Both the inter- and intra-particle porosity increase with decreasing air rate. Significant differences (approx. 0.18ml/g) in cumulative volume in the intra-particle porosity region are noted between samples taken when spray dried at an air rate of 73.23kg/min and samples that have been spray dried at an air rate of 26.55kg/min, illustrating the large range of porosities obtainable due only to variation of inlet air rate. The intra-porosity reaches a maximum value between inlet air rates of 25-30kg/min, possibly indicating that the maximum intra-particle liquid uptake achievable for the tower/burkeite combination is approximately 0.52ml/g.

Nozzle Diameter Ratio(mm)	Inter-particle Pore Size (μm)	Intra-particle Pore Size (μm)	Total Porosity (ml/g)	Internal Porosity (ml/g)
3.05/2.54	103	0.25	1.61	0.45
2.54/1.78	70	0.25	1.50	0.43
2.29/1.52	100	0.22	1.62	0.39

Table 7.13: Analysis of the effect of nozzle variation on resultant powder porosity.

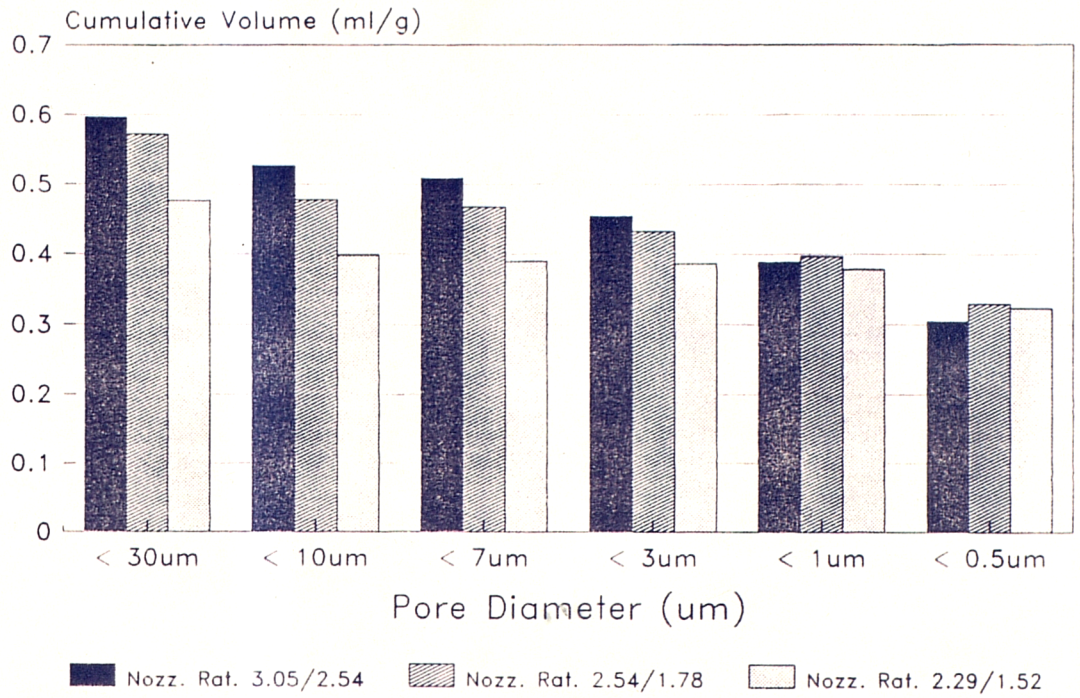

Figure 7.24: Cumulative volume versus pore diameter as a function of nozzle variation.

Sample number	Inter-particle Pore Size (μm)	Intra-particle Pore Size (μm)	Total Porosity (ml/g)	Internal Porosity (ml/g)
1#	70	0.30	1.46	0.32
2#	63	0.30	1.55	0.41
3#	82	0.25	1.63	0.43
4#	60	0.22	1.49	0.42
5%	60	0.22	1.48	0.44
6%	90	0.23	1.65	0.47
7%	90	0.30	1.54	0.53
8%	100	0.29	1.51	0.52

#Nozzle diameter ratio 2.29/1.52mm %Nozzle diameter ratio 2.54/1.78mm employed. Air Inlet Temperature and Nozzle Jet Pressure as in Table 8.5

Table 7.14: Analysis of the effect of inlet air variation on resultant powder porosity.

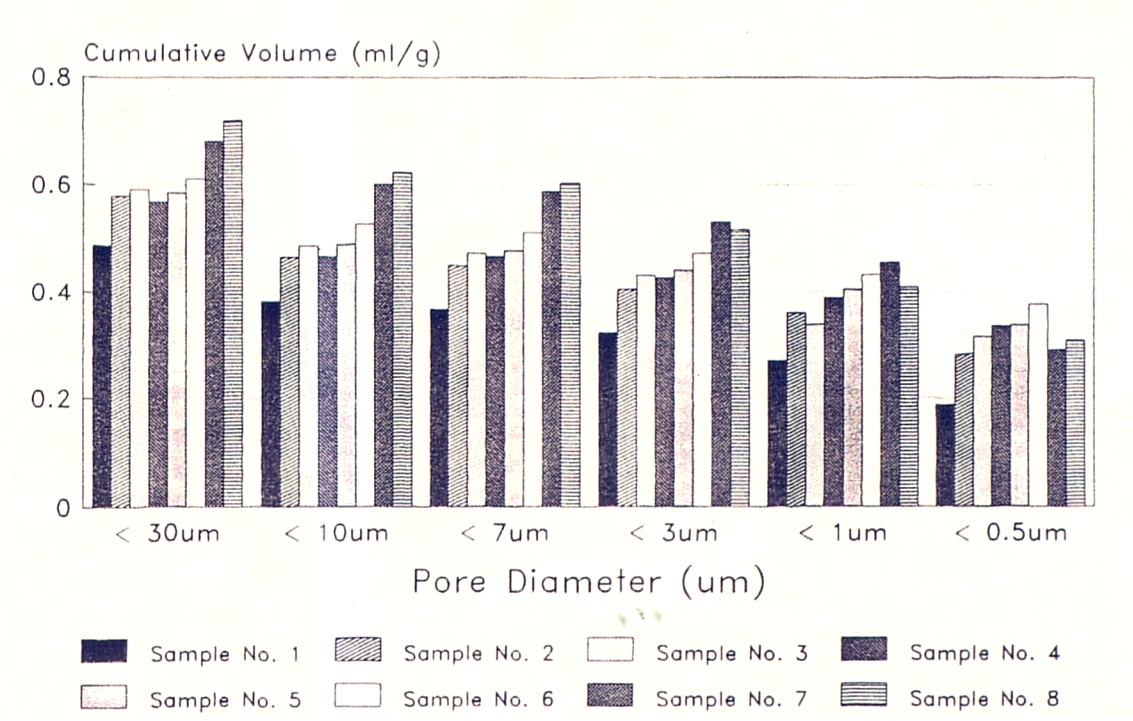

Figure 7.25: Cumulative volume versus pore diameter as a function of inlet air variation.

7.5 Conclusions

It was deduced that slurry agitation by different impellers can possibly influence crystallisation leading to different phases: Burkeite was observed to be the only phase crystallising during slurry agitation by the marine propeller and flat paddle impeller, whereas both Burkeite and sodium carbonate monohydrate were observed during slurry agitation by the turbine, M.S.P.B. and mini-anchor impellers. The high power input required for slurry agititation by the marine propeller and flat paddle impeller creates a higher intensity of turbulence, maximising slurry mixing and dissolution of sodium carbonate which leads to complete burkeite formation, whereas insufficient slurry agitation by the MSPB, turbine and mini-anchor impellers leads to incomplete dissolution of sodium carbonate with resultant hydration to sodium carbonate monohydrate. The presence of the larger sodium carbonate monohydrate crystallites disrupts the particle packing (shown to be small plates agglomerating by an "edge to face" mechanism) arrangements of burkeite and is clearly illustrated on examination of porosity measurements and Scanning Electron Micrographs. The slurry agitated by the marine propellor was most suited for liquid uptake, with approx. 70% of the total porosity attributed to internal porosity suitable for uptake.

Residence time studies highlighted the development of burkeite as a function of time, after materials addition was completed. Shortly after final materials addition, the phases present were identified as burkeite and sodium sulphate, the percentage of burkeite present increasing as time increased. Complete burkeite formation was observed to take place between 60 and 120 minutes residence time. Over a 120 minutes period no change in the pore size distribution was observed, implying that Ostwald ripening is not a factor in the crystallisation of burkeite.

From comparison of the liquid uptake of a burkeite slurry sample to a spray dried sample prepared under the same mixing conditions, it may be seen that at least 47% and up to 70% of liquid uptake in the desirable pore region occurs during the mixing/crystallisation stage. However, liquid uptake for a milled sample is much higher than the spray dried sample, which may be attributed to either the agglomerate breakdown by the milling process, exposing a greater percentage of particle internal porosity than is present in the spray dried sample, or possibly during the drying process solution dries on the surface of the spherical particles, thus blocking pores and reducing porosity. The removal of water rapidly during spray drying, disrupting particle formation and packing may also account for the apparent drop in porosity between the spray dried and milled samples.

Variation of nozzle diameter ratios at constant air rate influences the inter-particle porosity, but not intra-particle porosity to any great extent. The greater the nozzle inlet/outlet ratio, the greater the inter-particle porosity. Variation of the air inlet rate (at constant nozzle diameter ratio) effects both the inter- and intra-porosity. A decrease in air inlet rate leads to an increase in intra- and inter-particle porosity, until a maximum of 0.52ml/g cumulative volume was obtained for particle internal porosity, which seemed to represent the maximum liquid uptake available for this particular tower/burkeite combination.

7.6 References

1. L. Roth; Unilever Research Port Sunlight Laboratory Progress Report LPRPS81 1055

2. P.D. Evans; & P.C. Knight; Unilever Research Port Sunlight Laboratory Progress Report LPRPS83 1159

3. L. Roth & T. Taylor; Unilever Research Port Sunlight Laboratory Progress Report LPRPS81 1113

4. D.P. Jones; Unilever Reserch Port Sunlight Laboratory Progress Report LPRPS82 1315

5. D.P. Jones & P.C. Knight; Unilever Research Port Sunlight Laboratory Progress Report LPRPS 84 1115

6. D.P. Jones; Unilever Research Port Sunlight Laboratory Progress Report LPRPS84 1170

7. W.J. Iley & P.J. Russell; Unilever Research Port Sunlight Laboratory Progress Report LPRPS84 1534

8. P.J. Russell & M.J.H. Heybourne; Unilever Research Port Sunlight Laboratory Progress Report LPRPS86 1128

9. C.F. Irwin, C.V. Sabatino & J.A. Sinegra; Unilever Research Port Sunlight Laboratory Progress Report LPRED87 1016

10. P.J. Russell & M.J.H. Heybourne; Unilever Research Port Sunlight Laboratory Progess Report LPRPS86 1167

11. G.D; Golikieri;; Unilever Research Port Sunlight Laboratory Progress Report LPRED87 1025

12. C. Atkinson, M.J.H. Heybourne, W.J. Iley, P.C. Knight, P.J. Russell, T. Taylor, D.P. Jones; Eur. Pat. EP221776A 37pp1987

13. D. Ward; Unilever Research Port Sunlight Progress Report. LPRPS 88 6317

14. J.W. Gibbs; "Collected Works" Longmans Green (1928) London

15. L.N. Matusevich & K.N. Shabaline; Zh. Prikl. Khim., 25, 1157, (1952)

16. J.W. Mullin; Crystallisation. 2nd Ed., Butterworths, London (1972)

17. C. Misra & E.T. White; J. Crystal Growth, 8, 172-178, (1971)

18. M.B. Shah; Phd Thesis, University of London, (1980)

19. K. Sakamoto, M. Kanehara & K. Matushita; J. Chem. Eng. (Japan), **35**, 481, (1971)

20. M. Karel & J. Nyvlt; Ibid, 447, (1985)

21. M. Von Smoluchowski; Z. Phys. Chem. **92**, 129, 1917

22. P. Shamlou; Presented to the IFPRI Annual Meeting, Cambridge, 1988

23. G.B.J.; DeBoer; "Coagulation in Stirred Vessels" 1987

24. Kankiwala, & Staller; Unilever Research Port Sunlight Laboratory Progress Report LPRPS 83 1202

25. K. Masters; "Handbook Of Spray Drying", Wiley, New York (1978)

26. **COMPARE & GRAPH** , Unilever Research Analytical Division, Port Sunlight.

27. H.L. Ritter & L.C. Drake; Ind. Endng. Chem. Analyt. Edn. **17** 782 1945

28. B. Butterworth; "The Structure And Properties Of Porous Solids", 189, Butterworth, London, (1958)

29. P.K.C. Wiggs; " The Structure And Properties Of Porous Solids", 183, Buttterworth, London, (1958)

30. S.J. Gregg & K.S.W. Sing; "Adsorption, Surface Area And Porosity", Academic Press, London, (1967)

31. K. Yuregir; private communication

32. P. Knight; private communication

33. P.J. Russell, P.C. Knight, H.R. Grob & P. Eichenberger; Unilever Research Port Sunlight Laboratory Progress Report LPRPS86 1170

Chapter 8

Conclusions

Contents

8.1 Introduction

The aims of this study were to investigate various aspects of the structure, morphology and kinetics of some carbonates, sulphates and phosphates that form highly porous, high surface area powders of particular relevance to the detergent industry. The conclusions drawn from the study are summarised in section 8.2 and suggestions for further work are outlined in section 8.3.

8.2 Conclusions Of This Study

- Predicted morphologies based on the BFDH model, were obtained for $Na_5P_3O_{10}.6H_2O$, the various components of the Na_2CO_4-Na_2SO_4-H_2O system and β-K_2SO_4. Reasonable agreement was noted between predicted and observed growth morphologies and interfacial angles, highlighting how lattice geometry may be employed for prediction of the crystal morphology.

- Based on the combination of crystal structure and crystal chemistry, a mechanism for the habit modification of $Na_2CO_3.H_2O$ was postulated and extended to $Na_2CO_3.10H_2O$. The mechanism proposed the existence of cation rich zones in the crystal chemistry which could coulombically interact with carboxylate anions in a polyacrylate, leading to growth inhibition and resultant morphological modification from a prismatic to a dendritic morphology. This mechanism was confirmed by observations of the effects of carboxylate based di-acid, polyacid and polyacrylate impurities on the the crystal morphologies of $Na_2CO_3.H_2O$ and $Na_2CO_3.10H_2O$. Parallel trends were noted in each system. The concentration of impurity present and the ratio of carboxylate group/carbon chain length were the factors deciding whether modification occurred. Di-acid and polyacid impurities modified the crystal morphology to form macroscopic dendrites (mm); polyacrylate impurities modified the crystal morphology to form microscopic dendrites (approx. 10μm). Steric hindrance within an impurity did not adversely influence the ability to modify crystal morphology.

- Interionic potentials were empirically derived for β-potassium sulphate that accurately predict the structure and solid state properties, e.g. elastic constants etc. The potentials were successfully applied to the simulation of structure and crystal properties of sodium sulphate, highlighting that the interionic potentials describing the sulphate group can be successfully transferred to other systems. A predicted morphology based on interionic force calculations could not be obtained due to the predominant long range coulombic interactions, which prevented convergence of a lattice energy summation.

- The Na_2CO_3-Na_2SO_4-H_2O system was re-examined using x-ray powder diffraction, Scanning Electron Microscopy (SEM), Energy Dispersive X-ray Microanalysis (EDX) and chemical analysis. Bulk chemical composition may be identified by X-ray powder diffraction, whereas EDX enables the chemical composition of individual particles to be identified. Low angle supercell peaks were noted from powder diffraction studies, although no correlation between solution composition and precipitation temperature could be made. Extensive particle aggomeration was observed for solutions containing a high Na_2CO_3:Na_2SO_4 ratio; this agglomeration was progressively reduced as the Na_2SO_4 content of the solution was increased. The small burkeite particles present (typically 10-30μm) seemed to act as agglomeration nucleators, extensively binding to the larger sodium sulphate (typically 40-650 μm), sodium sulphate decahydrate (typically 200-850μm), and sodium carbonate monohydrate particles (typically 100-200μm). This was attributed to the disordered structure of burkeite, which leads to noncharged crystal forms, thus encouraging agglomeration. Particle size was determined to be a function of precipitation temperature; the lower the precipitation temperature, the larger the crystallites formed.

- The crystallisation kinetics of potash alum ($AlK(SO_4)_2.12H_2O$) and ammonium dihydrogen orthophosphate ($NH_4H_2PO_4$) were examined through the application of an automated crystallisation cell. Solution temperature, conductivity and turbidometry were compared and contrasted as means of detecting the onset of nucleation. In general it was found that greater changes in solu-

tion transmittance and higher rates of change of solution transmittance were recorded than for the corresponding conductivity measurements, which implied that turbidometry was more sensitive than conductivity to the onset of nucleation. The presence of heteronuclei in the crystallising solution lead to significant experimental scatter in precipitation based parameters, e.g. crystallisation temperatures, and induction times. In general, greater experimental scatter was observed for measured rates of change of solution transmittance and conductivity than for the corresponding induction times. Interfacial energies may only be derived from induction time measurements, since the rate of change of solution transmittance and conductivity are not equivalent to nucleation rate measurements. Hence, a further conversion factor is required before the rates of change of solution transmittance and conductivity may be equated to nucleation rates, for the subsequent calculation of interfacial energies.

The crystallisation kinetics of sodium sulphate decahydrate ($Na_2SO_4.10H_2O$) and sodium carbonate decahydrate ($Na_2CO_3.10H_2O$) were also examined through application of this cell. In general, good agreement was noted between the determined saturation curves and previous studies. The possibility of detection of metastable phases was highlighted by $Na_2SO_4.7H_2O$, which was observed by turbidometry during very slow cooling (^0C/hr) of a solution. Interfacial energies of the order (10^{-4}-10^{-3})Jm^{-2} were determined for the systems studied. These are somewhat lower than predicted interfacial energies, due to the influences of heteronucleation, and the need for further refinement of the model upon which the predicted interfacial energies are based.

Temperature as a means of detecting nucleation is dependent on the heat of crystallisation for the system studied and was only found to be applicable to $Na_2CO_3.10H_2O$ and $Na_2SO_4.10H_2O$.

- The crystallisation and agglomeration of habit modified burkeite and it's resultant conversion to a powder suitable for detergent operation was investigated. It was determined that a significant proportion (approx. 70%) of the desirable intra-particle pore size distribution required for efficient liquid uptake, occurred

during the initial batch crystallisation. The choice of impeller and power input dictated the degree of mixing in a crystallising system. This had ramifications for the porosity and phase composition of the crystallised slurry. No evidence for a crystallising burkeite slurry to tend towards a monosize particle distribution was noted, thus Ostwald ripening does not play a role during burkeite crystallisation. Milling of a slurry to prevent nozzle blockage during spray drying, was noted to significantly increase liquid uptake, possibly by agglomerate breakdown, exposing a greater percentage of a particles' internal pore structure. Variation of spray drying conditions influenced the liquid uptake of a powder. Increasing the feed input to the drying medium leads to more particle collisions, hence greater agglomeration. It was determined that the inter-, not the intraparticle porosity increased with increasing feed input to the drying medium. Decreasing the air inlet rate leads to milder drying conditions, which lessens the disruption of particle agglomeration. Decreasing the air inlet lead to a corresponding increase in the interparticle and intraparticle porosity.

8.3 Suggestions For Further Work

- It is clear that in order to predict morphologies based on interionic force calculations, an accelarated convergence routine should be incorporated into HABIT, to allow rapid convergence of ionic lattice energy sums. Thus attachment energies could be directly calculated to allow better correlation between predicted and observed growth morphologies.

  Current studies are directed towards the determination of interionic potentials to describe the structure and properties of Na_2CO_3. The combination of the determined potentials for Na_2CO_3 and Na_2SO_4 may allow the elucidation of potentials describing the structure and properties of burkeite, $Na_2CO_3(Na_2SO_4)_2$. At present, potentials describing hydrate interactions may only be calculated quantam mechanically; a methodology should be determined for the empirical derivation of such potentials.

- The habit modification of $Na_2CO_3.H_2O$ and $Na_2CO_3.10\ H_2O$ requires further investigation. A greater variety of impurities should be investigated, to improve the understanding of the impurity/crystal relationship for these systems. The growth kinetics of the forms predicted to act as sites for modification could be studied, to further investigate the effects of impurity concentration and absorption on the growth rates of these faces.

- The supercell reflections that were detected during the re-examination of the Na_2CO_3-Na_2SO_4-H_2O system require further examination to: completely identify all possible supercells that exist for burkeite and establish the connection between supercell formation, solution composition and precipitation temperature.

- In studies of crystallisation kinetics, the range of preheating time and temperature should be further expanded to improve the understanding of the influences of preheating time/temperature on crystallisation. A greater degree of solution agitation should be employed in future studies, to ensure greater homogenity of conditions throughout the solution.

  Light scattering at 90^0 is considered to be more sensitive than conventional 180^0 light reflectance. This in conjunction with a more intense light source (e.g. a He-Ne laser) (figure 6.36) should greatly improve the sensitivity of turbidometry to nucleation and should be further investigated. Attempts should be made to incorporate in-situ x-ray techniques into crystallisation studies. Such an incorporation would allow possible solution structure and ordering to be probed in detail and would also allow an investigation of the existence of pre-nuclei, which have previously been predicted.

- Spray drying is the preferred technique for the preparation of highly porous, high surface area powders, especially of use as carrier materials in the detergent industry. It was observed in this study that the powder porosity of a milled burkeite slurry was higher than the porosity of the resultant spray dried powder, implying that the capacity for liquid uptake (hence resultant efficiency of detergent carrier system) is reduced during spray drying. This would imply that

the conditions for spray drying are not at the optimum level for maximum liquid uptake. A fine balance must be struck during spray drying to obtain the desired powder moisture and porosity levels, e.g. if the drying rate is too high, then powder porosity is adversely affected. The inter-relationships between feed inlet rate, spray nozzle diameter ratio employed, drying air inlet rate and temperature require a detailed investigation, to further optimise the liquid uptake of a spray dried powder.

Appendix A - The Slow Cool/Heat Cycle

The methodology for the slow cool/heating cycle has been described in section 5.4.1. A controlled slow cooling/heating of a solution is conducted, with the resultant crystallisation/dissolution recorded by turbidometry and conductivity.

The computer program has been written in PASCAL for a BBC-B microcomputer in conjunction with a 65C102 second processor unit. Experimental conditions are initially inputted interactively. The determined solution temperature, transmittance and conductivity measurements are recorded to screen, printer and a second file "rawdata" on a second diskdrive. The resultant precipitation and dissolution temperatures based on turbidometric and conductivity measurements are recorded in two files, "datat" and "datac" respectively. A computer program to analyse these data files may be found elswhere [1]. Obviously there will be a limit to the number of readings that the computer memory can record. It has been found that the maximum length of time that can be employed for one cycle before the memory limit is exceeded is approximately five hours. However a delay routine "hangon" may be employed, which inserts an user-defined delay time between readings; consequently the maximum time that can be employed for one cycle before the memory limit is exceeded can be increased, but wih the disadvantage of introducing an error into the determination of precipitation and dissolution temperatures.

References

1. A.R. Gerson; PhD Thesis (1990) University of Strathclyde

Program "SLOW"

```
PROGRAM SLOW(INPUT,OUTPUT,DATAT,DATAC,RAWDATA);

VAR
  DATAC:TEXT;              {EXTERNAL FILE FOR CONDUCTIVITY DATA}
  DATAT:TEXT;              {EXTERNAL FILE FOR TURBIDITY DATA}
  RAWDATA:TEXT;            {RAW DATA OF THE RUNS, WRITTEN TO SECOND DISK DRIVE}
  N:INTEGER;               {NUMBER OF RATES}
  X,M,L,RUN,I,
  T,K:INTEGER;             {COUNTERS}
```

```
  RATE:ARRAY[1..100]
  OF REAL;                {TO STORE RATES}
  RN:INTEGER;             {NUMBER OF RUNS COMPLETE}
  LEVEL:REAL;             {TOP TEMPERATURE}
  TURBIDITY:REAL;         {AVERAGE TRANSMITTANCE RECORDED FOR A CLEAR SOLUTION}
  CONDUCTIVITY:REAL;      {AVERAGE CONDUCTIVITY RECORDED FOR A CLEAR SOLUTION}
  TURB:REAL;              {TURBIDITY}
  COND:REAL;              {CONDUCTIVITY}
  TEMPCELL:REAL;          {TEMPERATURE}
  BOTTOM:REAL;            {LOWEST TEMPERATURE}
  LOWEST:REAL;            {LOWEST TEMPERATURE ALLOWABLE}
  RESULT:INTEGER;         {RESULT
  TIM:INTEGER;            {TIME}
  MINS:INTEGER;           {LENGTH OF DELAY TIME BETWEEN READINGS}
  METATURB:REAL;          {COUNTER FOR RECORDING THE METASTABLE ZONE W.R.T. TURBIDITY}
  METACOND:REAL;          {COUNTER FOR RECORDING THE METASTABLE ZONE W.R.T.
                          CONDUCTIVITY
  PRETURB:REAL;           {FOR RECORDING THE META STABLEZONE W.R.T. TURBIDITY}
  PRECOND:REAL;           {FOR RECORDING THE META STABLEZONE W.R.T. CONDUCTIVITY}
  SATTURB:REAL;           {FOR RECORDING THE SATURATION TEMPERATURE W.R.T. TURBIDITY}
  SATCOND:REAL;           {FOR RECORDING THE SATURATION TEMPERATURE W.R.T.
                          CONDUCTIVITY}

{CALIBRATION PROCEDURE FOR TEMPERATURE}
PROCEDURE TEMPERATURE;
VAR
    M:INTEGER;
    I:INTEGER;
    MSB,LSB:REAL;
BEGIN
    M:=TIME;
    RESULT:=CODEO(&FFF4,&93,6,224+16+0) ;    {SETTING CHANNEL TO 9}
    WHILE (TIME-M)<10 DO BEGIN END;
    RESULT:=CODEO(&FFF4,&93,4,0);            {SETTING TO MONOPOLAR}
    WHILE (TIME-M)<20 DO BEGIN END;
    RESULT:=CODEO(&FFF4,&93,5,1);            {RANGE 0 TO 5 VOLT}
    WHILE (TIME-M)<30 DO BEGIN END;
    TEMPCELL:=0;
    I:=0;
    MSB:=0;
    LSB:=0;
    WHILE (TIME-M)< 1000 DO
BEGIN
    RESULT:=CODEO(&FFF4,&93,0,0);            {TO INTIATE CONVERSION}
    MSB:=(CODEO(&FFF4,&92,0,0)/&10000)+MSB; {READING MOST SIGNIFIGANT BYTE}
    LSB:=(CODEO(&FFF4,&92,1,0)/&10000)+LSB; {READING THE LEAST SIGNIFIGANT BYTE}
    I:=I+1;
END;
    MSB:=MSB/I;
    MSB:=((MSB/&100)-TRUNC(MSB/&100))*&100;
    LSB:=LSB/I;
    LSB:=((LSB/&100)-TRUNC(LSB/&100))*&100;
    TEMPCELL:=(MSB*16)+(LSB/16);
    TEMPCELL:=(0.0252236*TEMPCELL)-1.117;   {CALIBRATION LINE}
END;


{PROCEDURE TO CALIBRATE TURBIDITY}
 PROCEDURE MURKY;
VAR
    M:INTEGER;
    I:INTEGER;
    MSB,LSB:REAL;
BEGIN
    M:=TIME;
    RESULT:=CODEO(&FFF4,&93,6,224+16+13);   {SETTING TO CHANNEL 13}
    WHILE (TIME-M)<10 DO BEGIN END;
    RESULT:=CODEO(&FFF4,&93,4,2);           {SETTING TO BIPOLAR}
    WHILE (TIME-M)<20 DO BEGIN END;
    RESULT:=CODEO(&FFF4,&93,5,1);           {SETTING RANGE -5 TO 5 VOLTS}
```

```
    WHILE (TIME-M)<20 DO BEGIN END;
    I:=0;
    MSB:=0;
    LSB:=0;
    WHILE (TIME-M)<250 DO
    BEGIN
    RESULT:=CODEO(&FFF4,&93,0,0);
    MSB:=(CODEO(&FFF4,&92,0,0)/&10000)+MSB; {READING MOST SIGNIFICANT BYTE}
    LSB:=(CODEO(&FFF4,&92,1,0)/&10000)+LSB; {READING LEAST SIGNIFICANT BYTE}
    I:=I+1;
END;
    MSB:=MSB/I;
    MSB:=((MSB/&100)-TRUNC(MSB/&100))*&100;
    LSB:=LSB/I;
    LSB:=((LSB/&100)-TRUNC(LSB/&100))*&100;
    TURB:=(MSB*16)+(LSB/16);
    TURB:=(0.2442*TURB)-500;                {CALIBRATION LINE}
END;


{PROCEDURE TO CALIBRATE CONDUCTIVITY}
PROCEDURE IONIC;
VAR
    M:INTEGER;
    I:INTEGER;
    MSB,LSB:REAL;
BEGIN
    M:=TIME;
    RESULT:=CODEO(&FFF4,&93,6,224+16+11);   {SETTING TO CHANNEL 11}
    WHILE (TIME-M)<10 DO BEGIN END;
    RESULT:=CODEO(&FFF4,&93,4,2);           {SETTING TO BIPOLAR}
    WHILE (TIME-M)<20 DO BEGIN END;
    RESULT:=CODEO(&FFF4,&93,5,1);           {SETTING RANGE -5 TO 5 VOLTS}
    WHILE (TIME-M)<20 DO BEGIN END;
    I:=0;
    MSB:=0;
    LSB:=0;
    WHILE (TIME-M)<250 DO
BEGIN
    RESULT:=CODEO(&FFF4,&93,0,0);
    MSB:=(CODEO(&FFF4,&92,0,0)/&10000)+MSB; {READING MOST SIGNIFICANT BYTE}
    LSB:=(CODEO(&FFF4,&92,1,0)/&10000)+LSB; {READING LEAST SIGNIFICANT BYTE}
    I:=I+1;
END;
    MSB:=MSB/I;
    MSB:=((MSB/&100)-TRUNC(MSB/&100))*&100;
    LSB:=LSB/I;
    LSB:=((LSB/&100)-TRUNC(LSB/&100))*&100;
    COND:=(MSB*16)+(LSB/16);
    COND:=(COND*0.245356)-502.965;          {CALIBRATION LINE}
END;


{PROCEDURE TO SET TEMPERATURE}
PROCEDURE CELL(TEMP:REAL);
VAR
    M:INTEGER;
    POWER:REAL;
    MSB,LSB:INTEGER;
BEGIN
    M:=TIME;
    IF TEMP>=(-0.9) THEN
BEGIN
    RESULT:=CODEO(&FFF4,&93,&A,7);          {SETTING 0 TO 1 VOLTS}
    TEMP:=TEMP+0.90;
END
    ELSE
BEGIN
    RESULT:=CODEO(&FFF4,&93,&A,6);          {SETTING -1 TO 0 VOLTS}
    TEMP:=TEMP+0.90;
```

```
END;
    WHILE (TIME-M)<10 DO BEGIN END;
    POWER:=ABS(TEMP*41.2525)-16.591;        {CALIBRATION LINE}
    MSB:=TRUNC(POWER/16);                   {SENDING MOST SIGNIFICANT BYTE}
    LSB:=TRUNC((POWER-(MSB*16))*16);        {SENDING LEAST SIGNIFICANT BYTE}
    RESULT:=CODEO(&FFF4,&93,8,LSB);
    RESULT:=CODEO(&FFF4,&93,9,MSB);
    RESULT:=CODEO(&FFF4,&93,8,LSB);
END;


PROCEDURE HANGON(MINS:INTEGER);
VAR
   BEGTIME:INTEGER;
BEGIN
   WHILE ((TIME-BEGTIME)/6000) < MINS DO
BEGIN
BEGIN
END;
END;
END;

BEGIN   {MAIN PROGRAM}
WRITELN;
WRITELN(' THIS PROGRAM ALLOWS THE DETERMINATION OF ');
WRITELN(' PRECIPITATION AND DISSOLUTION TEMPERATURES');
WRITELN;
WRITE('HOW MANY DIFFERANT TEMPERATURE INCREASE RATES DO YOU WANT ? ');
READLN(N);
WRITELN;
WRITELN('STATE RATES IN DEGREES/HOUR-ONE RATE PER LINE ');
FOR I:=1 TO N DO
READLN(RATE[I]);
WRITELN;
WRITE('HOW LONG (IN MINUTES) DO YOU WANT TO HEAR THE SOLUTION FOR ?');
READLN(TIM);
WRITELN;
WRITE('HOW MANY RUNS DO YOU WANT FOR EACH RATE ? ');
READLN(RN);
WRITELN;
WRITELN('WHAT IS THE MAXIMUM TEMPERATURE THE SOLUTION SHOULD BE HEATED TO ?');
WRITELN('IF THE TEMPERATURE YOU INPUT IS EXCEEDED BEFORE THE');
WRITELN('PRECIPITATION FULLY DISSOLVES THE PROGRAM WILL STOP');
READLN(LEVEL);
WRITELN;
WRITELN('WHAT IS THE MINIMUM TEMPERATURE THE SOLUTION SHOULD BE COOLED TO ?');
WRITELN('IF THIS TEMPERATURE IS REACHED BEFORE PRECIPITATION OCCURS');
WRITELN('THE PROGRAM WILL STOP');
READLN(LOWEST);
WRITELN;
WRITELN('WHAT IS THE DELAY TIME?');
READLN(MINS);

    SETTIME(0);
    RESULT:=CODEO(&FFF4,&93,&F,1);     {SETTING OUPUT TO CHANNELS 2 AND 3}
    WHILE TIME<10 DO BEGIN END;
    REWRITE(DATAC, 'DATAC');
    WRITELN(DATAC,'  HEATING RATE      TEMPERATURE OF      PRECIPITATION');
    WRITELN(DATAC,'  (C/MIN)           DISSOLUTION(C)      TEMPERATURE (C)');
    REWRITE(RAWDATA, ':1.RAWDATA');
    WRITELN(RAWDATA,' TIME     TEMPERATURE          TURBIDITY           CONDUCTIVITY');
    WRITELN(RAWDATA,'  (MINS)     (DEG C)        (% TRANSMITTANCE)        (1000US/CM)');
    REWRITE(DATAT, 'DATAT');
    WRITELN(DATAT,' HEATING RATE      TEMPERATURE OF      PRECIPITATION');
    WRITELN (DATAT,'  (C/MIN)         DISSOLUTION(C)      TEMPERATURE (C)');
    METATURB:=2;
    METACOND:=2;
    SATTURB:=2;
    SATCOND:=2;
    FOR K:=1 TO N DO
```

```
BEGIN
    FOR M:=1 TO RN DO
BEGIN
    IF (METATURB=2) OR (METACOND=2) THEN
BEGIN
    METATURB:=0;
    METACOND:=0;
    SATTURB:=0;
    SATCOND:=0;
    WRITELN;
    WRITELN;
    WRITELN;
    WRITELN;
    WRITELN;
    I:=0;
    TURBIDITY:=0;
    CONDUCTIVITY:=0;
    SETTIME(0);
    CELL(LEVEL);
    TEMPERATURE;
    WHILE (TIME < (5*6000)) DO TEMPERATURE;
    I:=0;
    SETTIME(0);
    WRITELN('HOLDING THE TEMPERATURE STEADY ');
    WRITELN('FOR ',TIM:4,'  MINUTES AT APPROXIMATELY ',LEVEL:6:2,' DEGREES');
    WRITELN;
    WRITELN('  TIME         TEMPERATURE          TURBIDITY          CONDUCTIVITY');
    WRITELN('  (MIN)        (CELCIUS)         (%TRANSMITTANCE)    (1000uS/CM)');
    SETTIME(0);
    WHILE TIME< (TIM*6000) DO       {TIM  MINUTES}
BEGIN
    TEMPERATURE;
    MURKY;
    IONIC;
    IF (TIME MOD 30000) < 5000 THEN
BEGIN
    I:=I+1;
    TURBIDITY:=TURBIDITY+TURB;
    CONDUCTIVITY:=CONDUCTIVITY+COND;
    WRITELN('  ',TIME/6000:6:3,'         ',TEMPCELL:6:2,'              ',TURB:6:2,'
          ',COND:6:2);
    WRITELN(RAWDATA,' ',TIME/6000:6:3,'    ',TEMPCELL:6:2,'              ',TURB:6:2,'
          ',COND:6:2);
END;
END;
    TURBIDITY:=TURBIDITY/I;
    CONDUCTIVITY:=CONDUCTIVITY/I;
    WRITELN;
    WRITELN('THE AVERAGE TRANSMITTANCE OVER A "TIM" MINUTE PERIOD WHILE');
    WRITELN('THE SOLUTION WAS AT ITS MAXIMUM PERMITTED TEMPERATURE');
    WRITELN('WAS ',TURBIDITY:6:2);
    WRITELN(RAWDATA,'THE AVERAGE TRANSMITTANCE OVER A "TIM" MIN PERIOD WHILE');
    WRITELN(RAWDATA,'THE SOLUTION WAS AT ITS MAXIMUM PERMITTED TEMPERATURE');
    WRITELN(RAWDATA,'WAS',TURBIDITY:6:2);
    WRITELN;
    WRITELN('THE AVERAGE CONDUCTIVITY OVER A "TIM" MINUTE PERIOD WHILE');
    WRITELN('THE SOLUTION WAS AT ITS MAXIMUM PERMITTED TEMPERATURE');
    WRITELN('WAS ',CONDUCTIVITY:6:2);
    WRITELN(RAWDATA,'THE AVERAGE CONDUCTIVITY OVER A "TIM" MINUTE PERIOD WHILE');
    WRITELN(RAWDATA,'THE SOLUTION WAS AT ITS MAXIMUM PERMITTED TEMPERATURE');
    WRITELN(RAWDATA,'WAS ',CONDUCTIVITY:6:2);
    WRITELN;
    WRITELN;
    WRITELN;

    WRITELN('COOLING THE SOLUTION DOWN FROM ',LEVEL:6:2,' TO ',LOWEST:6:2);
    WRITELN('OR UNTIL THE TURBIDITY AND CONDUCTIVITY CHANGE BY 10% AND 50% ');
    WRITELN(' RESPECTIVELY AT RATE ',RATE[K]:6:2,' DEGREES PER HOUR');
    WRITELN(RAWDATA,'COOLING THE SOLUTION DOWN FROM ',LEVEL:6:2,' TO ',LOWEST:6:2);
    WRITELN(RAWDATA,'AT RATE ',RATE[K]:6:2,' DEGREES PER HOUR');
```

```
    WRITELN;
    WRITELN(RAWDATA,' TIME     TEMPERATURE     TURBIDITY        CONDUCITIVTY');
    WRITELN(RAWDATA,' (MIN)      (DEG C)    (% TRANSMITTANCE)   (1000US/CM)');
    WRITELN('   TIME         TEMPERATURE      TURBIDITY      CONDUCTIVITY');
    WRITELN('  (MIN)          (CELCIUS)     (%TRANSMITTANCE)    (1000uS/CM)');
    TEMPERATURE;
    MURKY;
    IONIC;
    SETTIME(0);
    WHILE (TEMPCELL-LOWEST>0) AND ((METATURB=0) OR (METACOND=0)) DO
BEGIN
    HANGON(MINS);
    BOTTOM:=LEVEL-(TIME*RATE[K]/6000);
    CELL(BOTTOM);
    TEMPERATURE;
    MURKY;
    IONIC;
    IF (((TURBIDITY-TURB)>10) AND (METATURB=0)) THEN
    BEGIN
    PRETURB:=TEMPCELL;
    METATURB:=1;
END;
    IF (((CONDUCTIVITY-COND)>50) AND (METACOND=0)) THEN
BEGIN
    METACOND:=1;
    PRECOND:=TEMPCELL;
END;
    IF (TIME MOD 30000) < 2000 THEN
    WRITELN(' ',TIME/6000:6:3,'        ',TEMPCELL:6:2,'         ',TURB:6:2,'
        ',COND:6:2);
    WRITELN(RAWDATA,' ',TIME/6000:6:3,'  ',TEMPCELL:6:2,'         ',TURB:6:2,'
        ',COND:6:2);
END;

    IF METATURB=0 THEN
BEGIN
    WRITELN;
    WRITELN('THE TURBIDITY OF THE SOLUTION CHANGED BY LESS THAN 10%');
    WRITELN('ON COOLING BETWEEN ',LEVEL:6:2,' AND ',TEMPCELL:6:2,' THIS IMPLIES');
    WRITELN('THAT NO SIGNIFIGANT PRECIPATATION OCCURED');
    WRITELN(DATAT,' NO PRECIPATATION OCCURED BY THE LOWEST TEMPERATURE');
    WRITELN(DATAT,TEMPCELL:6:2);
    WRITELN(DATAT);
END;
    IF METACOND=0 THEN
BEGIN
    WRITELN;
    WRITELN('THE CONDUCTIVITY OF THE SOLUTION CHANGED BY LESS THAN 50%');
    WRITELN('ON COOLING BETWEEN ',LEVEL:6:2,' AND ',TEMPCELL:6:2,' THIS IMPLIES');
    WRITELN('THAT NO SIGNIFICANT PRECIPITATION OCCURED');
    WRITELN(DATAC,' NO PRECIPITATION OCCURED BY THE LOWEST TEMPERATURE');
    WRITELN(DATAC,TEMPCELL:6:2);
    WRITELN(DATAC);
END;
    IF (METATURB=1) THEN
BEGIN
    WRITELN;
    WRITELN('THE META STABLE ZONE EDGE AS INDICATED BY A 10% DROP IN');
    WRITELN('TRANSMITTANCE FOR THE COOLING RATE OF ',RATE[K]:6:2,' DEGREES');
    WRITELN('PER MINUTES WAS AT ',PRETURB:6:2,' DEGREES');
    WRITELN;
END;
    IF (METACOND=1) THEN
BEGIN
    WRITELN;
    WRITELN('THE META STABLE ZONE EDGE AS INDICATED BY A 50% DROP IN');
    WRITELN('CONDUCTIVITY FOR THE COOLING RATE OF ',RATE[K]:6:2,' DEGREES');
    WRITELN('PER MINUTES WAS AT ',PRECOND:6:2,' DEGREES');
    WRITELN;
END;
```

```
    WRITELN('    TIME        TEMPERATURE        TURBIDITY        CONDUCTIVITY ');
    WRITELN('    (MIN)         (DEG C)     (% TRANSMITTANCE)       (1000US/CM) ');
    WHILE (TEMPCELL-LOWEST>0) DO
BEGIN
    HANGON(MINS);
    BOTTOM:=LEVEL-(TIME*RATE[K]/6000);
    CELL(BOTTOM);
    TEMPERATURE;
    MURKY;
    IONIC;
    IF (TIME MOD 15000) < 2000 THEN
    WRITELN('   ',TIME/6000:6:3,'          ',TEMPCELL:6:2,'          ',TURB:6:2,'
         ',COND:6:2);
    WRITELN(RAWDATA,' ',TIME/6000:6:3,'     ',TEMPCELL:6:2,'          ',TURB:6:2,'
        ',COND:6:2);
END;

    IF ((METATURB=1) AND (METACOND=1)) THEN
    WRITELN;
    WRITELN('HEATING THE SOLUTION UP FROM ',TEMPCELL:6:2,' TO ',LEVEL:6:2);
    WRITELN('AT ',RATE[K]:6:2,' DEGREES PER MINUTE');
    WRITELN(RAWDATA,' HEATING THE SOLUTION UP FROM ',TEMPCELL:6:2,' TO ',LEVEL:6:2);
    WRITELN(RAWDATA,'AT ',RATE[K]:6:2,' DEGREES PER MINUTE');
    WRITELN;
    SETTIME(0);
    WRITELN('    TIME          TEMPERATURE         TURBIDITY     CONDUCTIVITY');
    WRITELN('    (MIN)          (CELCIUS)     (% TRANSMITTANCE)  (1000uS/CM)');
    WHILE (TEMPCELL<LEVEL) AND ((METATURB=1) OR (METACOND=1)) DO
BEGIN
    HANGON(MINS);
    CELL(((TIME*RATE[K])/6000)+LOWEST);
    MURKY;
    IONIC;
    TEMPERATURE;
    IF ((TURBIDITY-TURB)<10) AND (METATURB=1) THEN
BEGIN
    SATTURB:=TEMPCELL;
    METATURB:=2;
END;
    IF ((CONDUCTIVITY-COND)<50) AND (METACOND=1) THEN
BEGIN
    SATCOND:=TEMPCELL;
    METACOND:=2;
END;
    IF (TIME MOD 15000) <2000 THEN
    WRITELN('     ',TIME/6000:6:3,'           ',TEMPCELL:6:2,'          ',TURB:6:2,'
          ',COND:6:2);
    WRITELN(RAWDATA,' ',TIME/6000:6:3,'        ',TEMPCELL:6:2,'          ',TURB:6:2,'
         ',COND:6:2);
END;

    IF METATURB=1 THEN
BEGIN
    WRITELN;
    WRITELN('THE TURBIDITY DID NOT COME WITHIN 10% TRANSMITTANCE');
    WRITELN('OF THE AVERAGE RECORDED FOR A CLEAR SOLUTION');
    WRITELN(DATAT,'  ',RATE[K]:6:2,'          ',PRETURB:6:2);
    WRITELN(DATAT,' THE TURBIDITY DID NOT COME WITHIN 10%');
    WRITELN(DATAT,' OF THE AVERAGE RECORDED FOR A CLEAR');
    WRITELN(DATAT,' SOLUTION');
END;

    IF METACOND=1 THEN
BEGIN
    WRITELN;
    WRITELN('THE CONDUCTIVITY DID NOT COME WITHIN 50% CONDUCTANCE');
    WRITELN('OF THE AVERAGE RECORDED FOR A CLEAR SOLUTION');
    WRITELN(DATAC,'  ',RATE[K]:6:2,'        ',PRECOND:6:2);
    WRITELN(DATAC);
    WRITELN(DATAC,' THE CONDUCTIVITY DID NOT COME WITHIN 50%');
```

```
    WRITELN(DATAC,'  OF THE AVERAGE RECORDED FOR A CLEAR');
    WRITELN(DATAC,' SOLUTION');
END;

    IF METATURB=2 THEN
BEGIN
    WRITELN;
    WRITELN('THE TEMPERATURE AT WHICH THE SOLUTION REACHED A VALUE');
    WRITELN('WITHIN 10% TRANSMITTANCE OF THE AVERAGE RECORDED');
    WRITELN('FOR A CLEAR SOLUTION WAS ',SATTURB:6:2);
    WRITELN(RAWDATA,'THE TEMPERATURE AT WHICH THE SOLUTION REACHED A VALUE');
    WRITELN(RAWDATA,' WITHIN 10% TRANSMITTANCE OF THE AVERAGE RECORDED');
    WRITELN(RAWDATA,' FOR A CLEAR SOLUTION WAS ',SATTURB:6:2);
    WRITELN(DATAT,'  ',RATE[K]:6:2,'          ',SATTURB:6:2,'
    ',PRETURB:6:2);
END;

    IF METACOND=2 THEN
BEGIN
    WRITELN;
    WRITELN('THE TEMPERATURE AT WHICH THE SOLUTION REACHED A VALUE');
    WRITELN('WITHIN 50% CONDUCTANCE OF THE AVERAGE RECORDED');
    WRITELN('FOR A CLEAR SOLUTION WAS ',SATCOND:6:2);
    WRITELN(DATAC,'  ',RATE[K]:6:2,'          ',SATCOND:6:2,'
    ',PRECOND:6:2);
    WRITELN(RAWDATA,'THE TEMPERATURE AT WHICH THE SOLUTION REACHED A VALUE');
    WRITELN(RAWDATA,'WITHIN 50% CONDUCTANCE OF THE AVERAGE RECORDED');
    WRITELN(RAWDATA,'FOR A CLEAR SOLUTION WAS',SATCOND:6:2);
END;
    WRITELN(' TIME        TEMPERATURE        TURBIDITY        CONDUCTIVITY ');
    WRITELN(' (MIN)          (DEG C)      (% TRANSMITTANCE)     (1000US/CM) ');
    WRITELN(RAWDATA,' TIME    TEMPERATURE     TURBIDITY       CONDUCTIVIY ');
    WRITELN(RAWDATA,' (MIN)    (DEG C)    (% TRANSMITTANCE)  (1000US/CM) ');
    WHILE (TEMPCELL<LEVEL) DO
BEGIN
    HANGON(MINS);
    CELL(((TIME*RATE[K])/6000)+LOWEST);
    TEMPERATURE;
    MURKY;
    IONIC;
    IF (TIME MOD 30000) < 2000 THEN
    WRITELN('    ',TIME/6000:6:3,'      ',TEMPCELL:6:2,'      ',TURB:6:2,'
    ',COND:6:2);
    WRITELN(RAWDATA,' ',TIME/6000:6:3,'  ',TEMPCELL:6:2,'     ',TURB:6:2,'
    ',COND:6:2);
END;

END;  {CHECK}
END;  {OF RUNS}
END;  {OF RATES}
END.  {OF PROGRAM}
```

Appendix B - The Crash Cool Cycle

The crash cool has been been described in section 5.4.2. A solution is cooled quickly at a controlled rate. The elapsed time time before crystallisation and the resultant nucleation rate is measured by turbidometry and conductivity. As for the computer program "SLOW", experimental conditions are initially inputted interactively. The solution temperature,transmittance and conductivity measurements are recorded to screen, printer and a data file "rawdata" on a second diskdrive. The measured induction times and nucleation rates based on transmittance and conductivity are written to two data files, "datat" and "datac" respectively. A computer program to analyse these data files may be found elsewhere [1]. As for the computer program "SLOW", an user defined delay time may be introduced to increase the maximum time limit for one cycle, although with the incurred errors previously mentioned.

References

1. A.R. Gerson; PhD Thesis (1990), University of Strathclyde

Program "CRASH"

```
{$W-}
 PROGRAM CRASHCOOL(INPUT,OUTPUT,DATAC,DATAT,RAWDATA);
VAR
   TIM:INTEGER;              {PREHEATING TIME}

{EXPERIMENTAL RESULT STORAGE}
   DATAC:TEXT;               {EXTERNAL FILE FOR RECORDING OF CONDUCTIVITY DATA}
   DATAT:TEXT;               {EXTERNAL FILE FOR RECOORDING OF TURBIDITY DATA}
   RAWDATA:TEXT;             {RAW DATA OF THE RUNS}

{CRYSTALLISATION VARIABLES}
   TURBCRYSTTIME:REAL;       {CRYSTALLISATION TIME BASED ON TURBIDITY}
   CONDCRYSTTIME:REAL;       {CRYSTALLISATION TIME BASED ON CONDUCTIVITY}
   TURBCRYSTTURB:REAL;       {FIRST DETECTION POINT OF CRYSTALLISATION,
                              BASED ON TURBIDITY}
   CONDCRYSTCOND:REAL;       {FIRST DETECTION POINT OF CRYSTALLISATION,
                              BASED ON CONDUCTIVITY}
   FINTURBCRYSTTIME:REAL; {FINAL TIME MEASURED W.R.T. TURBIDITY DURING
                           CRYSTALLISATION, BEFORE POSSIBLE TURBIDITY
                           INCREASE DUE TO HEAT OF CRYSTALLISATION}
   FINCONDCRYSTTIME:REAL; {FINAL TIME MEASURED W.R.T. CONDUCTIVITY DURING
                           CRYSTALLISATION, BEFORE POSSIBLE CONDUCTIVITY
                           INCREASE DUE TO HEAT OF CRYSTALLISATION}
   FINTURBCRYSTTEMP:REAL; {FINAL TEMPERATURE RECORDED W.R.T. TURBIDITY DURING
                           CRYSTALLISATION, BEFORE POSSIBLE TURBIDITY INCREASE
```

```
                          DUE TO HEAT OF CRYSTALLISATION}
    FINCONDCRYSTTEMP:REAL; {FINAL TEMPERATURE RECORDED W.R.T. CONDUCTIVITY DURING
                          CRYSTALLISATION, BEFORE POSSIBLE INCREASE DUE TO
                          HEAT OF CRYSTALLISATION}
    FINTURBCRYSTTURB:REAL; {FINAL TURBIDITY MEASURED DURING CRYSTALLISATION,
                          BEFORE POSSIBLE INCREASE DUE TO HEAT OF
                          CRYSTALLISATION}
    FINCONDCRYSTCOND:REAL; {FINAL CONDUCTIVITY MEASURED DURING CRYSTALLISATION,
                          BEFORE POSSIBLE INCREASE DUE TO HEAT OF
                          CRYSTALLISATION}
    COOLINGRATE:REAL;     {MAXIMUM COOLING RATE OF PARTICULAR HAAKE}
    TURBNUCRATE:REAL;     {NUCLEATION RATES BASED ON TURBIDITY}
    CONDNUCRATE:REAL;     {MEASURED NUCLEATION RATES BASED ON CONDUCTIVITY}
    TURBINDUCT:REAL;      {MEASURED INDUCTION TIMES BASED ON TURBIDITY}
    CONDINDUCT:REAL;      {MEASURED INDUCTION TIMES BASED ON CONDUCTIVITY}
    TURBCRYSTTEMP:REAL;   {TEMPERATURE DURING CRYSTALLISATION
                          WHERE CRYSTALLISATION DEFINED W.R.T. TURBIDITY}
    CONDCRYSTTEMP:REAL;   {TEMPERATURE DURING CRYSTALLISATION
                          WHERE CRYSATLLISATION DEFINED W.R.T. CONDUCTIVITY}
    RUN:INTEGER;          {NUMBER OF RUNS DONE FOR THE BOTTOM POWER}
    R:INTEGER;            {NUMBER OF RUNS REQUIRED FOR EACH  BOTTOM POWER}
    N:INTEGER;            {TOTAL NUMBER OF RUNS COMPLETED}
    SP:REAL;              {THE REQUIRED SPACINGS OF THE BOTTOM POWERS}
    POWER:INTEGER;        {NUMBER OF BOTTOM TEMPERATURES REQUIRED}
    NP:INTEGER;           {NUMBER OF BOTTOM POWERS TO BE DONE}
    BP:REAL;              {THE LOWEST OF THE BOTTOM POWERS}
  TURBIDITY,TURBNEW,
  TURBID:REAL;            {FOR COMPARISON OF TURBIDITY IN THE CELL}
  CONDUCTIVITY,CONDNEW,
  CONDUCT:REAL;           {FOR COMPARISON OF CONDUCTIVITY IN THE CELL}
  LEVEL:REAL;             {POWER REQUIRED}
  SATURATION:REAL;        {SATURATION TEMPERATURE}
  A,B,K,FINALA,FINALB,
  M,L,Z,T,I:INTEGER;      {COUNTERS}
  BEGTIME:INTEGER;        {TIME VARIABLE TO SET DELAY TIME}
  MINS:INTEGER;           {USER-DEFINED DELAY TIME}
  X:REAL;                 {POWER SETTING}
  RESULT:INTEGER;         {TO SET INPUT AND OUTPUT CHANNELS}
  TEMPCELL:REAL;          {SOLUTION TEMPERATURE }
  TURBOLD,TURB,
  CONDOLD,COND:REAL;      {TURBIDITY AND CONDUCTIVITY READINGS
                          DURING HEATING & INITIAL COOLING}

{CALIBRATION FUNCTION FOR THE INPUT FROM THE EXPERIMENTAL CELL}
PROCEDURE TEMPERATURE;
VAR
    M:INTEGER;
    I:INTEGER;
    MSB,LSB:REAL;
BEGIN
    M:=TIME;
    RESULT:=CODEO(&FFF4,&93,6,224+16+0);          {SETTING TO CHANNEL 0}
    WHILE (TIME-M)<10 DO BEGIN END;
    RESULT:=CODEO(&FFF4,&93,4,0);                 {SETTING TO MONOPOLAR}
    WHILE (TIME-M)<20 DO BEGIN END;
    RESULT:=CODEO(&FFF4,&93,5,1);                 {RANGE OF 0 TO 5 VOLT}
    WHILE (TIME-M)<30 DO BEGIN END;
    TEMPCELL:=0;
    I:=0;
    MSB:=0;
    LSB:=0;

    WHILE (TIME-M)<1000 DO
BEGIN
    RESULT:=CODEO(&FFF4,&93,0,0);                 {TO INITIATE CONVERSION}
    MSB:=(CODEO(&FFF4,&92,0,0)/&10000)+MSB;       {READING MOST SIGNIFIGANT BYTE}
    LSB:=(CODEO(&FFF4,&92,1,0)/&10000)+LSB;       {READING LEAST SIGNIFIGANT BYTE}
    I:=I+1;
END;
```

```
    MSB:=MSB/I;
    MSB:=((MSB/&100)-TRUNC(MSB/&100))*&100;
    LSB:=LSB/I;
    LSB:=((LSB/&100)-TRUNC(LSB/&100))*&100;
    TEMPCELL:=(MSB*16)+(LSB/16);
    TEMPCELL:=(0.0252276*TEMPCELL)-1.117;       {CALIBRATION LINE}
    END;


{FUNCTION TO CALIBRATE TURBIDITY}
PROCEDURE MURKY;
VAR
    M:INTEGER;
    I:INTEGER;
    MSB,LSB:REAL;
BEGIN
    M:=TIME;
    RESULT:=CODEO(&FFF4,&93,6,224+16+13);      {SETTING TO CHANNEL 13}
    WHILE  (TIME-M)<10 DO BEGIN END;
    RESULT:=CODEO(&FFF4,&93,4,2);              {SETTING TO BIPOLAR}
    WHILE (TIME-M)<20 DO BEGIN END;
    RESULT:=CODEO(&FFF4,&93,5,1);              {SETTING RANGE -5 TO 5VOLTS}
    WHILE (TIME-M)<30 DO BEGIN END;
    I:=0;
    MSB:=0;
    LSB:=0;
    WHILE (TIME-M)<250 DO
BEGIN
    RESULT:=CODEO(&FFF4,&93,0,0);              {INITIATING A 12 BIT A-D CONVERSION}
    MSB:=(CODEO(&FFF4,&92,0,0)/&10000)+MSB;    {READING MOST SIGNIFIGANT BYTE}
    LSB:=(CODEO(&FFF4,&92,1,0)/&10000)+LSB;    {READING LEAST SIGNIFIGANT BYTE}
    I:=I+1;
    END;
    MSB:=MSB/I;
    LSB:=LSB/I;
    MSB:=((MSB/&100)-TRUNC(MSB/&100))*&100;
    LSB:=((LSB/&100)-TRUNC(LSB/&100))*&100;
    TURB:=(MSB*16)+(LSB/16);                   {CALIBRATION LINE}
    TURB:=(TURB*0.2442)-500;
END;


{PROCEDURE TO CALIBRATE CONDUCTIVITY}
PROCEDURE IONIC;
VAR
    M:INTEGER;
    I:INTEGER;
    MSB,LSB:REAL;
BEGIN
    M:=TIME;
    RESULT:=CODEO(&FFF4,&93,6,224+16+11);      {SETTING TO CHANNEL 11}
    WHILE (TIME-M)<10 DO BEGIN END;
    RESULT:=CODEO(&FFF4,&93,4,2);              {SETTING TO BIPOLAR}
    WHILE (TIME-M)<20 DO BEGIN END;
    RESULT:=CODEO(&FFF4,&93,5,1);              {SETTING RANGE -5 TO 5 VOLTS}
    WHILE (TIME-M)<20 DO BEGIN END;
    I:=0;
    MSB:=0;
    LSB:=0;
    WHILE (TIME-M)<250 DO
BEGIN
    RESULT:=CODEO(&FFF4,&93,0,0);              {INITIATING A 12 BIT A-D CONVERSION}
    MSB:=(CODEO(&FFF4,&92,0,0)/&10000)+MSB;    {READING MOST SIGNIFICANT BYTE}
    LSB:=(CODEO(&FFF4,&92,1,0)/&10000)+LSB;    {READING LEAST SIGNIFICANT BYTE}
    I:=I+1;
END;
    MSB:=MSB/I;
    MSB:=((MSB/&100)-TRUNC(MSB/&100))*&100;
    LSB:=LSB/I;
    LSB:=((LSB/&100)-TRUNC(LSB/&100))*&100;
```

```
    COND:=(MSB*16)+(LSB/16);
    COND:=(0.245356*COND)-502.965;          {CALIBRATION LINE}
END;


{FOR ANALOGUE OUTPUT, WRITTEN TO PROCEDURE THE TEMPERATURE DESIRED}
PROCEDURE CELL(TEMP:REAL);
VAR
    M:INTEGER;
    POWER:REAL;
    MSB,LSB:INTEGER;
BEGIN
    {ONLY USING CHANNEL 2 WHICH IS IN A}
    {SET FOR RANGE -1 TO 0 OR 0 TO 1 VOLT FOR A}
    POWER:=ABS(41.2525*TEMP)-16.591;        {CALIBRATION LINE}
    M:=TIME;
    IF TEMP>=0 THEN
BEGIN
    RESULT:=CODEO(&FFF4,&93,&A,7);
END
    ELSE
BEGIN
    RESULT:=CODEO(&FFF4,&93,&A,6);
END;
    WHILE (TIME-M)<10 DO BEGIN END;
    MSB:=TRUNC(POWER/16);
    LSB:=TRUNC((POWER-(MSB*16))*16);
    RESULT:=CODEO(&FFF4,&93,8,LSB);         {SENDING MOST SIGNIFIGANT BYTE}
    RESULT:=CODEO(&FFF4,&93,9,MSB);         {SENDING LEAST SIGNIFIGANT BYTE}
    RESULT:=CODEO(&FFF4,&93,8,LSB);
END;


PROCEDURE HANGON(MINS:INTEGER);
VAR
    BEGTIME:INTEGER;
BEGIN
    BEGTIME:=TIME;
    WHILE ((TIME-BEGTIME)/6000) < MINS DO
BEGIN
BEGIN
END;
END;
END;


BEGIN    {MAIN PROGRAM}
{PART ONE: EXPERIMENTAL}

WRITELN('THIS PROGRAM ALLOWS MEASUREMENTS OF INDUCTION TIMES');
WRITELN(AND NUCLEATION RATES. TO DISSOLVE RESIDUE CRYSTALS THE');
WRITELN('SOLUTION IS HEATED TO 20 DEGREES ABOVE THE SATURATION TEMPERATURE.');
WRITE('THE SATURATION TEMPERATURE IS ');
READLN(SATURATION);
WRITELN;

WRITE('HOW LONG (IN MINUTES) DO YOU WANT TO HEAT THE SOLUTION FOR ? ');
READLN(TIM);
WRITELN;

WRITE('HOW MANY LOWER TEMPERATURES DO YOU WANT? ');
READLN(NP);
WRITELN;

WRITE('WHAT IS THE LOWEST TEMPERATURE YOU WANT ?');
READLN(BP);
WRITELN;

WRITE('HOW MANY RUNS DO YOU WANT FOR EACH TEMPERATURES? ');
READLN(R);
```

```
WRITELN;

WRITE('AT WHAT SPACING DO YOU WANT YOUR BOTTOM TEMPERATURES? ');
READLN(SP);
WRITELN;

WRITE('WHAT RATE OF COOLING DO YOU WANT? ');
READLN(COOLINGRATE);
WRITELN;

WRITE('WHAT IS THE DELAY BETWEEN READINGS?');
READLN(MINS);
WRITELN;

SETTIME(0);

    {SETTING OUTPUT CHARACTERISTICS}
    SETTIME(0);
    RESULT:=CODEO(&FFF4,&93,&F,1);    {SETTING OUPUT TO CHANNEL 2(BANK A)
    REWRITE(DATAT, 'DATAT');
    WRITELN(DATAT,'THE SATURATION TEMPERATURE WAS ', SATURATION:6:2);
    WRITELN(DATAT);
    WRITELN(DATAT,'THE COOLING RATE WAS ', COOLINGRATE:6:2);
    WRITELN(DATAT);
    WRITELN(DATAT,'TEMPERATURE OF         INDUCTION TIME         NUCLEATION RATE');
    WRITELN(DATAT,'CRYSTALLISATION           (MIN)              (DELTA%TURB/MIN)');
    REWRITE(DATAC, 'DATAC');
    WRITELN(DATAC,'THE SATURATION TEMPERATURE WAS ', SATURATION:6:2);
    WRITELN(DATAC);
    WRITELN(DATAC,'THE COOLING RATE WAS ', COOLINGRATE:6:2);
    WRITELN(DATAC);
    WRITELN(DATAC,'TEMPERATURE OF        INDUCTION TIME         NUCLEATION RATE');
    WRITELN(DATAC,'CRYSTALLISATION           (MIN)          (DELTAUS1000/CM/MIN)');
    REWRITE(RAWDATA, ':1.RAWDATA');
    WRITELN(RAWDATA,'THE SATURATION TEMPERATURE WAS ', SATURATION:6:2);
    WRITELN(RAWDATA);
    WRITELN(RAWDATA,'THE COOLING RATE WAS ', COOLINGRATE:6:2);
    WRITELN;
    WRITELN;
    {SETTING OF COUNTERS}
    N:=0;
    FOR POWER:=1 TO NP DO
BEGIN
    FOR RUN:=1 TO R DO      {RUNS TO BE DONE FOR EACH BOTTOM TEMPERATURE}
BEGIN
    LEVEL:=(SP*(POWER-1))+BP;
    WRITELN('NOW DISSOLVING CRYSTALS BY HEATING THE');
    WRITELN('SOLUTION TO 20 DEGREES ABOVE THE SATURATION');
    WRITELN('TEMPERATURE FOR ',TIM:4,' MINUTES');
    WRITELN;
    SETTIME(0);
    WHILE TIME<(5*6000) DO CELL(SATURATION+20);
    WRITE(' TIME(MIN)    TEMPERATURE (C)  TURBIDIY(%TRANS)');
    WRITELN(             'CONDUCTIVITY (1000US/CM)');
    WRITELN(RAWDATA,' TIME       TEMPERATURE       TURBIDITY       CONDUCTIVITY');
    WRITELN(RAWDATA,' (MIN)        (DEG C)          (% TRANS)      (1000US/CM)');
    SETTIME(0);
    TURBIDITY:=0;
    CONDUCTIVITY:=0;
    TEMPERATURE;
    MURKY;
    IONIC;
    WHILE TIME<(5*6000) DO BEGIN END;
    SETTIME(0);
    I:=0;
    WHILE TIME < (TIM*6000)  DO
BEGIN
    IF (TIME MOD 60000<1000) THEN       {EVERY FIVE MINUTES}
BEGIN
    WRITELN(TIME/6000:7:3,'          ',TEMPCELL:6:2,'          ',TURB:6:2,'
```

```
      ',COND:6:2);
    WRITELN(RAWDATA,'   ',TIME/6000:7:3,'      ',TEMPCELL:6:2,'      ',TURB:6:2,'
      ',COND:6:2);
END;
    IF (TIME MOD 3000)<1500 THEN
BEGIN
    TEMPERATURE;
    MURKY;
    IONIC;
    I:=I+1;
    TURBIDITY:=TURBIDITY+TURB;
    CONDUCTIVITY:=CONDUCTIVITY+COND;
END;
END;
    TURBIDITY:=TURBIDITY/I;
    CONDUCTIVITY:=CONDUCTIVITY/I;
    WRITELN;
    WRITELN('THE AVERAGE TURBIDITY RECORDED WAS ', TURBIDITY:6:2);
    WRITELN(RAWDATA,' THE AVERAGE TURBIDITY RECORDED WAS ', TURBIDITY:6:2);
    WRITELN('THE AVERAGE CONDUCTIVITY RECORDED WAS ', CONDUCTIVITY:6:2);
    WRITELN(RAWDATA,' THE AVERAGE CONDUCTIVITY RECORDED WAS ', CONDUCTIVITY:6:2);
    I:=0;
    A:=0;
    B:=0;
    FINALA:=0;
    FINALB:=0;
    WRITELN;

    WRITELN('COMMENCING CRASH COOL');
    WRITELN(RAWDATA,' COMMENCING CRASH COOL');
    WRITELN('RUN ',RUN:2,' FOR THE LOWER TEMPERATURE OF ',LEVEL:6:2);
    WRITELN(RAWDATA,'RUN ',RUN:2,' FOR THE LOWER TEMPERATURE OF ',LEVEL:6:2);
    WRITELN;
    SETTIME(0);
    WRITELN('TIME            TEMPERATURE         TURBIDITY         CONDUCTIVITY ');
    WRITELN('(MIN)             (DEG C)           (%TRANS)           (1000US/CM) ');
    WRITELN(RAWDATA,' TIME         TEMPERATURE        TURBIDITY     CONDCUTIVITY ');
    WRITELN(RAWDATA,'  (MIN)        (DEG C)           (% TRANS)     (1000US/CM) ');
    WHILE TEMPCELL>SATURATION DO
BEGIN
    TEMPERATURE;
    CELL(SATURATION);
    IF (TIME MOD 30000) < 1500 THEN
    WRITELN(' ',TIME/6000:7:3,'           ',TEMPCELL:6:2,'             ',TURB:6:2,'
          ',COND:6:2);
    WRITELN(RAWDATA,' ',TIME/6000:7:3,'     ',TEMPCELL:6:2,'             ',TURB:6:2,'
          ',COND:6:2);
    END;
    Z:=0;
    M:=TIME;
    L:=TIME;
    TURBOLD:=TURB;
    TURBNEW:=TURB;
    CONDOLD:=COND;
    CONDNEW:=COND;
    WRITELN;
    WRITELN('NOW AT SATURATION TEMPERATURE ', SATURATION:6:2);
    WRITELN('DEG C; STARTING INDUCTION TIME MEASUREMENTS ');
    WRITELN(RAWDATA,' NOW AT SATURATION TEMPERATURE ', SATURATION:6:2);
    WRITELN;
    K:=TIME;
    WHILE ((A<2) OR (B<2)) AND ((TIME-K) < 1800000 ) DO
BEGIN
    HANGON(MINS);
    TEMPERATURE;
    MURKY;
    IONIC;
    IF ((TIME-K) MOD 30000) < 1500 THEN
    WRITELN(' ',(TIME-K)/6000:7:3,'           ',TEMPCELL:6:2,'
    ',TURB:6:2,'          ',COND:6:2);
```

```
    WRITELN(RAWDATA,' ',(TIME-K)/6000:7:3,'    ',TEMPCELL:6:2,'
    ',TURB:6:2,'          ',COND:6:2);
    IF ((TEMPCELL>BP) OR (TEMPCELL>LEVEL) AND (Z=0)) THEN
BEGIN
    X:=(SATURATION-((TIME-K)*COOLINGRATE/6000));
    CELL(X);
END;
    IF ((TEMPCELL>BP) OR (TEMPCELL=LEVEL) AND (Z=0)) THEN
BEGIN
    Z:=1;
    CELL(LEVEL);
END;

    IF (((TURBIDITY-TURB)>10) AND (A<1)) THEN
BEGIN
    A:=1;
    TURBCRYSTTURB:=TURB;
    TURBCRYSTTIME:=(TIME-K)/6000;
    TURBCRYSTTEMP:=TEMPCELL;
    M:=TIME;
END;
    IF (A=1) THEN
BEGIN
    TURBOLD:=TURBCRYSTTURB;
    TURBNEW:=TURB;
END;

    IF (((CONDUCTIVITY-COND) >50) AND (B<1)) THEN
BEGIN
    B:=1;
    CONDCRYSTCOND:=COND;
    CONDCRYSTTIME:=(TIME-K)/6000;
    CONDCRYSTTEMP:=TEMPCELL;
    L:=TIME;
END;
    IF (B=1) THEN
BEGIN
    CONDOLD:=CONDCRYSTCOND;
    CONDNEW:=COND;
END;

    IF (((TURBOLD-TURBNEW)<0) AND (A=1)) THEN
BEGIN
    FINTURBCRYSTTURB:=TURB;
    TURBOLD:=FINTURBCRYSTTURB;
    FINTURBCRYSTTIME:=(TIME-K)/6000;
    FINTURBCRYSTTEMP:=TEMPCELL;
    A:=2;
    FINALA:=1;
END
    ELSE
BEGIN
    TURBOLD:=TURBNEW;
    TURBNEW:=TURB;
END;
    IF (FINALA<>1) THEN
BEGIN
    IF (A=1) AND ((TIME-M)>600) THEN
BEGIN
    FINTURBCRYSTTURB:=TURB;
    FINTURBCRYSTTIME:=(TIME-K)/6000;
    FINTURBCRYSTTEMP:=TEMPCELL;
    A:=2;
END;
END;

    IF (((CONDOLD-CONDNEW)<0) AND (B=1)) THEN
BEGIN
    FINCONDCRYSTCOND:=COND;
    CONDOLD:=FINCONDCRYSTCOND;
```

```
    FINCONDCRYSTTIME:=(TIME-K)/6000;
    FINCONDCRYSTTEMP:=TEMPCELL;
    B:=2;
    FINALB:=1;
END
    ELSE
BEGIN
    CONDOLD:=CONDNEW;
    CONDNEW:=COND;
END;
    IF (FINALB<>1) THEN
BEGIN
    IF (B=1) AND ((TIME-L)>600) THEN
BEGIN
    FINCONDCRYSTCOND:=COND;
    FINCONDCRYSTTIME:=(TIME-K)/6000;
    FINCONDCRYSTTEMP:=TEMPCELL;
    B:=2;
END;
END;
END;

    IF (A=0) THEN
BEGIN
    WRITE('THE SOLUTION DID NOT CRYSTALLISE ACCORDING TO TURBIDITY MEASUREMENTS');
    WRITE('THE LAST TEMPERATURE RECORDED WAS  ',TEMPCELL:6:2);
    WRITELN;
    WRITELN(DATAT,' THE SOLUTION DID NOT CRYSTALLISE ACCORDING TO TURBIDITY
    MEASUREMENTS');
    WRITELN(DATAT);
    WRITELN(RAWDATA,' THE SOLUION DID NOT CYSTALLISE ACCORDING TO TURBIDITY
    MEASUREMENTS');
END;

    IF (A=1) THEN
BEGIN
    WRITE('THE SOLUTION CRYSTALLISED ACCORDING TO TURBIDITY MEASUREMENTS AT POINT');
    WRITE(TURBCRYSTTEMP:6:2,' AFTER TIME ',TURBCRYSTTIME/100:6:3);
    WRITELN(DATAT,'THE SOLUTION CRYSTALLISED AT', TURBCRYSTTEMP:6:2,' AFTER TIME
    ',TURBCRYSTTIME:6:3);
    WRITELN(RAWDATA,'THE SOLUTION CRYSTALLISED AT', TURBCRYSTTEMP:6:2,' AFTER TIME
    ', TURBCRYSTTIME:6:3);
END;

    IF (A=2) THEN
BEGIN
    TURBNUCRATE:=(TURBCRYSTTURB-FINTURBCRYSTTURB);
    TURBNUCRATE:=(60*100*TURBNUCRATE)/(FINTURBCRYSTTIME-TURBCRYSTTIME);
    TURBINDUCT:=TURBCRYSTTIME;
    WRITELN;
    WRITELN('TEMPERATURE OF             INDUCTION              NUCLEATION RATE');
    WRITELN('CRYSTALLISATION            TIME(TURB)            (DELTA%TURB/MIN)');
    WRITELN('    ',TURBCRYSTTEMP:6:2,'                ',TURBINDUCT:6:2,'
    ',TURBNUCRATE:12:8);
    WRITELN(RAWDATA,' TEMPERATURE OF     INDUCTION              NUCLEATION RATE');
    WRITELN(RAWDATA,' CRYSTALLISATION     TIME(TURB)            (DELTA%TURB/MIN)');
    WRITELN(RAWDATA,'   ',TURBCRYSTTEMP:6:2,'             ',TURBINDUCT:6:2,'
    ',TURBNUCRATE:12:8);
    WRITELN(RAWDATA);
    WRITELN;
    WRITELN(DATAT,'  ',TURBCRYSTTEMP:6:2,'               ',TURBINDUCT:6:2,'
    ',TURBNUCRATE:12:8);
END;

    IF (B=0) THEN
BEGIN
    WRITE('THE SOLUTION DID NOT CRYSTALLISE ACCORDING TO CONDUCTIVITY MEASUREMENTS');
    WRITELN;
    WRITELN(DATAC);
    WRITELN(DATAC,'THE SOLUTION DID NOT CRYSTALLISE ACCORDING TO CONDUCTIVITY
```

```
    MEASUREMENTS');
    WRITELN(DATAC);
    WRITELN(RAWDATA,' THE SOLUTION DID NOT CRYSTALLISE ACCORDING TO CONDUCTIVITY
    MEASUREMENTS');
END;

    IF (B=1) THEN
BEGIN
    WRITELN('THE SOLUTION CRYSTALLISED ACCORDING TO CONDUCTIVITY MEASUREMENTS AT
    POINT', CONDCRYSTTEMP:6:2,' AFTER TIME ',CONDCRYSTTIME:6:3);
    WRITELN;
    WRITELN(DATAC);
    WRITELN(DATAC,'THE SOLUTION CRYSTALLISED AT POINT', CONDCRYSTTEMP:6:2,'
    AFTER TIME ',CONDCRYSTTIME:6:3);
    WRITELN(DATAC);
    WRITELN(RAWDATA,'THE SOLUTION CRYSTALLISED AT POINT', CONDCRYSTTEMP:6:2,'
    AFTER TIME  ',CONDCRYSTTIME:6:3);
END;

    IF (B=2) THEN
BEGIN
    CONDNUCRATE:=(CONDCRYSTCOND-FINCONDCRYSTCOND);
    CONDNUCRATE:=(60*100*CONDNUCRATE)/(FINCONDCRYSTTIME-CONDCRYSTTIME);
    CONDINDUCT:=CONDCRYSTTIME;
    WRITELN('TEMPERATURE OF            INDUCTION          NUCLEATION RATE');
    WRITELN('CRYSTALLISATION           TIME(COND)     (DELTA 1000US/CM/MIN)');
    WRITELN(' ',CONDCRYSTTEMP:6:2,'                    ',CONDINDUCT:6:2,'
    ',CONDNUCRATE:12:8);
    WRITELN(RAWDATA,'TEMPERATURE OF      INDUCTION        NUCLEATION RATE');
    WRITELN(RAWDATA,'CRYSTALLISATION      TIME(COND)    (DELTA 1000US/CM/MIN)');
    WRITELN(RAWDATA,'  ',CONDCRYSTTEMP:6:2,'            ',CONDINDUCT:6:2,'
    ',CONDNUCRATE:6:2);
    WRITELN(RAWDATA);
    WRITELN;
    WRITELN(DATAC,'   ',CONDCRYSTTEMP:6:2,'             ',CONDINDUCT:6:2,'
    ',CONDNUCRATE:6:2);
END;
    SETTIME(0);
    WHILE (TIME < 360000) DO
BEGIN
    CELL(LEVEL);
    TEMPERATURE;
    MURKY;
    IONIC;
    WRITELN('   ',TIME/6000:7:3,'     ',TEMPCELL:6:2,'     ',TURB:6:2,'
    ',COND:6:2);

END;

END;   {OF THREE RUNS}
END;   {OF TEN BOTTOM TEMPERATURES}
END. {PROGRAM}
```

Appendix C: Publications Resulting From This Study

1. "Understanding and controlling the crystal morphology of some ionic salts": P. Meenan, K.J. Roberts, J.N. Sherwood and K.R. Yuregir; Powder Technology 65 1991 219-225

2. "Phase composition and morphology of particulates crystallised within the NA_2CO_3-Na_2SO_4-H_2O system": P. Meenan, K.J. Roberts and J.N. Sherwood : To be published in Transtech Publications as part of the ECCG-3 conference proceedings.

Posters Presented

1. "Crystallisation, growth morphology and habit modification of sodium carbonate monohydrate": P. Meenan, K.J. Roberts and J.N. Sherwood; Presented at the Ad-Hoc Crystal Workshop, Ross Priory, University of Strathclyde, 1989.

2. "The crystal morphology and crystal chemistry of some ionic salts": P. Meenan, K.J. Roberts and J.N. Sherwood; Presented at the Industrial Group Symposium, B.C.A. Spring Meeting, Oxford 1989.

3. "Computer modelling studies on beta potassium sulphate": P. Meenan, R.A. Jackson, M. Leslie and G.D. Price; Presented at the Symposium on "Structural Aspects of Crystal Growth", B.C.A. Spring Meeting, Exeter 1990.

4. "Industrial crystallisation of high surface area powders from mixtures of sodium carbonate and sodium sulphate": P. Meenan, K.J. Roberts and J.N. Sherwood; Presented at the B.A.C.G. 21st Annual Conference, Birmingham 1990.

5. "Understanding and controlling the crystal morphology of some ionic salts": P. Meenan, K.J. Roberts, J.N. Sherwood and K.R. Yuregir; Presented at the Second Symposium on Advances in Particulate Technology, Guilford 1991.

6. "Phase composition and morphology of particulates crystallised within the Na_2CO_3-Na_2SO_4-H_2O system":P. Meenan, K.J. Roberts and J.N. Sherwood; Presented at the Third European Conference on Crystal Growth, Budapest 1991.